Detonation Interaction with Sharp and Diffuse Interfaces

Thesis by

Daniel Lieberman

In Partial Fulfillment of the Requirements

for the Degree of

Doctor of Philosophy

California Institute of Technology

Pasadena, California

2006

(Submitted November 11th, 2005)

Acknowledgments

I am truly indebted to my advisor Professor Joseph Shepherd for being a source of inspiration and a role model, guiding my professional development. He instilled in me the qualities necessary for practicing "good" science. Professor Hans Hornung has been a great help throughout my years at Caltech, providing much insight into my research activities. I gratefully acknowledge the help of the other members of my doctoral committee, Professors Oscar Bruno, Anthony Leonard, and Dale Pullin.

I would like to acknowledge the past and present members of the Explosion Dynamics Research Group including Joanna Austin, Shannon Browne,Tony Chao, Marcia Cooper, Scott Jackson, James Karnesky, Christopher Krok, Florian Pintgen, and Eric Wintenberger for fostering a fun and positive learning atmosphere in the lab. Specifically, I would like to thank Florian Pintgen for countless engaging discussions and Shannon Browne and Alexandra Katsas for meticulously reading my thesis.

There are numerous people whose help along the way made graduating possible. Suzy Dake has been so vital that she is, in many ways, the glue that held my research together. Much thanks goes to Joe Haggerty, Brad St. John, and Ali Kiani for providing a great deal of technical assistance and making sure I did not lose any fingers. I must thank Amy Lam for being the ideal office mate and bestowing upon me the art of making membranes. To all my other colleagues whose names I must regretfully omit, thank you.

My deepest gratitude goes to all my family and friends for their encouragement and support throughout my life, and to my skiing and climbing buddies for giving me every opportunity to "red line the fun meter." Most importantly, I would like to thank Anne-Laure, for being the best partner I could ever hope for.

This research was supported by Sandia National Laboratories under the guidance of Dr. Michael Kaneshige.

Abstract

Detonation interaction with an interface was investigated, where the interface separated a combustible from an oxidizing mixture. The ethylene-oxygen combustible mixture had a fuel-rich composition to promote secondary combustion with the oxidizer in the turbulent mixing zone that resulted from the interaction. Both sharp and diffuse interfaces were studied.

Diffuse interfaces were created by the formation of a gravity current using a sliding valve that initially separated the test gas and combustible mixture. Opening the valve allowed a gravity current to develop before the detonation was initiated. By varying the delay between opening the valve and initiating the detonation it was possible to achieve a wide range of interface conditions. Sharp interfaces were created by using a nitro-cellulose membrane to separate the two mixtures. The membrane was destroyed by the detonation wave.

The interface orientation and thickness with respect to the detonation wave have a profound effect on the outcome of the interaction. Diffuse interfaces result in curved detonation waves with a transmitted shock and following turbulent mixing zone. Sharp interfaces result in an interaction occurring at a node point similar to regular shock refraction (Henderson, 1989). The impulse was measured to quantify the degree of secondary combustion accounting for 5-6% of the total impulse. A model was developed that estimated the volume expansion of a fluid element due to combustion in the turbulent mixing zone (Dimotakis, 1991) to predict the impulse in the limit of infinite Damköhler number.

Contents

List of Figures

List of Tables

Nomenclature

Calligraphic characters

$\mathcal{C}$	constant	
$\mathcal{D}$	species diffusivity	m^2/s
$\mathcal{W}$	mixture average molecular weight	g/mol
$\mathcal{W}_i$	species i molecular weight	g/mol

Greek symbols

α	interface angle	
α^*	angle of intromission	
β	shock angle	
Δh	relative specific enthalpy	J/kg
Δt	adjustable experimental delay time	s
Δ	detonation induction zone length	m
δ	deflected contact surface angle	
$\delta_D(t)$	Dirac delta function	
δ_G	shear layer thickness	m
δ_m	thickness of molecularly mixed fluid in the shear layer	m

δ_p	thickness of chemically reacted fluid in the shear layer	m
$\Delta_R h^\circ$	standard heat of reaction	kJ/mol
$\dot{\omega}_i$	species i molar production rate	mol/s
η	detonation products deflection angle	
Γ	fundamental gas derivative	
γ	ratio of specific heats	
κ	curvature	
λ	detonation cell size	m
μ_1	leading reflected expansion characteristic angle	
μ_2	trailing reflected expansion characteristic angle	
ν	kinematic viscosity	m^2/s
Φ	equivalence ratio	
ϕ	transmitted shock angle	
ρ	density	kg/m^3
σ_E	expansion ratio	
τ	chemical time scale	s
τ_m	molecular mixing timescale	s
τ_p	time to open sliding valve	s
θ	flow deflection angle	
θ_E	Prandtl-Meyer flow deflection angle	
Θ_{gap}	angle between transmitted shock and turbulent mixing zone	

Θ_{max}	maximum flow deflection angle	
Θ_{model}	turbulent mixing zone growth angle	
φ_i	angle between curvilinear and cartesian reference frames	
ξ	interface perturbation amplitude	m

Roman characters

$\vec{w}_i$	velocity in region i in wave-fixed reference frame	m/s
A	Atwood number	
BR	blockage ratio	
c	sound speed	m/s
c_p	mixture average specific heat	J/kg·K
C_δ	shear-layer growth-rate constant	
E_a	reduced activation energy	
E_v	volumetric entrainment ratio	
f_∞	compressible shear layer asymptotic constant	
f_{cm}	combustible mixture mass fraction	
f_{O_2}	oxygen mass fraction	
g	constant of gravity	m/s^2
h	channel height	m
h_i	species i specific enthalpy	J/kg
I	impulse	kg/m/s
k	Arrhenius pre-exponential	1/s

k	interface wave number	1/m
L	DDT run-up length	m
M	Mach number	
m_{fuel}	mass of fuel	kg
m_{O_2}	mass of oxygen	kg
n_R	index of refraction	
P	pressure	Pa
q	heat release	J/kg
R	ideal specific gas constant	
r	velocity ratio across the shear layer	
R_{GDT}	detonation tube radius	m
Re	Reynolds number	
s	density ratio across the shear layer	
S_i	thermodynamic state of region i	
S_u	laminar flame burning velocity	m/s
Sc	Schmidt number	
T	temperature	K
U	horizontal displacement velocity of the transmitted shock	m/s
u	velocity of fluid	m/s
U_p	sliding plate velocity	m/s
V_{CJ}	Chapman-Jouguet detonation velocity	m/s

V_{GC}	gravity current head velocity	m/s
x	horizontal cartesian coordinate	
x^*	thickness of turbulent mixing zone	m
X_i	species i mole fraction	
y	vertical cartesian coordinate	
y_i	species i mass fraction	

Sub-scripts

$\circ$	free stream or initial conditions
c	shear layer convective reference frame
eq	equilibrium chemistry
exp	experimental measurement
fr	frozen chemistry
n	shock wave normal component
v	tangent component to a shock wave
vN	von Neumann point

Chapter 1

Introduction

1.1 Motivation

Detonation propagation through interfaces plays an important role in hazard analysis and propulsion as well in understanding the fundamental mechanisms relevant to detonation decoupling. From a safety standpoint, the sudden rupture of a vessel can exhaust a combustible mixture into the atmosphere. As depicted in Fig. 1.1, the vented combustible mixture can result in a varying interface with sharp and diffuse regions, where f_{cm} refers to the combustible mixture mass fraction with respect to the atmosphere. If a detonation propagates through the combustible mixture, it will eventually meet the surrounding atmosphere where the details of detonation decoupling are instrumental in predicting the outcome of such an event. There is also the possibility that if the combustible mixture is fuel-rich, subsequent chemical reactions can occur at the interface and result in a larger total energy release. For propulsion applications, it is possible that the output of a combustor can be augmented by burning the remaining partially oxidized detonation products with some bypass air.

From a scientific standpoint, the characteristic thickness of an interface results in very different gas dynamic features upon interaction with a detonation wave. In the case of a sharp interface the wave system is linear and steady in the reference frame of the node point. Diffusive interfaces result in highly curved detonation waves that eventually decouple and fail. These different mechanisms, involved in the ultimate decoupling of a detonation, are of paramount interest to predict such events. The

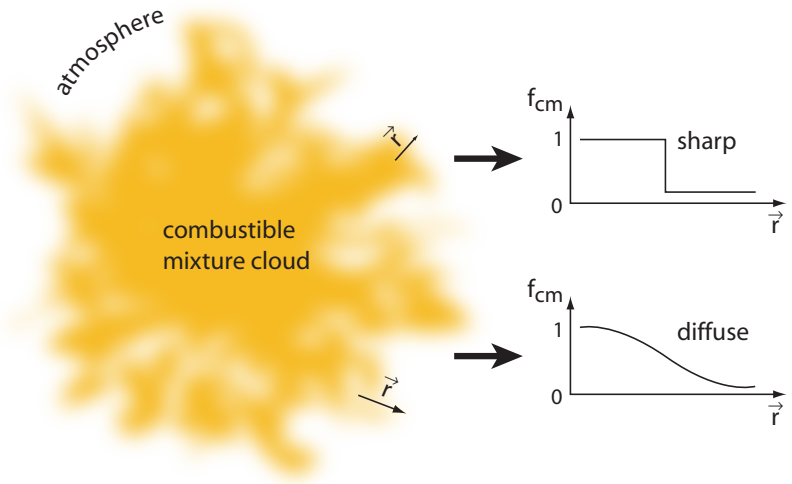

Figure 1.1: Dispersion of a combustible mixture in the atmosphere leads to a complex diffuse interface.

experiments and analysis also serve as a basis for numerical computations with the goal of resolving the complex interaction process.

This study is an extension of experiments by Pintgen and Shepherd (2005) on secondary pressure waves from rich fireballs. In that study a spherical balloon filled with a fuel-rich combustible mixture was ignited by a detonation exiting a small tube at the balloon center. The static pressure was measured outside the balloon using a sting located at about one to two meters from the point of ignition. The goal was to quantify the amount of secondary combustion that resulted when the fuel-rich combustible mixture mixed with the surrounding atmosphere. This proved difficult as it was hard to discern what fraction of the unreacted mixture burned in the initial and secondary combustion phases. The challenge was being able to ignite the entire fuel-rich combustible mixture inside the balloon with the detonation wave that emerged from the small tube. As a proposed solution, the current set of experiments were carried out in a quasi one-dimensional geometry. A detonation was initiated, and propagated down the channel to combust the entire initial mixture before mixing with an oxidizer.

A detonation wave is a supersonic mode of combustion that comprises a leading shock followed by a zone of chemical energy release (see Fig. 1.2a). The shock

waves act to compress and raise the temperature of the combustible mixture, which then undergoes chemical reactions that reinforce the shock via compression waves. Typical gas phase detonations in hydrocarbon-air mixtures propagate at roughly two kilometers per second. The propagation is largely a balance between convection and reaction. Conversely, a deflagration is a subsonic combustion wave dominated by diffusion and reaction. In reality a detonation wave is a complex three-dimensional cellular structure with a characteristic cell size, λ, commonly used to denote the detonation sensitivity. The cell size is often measured using the soot foil technique, shown in Fig. 1.2b, discussed further in Sec. 2.3.

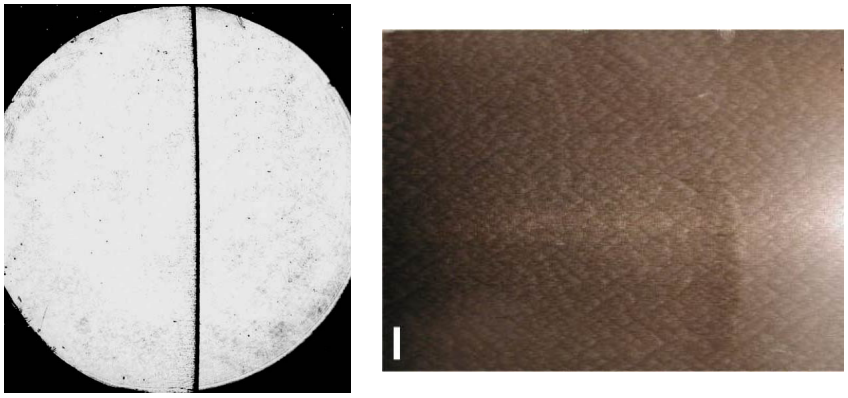

(a) (b)

Figure 1.2: A schlieren image of a detonation wave (a) and the corresponding soot tracks (b) indicative of the cellular structure. An ethylene-oxygen mixture with an equivalence ratio equal to 2.5 with initial pressure and temperature of 15 kPa and 300 K, respectively. The flow is from left to right and the white bar denotes a length of 1 cm.

1.2 Detonation wave interaction with an interface

When a detonation wave propagating in a gaseous combustible mixture is confined by another gas, a complex interaction results between the detonation and interface. The details of this interaction are dependent on the mixture compositions, the relative geometry of the detonation and interface, and the characteristic thickness of the interface. Interfaces are classified by comparing the length scale of the detonation

and the interface thickness. A sharp interface occurs when the detonation cell size is much greater than the interface thickness. Diffuse interfaces result when the cell size is comparable to or much less than the interface thickness.

A sharp-interface-detonation configuration is shown in Fig. 1.3. In this configuration, a detonation wave propagates from left to right in a combustible mixture and through the interface. The interface is at an angle α and separates the combustible mixture from the test gas. Practically, this is accomplished using a removable plate or thin polymeric membrane (see Puranik et al., 2004, Brouillette, 2002).

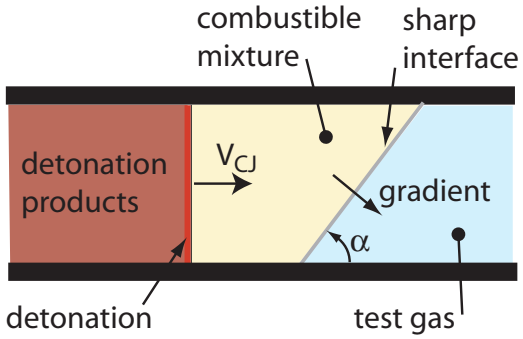

Figure 1.3: A detonation propagating from left to right through a sharp interface.

Figure 1.4 is a schematic showing a diffuse-interface-detonation configuration, which in the context of this work is created by a gravity current. The gravity current propagation is illustrated by left and right arrows showing the direction of propagation of the diffuse interface in Fig. 1.4. Britter and Simpson (1978) describe the diffusive, unstable interfaces that arise in gravity currents. The angle, α, in the case of the diffusive interface is a function of position along the interface. The limiting case of $\alpha = 0°$ is attained by allowing the gravity current enough time to develop, such that for the majority of the interface $\alpha = 0°$ and only the two ends will have $\alpha \neq 0°$.

The interface angle, α, between the detonation wave velocity, V_{CJ}, and the gradient of the interface is critical in determining the nature of the interaction (see Fig. 1.3). When the angle is 90°, both vectors are parallel and the interaction is largely one-dimensional in behavior, similar to shock transmission-reflection phenom-

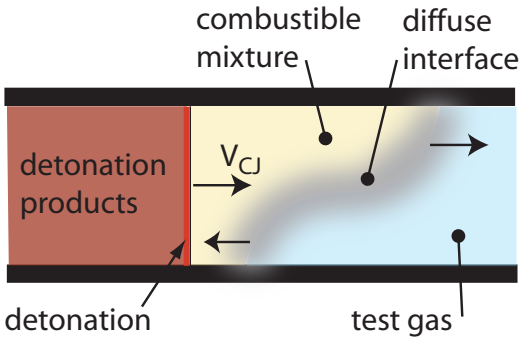

Figure 1.4: A detonation propagating from left to right through a diffuse interface created by a gravity current.

ena (see Liepmann and Roshko, 2001). As the angle decreases, the problem exhibits more two-dimensional features consistent with shock wave refraction theory (see Henderson, 1989).

Both interface-detonation interactions described above ultimately result in the emergence of transmitted and reflected waves with a modified interface that evolves into a turbulent mixing zone (TMZ) as shown in Fig. 1.5. This occurs in all cases when the fluids on either side of the interface have different acoustic impedances, ρc, where ρ and c are the local density and sound speed, respectively (see Thompson, 1988). In the context of the current work, as the detonation moves through the interface a transmitted shock emerges and a reflected expansion fan moves in the opposite direction. The interface also grows and develops through turbulence and mixing due to the Richtmyer-Meshkov (RM) instability (see Brouillette, 2002) and shear growth via the Kelvin-Helmholtz instability (see Dimotakis, 1991).

It is possible for combustion to occur in the turbulent mixing zone (TMZ) by choosing a detonating mixture such that the combustion products are incompletely oxidized. This allows further reactions to take place if the mixture downstream of the interface contains an oxidizer (see Pintgen and Shepherd, 2005). This idea is explored using a rich ($\Phi > 1$) ethylene-oxygen detonation mixture with oxygen as the oxidizing gas downstream of the interface. For example, at $\Phi = 3$, the detonation products,

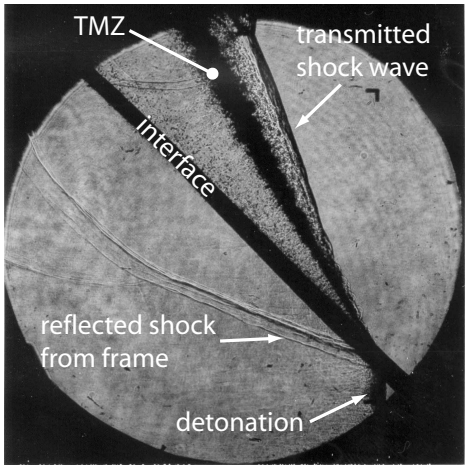

Figure 1.5: Detonation refraction through an interface resulting in a transmitted shock and a turbulent mixing zone (TMZ). The detonation propagates from left to right through the interface made of a thin polymeric membrane mounted on a wood frame.

determined using the STANJAN equilibrium code (see Reynolds, 1986), are

$$3C_2H_4 + 3O_2 \longrightarrow 5.99CO + 5.69H_2 + 0.68H \tag{1.1}$$

with a corresponding enthalpy of combustion $\Delta h = 2.36$ MJ/kg where the products of combustion remain at the detonation equilibrium state. If the carbon monoxide and hydrogen mix with oxygen at $T_\circ = 300$ K to stoichiometric proportions and the mixture undergoes a constant volume explosion, an additional $\Delta h = 1.94$ MJ/kg is released that is 83% of the initial Δh.

1.3 Goals of the investigation

The primary goal of this investigation is to address the differences in decoupling mechanisms observed when a detonation wave propagates through a sharp or diffuse interface. The comparison is based on a set of experiments that capture the detonation-interface-interaction in both cases. The physical mechanisms responsible for both sharp and diffuse interfaces are identified and incorporated analytically to address the decoupling mechanisms and explain the experimental results.

The presence of secondary combustion is also examined at the turbulent interface separating the partially oxidized combustion products and oxidizer. The degree to which secondary combustion occurs in the TMZ is a topic that is not fully resolved in the literature.

Two sets of experiments are carried out in this study. The first involved the interaction of a detonation and diffuse interface created by the formation of a gravity current. This was accomplished using a sliding valve that initially separates the test gas and combustible mixture and then allows a specified amount of time, denoted as the delay time, for the gravity current to develop. The valve was designed such that for a delay time of 0 s the interface is planar. The second set of experiments investigated a detonation propagating through a sharp interface where the combustible mixture and test gas were separated by a nitro-cellulose membrane.

1.4 Background

1.4.1 Detonation refraction

Various numerical and laboratory experiments have been carried out in the field of detonation refraction. They are grouped according to the type of interface, orientation to the oncoming flow, and the choice of mixture; combustible or non-combustible both upstream and downstream of the interface. Large areas in this parameter space, in particular detonation interaction with diffuse interfaces for $\alpha < 90°$, have received little attention. In fact a large portion of the work done in this field has dealt with shock wave refraction in chemically frozen flows.

Experiments with detonation-diffuse-interface interactions where the detonation velocity and gradient vectors are parallel ($\alpha = 90°$) were performed by Thomas et al. (1991) in a vertical detonation tube where two mixtures were allowed to diffuse upon removal of a sliding plate. Other experimentation by Bjerketvedt et al. (1986) looked at re-initiation of detonations across inert regions. In the same configuration, Kuznetsov et al. (1997) investigated detonation transmission through a mixture

discontinuity corresponding to the limit of a sharp interface.

Detonation propagation perpendicular to a diffuse mixture gradient ($\alpha = 0°$) results in a curved detonation wave (see Chap. 4). This is due in part to the dependence of the detonation velocity on the equivalence ratio. Then the component of velocity normal to the curved wave is equal to the local Chapman-Jouguet detonation velocity. There has been limited work done in this area. Ishii and Kojima (2004) experimentally made and measured concentration gradients by diffusion and used soot foils to characterize the detonation propagation. Calhoon and Sinha (2005) used concentration gradients in a numerical study to investigate the possibility of a flame occurring in the incomplete combustion products. In both research efforts, no direct observations were made of the interaction process.

Detonation refraction where $\alpha < 90°$ and the interface is sharp was investigated by Gvozdeva (1961). In her experiments, a methane-oxygen detonation propagated through a nitro-cellulose membrane at various interface angles with respect to the detonation velocity. The test gases were less sensitive methane-oxygen mixtures or air. Dabora et al. (1991) and Tonello and Sichel (1993) have investigated detonation diffraction, where $\alpha = 0°$ of various combustible mixtures separated in parallel channels. In the experiments, oblique detonation waves were observed.

There has been some previous shock-polar analysis that included chemical reactions. Dabora et al. (1965) has modeled the deflection of a contact surface arising from a detonation propagating through a channel with a compressible, non-reacting boundary. Dabora et al. looked at the limiting case, $\alpha = 0°$, where the detonation is normal to the interface. Aslam and Bdzil (2002) carried out a numerical and theoretical analysis of a detonation in a condensed phase explosive confined by an inert gas. Samtaney and Pullin (1998) and Sanderson et al. (2003) investigated the role of ideal gas dissociation during shock wave refraction with an interface and multiple shock wave interaction. The vast majority of shock refraction research summarized in Henderson (1989) deals with non-reactive flows.

1.4.2 Detonation models

Chapman-Jouguet (CJ) hydrodynamic detonation theory and the ZND detonation theory are two simple models used to describe detonations. Fickett and Davis (1979) discuss the complete details of these models.

The CJ detonation is a zero-dimensional model that assumes an infinitely thin reaction zone, i.e., a point of discontinuity. The conservation of mass, momentum, and energy along with the thermodynamic properties of the reactant mixture are used to determine the possible product states. In general, an infinite number of solutions exist for a specified set of initial conditions. Chapman (1899) and Jouguet (1905) closed the problem by reasoning that the equilibrium products have velocity equal to the detonation product sound speed in the wave fixed reference frame. The unique CJ solution determines the composition of the products and the detonation velocity, and is the only observed wave speed measured in the laboratory. Experimental measurements of the detonation velocity are typically within 5% of the predicted CJ value. There are various solvers used to determine the CJ state by iteration (see Kuo, 1986) based on the initial conditions and associated thermodynamic properties. In the present study, a routine developed by Browne (2005) was implemented using the Cantera chemical equilibrium software developed by Goodwin (2005).

The ZND (Zel'dovich, 1950, von Neumann, 1942, Döring, 1943) model of a detonation resolves the detonation structure by considering the one-dimensional steady reactive Euler equations using finite rate chemistry. Figure 1.6 is a ZND calculation showing the basic detonation structure for an ethylene-oxygen mixture with equivalence ratio, Φ=2.5, with the shock located at a distance of 0 mm. The ZND detonation is comprised of a leading shock wave followed by a region of chemical reactions and energy release. The frozen post shock state is termed the von Neumann (vN) point. Finite rate chemistry translates to a length scale associated with reaction progress. This length scale is known as the induction zone length, Δ, and is defined as the distance from the leading shock wave to the point where the thermicity is 10% of its maximum value.

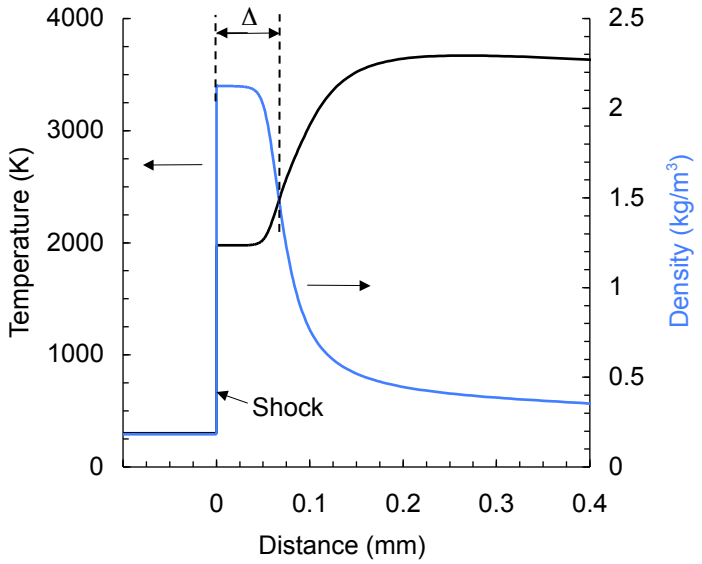

Figure 1.6: ZND calculated thermodynamic profile of $2.5C_2H_4{+}3O_2$, $T_\circ = 300$ K, $P_\circ = 15$ kPa. The von Neumann (vN) point corresponds to the post shock state.

1.4.3 Detonation cellular structure

Detonations in gases observed in the laboratory are intrinsically unstable. It was first observed visually by White (1961) that a detonation is a complex three-dimensional cellular structure. Shchelkin and Troshin (1965) and Denisov and Troshin (1959) were able to measure the size of the cells using a sooted foil technique (see for example Fig. 1.2b). The cell size, λ, has become a fundamental parameter of gaseous detonations (see Lee, 1984) and is linked to the chemical sensitivity of the mixture. The induction zone length, Δ, defined in Sec. 1.4.2 can be empirically correlated with the detonation cell size $\lambda = \mathcal{C}\Delta$. The constant, $\mathcal{C}$, depends on the particular combustible mixture and ranges between $10 < \mathcal{C} < 100$. In general, the correlation is used as a preliminary estimate of the cell size when no experimental data exist. For the experiments in this work, it was desired to have a cell size much smaller than the width of the experimental test section. Ethylene-oxygen mixtures were chosen in part because their corresponding cell sizes are on the order of millimeters.

1.4.4 Mixing zone instabilities

The turbulent mixing zone observed in Fig. 1.5 is formed via instabilities occurring at the deflected interface of the detonation refraction event. Both the Richtmyer-Meshkov instability and the Kelvin-Helmholtz instability are considered in this work and are described below.

1.4.4.1 Richtmyer-Meshkov instability

The Richtmyer-Meshkov (RM) instability results when an impulsive acceleration is applied at an interface between two different fluids. There is a vast amount of research available on this subject. The review by Brouillette (2002) summarizes the basic theories, experiments, and computations. In the scope of the present work, it is useful to highlight the key parameters responsible for RM growth. This is accomplished by examining the linear theory valid during the early times of the unstable growth.

RM theory at early times or small perturbation amplitude, ξ, is described by modifying the linear theory of Taylor (1949) used to define the Rayleigh-Taylor instability. Taylor's theory is used for instabilities at an interface between two fluids of different densities under a constant acceleration where the interface perturbation amplitude, ξ, is governed by the equation

$$\frac{d^2\xi}{dt^2} - kgA\xi = 0, \tag{1.2}$$

where the Atwood number is

$$A = \frac{\rho_2 - \rho_1}{\rho_2 + \rho_1}, \tag{1.3}$$

g is the constant of gravity, and k is the wave number of the interface. By replacing the constant acceleration by an impulse derived from a shock wave passing the interface so that $g = [u]\delta_D(t)$, Eqn. 1.3 becomes

$$\frac{d^2\xi}{dt^2} = k[u]\delta_D(t)A\xi. \tag{1.4}$$

Here, $\delta_D(t)$ is the Dirac delta function and $[u]$ is the change in velocity across the interface as a result of the shock wave. Integration of Eqn. 1.4 results in the linear growth rate of the interface

$$\frac{d\xi}{dt} = k[u]A\xi_o \tag{1.5}$$

with ξ_o defined as the initial interface amplitude. For the RM instability, A is a function of the post shock densities. The Atwood number can be calculated for a given choice of gases. In the context of the current work the Atwood number is calculated using the post shock state of the test gas and the CJ detonation product state of the combustible mixture (see Chap. 5).

1.4.4.2 Turbulent shear layer growth and mixing

Turbulent shear layers have received much attention in the literature. It is of interest to highlight some of the important features that affect the growth and mixing of shear layers relevant to this study. The reader is encouraged to view more complete descriptions of this phenomena in review articles by Dimotakis (1991) or more recently Dimotakis (2005).

A shear layer forms at an interface separating two fluids moving at different velocities (see Fig. 1.7) and is characterized by thickness δ_G. The shear layer grows as fluid from the two streams are entrained and mixed. The entrainment and subsequent growth is highly dependent on the flow conditions of the two streams, namely the density ratio, $s = \rho_2/\rho_1$, and velocity ratio, $r = U_2/U_1$. The growth rate of the shear layer is characterized by δ_G/x, where x is the distance with origin located at the shear layer starting point.

When considering the role of combustion in the shear layer, it is of interest to define the region of fluid, characterized by length scale, δ_m, that is mixed on a molecular level, at a given distance x. The molecularly mixed region is critical for combustion to occur inside the shear layer as it is the mechanism by which the fuel and oxidizer mix. A reaction thickness, δ_p, is defined to represent the region in which the chemical reac-

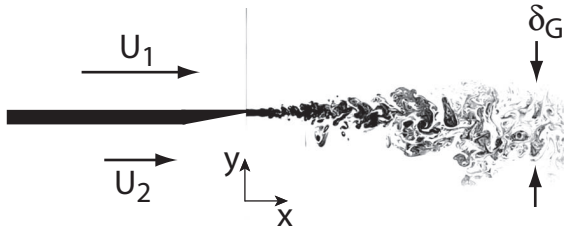

Figure 1.7: A schematic of a turbulent shear layer that forms when fluids with velocities U_1 and U_2 meet at the end of a splitter plate. The size of the shear layer at position x is denoted by the symbol, δ_G (Dimotakis, 2005).

tions have reached completion. It is possible to obtain a measure of the stream-wise reaction-distance ratio, δ_p/x, by considering the product of length scales, suggested by Dimotakis (1991), to be

$$\frac{\delta_p}{x} = \frac{\delta_G}{x}\frac{\delta_m}{\delta_G}\frac{\delta_p}{\delta_m}. \tag{1.6}$$

It is reasoned that chemical reactions represent some fraction of the mixed region, δ_m, with the mixed region being some fraction of the size of the shear layer, δ_G, which in turn is bounded by the growth rate of the shear layer δ_G/x.

1.5 Presentation outline

Chapter 2 gives a description of the experimental setup used in the study. The details of the diagnostics, timing, and methodology are described.

An overview of the gravity current experiments used to characterize the diffuse interface is presented in Chapter 3. Two sets of experiments was carried out. The first set of experiments was carried out in a half-scale water channel to look at the early development of the gravity current. The second set of experiments was carried out in the Galcit Detonation Tube (GDT) and used an acetone-helium mixture as a surrogate for the combustible mixture for planar laser induced visualization.

Chapter 4 is a theoretical description of detonation waves in a concentration gradient. The discussion focusses primarily on the case when the detonation velocity is

perpendicular to the concentration gradient, $\alpha = 0°$. The decoupling mechanisms of the detonation wave are considered by exploring the role of composition gradient.

In Chapter 5 a description of the experimental results using the sliding valve is given. The results for a planar interface, $\alpha = 90°$, and gravity current interfaces with variable α are presented. The experiments are compared with the theory discussed in Chapter 4. The impulse is determined at each pressure transducer location, and a model is developed to estimate the role of secondary combustion in the shear layer.

A theoretical description of a detonation propagating through a sharp interface is presented in Chapter 6.

Chapter 7 presents the experimental results of a detonation propagating through a sharp interface and compared with the theory developed in Chapter 6. Some specific experimental details particular to this section are described. An analysis of the shear layers and Mach reflections visible in the schlieren images is made in an effort to verify the presence of combustion in the shear layer.

Conclusions are drawn in Chapter 8 for both diffuse and sharp interfaces. Future work in this subject is proposed.

Chapter 2

Experimental Setup

Both sharp interface and diffuse interface experiments were carried out using the GALCIT Detonation Tube (GDT) shown in Fig. 2.1. The GDT is 7.3 m long with an inside diameter of 280 mm. It is connected to a 0.762 m long square test section with inside dimensions of 15 cm by 15 cm. A wave cutting device, informally referred to as a cookie cutter, extends 1 m into the end of the GDT (see Fig 2.1) to cut out a square section of the circular detonation front before entering the test section. A sliding valve assembly is placed in between the GDT and test section to separate the two sections during the experimental preparation. In the sharp interface experiments a nitro-cellulose membrane was placed in the optical viewport of the test section.

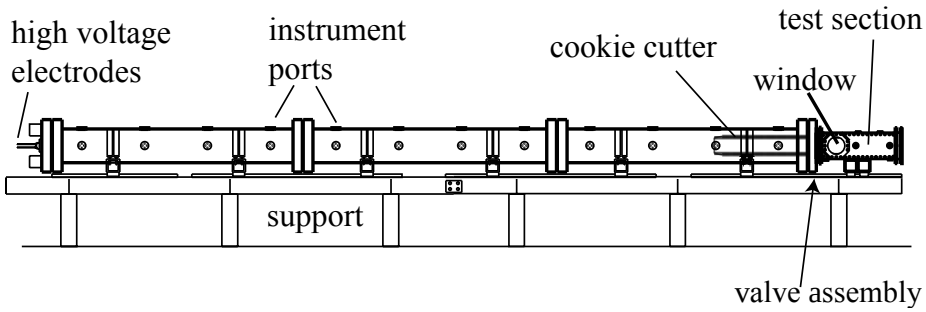

Figure 2.1: A schematic of the GALCIT Detonation Tube with the test section.

Figure 2.2 is a view of the test section illustrating the location of the end flange of the GDT, the sliding valve assembly, and the test section. Visualization for the experiments was made through one optical viewport that could be arranged in two separate positions. The first position is located 27.5 cm downstream of the sliding

valve and is referred to as port 1. The second viewport position is located 56 cm downstream of the sliding valve (see Fig. 2.2) and is referred to as port 2. Switching from the port 1 to the port 2 experimental configuration involves rotating the entire test section by 180 degrees. The locations of the pressure transducers and a quartz window on the end wall used for fluorescence imaging are also shown. Further details on the GDT can be found in Akbar (1997) and Austin (2003). The driver gas in these experiments was a combustible mixture while the test gas in the test section was an oxidizer or diluent. Specifically ethylene-oxygen mixtures occupied the GDT, and either oxygen, nitrogen, or nitrous oxide occupied the test section.

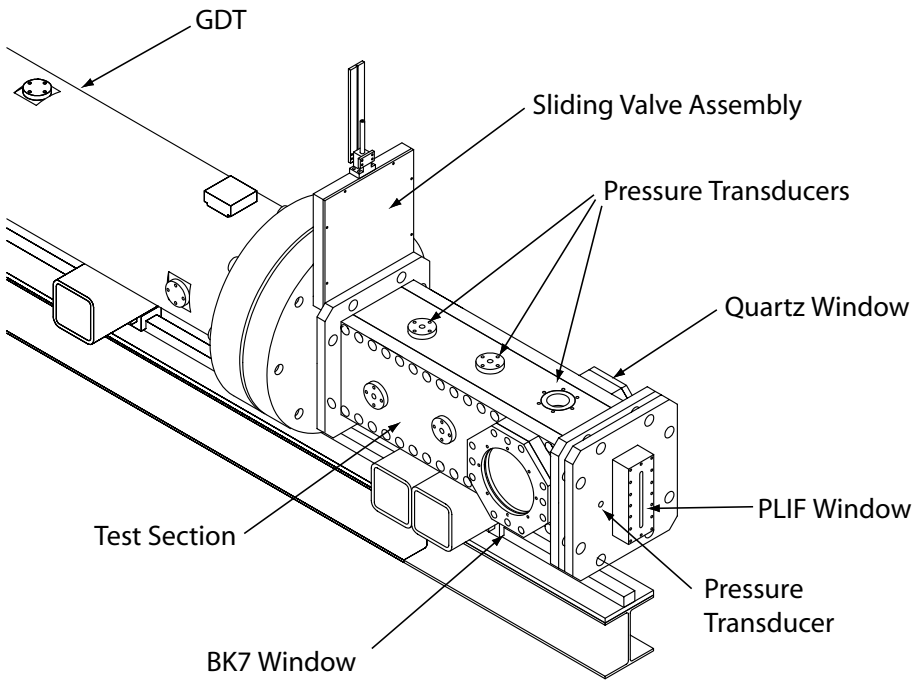

Figure 2.2: A schematic of the test section with the sliding valve assembly and the end flange of the GDT.

Detonations were initiated by discharging a 2 μF bank of capacitors charged to 9 kV through a 0.16 mm copper wire. The exploding wire resulted in a combustion front that was immediately accelerated through a set of obstacles. The obstacles' design followed the model developed by Veser et al. (2002) to minimize the deflagration to detonation transition (DDT) run-up distance. Veser et al. modeled the scaling for

the length L to tube radius R_{GDT} as

$$\frac{L}{R_{GDT}} = \frac{c_b}{S_u 10(\sigma_E - 1)} \frac{1 - BR}{1 + BR} \tag{2.1}$$

where c_b is the sound speed of the burned products, σ_E is the expansion ratio defined as the ratio of the density of the reactants to that of the burned products, and BR is the blockage ratio. The blockage ratio for these experiments was 0.39 and is defined as the ratio of unobstructed area to the total cross-sectional area of the tube. For the experiments in this study L/R_{GDT} reaches a maximum value of 3.5 for an ethylene-oxygen mixture with an equivalence ratio of 3.

2.0.1 Sliding valve

A substantial effort was invested into the design of the sliding valve. The goal was to design a valve that completely isolates both the combustible mixture and test gas, as well as to open sufficiently fast to control the formation of gravity currents. The sliding valve system shown in Fig. 2.3 is comprised of the sliding valve assembly, the support truss, and the mass actuator. A steel wire connects the sliding plate to the mass actuator through a system of sheaves. The mass actuator is triggered via a TTL pulse, by the removal of a pin, with a 4:1 mechanical advantage. Unwanted vibrations of the falling mass that can misalign the optical system are suppressed using a compression spring located at the base of the guide (see Fig. 2.3) and a sand bed under the falling mass platform.

The valve body shown in Fig. 2.4 consists of a sealing bracket and plate enclosure assembly. Buna-N o-rings are used for sealing the sliding plate with the valve body. The sliding plate is actuated by a rod that is guided by a copper bearing with a dynamic o-ring seal.

The sliding valve was measured to open in 170 ms with an uncertainty of 10 ms. The mass needed to achieve this opening time was 55 kg.

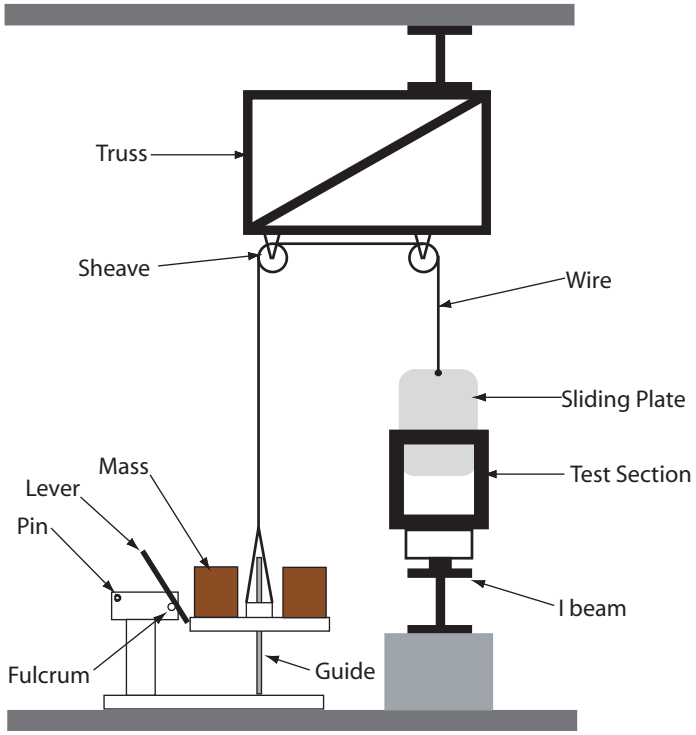

Figure 2.3: A schematic of the sliding valve system.

2.0.2 Nitro cellulose membrane

Nitro cellulose membranes were used in some experiments to create a sharp interface between the combustible mixture and the oxidizer (or inert gas). The membrane was mounted on a wooden frame and inserted into the test section (Fig. 2.5) by removing one window. Two brackets were used to hold the frame in place. Figure 2.5 includes a schlieren image of the frame mounted in the test section. False color indicates the location of the combustible mixture and oxidizer. The wooden frames were made out of cedar strips that were 3 mm thick and 9.5 mm wide. The wood strips were cut to length and glued together to form the frame. An image of a wooden frame with a nitro cellulose membrane is shown in Fig. 2.6.

2.0.2.1 Methodology to prepare a membrane

There are several steps required to produce a wooden frame with a membrane as shown in Fig. 2.6. The procedure can be divided into four steps: preparing the

Figure 2.4: An image of the sliding valve body.

membrane solution, making the wooden frame, mounting the membrane on the frame using spray adhesive, and inserting the frame into the test section.

The membrane solution is prepared in a fume hood and involves mixing Nitrocellulose with Castor oil and five additional highly corrosive and flammable chemicals. Detailed instructions to prepare this solution are described in Kumar (2002, pg. 41).

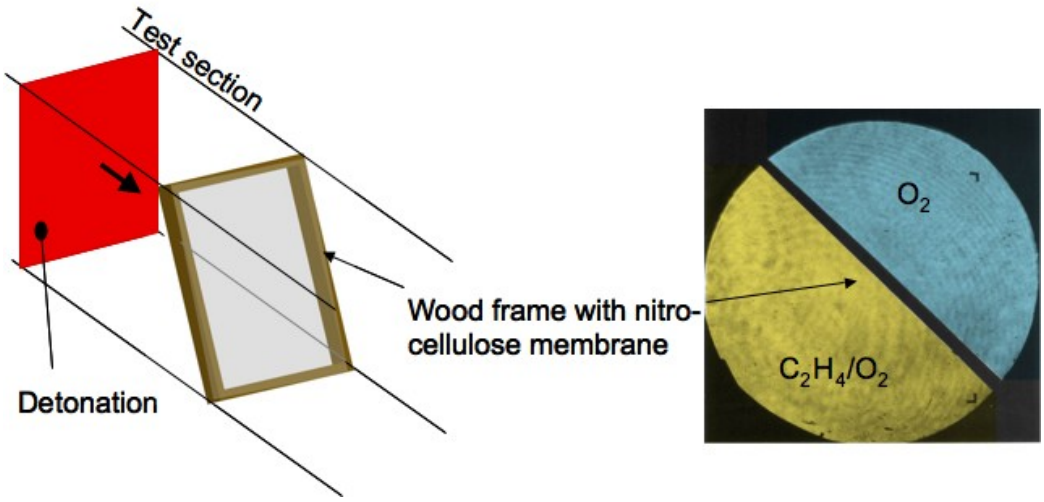

Figure 2.5: An illustration of the frame mounted in the test section along with a schlieren image of the actual setup. False color has been added to the schlieren image to indicate the location of the combustible mixture and oxidizer.

Figure 2.6: A photograph of a wooden frame 15.2 cm wide by 21.5 cm in length with a nitro cellulose membrane glued on the surface.

It is necessary to wear gloves, a lab coat, and protective eye wear when handling these chemicals.

The wood frame is glued together as described above, and for handling ease two

wood nails are lightly set into the frame, opposite to the side where the membrane will be placed. Masking tape prevents the spray-on-adhesive from coating the inside edge of the frame during the process.

Membranes are made by spreading the membrane solution over a surface of de-ionized water. This is accomplished by using a container at least twice the size of the frame filled 10 cm deep with distilled water. The large container is essential when removing the frame. The membrane solution should be constantly stirred by a magnetic stirring rod and kept in a small squeezable plastic bottle. The bottle should have a screw-on cap with a 3-6 mm diameter nozzle that is at least 3 cm long. To prepare a membrane, place the nozzle tip just below the surface of the water in one corner of the container. Squeeze the bottle and slowly move across the width of the container until the nozzle tip reaches the opposite corner. The membrane solution will spread naturally over the surface of the water. Remove the nozzle tip from the water and immediately pull the membrane solution with both hands to the two remaining corners of the container. It is helpful to drape the membrane onto the plastic container to act as an anchor during the drying process. Allow the membrane to dry on the surface. The drying process is accompanied by a wrinkling of the membrane, which is a result of the membrane shrinking as it dries. At this point, spray adhesive (3M Super 77 spray adhesive) onto the frame and place the frame onto the most uniform section of the dried membrane. Try to avoid features that look like holes or cracks. It is very important that no dirt or remnant membrane pieces are floating on the surface of the water as this will result in holes and tears in future membranes. Allow the adhesive to dry and then, using scissors, cut away the excess membrane to leave a 1 cm membrane strip on the outside of the frame. Press the excess membrane to the side of the frame and then remove the frame from the container by gently gliding it off the water surface. Once the frame is off the water, the nails are removed, and the frame is allowed to dry for at least an hour.

Pieces of tape are placed on the edges of the frame to act as a seal around the frame. The frame is gently placed into the test section and locked into place using two aluminum brackets. Finally, the window is gently put into place by hand-tightening

the bolts.

2.0.3 Experimental procedure

The experimental procedure varies depending on which experiment is being carried out. In this section the methodology for producing diffuse interfaces via gravity currents is explained. Section 7.1 discusses the particular details involved in the sharp interface experiments. Each experiment begins by drawing a vacuum in the entire system. The sliding valve is then put into the closed position, and the GDT and test section are filled with their respective gas mixtures to the desired initial pressure. The combustible mixture in the GDT is recirculated for five minutes to ensure proper mixing. The pressures in the GDT and test section are then matched to minimize unwanted flow disturbances when the sliding valve is opened. All valves are then closed, and the diagnostics are initialized. The "fire button" is then pressed to initiate the firing sequence discussed in Sec. 2.2.

2.1 Diagnostics

Various diagnostics were used to understand the physical processes in the current study. Soot foil measurements (see Austin, 2003) were made by anchoring a soot-coated aluminum sheet in the detonation tube. The goal of the soot foil study was to determine what combustible mixtures were feasible for the experiments. An example of a soot foil is shown in Fig. 2.7 for an ethylene-oxygen mixture of equivalence ratio 2.5, with an initial temperature and pressure of 295 K and 15 kPa, respectively.

Seven pressure transducers (PCB #113A26), 3 in the GDT and 4 in the test section, were used to measure the local pressure and time of arrival of the shock or detonation wave. Detonation wave speeds measured in the GDT were always within 5% of the predicted Chapman-Jouguet detonation velocity.

Figure 2.7: An image of a soot foil for an ethylene-oxygen mixture of equivalence ratio 2.5. The initial temperature and pressure are 295 K and 15 kPa, respectively. A 1 cm white bar is included for scale.

2.1.1 Flow visualization

A schlieren system (Akbar, 1997) was used to visualize the gas dynamics. The schlieren system is setup in a Z configuration with both a horizontal and vertical knife edge and uses a ruby laser as a pulsed light source. The ruby laser consists of a ruby rod that is pumped by a xenon flash lamp to emit a light pulse at 693 nm. The 50 ns exposure pulse is Q-switched by a Pockels cell. The resulting light is expanded and collimated into a 150 mm diameter beam and then imaged onto high-speed 72x92 mm Polaroid 3000 ISO film. Figure 2.8a is a typical schlieren image of a detonation wave. The detonation is propagating from left to right in an ethylene-oxygen mixture ($\Phi = 2.5$) at 295 K and 15 kPa initial conditions. A system of transverse waves is visible just downstream of the detonation wave. However, the 2 mm detonation cell size makes the transverse waves difficult to see. Figure 2.8b is a schlieren image of a detonation (Austin, 2003) with a much larger cell size to highlight the complex transverse wave structure.

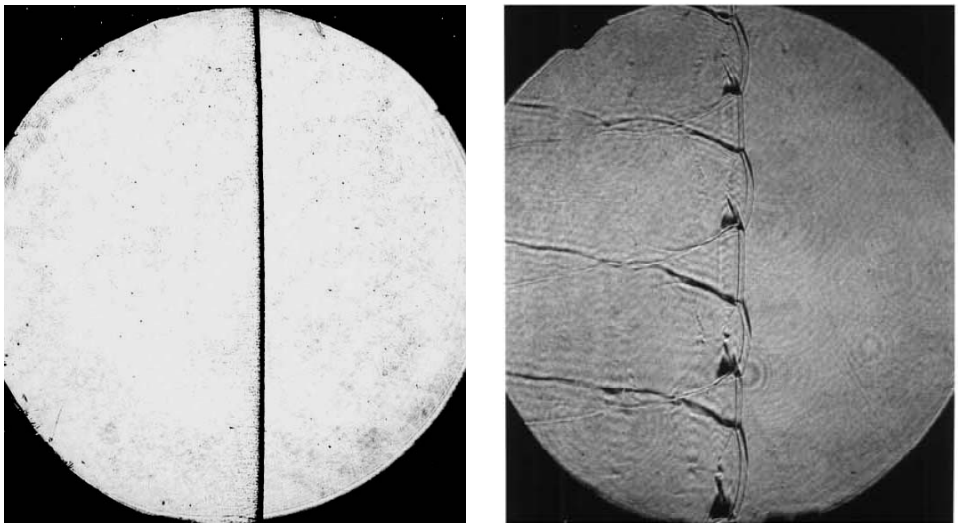

(a) (b)

Figure 2.8: Schlieren images of detonation waves propagating from left to right. (a) Ethylene-oxygen mixture ($\Phi = 2.5$) at 295 K and 15 kPa initial conditions. (b) $2H_2$-O_2-12Ar, 20 kPa initial pressure (Austin, 2003).

2.2 Experimental timing sequence

Certain timing measures were taken in order to synchronize the gravity current formation, schlieren image, and detonation propagation. The goal was to develop a flexible timing system able to accommodate different delay times in which a gravity current could form and then trigger the schlieren imaging system to obtain a picture. The sequence of events, divided into three basic stages each utilizing a digital delay generator, is illustrated in Fig. 2.9. The first stage acts as a startup and sequences events on a large time scale (order of seconds). These events include: charging the ruby laser flash lamp, opening the schlieren camera shutter, and actuating the sliding valve. The second set of timing sequences initiates when the sliding valve reaches the open position. At this point a signal is sent to trigger the data acquisition system and initiate a detonation via an exploding wire. When the detonation, propagating down the GDT, reaches pressure transducer P2, the third stage of the timing sequence is initiated to fire the ruby laser and obtain a schlieren image. One key feature in this system is the use of a latching edge Schmitt trigger to mitigate the possibility of a

laser misfire from high voltage noise.

There are four adjustable time settings (Δt subscripts 1-4) of which three are used to obtain a gravity current of a desired size and the fourth is used to control the ruby laser light pulse. Δt_1 controls the schlieren camera shutter. Δt_2 and Δt_3 are set together to allow the laser flash lamp at least 5 s to charge but to trigger the experiment before the flash lamp automatically discharges (6 s window).

The layout of the principal components used to implement the timing sequence in Fig. 2.9 are shown in Fig. 2.10. The layout shows the location of the experiment with respect to the optical tables and highlights the schlieren laser light source and optical path. The three delay generators are illustrated along with the capacitor discharge system and latching edge Schmitt trigger.

2.3 Soot foil measurements

A separate set of experiments listed in Tab. B.1 was carried out to measure the detonation cell size of potential mixtures. The combustible mixture filled both the GDT and test section. Soot foil measurements were made by placing a sooted plate of aluminum into the test section (Fig. 2.7). The goal of this study was to identify a set of combustible mixtures whose detonation cell sizes were small compared with the length scale of the experiment. The soot foil experimental study used ethylene-oxygen and hydrogen-oxygen mixtures at various equivalence ratios and initial pressures, the results of which are plotted in Fig. 2.11. Cells sizes less than 5 mm were considered adequate as a single cell would occupy less then 0.2% of the test section cross sectional area. This led us to consider ethylene-oxygen combustible mixtures between equivalence ratios of 2-3 at 15 kPa initial pressure. Hydrogen-oxygen mixtures were not used in the main experiments due to their larger cell size.

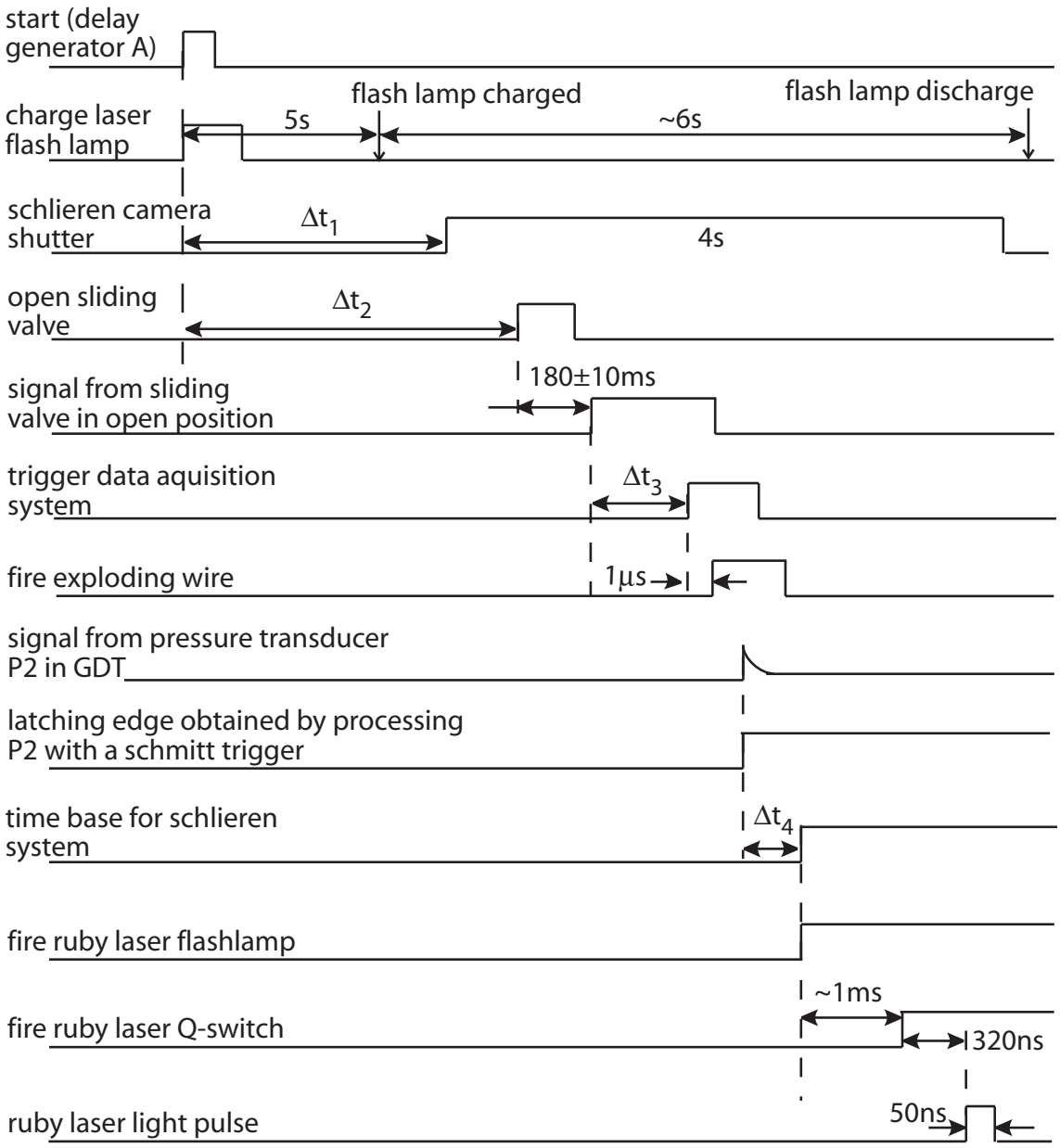

Figure 2.9: Timing diagram of triggering sequence for gravity current formation and schlieren imaging. Δt with subscripts 1, 2, 3 are specified for each experiment for a given delay time. Δt_4 is set to specify when the image is taken.

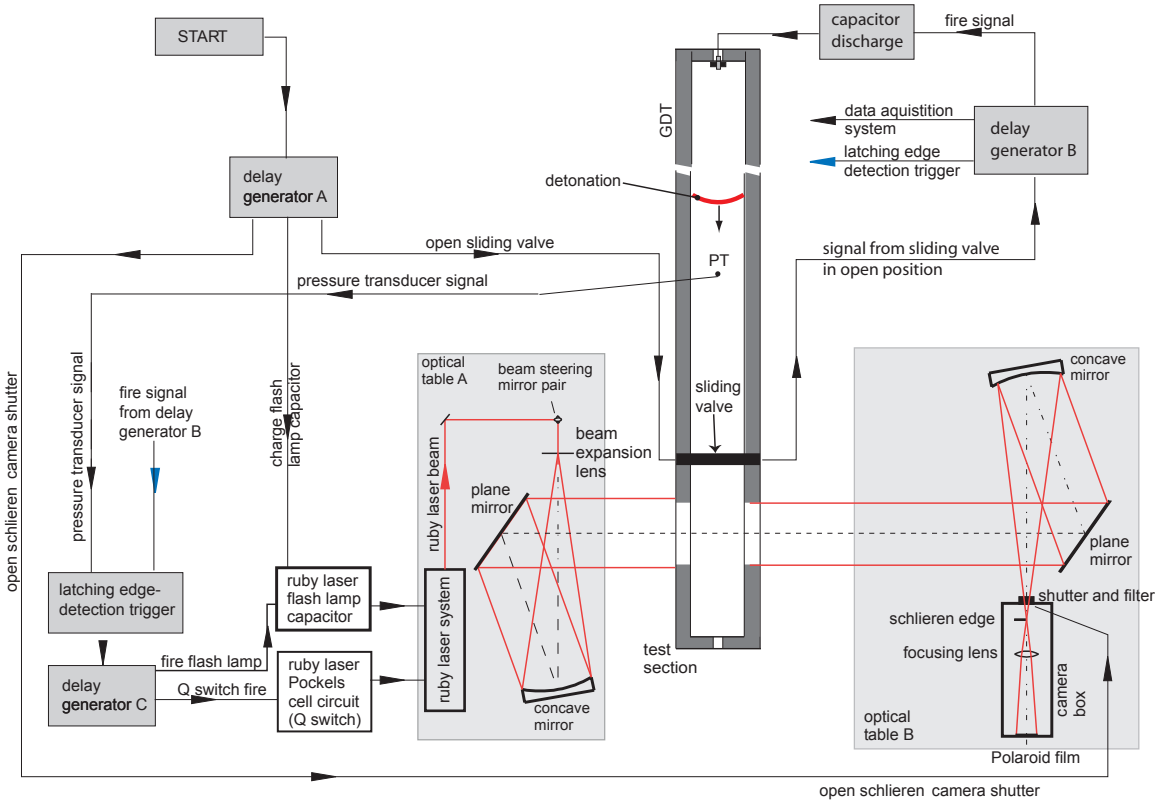

Figure 2.10: Schematic of experimental layout and wiring for diffuse interface experiments.

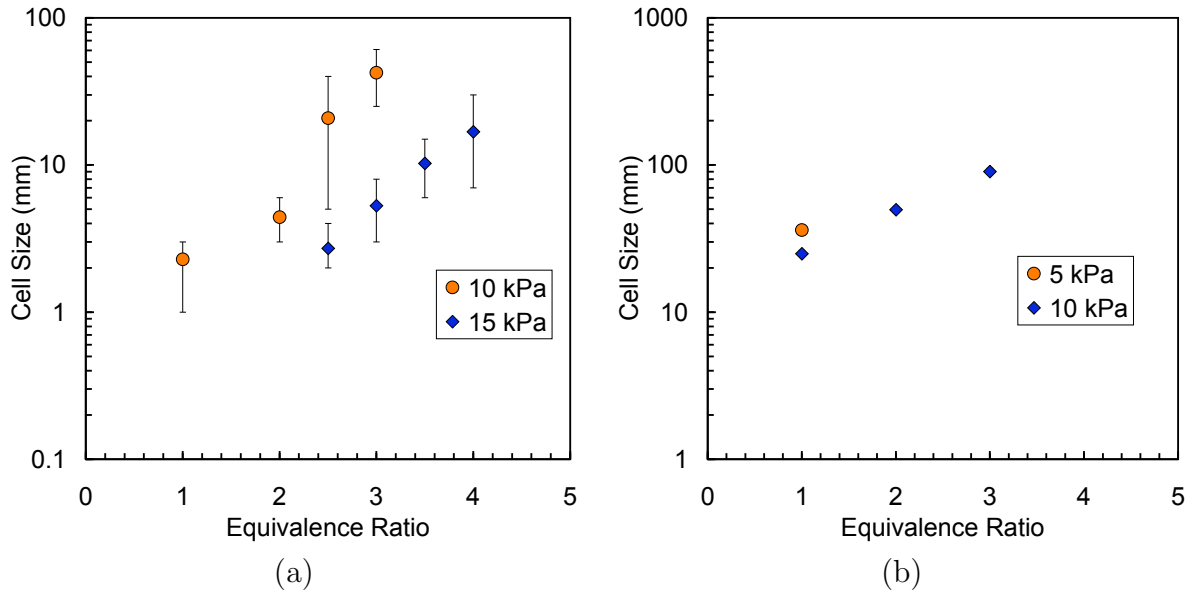

Figure 2.11: Cell size vs. equivalence ratio for (a) Φ C_2H_4 + 3 O_2 and (b) Φ H_2 + 0.5 O_2 at various initial pressures.

Chapter 3

Characterization of Gravity Current Interface

3.1 Gravity current

An experimental study of the formation of gravity currents (GC) has been carried out. The goal of the study was to understand how the gravity currents, occurring at the interface between the test section and the detonation tube (GDT), developed over time (Fig. 1.4). It was particularly helpful to examine the early stages of development and the non ideal interface, which are difficult to characterize with idealized theories.

Gravity currents occur when two fluids of differing densities are placed next to each other in the presence of a gravitational force. In an experiment, the two fluids are typically separated by a plate or membrane that is then removed at the start of the experiment. The fluid of higher density will flow beneath the lower density fluid forming what is called the gravity current head. The lighter density fluid will flow in the opposite direction on top of the heavier fluid. The two-fluid system evolves until it reaches its stable equilibrium point of the light fluid resting on top of the heavy fluid. There is a large body of scientific work that discusses gravity currents in many different physical situations. Simpson (1987) has written a comprehensive book that covers the many rich features of gravity currents. Various idealized theories, the first being established by Benjamin (1968), predict the velocity of a fully developed gravity current head. The instabilities associated with the development of the gravity

current head, namely the formation of billows, lobes, and clefs have been explored in various studies (see Hartel et al., 2000). Determining the growth rates for gravity currents at early times requires for the most part careful experimentation or numerical simulation. This is largely due to the fact that no tractable theory exists that can describe the nonlinear growth in the gravity current formation. This is also true with the instabilities that arise at the interface.

To characterize the gravity currents formed in the GDT, two sets of experiments were carried out using two separate configurations. The first experiment, performed in a water channel, looked at gravity current formation and the effects of the plate removal. The second, performed in the GDT, looked at the evolution of the gravity current head. The study was divided into two parts because it is not practical to visualize the gravity current at early times in the GDT as a result of the location of the sliding valve assembly, test section, and associated optical viewport.

3.2 The water channel

A water channel was built for testing the early time development of the gravity currents. The experiments were carried out by Marie Wolf (2005).

3.2.1 Matching criterion

In order to make gravity currents in the water channel similar to the gravity currents in the GDT, two non-dimensional parameters and a time-scale were matched. The first parameter identified was the Reynolds number, where the length scale is the height of the channel and the velocity is that of the plate being withdrawn. The Reynolds number was chosen to match the fluid motion induced by the plate withdrawal and subsequent wake. The normalized density ratio $(\rho_2 - \rho_1)/\rho_1$ was the second non-dimensional parameter defined where ρ represents density and subscripts 1 and 2 refer to the lighter and heavier gases, respectively. The square root of the normalized density difference is proportional to the velocity of a fully developed gravity current.

Benjamin (1968) used inviscid fluid theory to determine the velocity of the gravity current head according to the following expression

$$V_{GC} = \mathcal{C}\sqrt{gh\frac{\rho_2 - \rho_1}{\rho_1}}. \tag{3.1}$$

Here, g is the constant of gravity, h is the height of the channel, and $\mathcal{C}$ is a constant that is typically $1/\sqrt{2}$. Given the half-scale size of the water channel, we would expect the velocity of the gravity current in the GDT to be a factor of $\sqrt{2}$ faster than the gravity current in the water channel. The time-scale in this study, τ_p, is a measure of the time it takes for the plate to be removed from the channel. It is defined as

$$\tau_p = \frac{h}{U_p} \tag{3.2}$$

where U_p is the mean velocity of the plate. Table 3.1 lists all the relevant parameters and their numerical values used in the matching study. Physical characteristics of the GDT prescribed the water channel size and salt solution density.

	GDT	Water Channel
width, h (m)	0.15	0.075
ρ_1 (kg/m^3)	0.182	1000
ρ_2 (kg/m^3)	0.194	1066
ν (m^2/s)	8.63E-5	1.00E-5
Re	1569.5	1569.5
$(\rho_2 - \rho_1)/\rho_1$	0.066	0.066
τ_p	0.16	0.2

Table 3.1: A list of the important dimensions and non-dimensional parameters involved in the matching analysis.

3.2.2 Experimental setup

The 25.4 cm long water channel depicted in Fig. 3.1 was built of acrylic with height and width measuring 7.5 cm. The plate slid in two grooves that were milled into the side walls of the channel. The bottom of the water channel had a slot into which the plate slid. The plate was actuated by a 3.5 kg nominal falling mass. The mass was

attached to the plate via a cable that slid through eyelets mounted in place by a steel frame. Vacuum grease was used to seal one side of the plate from the other during the preparation stage of the experiment.

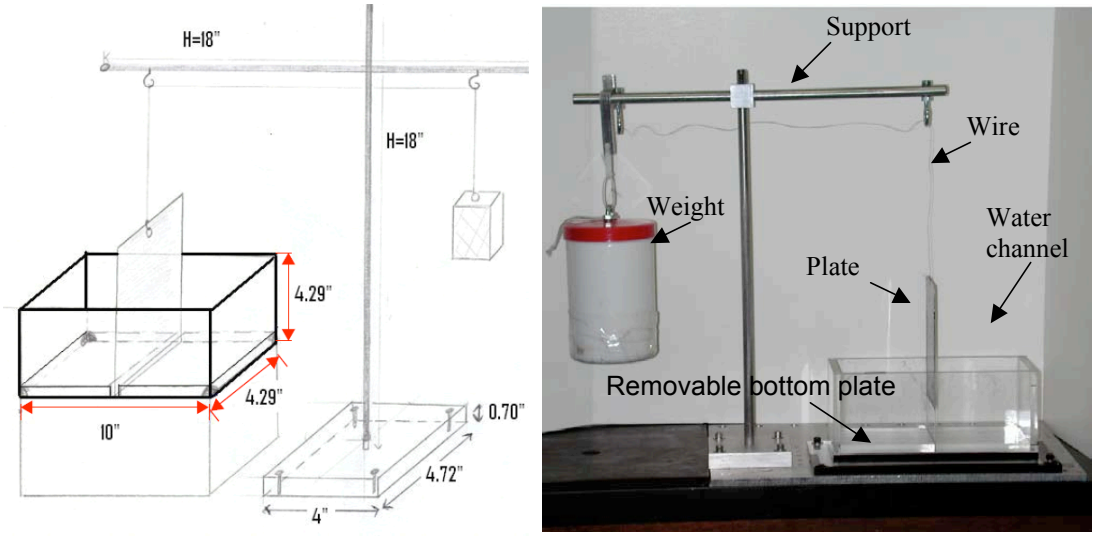

Figure 3.1: An image of the experimental setup. The plate separating the two mixtures in the channel is actuated by a falling mass.

3.2.2.1 Visualization techniques

The gravity current was visualized using two separate techniques: dye visualization and digital particle image velocimetry (DPIV). Figure 3.2 is a layout of the apparatuses used for the visualizations. The dye visualization was captured on a Vision Research Phantom (V5) digital movie camera, which has 1.44 megapixel resolution and was set to a 100 picture per second frame rate and a 7 ms exposure time. The dye used was a blue food coloring agent, and its density was measured to be within less than a percent of the density of water. The dye experiments provided time resolved images of the advancing gravity current head, with the limitation that the images acquired are an integration along the optical path of the water channel.

The DPIV experiments were carried out with the expertise of Emilio Castano Graff. The setup used a Wave Research Gemini PIV 200 laser to generate laser pulses at 532 nm. The laser beam passed through a cylindrical lens and turning

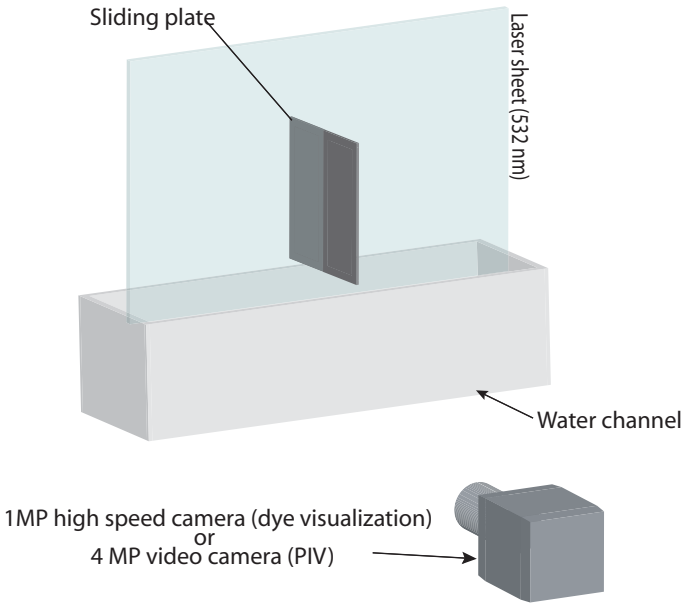

Figure 3.2: A schematic illustrating the layout of the water channel, camera, and light sheet (only for DPIV).

mirror to generate a light sheet large enough to span the water channel. The laser fired two pulses at a time with an inter pulse delay of 3 or 6 ms to generate an image pair used in the PIV cross-correlation analysis. The frequency of image pairs was either 7 or 15 Hz, the latter being the highest repetition rate that the laser can cycle. The laser light sheet entered the water channel from the top (see Fig. 3.2), 1.5 cm from the centerline, to avoid interfering with the steel mount used to extract the plate. Each image appears to be a collection of white dots on a black background, obtained by seeding both the water and saline solution with 0.44 micron hollow glass beads that reflect the laser sheet. The concentration of beads was estimated to be several hundred beads per cubic centimeter. The details of the setup and image processing techniques are discussed, for example, by Willert and Gharib (1991) and Huang et al. (1997).

3.2.3 Results

A typical case of gravity current formation is shown in Fig. 3.3. These images show the development of the gravity current at four instances in time. The head of the gravity current, which in this case is the dark colored liquid, propagates from right to left. One of the more striking features are the billows that develop as a result of the Kelvin-Helmholtz instability present at the interface (see Simpson, 1987). The mean velocity of the gravity current measured in these sequences is 81 ±12 mm/s, which has the correct magnitude when considering the length of the channel and the test time. The test time is defined as the duration between when the plate just exits the water to when the gravity current head touches the end wall.

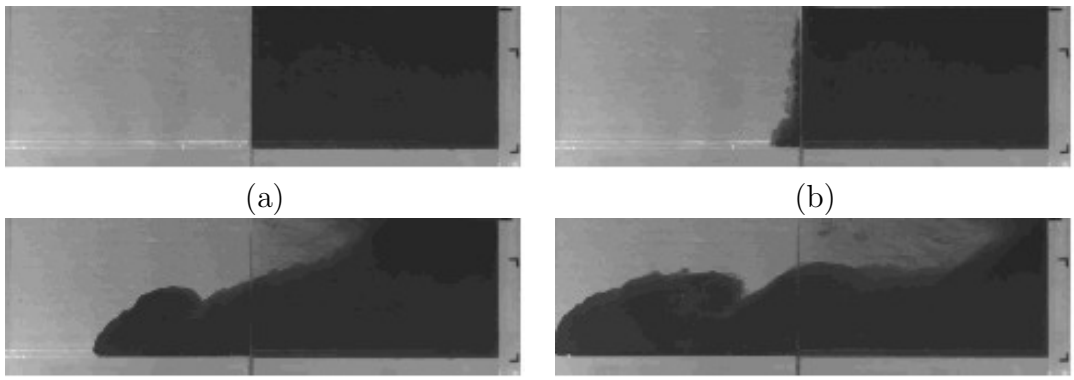

Figure 3.3: Time sequence illustrating the development of a gravity current using dye visualization. The gravity current head is propagating from right to left. The dark colored fluid is the salt water solution and the clear fluid is de-ionized water. (a) 0 s, (b) 0.16 s, (c) 0.84 s, (d) 1.35 s.

The dye visualization was effective in obtaining the gravity current head velocity. To obtain a more complete picture, DPIV was used to resolve the flow structure. DPIV does not integrate over the span of the gravity current, but examines a slice about 1-2 mm thick. Figure 3.4 is a sequence of images corresponding to the same progression as Fig. 3.3. The bulk flow velocity here is characterized by vectors of 0.15 ±0.05 m/s. The billows are visible on the interface and have been shown (see Britter and Simpson (1978)) to entrain the light fluid on top. The lack of vectors in

the interface region is a result of a glass bead seeding difficulty.

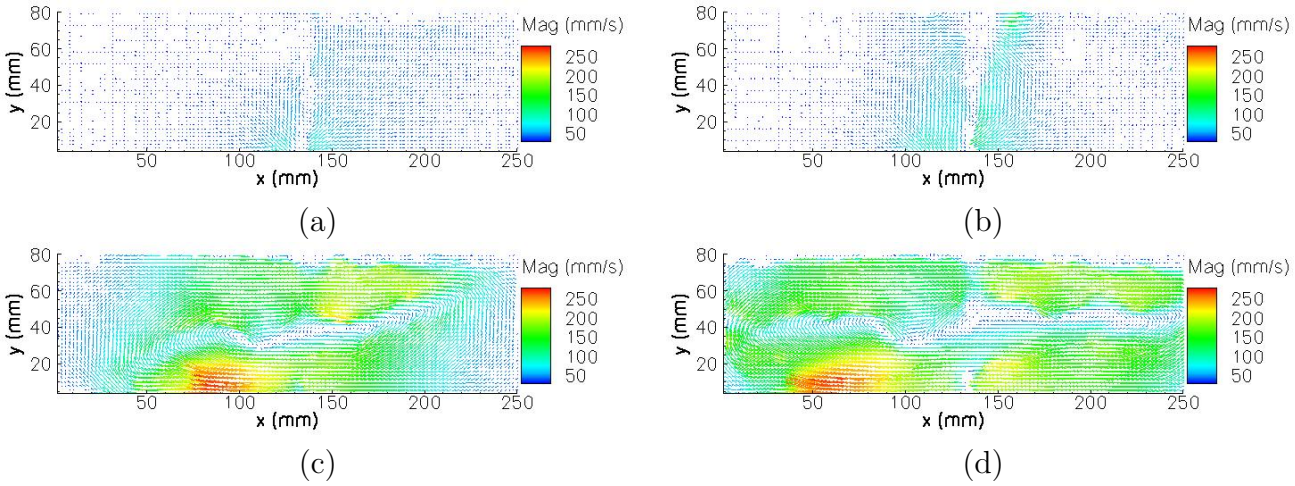

Figure 3.4: Time sequence illustrating the velocity development of a gravity current using DPIV. The gravity current head is propagating from right to left. The vectors represent flow direction and velocity magnitude. (a) 0 s, (b) 0.16 s, (c) 0.84 s, (d) 1.35 s.

The vorticity generated during gravity current formation is examined in Fig. 3.5 where a sequence of images shows the production of vorticity as the plate is removed and billows form at the interface. The vorticity generated as the interface develops is dissipated after the gravity current reaches the end wall, on a time scale of several seconds. The location and profile of the highest magnitudes of vorticity coincide with the location of the billows along the interface. Negative values of vorticity correspond to vortex motion in the clockwise direction while positive values correspond to vortex motion in the counter clockwise direction.

A characteristic interface thickness is defined by examining the DPIV images. The interface thickness is used to divide the flow field into three idealized regions: saline solution, water, and mixed region. The interface thickness varies both spatially and temporally, but for the purposes of this study, it has been measured as 14 mm after being averaged in both space and time. The thickness, defined along the vertical (y) axis of the water channel, is measured between points in the flow where the magnitude of the vorticity is greater than 0.1 s^{-1}.

The thickness of the wake region caused by the plate withdrawal is investigated.

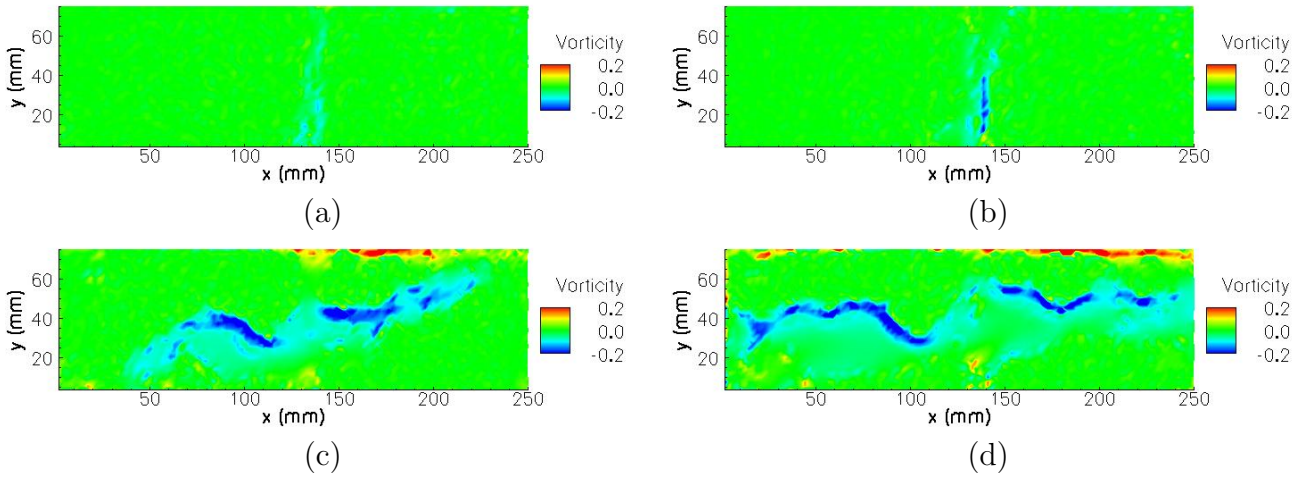

Figure 3.5: Time sequence illustrating the vorticity development of a gravity current using DPIV. The gravity current head is propagating from right to left. (a) 0 s, (b) 0.16 s, (c) 0.84 s, (d) 1.35 s.

The water channel was filled on one side with water and the other with colored water, both measured to ensure equal densities (Fig. 3.6, 0 s). The plate was then withdrawn (0.16 s) and the wake region developed.

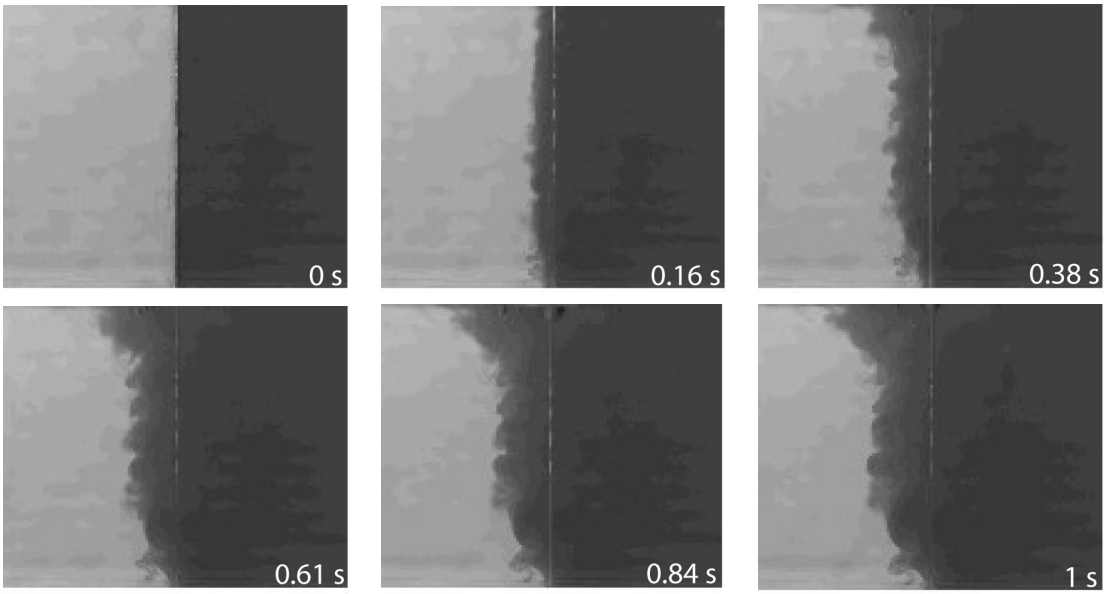

Figure 3.6: A sequence of dye visualization images illustrating the plate withdrawal. The plate is initially in the closed position (0 s) and reaches the open position at 0.16 s. The dark-colored and light-colored fluid densities are matched.

The growth rate of the mixing region is plotted in Fig. 3.7. The growth, or spreading, of the dye is shown to have two different phases of behavior. In the first 0.4 s the mixing wake region (a) is measured to grow at 34 mm/s with the plate reaching the open position after 0.16 s. For times greater than 0.4 s the dye (b) is measured to advance at 0.14 mm/s with the overall thickness of the wake region at approximately 1.2 cm. Additionally, the rate at which the dye advances is negligible to the 81 mm/s velocity of the gravity current head. The thickness of the wake region immediately after the plate has been removed, normalized by the thickness of the plate, is calculated to be 15.7.

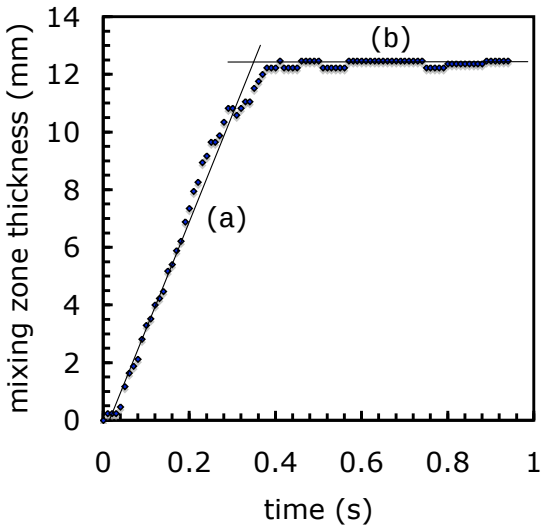

Figure 3.7: Mixing zone thickness as a function. The mixing zone (a) grows at a rate of 34 mm/s while the dye (b) is measured to advance at a rate of 0.14 mm/s.

3.3 Gravity currents in the GDT

The second experimental setup visualizes gravity currents in the GDT test section. The imaging is accomplished using planar laser-induced fluorescence of the acetone molecule. The gravity current study described in this section is non-reactive. The images from this study are very useful as they can be directly overlaid with the schlieren images obtained from the actual combustion experiments. The overlay helps

explain the behavior of the detonation wave and transmitted wave features. The combustible mixture was replaced by a surrogate acetone-helium mixture with an equivalent mean density to match the normalized density ratio, $(\rho_2 - \rho_1)/\rho_1$. The large concentration of acetone provided a high fluorescence yield. A list of the experimental details for each run can be found in Appendix C. A typical experiment was carried out by filling the GDT with acetone and helium through the method of partial pressures. The sliding valve was kept in the closed position while nitrogen or oxygen was inserted into the test section. Finally the fire button is then pressed, which opens the sliding valve and triggers the laser.

3.3.1 Planar laser-induced fluorescence visualization

Acetone PLIF was chosen as a diagnostic largely because it provides a two-dimensional slice of the flow field and is relatively easy to implement. A substantial body of work (see Thurber and Hanson, 1999) is available, and the Ph.D thesis by Thurber (1999) outlines the key issues involved in implementing this diagnostic. This section will only describe the basic setup.

Figure 3.8 is a schematic showing the orientation of the laser light sheet and the GDT test section. An excimer laser was used to produce a 308 nm rectangular light beam 1 cm by 2 cm in size. The pulse length was 20 ns and the laser was set to a 5 Hz repetition rate. The laser beam was steered through a periscope to line up with the test section and passed through a cylindrical lens with a 35 mm focal length. The orientation of the rectangular beam was such that the longer (2 cm) side was expanded through the lens leaving a light sheet of 0.7 cm at the test section viewport, as a result of the slow convergence of the narrow side of the rectangular beam through the lens.

The fluorescence signal was imaged perpendicularly to the light sheet on a Princeton Instruments ITE/ICCD-576 intensified CCD camera with 576 x 384 pixel and 12 bit resolution. The camera was set to a 5 Hz frame rate, operated with a 50 μs exposure time, and used a Nikon 50 mm f/1.8 lens. To obtain a 5 Hz frame rate, the

number of pixels used was reduced to satisfy acquisition limitations of the camera.

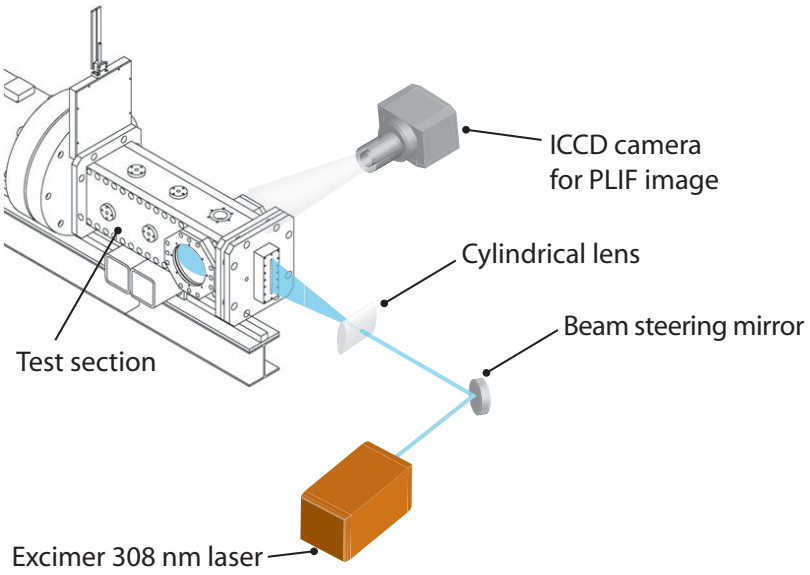

Figure 3.8: A schematic illustrating the orientation of the test section and the excimer laser light sheet. Note that the window location in the actual experiments is at port 1. This schematic has the window shown at the port 2 position.

3.3.2 Results

A typical sequence of images obtained from the PLIF setup is shown in Fig. 3.9. The images show the gravity current head propagating from left to right with an average velocity of 96 ±12 mm/s. The acetone-helium mixture corresponds to the white portion of the image. The dark parts of the image represent either the nitrogen or oxygen used in a particular experiment. The first image corresponds to 0.6 s after the sliding valve reached the open position. Each subsequent image is delayed by 0.2 s.

To compare both gravity current experiments, we must determine the time frame in which they overlap. This is accomplished by comparing profiles at various times. Because the channel heights differ by a factor of two, the velocity of the GC in GDT experiments will be $\sqrt{2}$ faster than in the water channel (see Eqn. 3.1). The GC velocity in the GDT, once calibrated to correspond to the water channel height, is

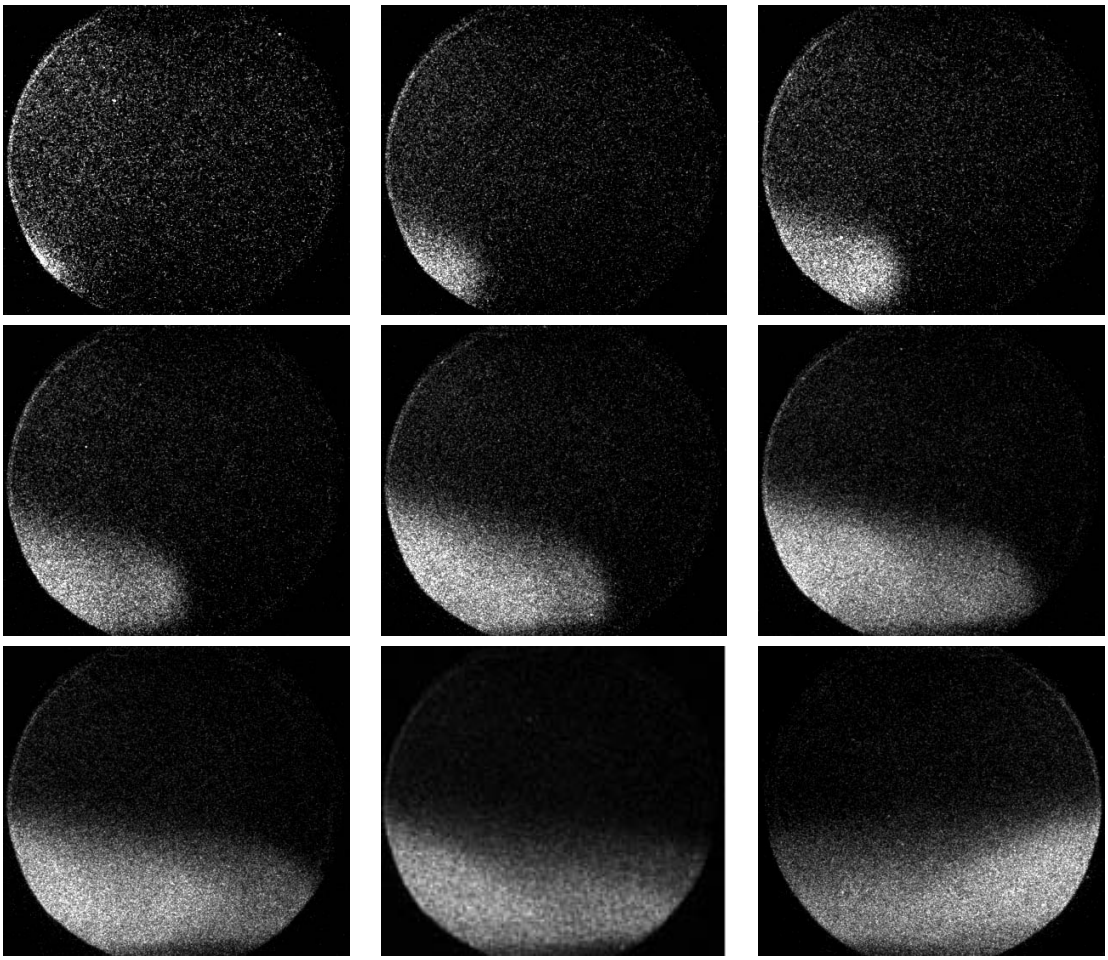

Figure 3.9: A sequence of planar laser-induced fluorescence images showing the gravity current propagation. The first image corresponds to a time of 0.6 s measured from when the plate in the sliding valve assembly moves to the open position. Each image is taken at a 0.2 s time increment.

68 ±8 mm/s compared with the 81 ±12 mm/s velocity reported in Sec. 3.2.3. These values have a 16% difference, which is within the envelope of experimental uncertainty. It must also be noted that the value of the constant $\mathcal{C}$ in Eqn. 3.1 is not necessarily the same in both experiments. $\mathcal{C}$ is usually determined experimentally for a given system. Theoretically the value of $\mathcal{C}$ is $1/\sqrt{2}$; however, Keulegan (1957) found $\mathcal{C}$=1.05 from detailed experimental measurements of saline-water systems.

3.4 Concluding remarks

The experiments described in this chapter have led to an understanding of the initial formation and propagation of gravity currents in the GDT. The water channel addressed the role of the retracting plate in generating a turbulent wake region. It was found that the wake region grows at a rate of 34 mm/s and reaches a thickness of 12 mm after 0.4 s. When the valve delay time equals 0 s the thickness of the wake region is 7 mm when the plate reaches the open position ($t = 0.2$ s).

The gravity current velocity in the GDT was measured to be 68 mm/s. The billows that form at the interface (a consequence of the Kelvin-Helmholtz instability) resulted in a region of vorticity with a thickness on the order of 14 mm. These results will be used in Chaps. 4 and 5 to understand the detailed gas dynamic features observed in the detonation-diffuse interface interactions.

Chapter 4

Detonations in Transverse Composition Gradients

The problem of a detonation propagating in a composition gradient can be divided into two main categories. The first is when the detonation propagation is parallel to the direction of the gradient, and the second is when it is perpendicular. In general, the gradient vector and the propagation vector are not parallel or perpendicular but at some intermediate angle. For the purpose of this discussion, the composition gradient can be represented as a combustible mixture that has a varying equivalence ratio $\Phi(x, y)$. Figure 4.1 and 4.2 are sketches illustrating both parallel and perpendicular cases.

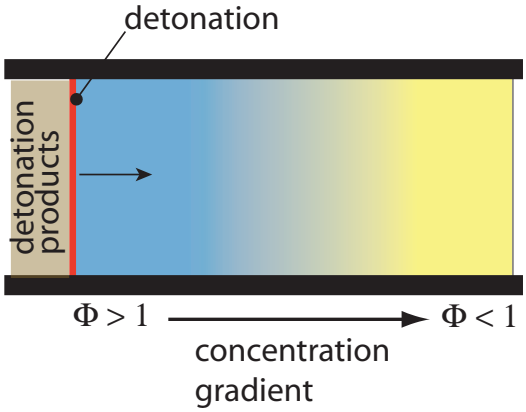

Figure 4.1: A sketch illustrating a detonation propagating parallel to a concentration gradient.

Detonations propagating in a composition gradient parallel to the direction of

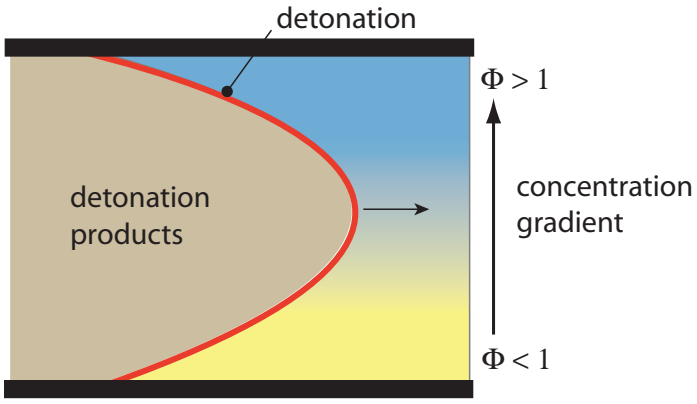

Figure 4.2: A sketch illustrating a curved detonation propagating perpendicular to a composition gradient.

propagation (Fig. 4.1) have received some attention in the literature. The problem is characterized as a detonation transmission phenomena. Thomas et al. (1991) carried out experiments in a vertical detonation tube where two mixtures were allowed to diffuse upon removal of a sliding plate. Other experiments by Bjerketvedt et al. (1986) looked at re-initiation of detonations across inert regions. Kuznetsov et al. (1997) investigated detonation transmission through a sharp interface into a combustible mixture and an oxider.

When the detonation propagation direction is perpendicular to the mixture gradient, a curved detonation wave results. There has been little work done on propagation perpendicular to a continuous composition gradient. This is due in part to the dependence of the detonation velocity on the equivalence ratio. For an ideal detonation, the normal component of the curved wave will correspond to the local Chapman-Jouguet detonation velocity. Ideal detonations refer to a zero thickness reaction zone whereas real detonation waves have a finite thickness related to the chemical reactions. The main difference is that ideal detonations do not depend on any feature with a length scale such as curvature, channel height, and interface thickness. Ishii and Kojima (2004) experimentally made and measured concentration gradients by diffusion and used soot foils to characterize the detonation propagation. Calhoon and Sinha (2005) examined concentration gradients in a numerical study to investigate the possibility

of a flame occurring in the incomplete combustion products.

The aim of the following discussion is to address the key physical issues that arise when a detonation propagates in the direction normal to a concentration gradient, as illustrated in Fig. 4.2. Some of the main issues to be discussed are the general shape of the detonation wave, effects of wave curvature, and the decoupling of the shock wave and reaction zone. The special case of a detonation propagates in the direction normal to a sharp concentration gradient is discussed in Chap. 6.

4.1 Physical considerations

To predict the shape and propagation velocity of a curved detonation wave in a mixture gradient (Fig. 4.2), it is first required to establish how the detonation velocity varies with equivalence ratio. The inflow velocity needed to keep the curved detonation wave in a wave-fixed coordinate system equals the maximum CJ velocity found over the range of equivalence ratios. The detonation velocity is plotted as a function of the equivalence ratio for ethylene, methane, and propane with oxygen in Fig. 4.3. The velocity in all cases peaks at equivalence ratios between 2 and 3. This is an important observation for modeling purposes as most simple one step chemistry models (Calhoon and Sinha, 2005) have a maximum detonation velocity at stoichiometric conditions. This means that any curved wave will have its apex on the fuel rich side of the gradient.

The extremities of the curved detonation wave on the fuel rich and fuel lean sides eventually reach mixture compositions incapable of supporting a detonation. These limits have been obtained experimentally for various fuel-air mixtures (see Coward and Jones, 1952). If we consider the ZND model to describe a detonation wave, then the detonability limit coincides with an uncoupling of the reaction zone from the leading shock wave. In a more realistic description, the front curvature and transverse waves (Radulescu and Lee, 2002) associated with the actual cellular detonation front need to be considered.

In this study, we will make use of the induction time to explain the decoupling of

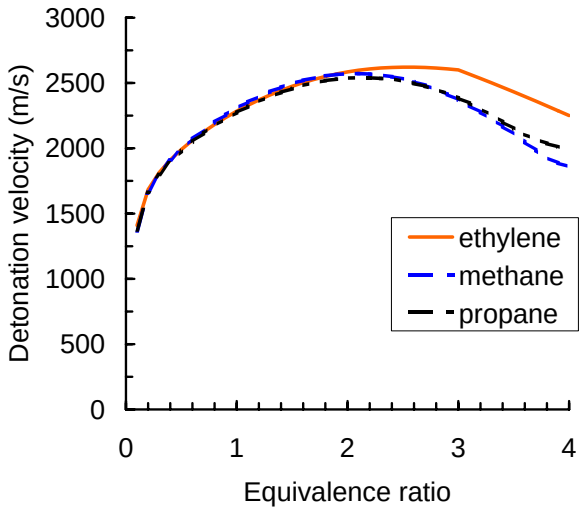

Figure 4.3: Detonation velocity versus equivalence ratio for ethylene, methane, and propane with oxygen.

the detonation wave. Large induction times are a consequence of the low post-shock temperatures for insensitive mixture compositions and translate to a large cell size (see Sec. 1.4.3). A plot of ZND induction time versus equivalence ratio is shown in Fig. 4.4. Ethylene-oxygen mixtures have the lowest induction time at any given equivalence ratio, followed sequentially by propane-oxygen and methane-oxygen. The sharp rise in induction time as the equivalence ratio approaches zero and four indicates the difficulty that arises in trying to detonate very lean or very rich mixtures.

4.2 Curved detonation wave structure

It is possible to construct the shape of a curved detonation if we assume an ideal, i.e., zero thickness, wave front moving at a constant axial speed. The detonation wave is assumed to be stationary in the wave-fixed reference frame by imposing the maximum detonation velocity over the range of equivalence ratios as the inflow velocity. For ethylene-oxygen this corresponds to an inflow velocity of 2622 m/s at $\Phi = 2.5$. The methane and propane maximum detonation velocities are 2571 m/s and 2540 m/s, respectively at $\Phi = 2.1$. Figure 4.5 illustrates the general layout of this problem. A set of coordinates is defined with one axis ($\vec{n}$) locally tangent to the detonation wave

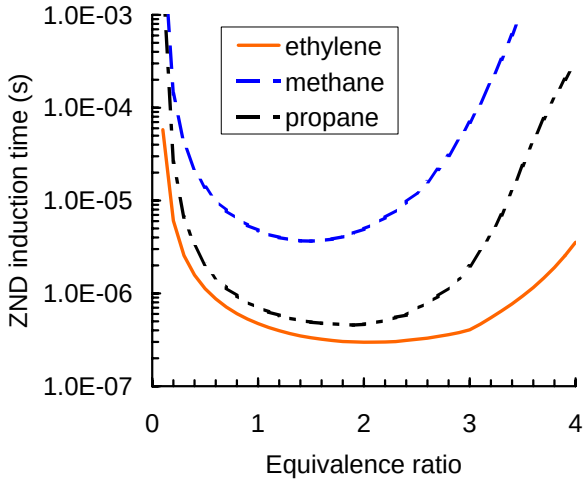

Figure 4.4: ZND induction time versus equivalence ratio for ethylene, methane, and propane with oxygen.

and the other axis ($\vec{s}$) normal to it.

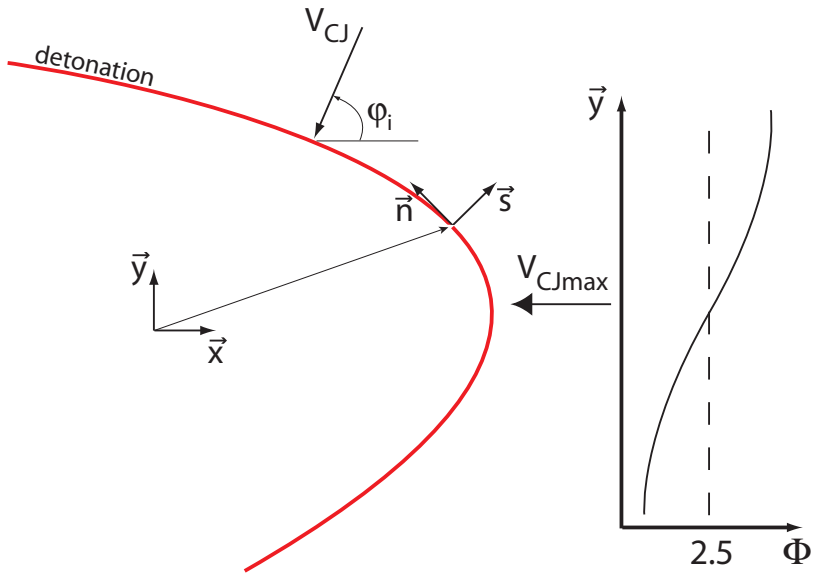

Figure 4.5: A schematic illustrating a curved detonation in a wave fixed reference. The inflow velocity corresponds to the maximum CJ velocity over the range of equivalence ratios. Axes $\vec{n}$ and $\vec{s}$ represent the tangential and normal components of the curve.

The local angle, φ_i, of the curved detonation is specified by setting the normal

component of the velocity equal to the local CJ detonation velocity,

$$\varphi_i(y) \;=\; \cos^{-1}\left(\frac{V_{CJ}(y)}{V_{CJmax}}\right), \tag{4.1}$$

where V_{CJ} is a function of equivalence ratio and therefore a function of position (y) in this analysis. φ_i also corresponds to the angle between the fixed reference frame ($\vec{x}, \vec{y}$) and wave frame ($\vec{n}, \vec{s}$). From the geometry of the front, the co-slope of the wave is

$$\frac{dx}{dy} \;=\; \tan(\varphi_i(y)), \tag{4.2}$$

which can be solved numerically to give the shape. The wave structures for various fuels are shown in the wave-fixed frame in Fig. 4.6. The portion of the curved detonation that touches the vertical axis corresponds to the max CJ velocity. The equivalence ratios for these cases are 2.5 and 2.1 for ethylene and methane or propane, respectively. The x and y coordinates have the same scale to highlight the curved detonation wave structure. These shapes are particular to the linear composition gradient, and the shape will be different in the actual experiments.

The analysis can be taken one step further to include the decoupling of the detonation wave at both fuel rich and fuel lean limits. This requires the knowledge of the detonation decoupling point and the subsequent analysis to compute the angle of the transmitted and reflected wave system. The transmitted shock angle is determined by considering the composition gradient to be so steep that the width of the gradient region is much less than the detonation cell size. In this case, the analysis simplifies to a detonation interacting with a sharp interface (see Chap. 6). This corresponds to a planar detonation interacting at a node, and the transmitted and reflected wave structure can be determined. In this fashion, we can use the sharp interface solution to obtain a limiting transmitted shock wave angle far from the interface in the case of a diffuse interface.

For composition gradients whose length scales are on the order of the reaction zone length or greater, the role of the composition gradient (and possibly the detonation wave curvature) needs to be factored into the analysis to estimate the point at which

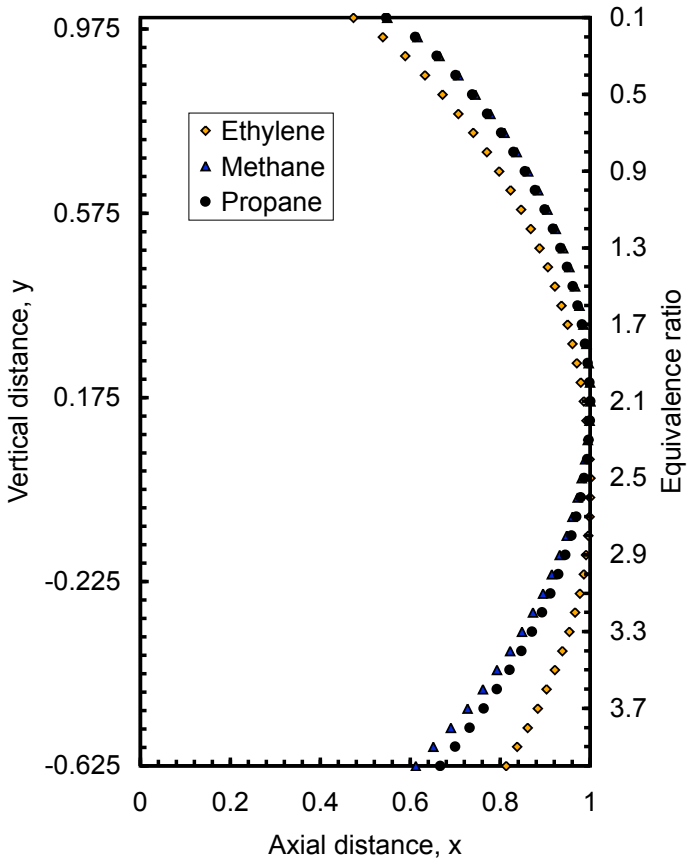

Figure 4.6: A plot of the curved detonation wave shape using an arbitrary scale for distance. The equivalence ratio is also shown. Note that the wave speed maximums for ethylene, methane, and propane occur between $\Phi = 2$ and 3.

the detonation wave will decouple. The following section will explore the implications of a composition gradient on the curved detonation wave profile and ZND induction time.

4.3 Composition gradient

The composition gradient is largely responsible for the decoupling of the detonation wave due to the Arrhenius dependence of the reaction rates on post-shock temperature and the variation of CJ wave speed with composition. The composition gradient is estimated from the gravity current measurements in Chap. 3 to understand more precisely the role that the composition profile plays. A comparison of the predicted

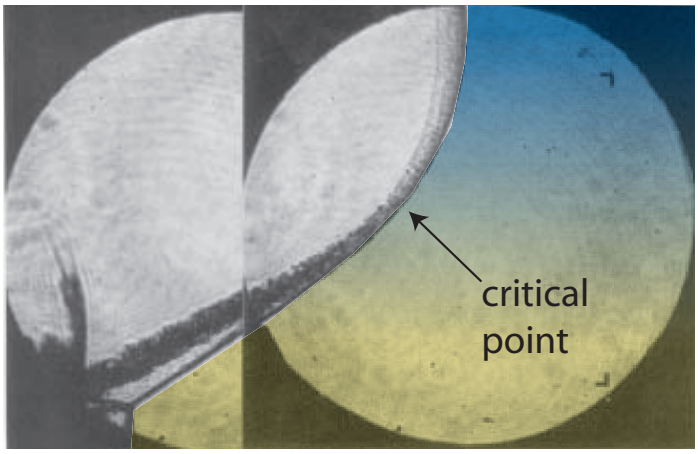

Figure 4.7: A schlieren image of a curved detonation propagating in a composition gradient (shown in false color). The detonation is moving from left to right into a $\Phi = 2.5$ ethylene-oxygen mixture on top separated by a diffuse interface with oxygen on the bottom. The reaction zone is seen decoupling from the shock front.

wave shape to the measured shape is given in Sec. 5.2.2. A simple error function profile of the form

$$X_i = \mathcal{C}_1 \left[1 + \mathrm{erf}\left(\frac{y - y_\circ}{\delta_c} \right) \right] + \mathcal{C}_3 \tag{4.3}$$

is assumed for the species mole fraction X_i as a function of the vertical distance y. The constants $\mathcal{C}_1$, δ_c, $\mathcal{C}_3$, and $y_\circ$ are specific to each experiment and delay time. The error function profile is motivated by appealing to the solution of the diffusion equation as well as knowing the boundary conditions at both limits of the y coordinate. The estimated profiles are only expected to be qualitative since the composition is not known precisely.

Two composition profiles are investigated in this section. The first is for a $\Phi = 2.5$ ethylene-oxygen mixture diluted with nitrogen, and the second is for a $\Phi = 2.5$ ethylene-oxygen mixture diluted with oxygen. Diluting with oxygen decreases the equivalence ratio whereas diluting with nitrogen does not alter the equivalence ratio but decreases the volume fraction of combustible mixture. The combustible mixture is located on top of the nitrogen in the nitrogen dilution case and below the oxygen in the oxygen dilution case because the ethylene-oxygen mixture has a molecular weight of 30 g/mol, which is between oxygen and nitrogen. The estimated mole fraction

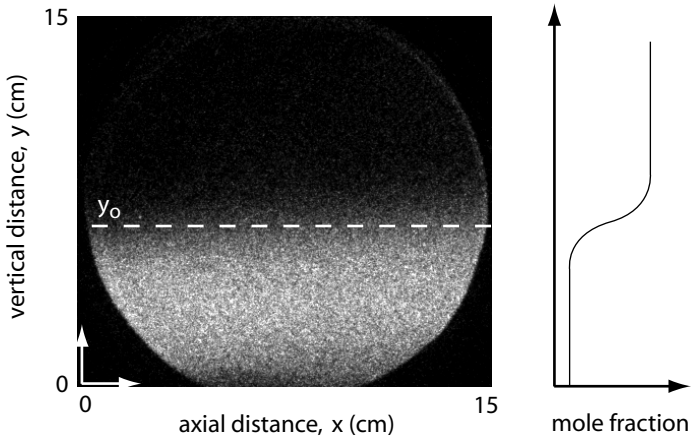

Figure 4.8: A planar laser induced fluorescence image of the gravity current in the test section after a delay time of 3 s. The horizontal line indicates the vertical distance $y_\circ$ the distance to which the composition gradient is fitted. A sketch of the expected composition variation is shown.

profiles are shown in Fig. 4.9 as a function of vertical distance in the test section. For oxygen dilution, the mole fraction of oxygen is equal to one at $y = 0$ cm and increases to 0.55 at $y = 15$ cm. For nitrogen dilution the mole fraction of nitrogen is equal to zero at $y = 0$ cm and one at $y = 15$ cm. The constants $\mathcal{C}_1$ and $\mathcal{C}_3$ are determined from the change in mole fraction. The constant δ_c is a measure of the diffuse interface thickness and is obtained by re-scaling the vorticity thickness by a factor of two to account for the difference in height measured in the water channel experiments (see Fig. 3.5). The values of the constants are listed in Table 4.1.

composition	$y_\circ$ [cm]	$\mathcal{C}_1$	δ_c [cm]	$\mathcal{C}_3$
O_2	9	0.23	3	0.55
N_2	6	0.5	3	0

Table 4.1: Table of constants used in Eqn. 4.3 to specify the composition profile.

The ZND induction time is plotted as a function of the vertical distance y in Fig. 4.10. The induction time (see Sec. 1.4.2) spans over four orders of magnitude, from microseconds in the undiluted sections of both oxygen and nitrogen profiles, and rapidly rises to milliseconds as the dilution increases. The dramatic increase in induction time has been observed (see Kuznetsov et al., 1997) to result in decoupling

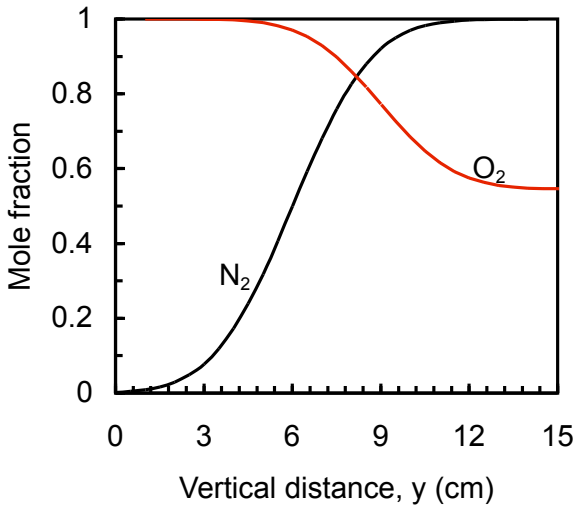

Figure 4.9: Estimated mole fraction plotted as a function of vertical distance y in the test section. Two profiles are shown based on Eqn. 4.3 for the oxygen dilution case (O_2) and the nitrogen dilution case (N_2).

of the reaction zone from the detonation in the case of propagation along the gradient direction.

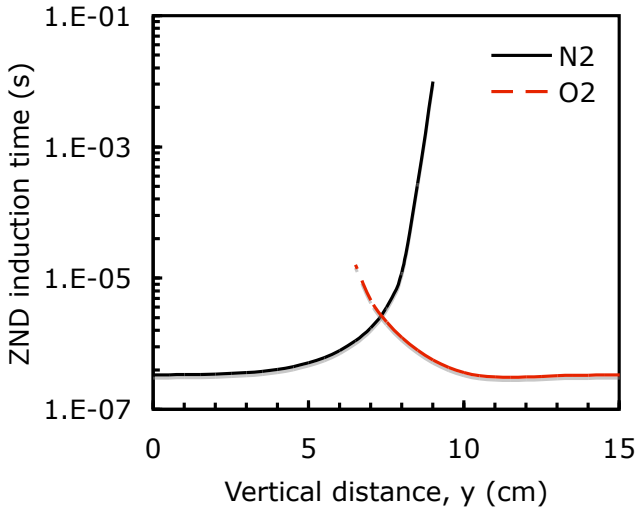

Figure 4.10: ZND induction time plotted as a function of vertical distance y in the test section. The profiles are shown for the oxygen dilution case (O_2) and the nitrogen dilution case (N_2).

The detonation velocity is plotted as a function of vertical distance y in Fig. 4.11. Dilution with nitrogen, at a distance of 0 cm indicates that the detonation velocity

equals 2622 m/s, corresponding to the undiluted limit. As the vertical distance increases, the nitrogen dilution increases, resulting in lower detonation velocities. The same is true when diluting with oxygen; however, the decrease in detonation velocity results when decreasing the equivalence ratio. In this case, it turns out that the maximum detonation velocity is at an equivalence ratio of 2.5 (see Fig. 4.6). In general, instead of the curve decreasing monotonically, there would be a peak at the equivalence ratio corresponding to the maximum detonation velocity.

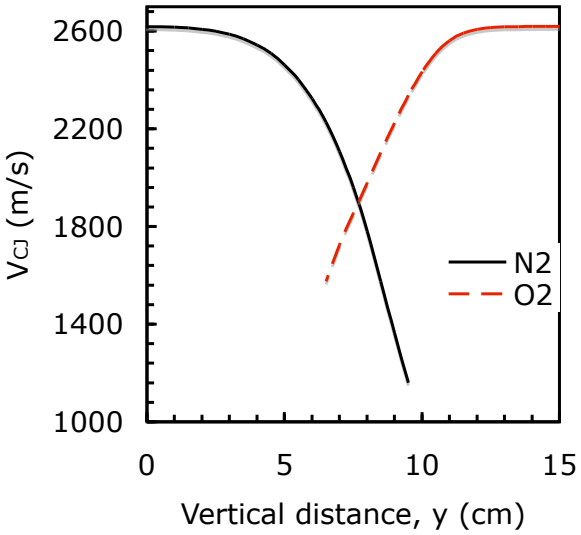

Figure 4.11: Estimated detonation velocity plotted as a function of vertical distance y. The profiles are shown for the oxygen dilution case (O_2) and the nitrogen dilution case (N_2).

The spatial profiles of the curved detonation waves with mixture compositions based on Eqn. 4.3 are shown in Fig. 4.12. The vertical and axial distances are plotted on the same scale. The leading front waves are both situated at an axial distance of 10 cm. The shape of the wave is determined using the velocity profile and Eqn. 4.2.

4.3.1 Wave curvature

Detonation wave curvature needs to be considered in a complete description of the reaction zone decoupling process. Experiments by Kaneshige (1999) and simulations by Hung (2003) have shown that curvature plays a substantial role in the decoupling

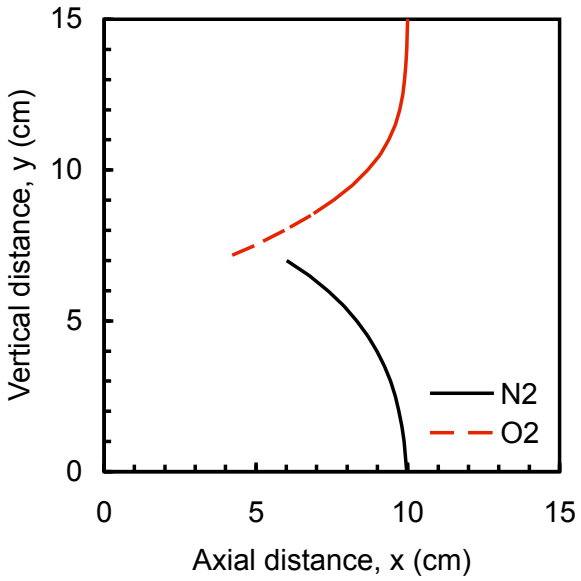

Figure 4.12: Estimated wave shape $y(x)$ for the oxygen dilution and the nitrogen dilution cases.

and initiation of projectile-driven detonations. A reaction zone decoupling model postulated by Kaneshige stated that immediately behind a curved shock wave at the von Neumann (vN) point, a fluid particle is subject to two competing effects: heat release via thermicity and gas-dynamic cooling as a result of streamline divergence. These competing effects alter the fluid particle induction time. There is a critical point that separates fluid particles with chemical induction times that follow a ZND detonation profile from those whose induction time is too large and results in the uncoupling of the shock and reaction zone.

The details of this model require precise measurements of the composition profile to obtain an accurate prediction of the detonation decoupling region. Lacking accurate measurements of the species profiles, only some general comments can be made regarding the importance of this effect.

4.3.1.1 Determining the wave curvature

The curved detonation profile (Fig. 4.7) is digitized using image thresholding and edge detection. This is implemented in a Matlab script that converts the grayscale

image to a binary format using a thresholding routine. The binary image is then edge detected using the Sobel method. The result of this procedure is shown in Fig. 4.13 corresponding to Exp. #1878, where the detected edge is overlaid with the original image. The angle β is defined in this reference frame along with the curvature κ.

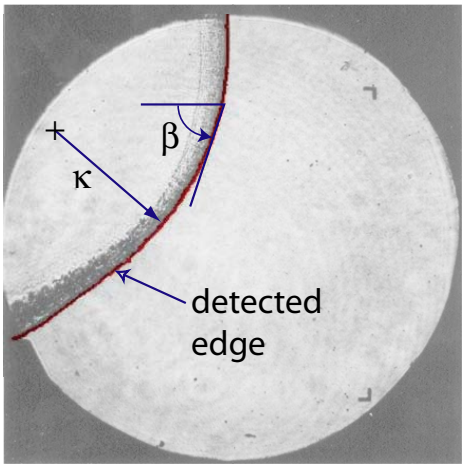

Figure 4.13: A schlieren image of a detonation wave (Exp. #1878) with an edge detected curve over-layed. The local shock angle β and curvature κ are defined.

The set of points collected from the edge detection script is then fitted to a third order polynomial with continuous first and second derivatives. The curvature κ is defined by the equation

$$\kappa = \frac{d^2y/dx^2}{(1+(dy/dx)^2)^{\frac{3}{2}}} \tag{4.4}$$

where the curved wave is defined by a function $y(x)$ that starts at the origin and is oriented concave up.

4.4 Concluding remarks

The analysis carried out in this chapter highlighted some of the key issues in detonations traveling with velocity normal to a composition gradient. A key result is that the detonation wave will not be symmetric about the $\Phi = 1$ point. The curved detonation wave will achieve its apex at the point of maximum detonation velocity

(Φ between 2 and 3 for most hydrocarbon fuels in oxygen).

Detonation decoupling is a result of a dramatic increase in the induction time due to the composition gradients. It was shown in Sec. 4.3 that variations in the mixture composition decreased the local detonation velocity resulting in wave curvature and lower post-shock temperature. Eventually, detonation decoupling occurs when the post-shock temperature becomes too low. Rapid chemical reaction ceases and the detonation becomes an oblique shock wave followed by a slowly-reacting turbulent mixing zone. Further experimentation is required to quantify the location of the failure point by accurately measuring the composition along the vertical direction.

Chapter 5

Results & Analysis: Detonation Interaction with a Diffuse Interface

This chapter discusses the experimental results for detonations interacting with diffuse interfaces. Diffuse interfaces are formed by allowing a gravity current to propagate through the test section as discussed in Chap. 3. The shape and extent of the gravity current are defined by the delay time that corresponds to the time elapsed between when the sliding valve reaches the open position and the instant that the detonation is initiated. The delay time is on the order of one to five seconds for most experiments and is therefore about three orders of magnitude longer than the experimental test time ($\approx$5 ms).

Detonations propagating through a planar interface with gradient vector parallel to the detonation velocity are presented first. These experiments highlight the principle gas dynamic features and transmission of a detonation into a non-combustible mixture. The analysis for non-planar interfaces discusses the observed features and decoupling of curved detonations. The roles of composition gradient and wave curvature are compared to the experimental results. The impulse is calculated by integrating the pressure signals from the transducers in the test section and is used to quantify the amount of secondary combustion that occurs in the turbulent mixing zone (TMZ). Finally, an impulse model is developed and compared to the experimental results.

5.1 Planar interface

The process of a detonation in a fuel-rich mixture propagating into an inert or oxidizing gas can be analyzed with varying degrees of realism. A realistic description of this problem must include all the gas dynamics of the detonation interaction with the interface, and the ensuing turbulent mixing and chemical reactions. To gain a basic understanding of the major features, we start by using simplified one-dimensional gas dynamic analysis. This analysis is quantitative for experiments in which the interface is planar with composition gradient vector parallel to the detonation wave. In terms of this experiment, this means situations for which the initial density difference across the interface is close to zero and the delay time is zero. When the interface becomes non-planar the simple one-dimensional analysis does not account for the multi-dimensional interaction process. Figure 5.1 highlights the principle gas dynamic features. A detonation wave that propagates with the CJ speed passes through the initial interface to yield a transmitted shock and a reflected expansion wave. The original interface is transformed into a contact surface that is set into motion towards the transmitted shock. The two possible locations of the window in the test section are shown on Fig. 5.1. They are labeled as port 1 and port 2. The window center in the port 1 location is 0.275 cm from the valve plane while port 2 is centered 0.56 m from the valve plane.

The wave structure in Fig. 5.1 is obtained by treating the flow field as being made up of uniform regions separated by simple waves and contact surfaces matching pressure and velocity between adjacent uniform regions (Thompson, 1988). The initial conditions are determined by the combustible mixture in GDT (driver gas) and the inert diluent or oxidizer in the test section (test gas). The post shock and CJ detonation states are determined using the Cantera chemical equilibrium code by Goodwin (2005). The solution is determined by matching the pressure and velocity across the contact surface. This is accomplished using a Newton solver to minimize the iterations needed to converge to the solution.

The detonation wave and transmitted shock evolution can be understood by look-

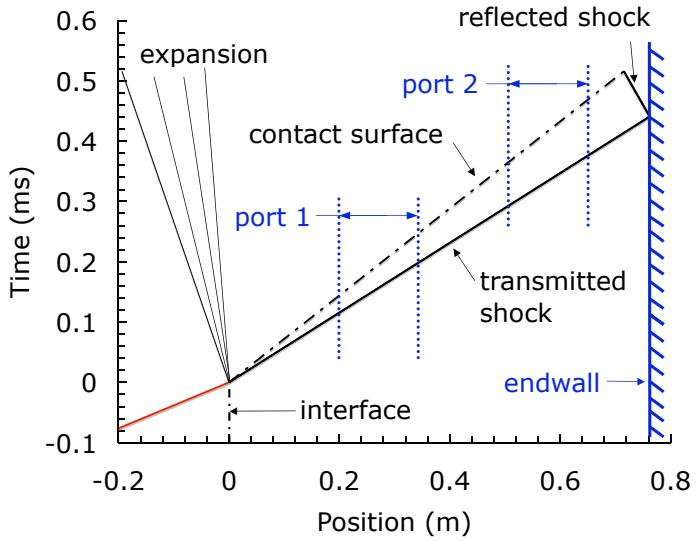

Figure 5.1: A space-time diagram illustrating the main features of the detonation transmission process. The window locations (port 1 and port 2) are included for reference. The calculations were made for a mixture corresponding to experiment 1831.

ing at a typical pressure versus time plot shown in Fig. 5.2. The figure includes seven pressure time histories: P1-P3 located in the GDT and P4-P7 located in the test section. Each pressure trace is vertically shifted by 1 MPa for clarity. Zero on the time axis corresponds to the instant when the combustion was ignited in the detonation tube. The pressure histories show a detonation propagating from P1 to P3 followed by a transmitted shock on transducers P4 to P7. In this particular experiment, the measured detonation velocity was 2620 m/s and the transmitted shock velocity was 1575 m/s for an ethylene-oxygen mixture at $\Phi = 2.5$ propagating into oxygen. An approximately 3 MPa reflected pressure is observed at P7 and the reflected shock can be observed on P6 to P4 traveling back toward the ignition end of the GDT.

The experimental time of arrival and the one-dimensional wave analysis are compared in Fig. 5.3. This is a space-time plot similar to that of Fig. 5.1 with the circles indicating the time of arrival of the transmitted shock wave at transducers P4 to P7. The data corresponding to the detonation arrival times at P1 to P3 are not shown due to large distances between the transducers. Of more value are the transmitted shock data where variations between experiment and theory can be as large as 7%

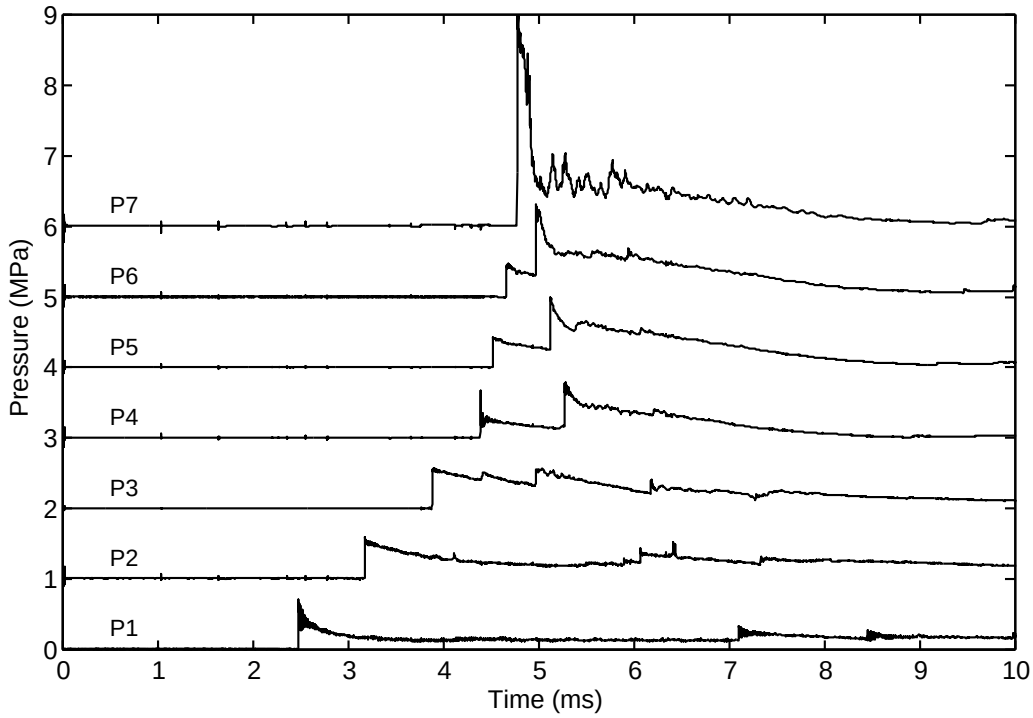

Figure 5.2: Pressure histories for seven pressure transducers on the experiment. P1-P3 are located on the GDT while P4-P7 are located on the test section (P7 is on the end wall). The pressure traces are offset at 1 MPa increments for visibility. The mixture is composed of $2.5C_2H_4 + 3O_2$ with O_2 as the test gas and corresponds to experiment 1833.

(see Appendix A, Fig. A.1).

A schlieren image sequence from three separate experiments is shown in Fig. 5.4. These images show the transmitted shock wave propagates from left to right followed by the contact surface. The transmitted shock is compressing oxygen in this case, which is separated from the partially oxidized combustion products located on the left side of the contact surface. The images are taken at times 18, 28, and 78 μs from the instant the transmitted shock reaches P6, which coincides with the center of the window. The mixture is composed of $2.5C_2H_4 + 3O_2$ with O_2 as the test gas. The delay time of the sliding valve was zero seconds to minimize the formation of a gravity current. The contact surface is nearly vertical and only slightly perturbed showing that under these conditions the role of gravity currents and RM instabilities play a minor role. The average distance of 117±3 mm between the shock and contact

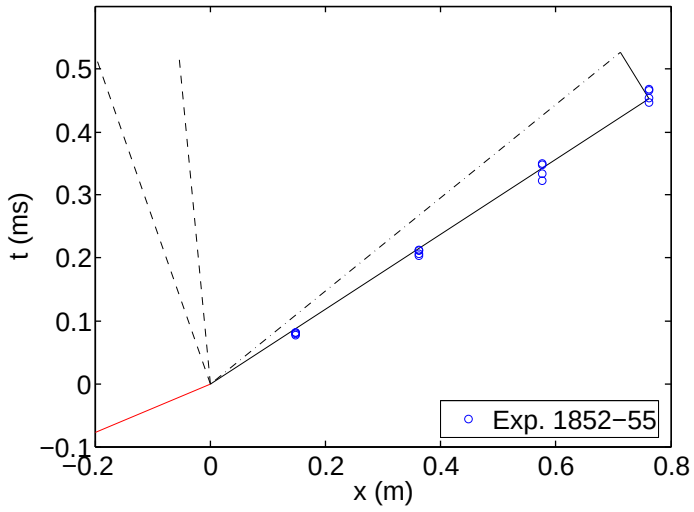

Figure 5.3: A space-time diagram comparing the experimental data with the one-dimensional gas dynamic calculations. The experimental data has been shifted so that $t = 0$ coincides with the instant when the shock reaches the interface. The mixture is composed of $3C_2H_4 + 3O_2$ with O_2 as the test gas and experiments 1852 to 1855 are shown.

surface in the middle image of Fig. 5.4 is obtained by edge detection and differs by 9% from the computed distance of 128 mm from one-dimensional theory at that time.

5.2 Non-planar interfaces

The experimental details of non-planar interfaces are addressed in this section. The general description of this problem, shown in Fig. 1.4, is of a detonation wave propagating through a diffuse interface generated by a gravity current. The gravity current (Chap. 3) and detonations in concentration gradients (Chap. 4) analyses have outlined the basic features. A schematic with supporting experimental observations of the interaction process is shown in Fig. 5.5. The diffuse interface is composed of ethylene-oxygen with $\Phi = 2.5$ above oxygen. The sequence begins with a detonation wave (a) that propagates into the diffuse interface. A curved detonation wave (b) results leading to a decoupled transmitted shock and TMZ. As the detonation exits the gravity current what remains is a transmitted shock followed by the TMZ (c). The shock wave and TMZ occupy a smaller axial distance than the curved detona-

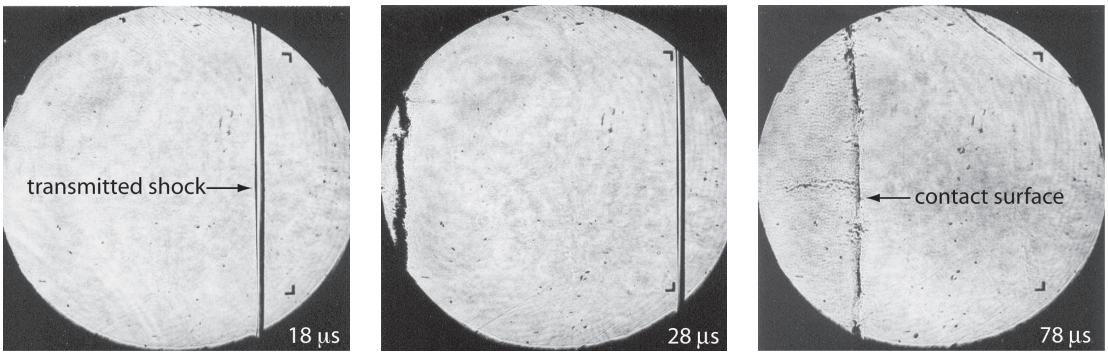

Figure 5.4: A sequence of schlieren images (port 2) that show the transmitted shock followed by the contact surface propagating from left to right. The valve delay time is zero and the mixture is composed of $2.5C_2H_4 + 3O_2$ with O_2 as the test gas. The time stamp of the image is shown on the bottom right corner and is with reference to when the shock reaches pressure transducer 6 (located at the center of the image).

tion wave with the distance between the shock and TMZ (d) increasing with time. When the shock reaches the endwall it reflects (e) and interacts with the interface a second time. The reflected-shock-interface interaction occurs in the space between the window and the endwall. Future experiments with a false endwall will enable visualization of the second interaction. The complex interaction of the shock wave with the lower experimental boundary (b), (c) produces a Mach reflection.

To examine the role of a non-planar interface, we must turn our attention to cases where the valve delay time is non-zero (Fig. 4.7). The formation of a gravity current introduces an important three-dimensional effect. This is shown in Fig. 5.6 and in more detail in Appendix A, Fig. A.2. Figure 5.6a is a position versus time plot for the case of a 5 s valve delay time, $2.5C_2H_4 + 3O_2$ driver mixture, and O_2 test mixture. The important feature in this figure is that the left two experimental data points, corresponding to P4 and P5, form a trajectory that has a velocity close to the detonation wave speed. Figure 5.6b is identical except for the test gas, which was N_2 in this case. In Fig. 5.6b, we observe that the trajectory of the transmitted wave coincides with the calculated wave speed. The difference is explained by the orientation of the gravity current formed upon opening the sliding valve and the location of the pressure transducers on the upper wall of the test section. As shown in

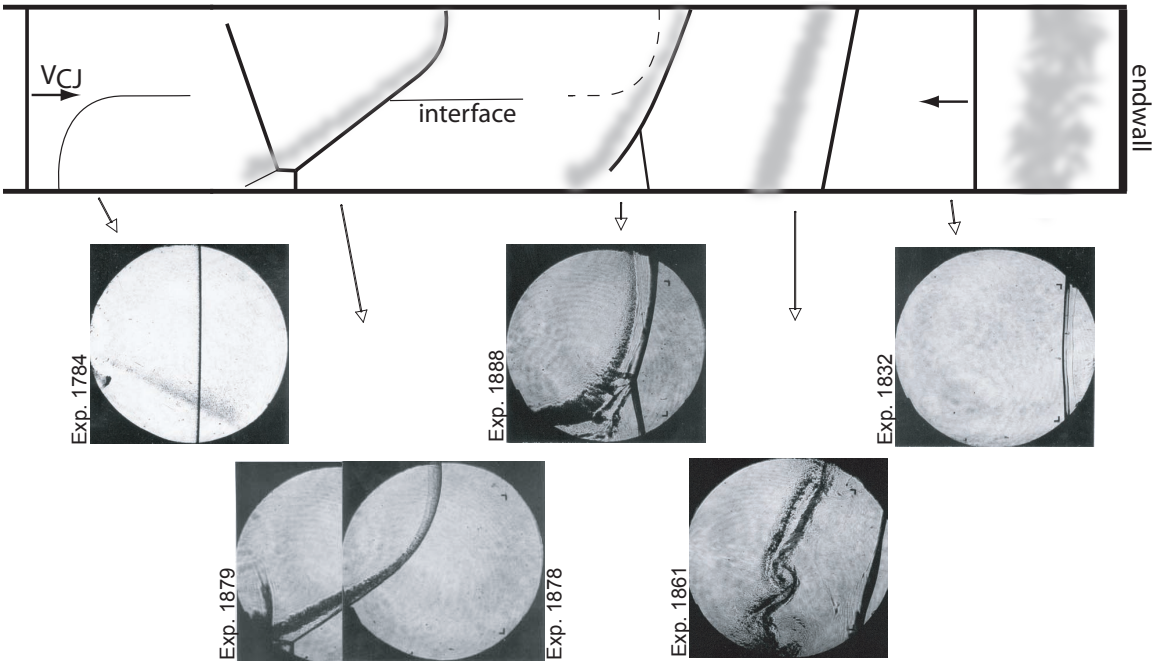

Figure 5.5: The interaction of a detonation with a diffuse interface is illustrated with supporting observations from experimental images. A detonation wave (a) interacts with the diffuse interface and forms a curved waved (b). Upon exiting the combustible mixture the detonation decouples completely resulting in a transmitted shock and TMZ (c) and (d). When the shock reaches the endwall it reflects (e) and interacts for a second time with the interface.

table 5.1, using O_2 in the driver section results in the combustible mixture remaining above the GC interface and O_2 below. This enables the detonation to advance in the upper half of the test section more rapidly than on the bottom thus resulting in a higher apparent transmitted wave speed. This is not the case when N_2 is used as the test gas, which results in the N_2 being above the combustible mixture corresponding to a negative value of the normalized density difference.

Test gas	ρ_1	ρ_5	ρ_{cj}	ρ_4	$\Delta\rho/\rho_1$	Atwood
O_2	0.185	0.196	0.339	1.165	0.059	0.549
N_2	0.185	0.171	0.339	0.938	-0.073	0.469
N_2O	0.185	0.269	0.339	2.521	0.457	0.763

Table 5.1: The Atwood and normalized density difference for a $2.5C_2H_4+3O_2$ mixture in the GDT.

Figure 5.7 is a composite schlieren image showing a curved detonation wave. The

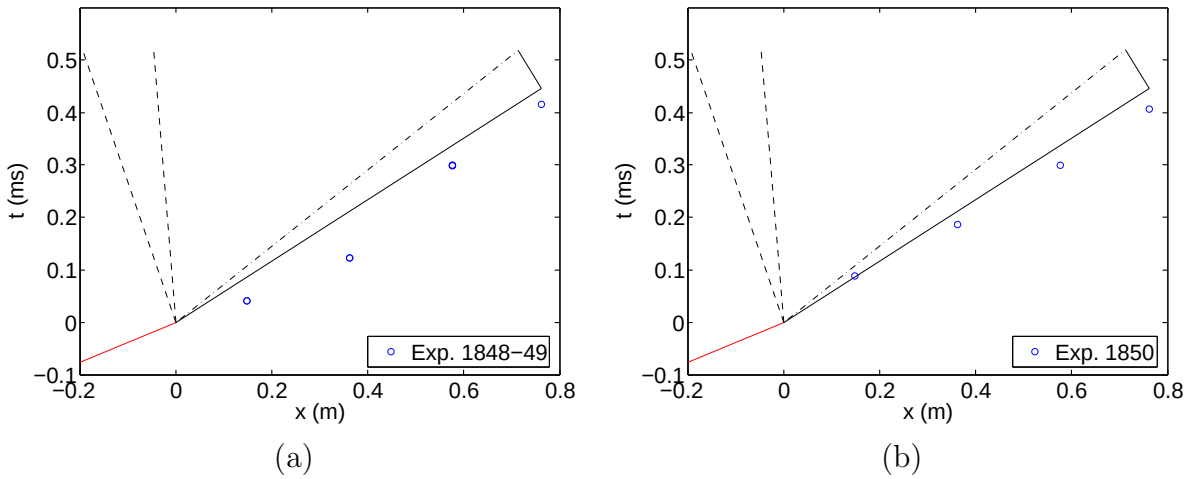

Figure 5.6: A time vs. position plot comparing the experimental data with one-dimensional shock transmission theory. The mixture in the GDT is $2.5C_2H_4$+$3O_2$ and in the test section (a) O_2 test gas, 5 s delay time, (b) N_2 test gas, 5 s delay time.

mixture gradient is formed by a gravity current composed of a $2.5C_2H_4 + 3O_2$ combustible mixture and N_2 as the test gas. The delay time is 3 s and corresponds to the PLIF image in Fig. 4.8. The denser combustible mixture (see Table 5.1) flows beneath the nitrogen resulting in a detonation wave (D) at the bottom of the image failing in the vertical direction and resulting in a shock wave (S). There is a Mach stem (MS) at the top wall that precedes a reflected shock wave (RS) and a transverse shock wave (TS). The TMZ appears to detach and grow behind the shock wave.

Table 5.2 lists the parameters varied in this study. The details are listed in Appendix B. The delay time is the experimental parameter that defines the shape of the interface. The combustible mixture equivalence ratio Φ controls the energetics and sensitivity of the detonation. The choice of test gas determines whether or not subsequent chemical reactions could occur and influences the Atwood number, important in the RM growth of the interface. Port 1 and 2 are used to investigate the system at different times in its evolution.

It is interesting to compare the curved detonation fronts in oxygen (Fig. 5.8a) and nitrogen (Fig. 5.8b). The most striking difference is that the detonation propagates on the top in image (a) and on the bottom in image (b) because the combustible mixture flows above oxygen and below nitrogen. Although these curved detonations

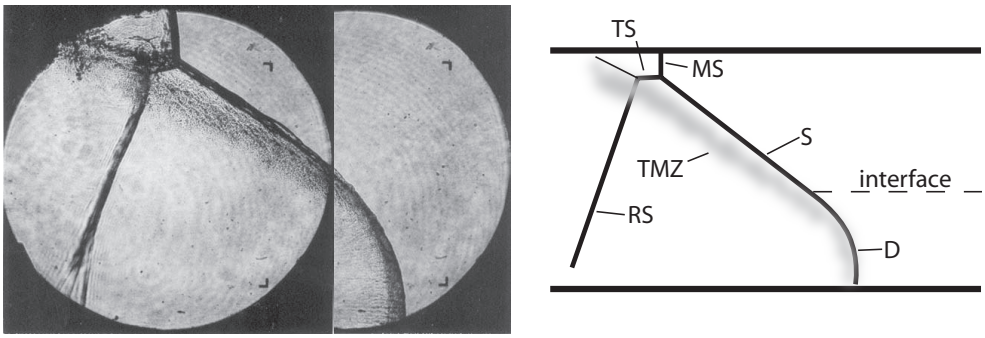

Figure 5.7: A composite schlieren image showing a detonation (D) propagating left to right on the bottom of the test section with an oblique transmitted shock (S) followed by a turbulent mixing zone (TMZ). The mixture gradient is formed by a gravity current composed of a $2.5C_2H_4 + 3O_2$ combustible mixuter and N_2 as the test gas. The delay time is 3 s and the images correspond to Exp. #1884,1883. Also shown are the Mach stem (MS), reflected shock (RS), and transverse shock (TS), a consequence of the confinement.

Window	Test gas	Φ	Delay time (s)
port 1	O_2	2	0
			1
port 2	N_2	2.5	3
	N_2O	3	5
			10

Table 5.2: A list of the parameters varied in the diffuse gradient experiments.

have the same overall shape, it is useful to compare the profiles of the leading wave. From an energetics standpoint, the concentration gradients in the two cases are quite different. In Fig. 5.8a the diffusive gradient starts at $2.5C_2H_4+3O_2$ on the top and ends with oxygen on the bottom. There is therefore a region where the mixture varies from $\Phi = 2.5$ to $\Phi \approx 0$. In Fig. 5.8b the mixture gradient starts with $2.5C_2H_4+3O_2$ on the bottom and ends with nitrogen on the top. This type of gradient is characterized by reducing the sensitivity of the combustible mixture with an inert diluent.

The images of the two curved detonations in Fig. 5.8 were processed (see Fig. 4.13) to determine the profile of the leading edge of the wave. Figure 5.9 is a plot of the wave shape with the data plotted in the concave up orientation. To accomplish this, image 5.8a was refleced along the horizontal axis and rotated 90° clockwise while image

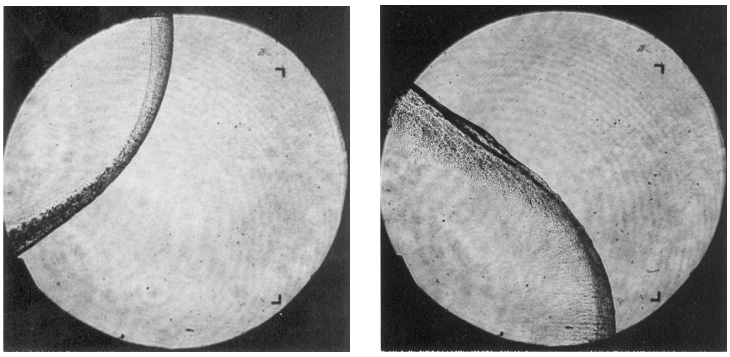

(a) (b)

Figure 5.8: Two schlieren images illustrating the role of the gravity current in detonation propagation. The mixture in the GDT is $2.5C_2H_4+3O_2$ and in the test section (a) O_2 test gas, 3 s delay time (Exp. #1878), (b) N_2 test gas, 3 s delay time (Exp. #1884).

5.8b was rotated 90° clockwise. Figure 5.9 plots the wave shape and the curvature κ defined by Eqn. 4.4. The wave shape of Exp. #1884 was fitted to a third order polynomial so that the derivatives could be taken. The curved detonation wave for Exp. #1884 corresponding to using nitrogen as the test gas has an overall higher curvature than Exp. #1878 where oxygen is used. The curvature close to the origin is about a factor of ten higher.

5.2.1 Overlay of gravity current and detonation

Laser induced fluorescence images of the gravity current (Chap. 3, Sec. 3.3.2) study were overlaid with schlieren images of the detonation waves to give insight into the detonation-shock-turbulent-mixing-zone (TMZ) structures. There are different types of wave structures that depend on the relative location of the detonation wave with the gravity current. The range of behavior is shown in Fig. 5.10 where four separate experiments are shown at different stages of the gravity current development. The gravity current is colored yellow for visibility. Figure 5.10a is an image of a shock wave followed by a TMZ. The delay time was 0 s, corresponding to a planar interface, and consequently explains why there is no gravity current visible on the overlay. This translates to a leading shock wave that is for the most part perpendicular to the top and bottom surface. There is, however, a small Mach stem at the top of the image

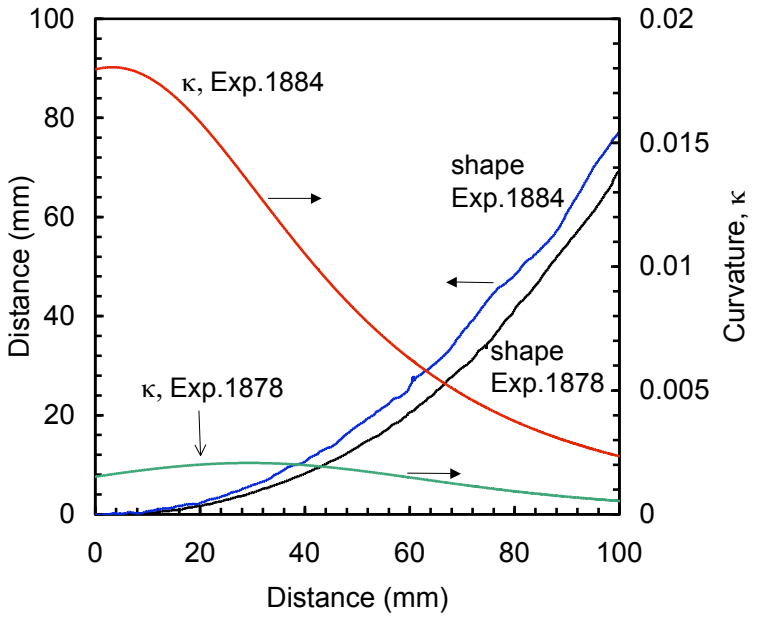

Figure 5.9: A plot comparing the wave shape $x(y)$ and curvature $\kappa(y)$ for Exp. #1878 and 1884. The wave shapes are oriented concave up, which requires the vertical distance of $y = 0$ mm to correspond to the bottom wall (Exp. #1884) or top wall (Exp. #1878). The schlieren images are shown in Fig. 5.8.

with a trailing shock. As the gravity current grows, the wave structure becomes more curved. Figure 5.10b shows the transmitted shock, TMZ, and the location of the gravity current before the combustible mixture was detonated with a delay time of 1 s. The leading shock wave is curved with a Mach stem at the top wall. Figure 5.10c shows the location of the gravity current after a 2 s delay time and the presence of a detonation propagating within 10% of the CJ velocity and transverse waves visible just behind the detonation front at the bottom of the figure. At a 3 s delay time, the curved detonation (Fig. 5.10d) looks similar to the detonation in Fig. 5.10c except that the gravity current occupies half the height of the test section thus changing the curvature of the leading wave.

5.2.2 Detonation decoupling

The importance of mixture composition on detonation decoupling was highlighted in Sec. 4.3. In this section we use the estimated mixture composition to predict wave

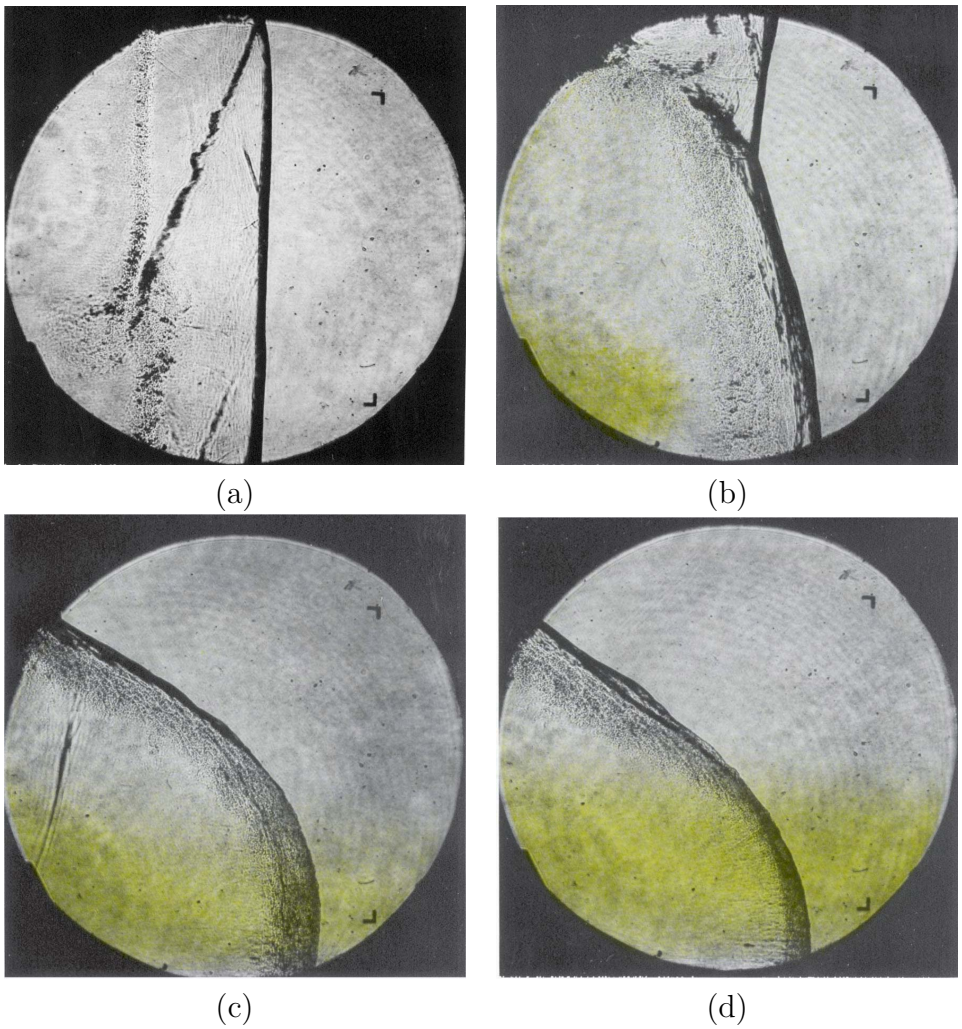

Figure 5.10: Four schlieren images from four separate experiments overlaid with the location of the gravity current at the instant of detonation initiation. Ethylene-oxygen (Φ=2.5) is the combustible mixture with nitrogen as the test gas. (a) Planar interface resulting from a 0 s delay time (Exp. #1891). (b) The gravity current just enters the field of view for a 1 s delay time. The detonation has already propagated through the combustible mixture (Exp. #1893). (c) A detonation propagating in a gravity current with a 2 s delay time (Exp. #1896). (d) A detonation propagating in a gravity current with a 3 s delay time (Exp. #1884).

shape and compare with the experimental images (see Fig. 5.9). The error function composition profile defined by Eqn. 4.3 and using the values in Table 4.1 was based on the experimental findings of the gravity current analysis. The agreement between the estimated composition profiles and the experimental results are shown in Fig. 5.11. For both oxygen and nitrogen composition gradients, a good agreement is observed

with the experiments below a vertical distance $y = 5$ cm. The point of separation in Fig. 5.11a and b are labeled on the induction time plot (Fig. 5.12) to give an indication of the mixture sensitivity. For both oxygen and nitrogen cases the separation point is located just as the induction time begins to dramatically increase.

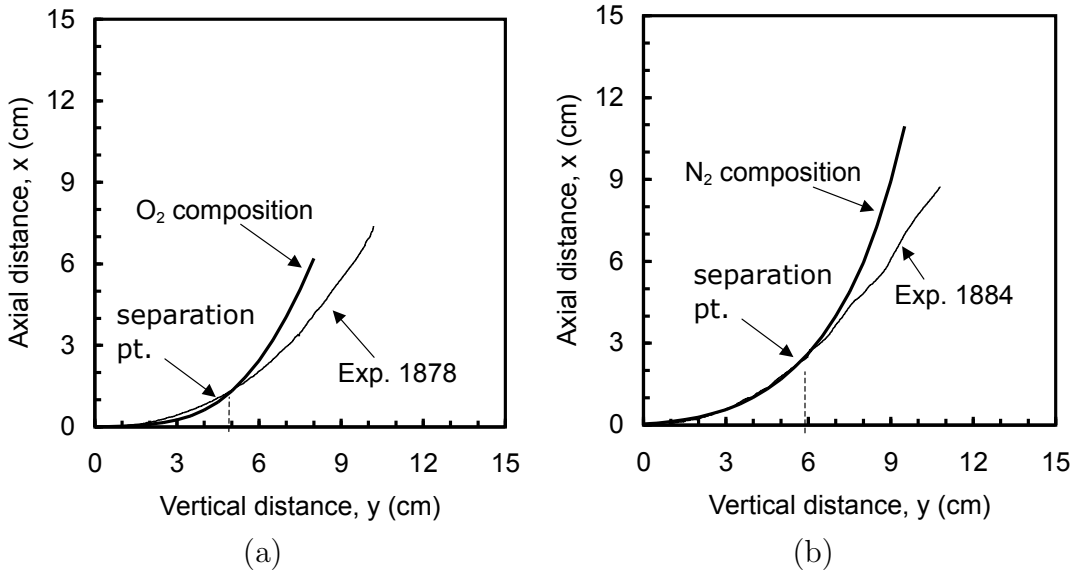

Figure 5.11: Comparison of the curved detonation wave shape with the estimated composition profile. (a) oxygen diluted composition and the edge detected wave profile of Exp. #1878, (b) nitrogen diluted composition and the edge detected wave profile of Exp. #1884.

The value of δ_c, which determines the width of the error function and thus the curvature of the wave shape, was determined by scaling the vorticity thickness measured in the water channel experiments. The constant $y_\circ$ was determined using the PLIF images. No effort was made to adjust the constant to fit the wave shape.

The wave shape predictions based on the composition profile are only valid in the region where a detonation is propagating. A closer examination of the decoupling region, shown in Fig. 5.13, indicates a change in structure. This is observed immediately behind the leading wave as a change in image contrast from light to dark. A closer examination reveals transverse waves in the lighter section. The darker region appears more turbulent and grows as it moves farther away from the decoupling point. It is observed in Fig. 4.7 that this dark region separates to become the TMZ.

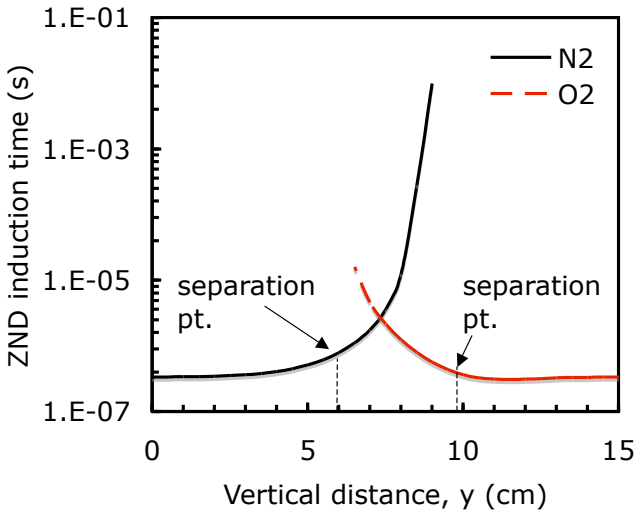

Figure 5.12: ZND induction time plotted as a function of vertical distance y in the test section. The profiles are shown for the oxygen dilution case (O_2) and the nitrogen dilution case (N_2).

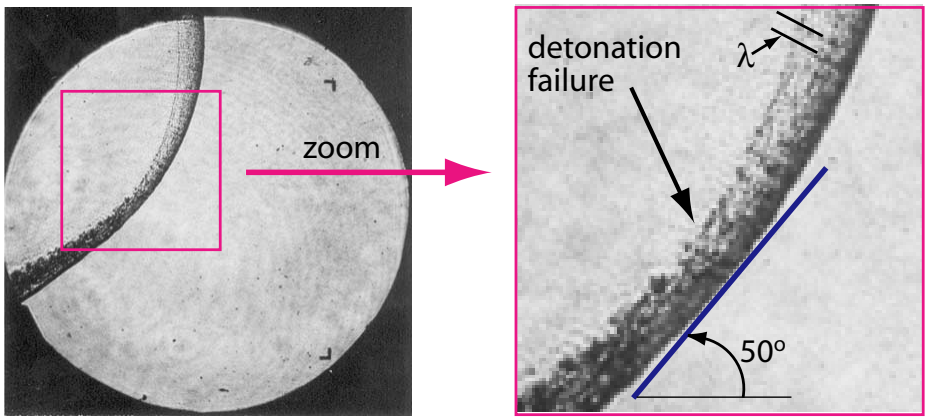

Figure 5.13: A zoom in of the decoupling point for Exp. #1878.

The detonation wave velocities determined using the composition gradient (Fig. 4.11) and the analysis of the detonation shape are compared. The detonation shape velocities are obtained from the images using

$$V_{CJ} = V_{CJmax} \cos(\beta) \tag{5.1}$$

The wave angle β is determined numerically from the wave shape. The maximum

detonation velocity is $V_{CJmax} = 2620$ m/s for an ethylene-oxygen combustible mixture with $\Phi = 2.5$. Figure 5.14 shows a comparison between the two methods for both oxygen and nitrogen mixture compositions. There is modest agreement between both methods when the vertical distance is small, $y < 2$ (or $y > 13$ for oxygen mixture compositions). This corresponds to the portion of the curved detonation close to the top wall (Exp. #1878) and bottom wall (Exp. #1884).

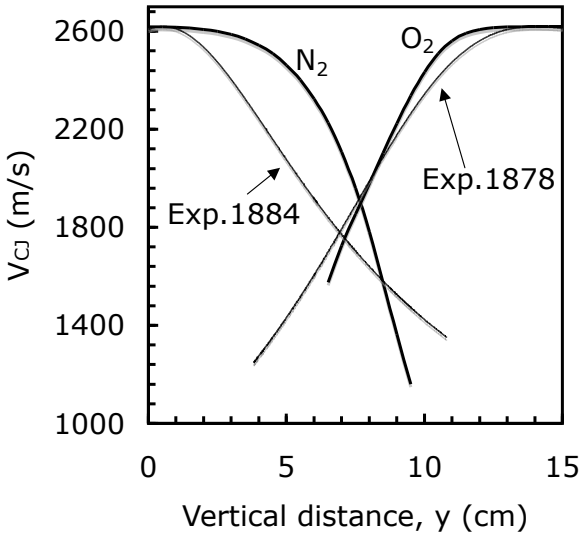

Figure 5.14: Detonation velocity plotted as a function of vertical distance (y) in the test section. The profiles are shown for the oxygen dilution case (O_2) and the nitrogen dilution case (N_2).

5.2.3 Changes in structure between viewports

Another interesting feature is the change in structure that occurs between port 1 and port 2. This is illustrated in Fig. 5.15 with (a) and (b) representing port 1 and port 2, respectively. One of the key visual differences is the overall size of the features. The curved detonation wave and TMZ in port 1 are approximately 20 cm long. The shock and TMZ in port 2 only span a distance of 10 cm with most of that distance occupying the space between them. The large vortex visible in port 2 is most likely due to baroclinic vorticity generation from the detonation or shock wave passing over density gradient visible in Fig. 3.9 .

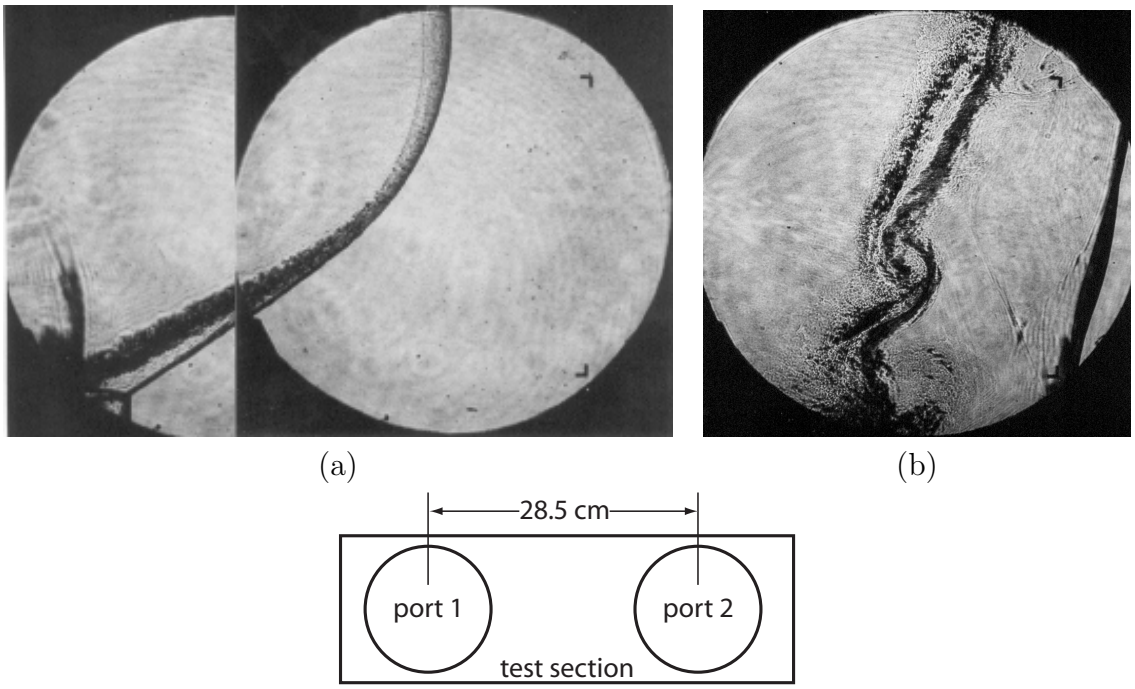

Figure 5.15: The transition in gas dynamic structure from port 1 (a) to port 2 for a 3 s delay time (Exp. #1878-79 and 1861). The test section gas is oxygen.

The compaction in thickness of the TMZ from port 1 to port 2 is addressed by considering the increase in fluid density occurring as the detonation propagates through the interface. Table 5.1 lists the densities of the various gas mixtures before and after the interaction process. The idealized interaction is sketched in Fig. 5.16. The density ratio of the detonation products to the unreacted combustible mixture is on the order of 2 depending on the test gas. The ratios of the shocked test gas to the respective initial state ρ_4/ρ_5 are 6, 5.5, 9.4 for oxygen, nitrogen, and nitrous oxide, respectively. These values are compared to the ratio of initial interface width determined from the gravity current experiments to the width of the TMZ in port 2. It is reasoned that the ratio of the widths

$$\frac{L_1}{L_2} = \frac{\rho_4}{\rho_5} \tag{5.2}$$

scales with the test gas density ratio. For the case shown in Fig. 5.15b the gravity current width after a delay time of 3 s is $L_1 = 41$ cm compared to a TMZ width of

$L_2 = 6.2$ cm. The resulting ratio is $L_1/L_2 = 6.6$, which is about the same as the density ratio $\rho_4/\rho_5 = 6.2$ when oxygen is used as the test gas.

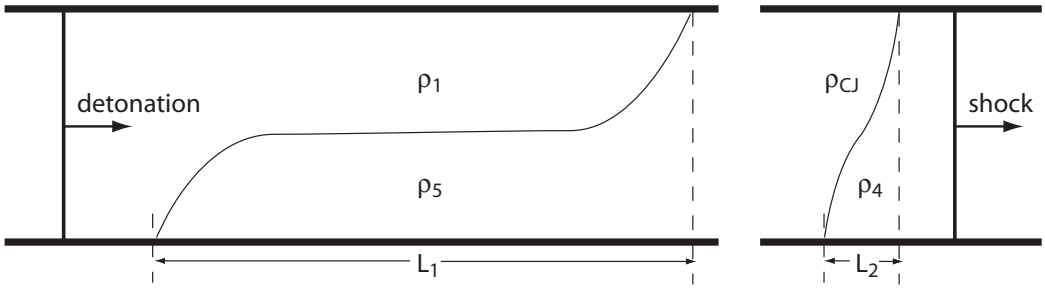

Figure 5.16: A sketch showing the change in width of the interface after interacting with the detonation wave.

5.3 Experimental impulse: The role of secondary combustion

The impulse is calculated from experimental pressure traces to quantify the amount of secondary burning that occurs in the TMZ. This is accomplished by integrating the pressure time histories of the four pressure transducers located in the test section. The integration is carried out using the two-point Newton-Cotes method and the results reported in MPa· s. Figure 5.17 is a plot of both pressure and impulse versus time at pressure transducer P5. The integration of the pressure trace starts at the arrival of the incident shock wave and terminates upon the arrival of pressure disturbances from the GDT approximately 5 ms later as shown on Fig. 5.17. The impulse has an abrupt change in slope at the arrival of the incident and reflected shocks.

Figure 5.18 shows the reproducibility of three overlaid pressure traces from separate experiments (shot 1831-1833) at the same initial conditions. In this case, a detonation in an ethylene-oxygen combustible mixture with $\Phi = 2.5$ is propagating into nitrogen. Pressure transducer P5 is shown as a typical example. While the absolute time differs over each experiment due to variations in ignition time on the order of 2 ms from the DDT process, the time axis of each experiment has been set

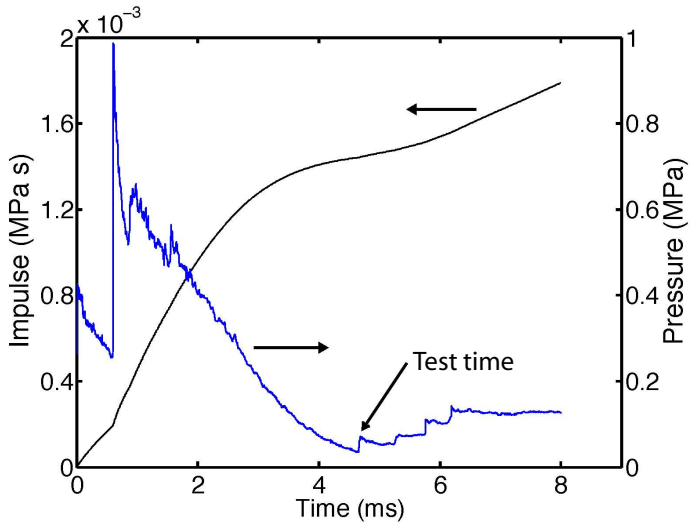

Figure 5.17: An overlay of pressure and impulse vs. time at pressure transducer P5. The mixture is composed of $2.5C_2H_4 + 3O_2$ with O_2 as the test gas.

to coincide with the incident shock.

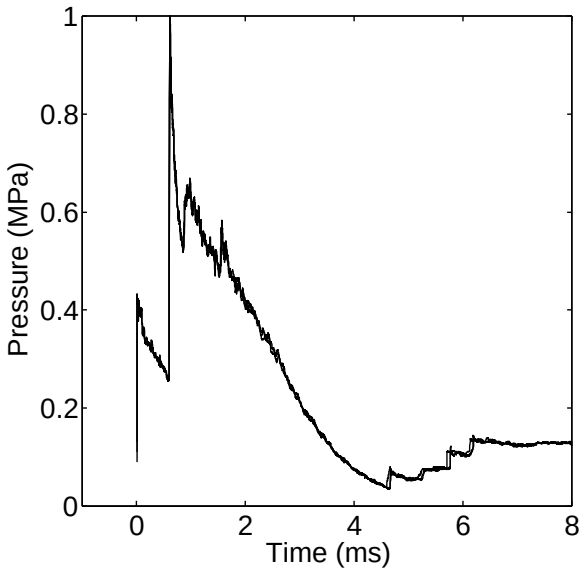

Figure 5.18: Pressure histories at pressure transducer P5. The mixture is composed of $2.5C_2H_4 + 3O_2$ with O_2 as the test gas. Experiments 1831-33 are used with the time base zeroed at the arrival of the incident shock.

The difference between oxygen and nitrogen test gas experiments is examined by subtracting the pressure histories. An example is shown in Fig. 5.19 of the difference

in pressure at transducer P5 with the pressure trace of Exp. #1840 to indicate the location of the incident ($t = 0$ ms) and reflected shock waves. When comparing the difference between using oxygen and nitrogen as the test gas with all other parameters being equal, the difference in pressure is always positive. It is also interesting to observe that a large portion of the pressure difference occurs before the arrival of the reflected shock wave.

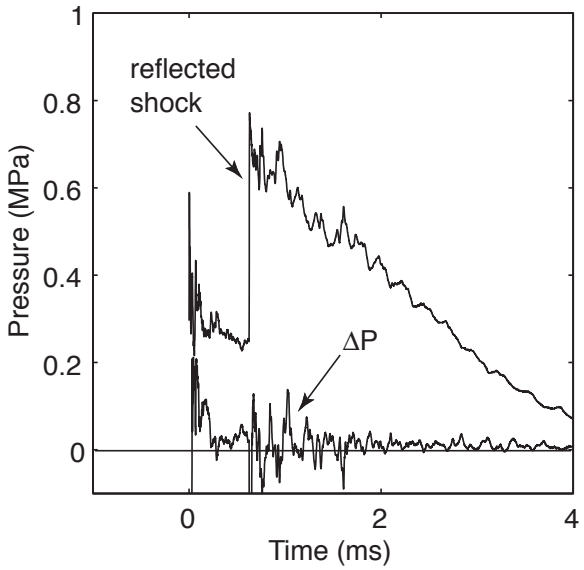

Figure 5.19: Difference in pressure ΔP at P5 between the pressure histories using oxygen as the test gas (Exp. #1840) from nitrogen as the test gas (Exp. #1843). The gravity current delay time is 3 s.

The impulse is compared for the cases with the experimental parameters listed in Table 5.2. The aim is to quantify the sensitivity of the impulse to these parameters. Figures 5.20a and b are plots of impulse versus valve delay time. The impulse reported on the plot corresponds to the integration up to the test time in the test section. Inspection of Fig. 5.20, which compares experiments where only the test gas is altered, shows that the impulses are different only after the passage of the reflected shock wave. The impulse is relatively insensitive to variations in delay time, increasing only slightly as the delay time is increased. Figure 5.20b, corresponding to nitrogen as the test gas, also shows a slight increase in impulse as the delay time is increased. The increase is attributed to the additional combustible mixture that

propagates into the test section via the formation of the gravity current. Therefore, a fair comparison of impulse gained from secondary combustion needs to account for the added combustible mixture by matching experiments with identical initial conditions varying only the test gas.

In all cases, the impulse is highest at transducer P7 and diminishes monotonically to P4. This may appear counterintuitive since the integration time is the least at P7 and increases with increasing distance of the gauges from the end wall, with the longest test time for P4. However, the decay in pressure of the reflected shock accounts for the large drop in impulse with increasing gauge distance from the endwall.

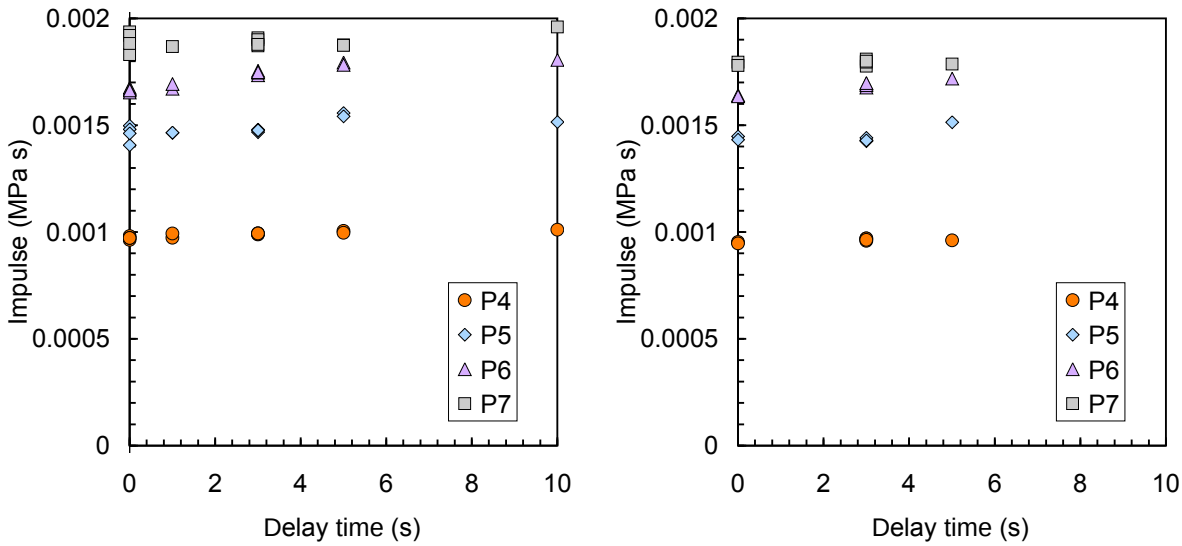

Figure 5.20: Impulse vs. valve delay time for pressure transducers P4-P7 located in the test section. (a) $2.5C_2H_4 + 3\ O_2$ with O_2 as the test gas and (b) $2.5C_2H_4 + 3\ O_2$ with N_2 as the test gas.

Although the impulse is mildly affected by the delay time, there is a profound difference in the structure of the post shock contact surface. Figures 5.22b and 5.24a compare the contact surface for two delay times, 0 s and 3 s, using the port 2 configuration. In both cases, the combustible mixture is ethylene-oxygen with an equivalence ratio of 2.5 propagating into oxygen. The most striking difference between the two contact surfaces is the large vortical structure found in Fig. 5.22b.

The interface inclination is vertical in Fig. 5.22a and tilted clockwise 20 degrees from vertical in Fig. 5.22b. The inclination is a result of the gravity current formation. It tilts from right to left because molecular oxygen is denser than the combustible mixture (see Table 5.1). This is discussed further in section 5.2.3.

The impulse is also plotted against equivalence ratio in Fig. 5.21a,b. Both figures indicate that equivalence ratio has a weak effect on impulse. The general features of the contact surface are also the same. Figure 5.22 shows schlieren images of the contact surface propagating from left to right for equivalence ratios Φ = 2, 2.5, 3. The contact surface in all three cases has the same vortical structure and inclination. This differs from that of Figs. 5.22b and 5.24a where the gas dynamic features have large structural differences.

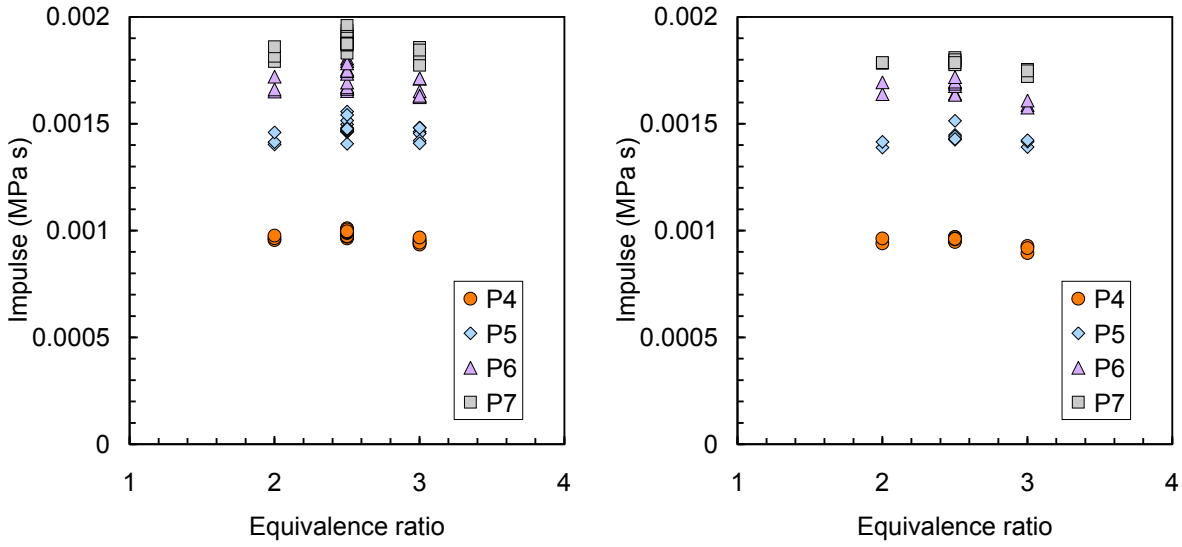

Figure 5.21: Impulse vs. equivalence ratio for pressure transducers P4-P7 located in the test section. (a) $2.5C_2H_4 + 3\ O_2$ with O_2 as the test gas and (b) $2.5C_2H_4 + 3\ O_2$ with N_2 as the test gas.

Impulse has also been measured with nitrous oxide as the test gas. The larger density of N_2O yields larger Atwood and Froude numbers than oxygen or nitrogen, which in turn helps promote mixing at the contact surface. Given the relative insensitivity of impulse to equivalence ratio, experiments were carried out with Φ = 2.5.

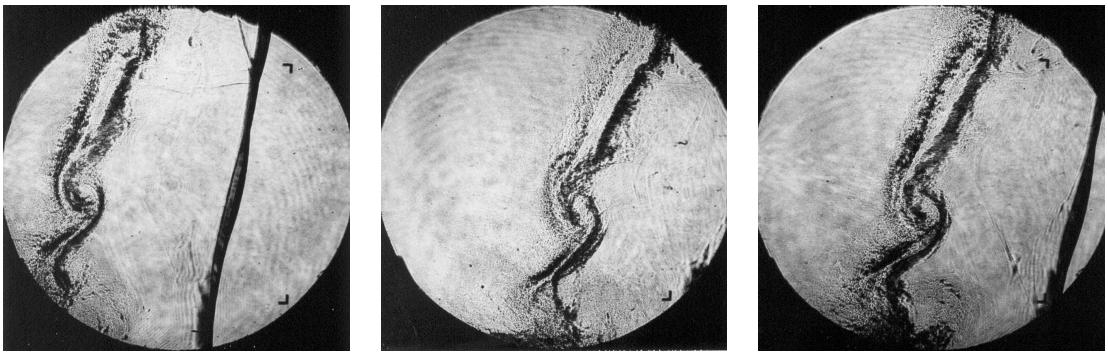

(a) (b) (c)

Figure 5.22: A schlieren image that shows the contact surface resulting from an ethylene-oxygen detonation propagating in oxygen 3 s gate (port 2). The equivalence ratio is (a) $\Phi = 2$, (b) $\Phi = 2.5$, (c) $\Phi = 3$.

Figure 5.23a is an impulse versus delay time plot for pressure transducers P4-P7. The delay time was kept to one second or less due to the rapid formation of the gravity current.

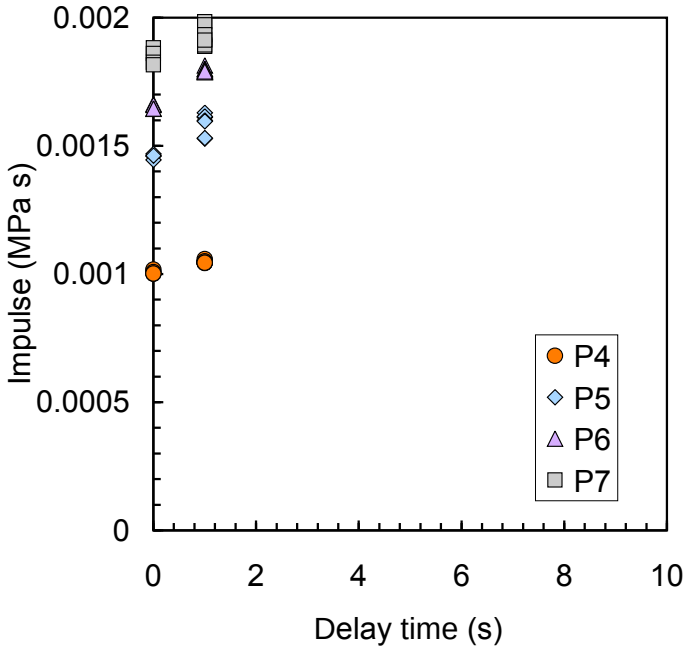

Figure 5.23: Impulse vs. valve delay time for pressure transducers P4-P7 located in the test section. A $2.5C_2H_4 + 3\ O_2$ combustible mixture is used with N_2O as the test gas.

The test gas has a visible impact on the structure of the contact surface. Figure

5.24 shows schlieren images of three separate experiments with oxygen, nitrous oxide, and nitrogen as the test gas. The delay time for these experiments is zero seconds.

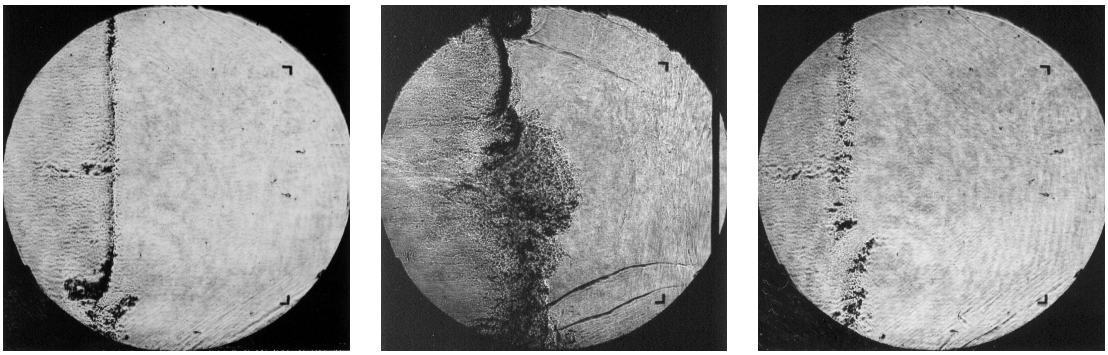

(a) (b) (c)

Figure 5.24: A schlieren image that shows the contact surface resulting from an ethylene-oxygen detonation propagating into various test gases with a 0 s delay time (port 2). The test gases are (a) oxygen, (b) nitrous oxide, and (c) nitrogen.

Comparing the impulse values listed above shows that, for a given set of experimental conditions, the impulse when oxygen is the test gas is 1-5% larger than with nitrogen as the test gas. The consistent impulse increment motivated the modeling carried out in the next section.

5.3.1 TMZ thickness

The TMZ thickness gives an estimate of the volume of gas that undergoes secondary combustion and is determined by measuring the thickness at multiple points (Fig. 5.25) in a given image for both port 1 and 2 experiments.

The experimentally measured TMZ thickness is plotted as a function of valve delay time in Fig. 5.26. The size of the TMZ is similar for both oxygen and nitrogen cases, which can be attributed to the increased growth rate of the mixing zone for interface gradients with normals more perpendicular to the detonation propagation direction (see Sec. 7.4)

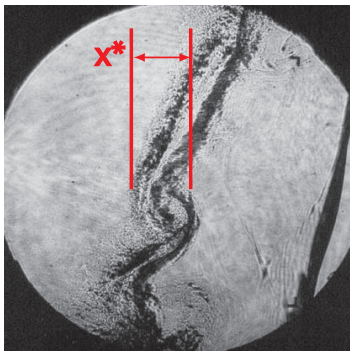

Figure 5.25: A schlieren image of the transmitted shock and TMZ. A characteristic thickness x^* is shown (port 2).

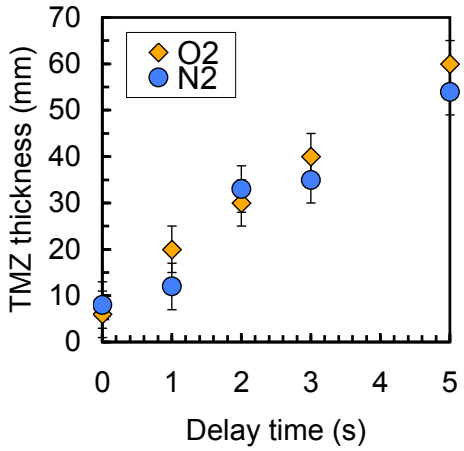

Figure 5.26: TMZ thickness versus delay time for experiments with nitrogen and oxygen as the test gas.

5.3.2 Time scale of combustion

This section addresses the chemical reaction time scale of the partially oxidized combustion products (CO and H_2) and the test gas. The goal is to determine the timescales required for the reaction to take place and estimate the volume expansion and temperature rise that result. The analysis is carried out by first mixing the detonation products with the shocked test section gas (test gas) keeping the composition frozen (Fig. 5.27) and then allowing the reaction to take place at constant pressure. Combining the two mixtures results in a new set of mass fractions and mixture enthalpy

$$y_{i,fr} = f_{O_2} + (1 - f_{O_2}) y_{i,CJ} \tag{5.3}$$

$$h_{fr} = h_{O_2} f_{O_2} + (1 - f_{O_2}) h_{CJ} \tag{5.4}$$

denoted with subscripts fr to indicate the frozen state. Subscripts i, O_2, and CJ refer to the individual species, shocked test gas mixture, and detonation product mixture, respectively. The oxygen mass fraction of the composite mixture f_{O_2} is defined as

$$f_{O_2} = \frac{m_{O_2}}{m_{O_2} + m_{CJ}} \tag{5.5}$$

where m_{O_2} and m_{CJ} are the masses of oxygen and partially oxidized detonation products, respectively.

The frozen mixture then reacts at constant enthalpy and pressure until equilibrium is reached. These calculations were carried out using Matlab and the Cantera equilibrium software (Goodwin, 2005) by integrating

$$\frac{dy_i}{dt} = \mathcal{W}_i \frac{\dot{\omega}_i}{\rho} \tag{5.6}$$

$$\overline{c_p} \frac{dT}{dt} = \sum_{i=1}^{k} h_i \frac{dy_i}{dt} \tag{5.7}$$

with species $i = 1...k$ where k denotes the total number of species. The molecular weight and molar production rate of species i are denoted by $\mathcal{W}_i$, and $\dot{\omega}_i$, respectively. The GRI 3.0 mechanism (Smith et al., 2004) was used in the calculations with the NASA polynomial fits (McBride et al., 1993) for species thermodynamic data up to a temperature of 6000 K.

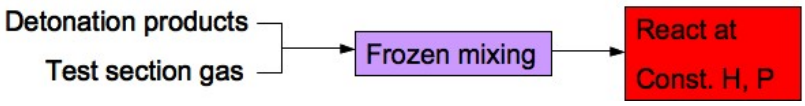

Figure 5.27: Homogeneous mixing ignition time model to characterize the time scale in which chemical reactions take place.

The results of this model are shown in Fig. 5.28. The mixture induction time is plotted against the oxygen mass fraction of the composite mixture. The induction time in this plot was obtained by finding the time when the temperature time derivative reached 90% of its peak value. The stoichiometric point for this mixture corresponds to f_{O_2}= 0.615. The main result of Fig. 5.28 is that the induction times for the majority of the oxygen mass fraction range are on the order of a couple of microseconds. The large induction time values occur in the limit as $f_{O_2} \rightarrow 0$ where the partially oxidized detonation products are already in equilibrium and as $f_{O_2} \rightarrow 1$ where the temperature of the frozen mixture decreases toward the post-shock temperature of oxygen (≈1600 K).

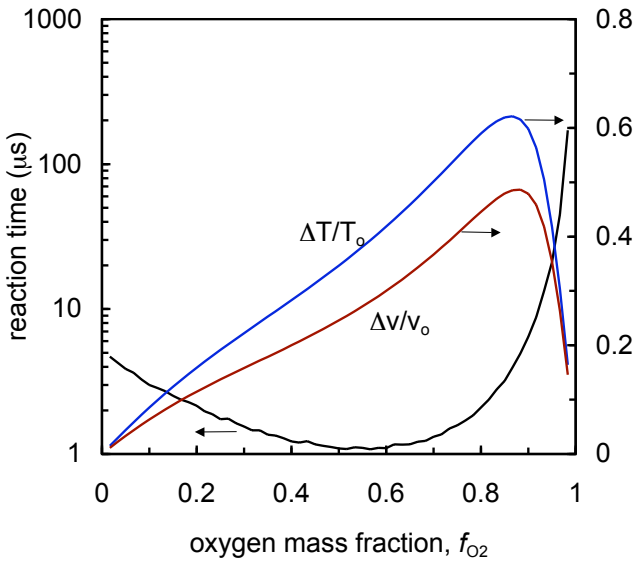

Figure 5.28: Induction time vs. oxygen mass fraction computed using a homogeneous mixing ignition time calculation (HMIT). The calculation uses the model illustrated in Fig. 5.27.

Both the change in temperature and specific volume normalized by the frozen composition state are shown. Both curves peak between $f_{O_2} = 0.8$ and 0.9 because of the decrease of the initial temperature and specific volume as the oxygen mass fraction increases. The values of ΔT and Δv are obtained by taking the difference of the peak value obtained during the reaction and the frozen composition value.

5.4 Secondary impulse model

A simple model is developed to predict the increase in impulse observed in experiments where oxygen is used as a test gas compared to nitrogen. The model estimates the growth of a reacting fluid element in the TMZ given the appropriate time scales, length scales, and degree of mixing. The expansion of the reacted fluid elements produce compression waves that strengthen the leading shock wave and therefore increase the impulse. The secondary impulse model does not account for many of the complex details associated with turbulent shear layers and detonation refraction that are important in this problem. The goal is to simply verify that the magnitude of the impulse increment, observed in the experimental pressure histories, is correct.

Figure 5.29 is an illustration indicating that the energy release in the TMZ acts to amplify the shock. The original contact surface line CS is shown as a straight dotted line.

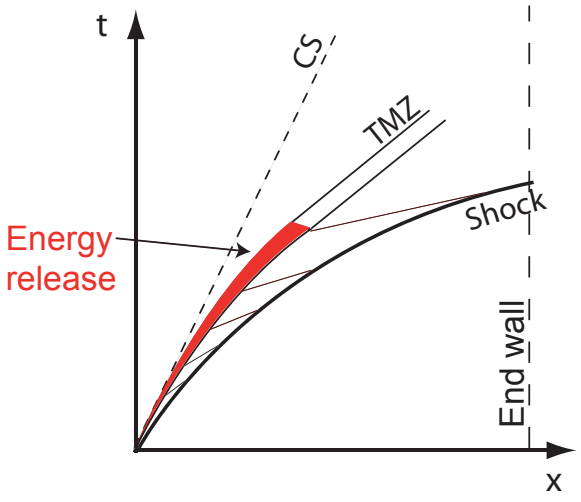

Figure 5.29: A position versus time schematic illustrating how the energy released in the TMZ could accelerate the leading shock wave to propagate at a higher Mach number.

5.4.1 Model outline

Consider a fluid element, moving in a flow with a convective velocity u_p. The growth of a fluid element resulting from chemical reactions is depicted in Fig. 5.30. The velocity of the left (δu_p^-) and right (δu_p^+) edges of the fluid element are combined to obtain an expression for the growth rate of the fluid element

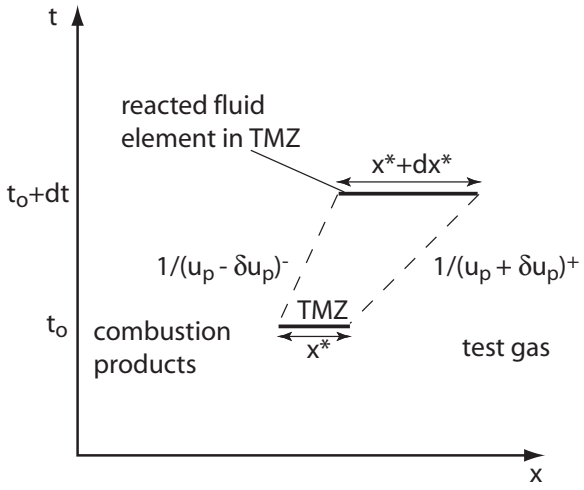

Figure 5.30: A sketch of a fluid element expanding during chemical reaction at constant pressure and enthalpy.

$$\frac{dx^*}{dt} = \delta u_p^+ - \delta u_p^-. \tag{5.8}$$

The increase in pressure is related to the velocity increase using the acoustic equation (see Liepmann and Roshko, 2001)

$$\delta P = \pm \rho c \, \delta u_p \tag{5.9}$$

where ρ and c are the local density and sound speed. The use of Eqn. 5.9 is motivated by the small increase in pressure observed in experiments with secondary combustion. Substituting Eqn. 5.9 into Eqn. 5.8 using the plus and minus sign for δu_p^+ and δu_p^- respectively, then isolating for δP results in

$$\delta P = \frac{\overline{\rho c}}{2} \frac{dx^*}{dt}. \tag{5.10}$$

With the average acoustic impedance $\overline{\rho c}$ defined as

$$\overline{\rho c} = 2\left(\frac{1}{(\rho c)^{+}} + \frac{1}{(\rho c)^{-}}\right)^{-1}, \tag{5.11}$$

where $(\rho c)^{-}$ and $(\rho c)^{+}$ represents fluid to the left and right of the TMZ, the combustion products and the test gas, respectively. It is assumed that the thermodynamic states of the test gas and combustion products do not change measurably as a result of chemical reactions in the TMZ. The acoustic analogy is based on the assumption that the chemical reactions occur at constant pressure and enthalpy, appropriate for diffusively controlled combustion within the shear layer.

The impulse I is defined as

$$I = \int P dt \tag{5.12}$$

where P is the local pressure. The impulse can be decomposed into two parts that represent the bulk flow impulse $I_{\circ}$ and the increment due to secondary chemical reactions I'. Similarly the pressure is decomposed in the same manner resulting in

$$I = I_{\circ} + I' = \int P dt = \int (P + \delta P) dt. \tag{5.13}$$

Isolating the contributions of impulse due to chemical reactions in Eqn. 5.13 and substituting Eqn. 5.10 for the pressure increment yields after integration

$$I' = \int \delta P dt = \frac{\overline{\rho c}}{2} \Delta x^{*}. \tag{5.14}$$

Δx^{*} refers to the total growth of the fluid element due to chemical reactions and is related to the volume expansion Δv via the expression

$$\frac{\Delta x^{*}}{x^{*}} = \frac{\Delta v}{v_{\circ}}. \tag{5.15}$$

Substituting Eqn. 5.15 into Eqn. 5.14 results in

$$I' = \mathcal{C} x^{*} \frac{\overline{\rho c}}{2} \frac{\Delta v}{v_{\circ}}. \tag{5.16}$$

An estimate of I' is obtained by substituting the local unreacted density and sound speed, the experimentally measured value of x^*, and the quantity $\Delta v/v_\circ$, obtained from solving the constant enthalpy and pressure equilibrium process. The present computation is clearly only an order of magnitude argument and a constant of proportionality $\mathcal{C}$ has been introduced in Eqn. 5.16. The value of $\mathcal{C}$ has to be determined by comparison with experiment.

The value x^* in Eqn. 5.16 reflects the size of the TMZ visible in port 2. x^* can be increased to account for additional combustion in the TMZ after the shock wave reflects off the end-wall. Vetter and Sturtevant (1995) have shown that TMZ growth can increase by a factor of six after the re-shock event. However, in the following calculations all the factors that can amount to an increase in impulse are lumped into the constant $\mathcal{C}$.

As discussed in Sec. 7.4, the visible growth rate of the shear layer does not increase with the addition of heat release, in fact the growth was shown to decrease (see Dimotakis, 1991). However, the shear layer displacement thickness changes from being negative to positive causing the surrounding fluid to be displaced thus reinforcing the shock wave.

5.4.2 Model predictions

Values for the variables on the right hand side of Eqn. 5.16 are obtained from the analyses in Sec. 5.3.1 and 5.3.2. The thermodynamic variables are specified for f_{O_2}= 0.615 corresponding to a stoichiometric mixture composition. The constant of proportionality $\mathcal{C}$ is varied from a value of 1 to 10 to account for interface growth after the shock reflection off the end-wall. A reference impulse of 1000 kg·m^{-1}·s^{-1} obtained from impulse measurements at pressure transducer P4 is used to calculate the increment.

The model prediction and experimental results for impulse increment are plotted in Fig. 5.31 as a function of delay time. The experimental impulse increment increases with delay time for pressure transducers P4, P5, and P6 and is bounded between

about 1-6%. The model prediction also increases with delay, largely a result of the TMZ thickness dependence on delay time. When the constant $\mathcal{C} = 1$, the model predicts lower impulses than the experiments. Increasing the constant $\mathcal{C}$ to 5 or 10 yields better quantitative agreement. This could be attributed to the importance of further reaction and growth in x^* during the re-shock phase. Given the simplicity of the model only order of magnitude agreement can be expected at best. The fact that theory estimates impulses on the same order as the experimental findings indicates that secondary combustion in the TMZ is a plausible explanation for the impulse increment.

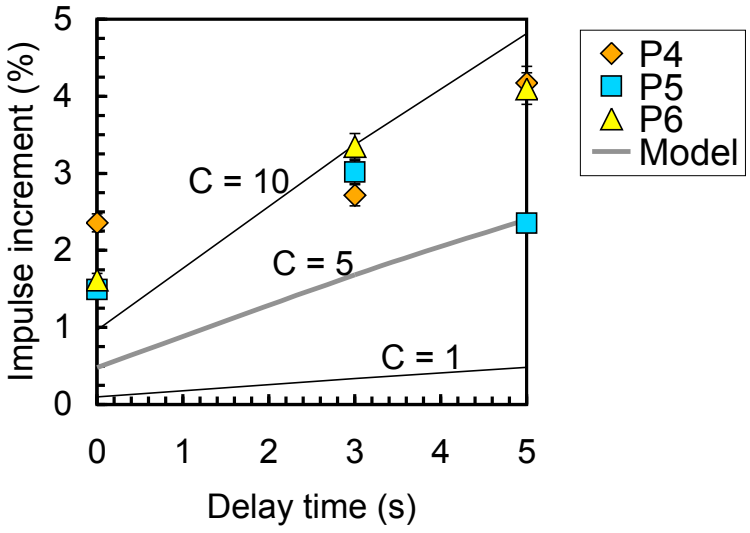

Figure 5.31: Impulse increment (%) for oxygen compared to nitrogen versus delay time. The impulse model prediction is plotted for a range of proportionality factors.

Chapter 6

Theory: Detonation Interaction with a Sharp Interface

6.1 Detonation refraction theory

Consider a detonation wave propagating through sharp interfaces at an oblique angle (Fig. 6.2). We analytically determine the strength of the transmitted and reflected waves as well as the thermodynamic states resulting from the interaction to compare with experimental results. Two extreme cases are examined. First, the interaction is considered sufficiently far from the interaction point (node) such that the combustion products are in chemical equilibrium. Second, the interaction is considered sufficiently near the node, i.e., much smaller than the induction zone length, such that no chemical reactions have occurred and the composition can be considered frozen but the gas is otherwise in thermal equilibrium.

The problem of shock wave refraction can be classified by the "refractive" index at the contact discontinuity. The refractive index n_R is defined by Henderson (1989) as

$$n_R = \frac{U_i}{U_t} \tag{6.1}$$

where U_i and U_t are the velocities of the incident and transmitted waves, respectively. If $U_i < U_t$, then the refraction is considered slow-fast. On the other hand if $U_i > U_t$, the refraction is considered fast-slow. If $n = 1$ there is no refraction. For a given

refractive index there are two types of wave systems: regular and irregular that are separated by an interface angle denoted the critical angle. Regular refraction consists of only waves that are straight and intersect at a single point called the node. Irregular refraction encompasses all scenarios that are not regular. Typically, irregular refraction exhibits added features such as Mach reflections and pre-cursor shock waves. In general a transmitted and reflected wave result when regular reflections occur which can be either a shock wave or an expansion fan. In the present experiments that use ethylene-oxygen as the combustible mixture, a transmitted shock and reflected expansion result. It is possible to have a reflected shock for example, by using a lean hydrogen-oxygen combustible mixture with nitrous oxide as the test gas. The type of solution is easily identified by looking at the graphical solution on a pressure-deflection plane (see Fig. 6.1). Regular interactions occur when either a reflected shock or expansion fan state intersects with the end state of the transmitted shock. No intersection results in an irregular reflection. Henderson (1989) has a complete discussion for non-reactive shock waves on the effect of the refractive index less than one as well as a treatment of the interface impedance Z, which quantifies the strength of the transmitted and reflected waves. In the present analysis, we consider fast-slow interactions that will be the case when the system is comprised of an incident detonation wave propagating into a non-reactive mixture.

There has been some previous work that included chemical reactions in the shock-polar analysis. Samtaney and Pullin (1998) and Sanderson et al. (2003) investigated the role of ideal gas dissociation during shock wave refraction with an interface and multiple shock wave interaction. Dissociation of gases behind strong shock waves is an endothermic process that absorbs energy from the post shock state as opposed to the largely exothermic reactions occurring in detonation waves. Dabora et al. (1965) has modeled the deflection of a contact surface arising from a detonation propagating through a channel with a compressible, non-reacting boundary for the limiting case of the detonation being normal to the interface.

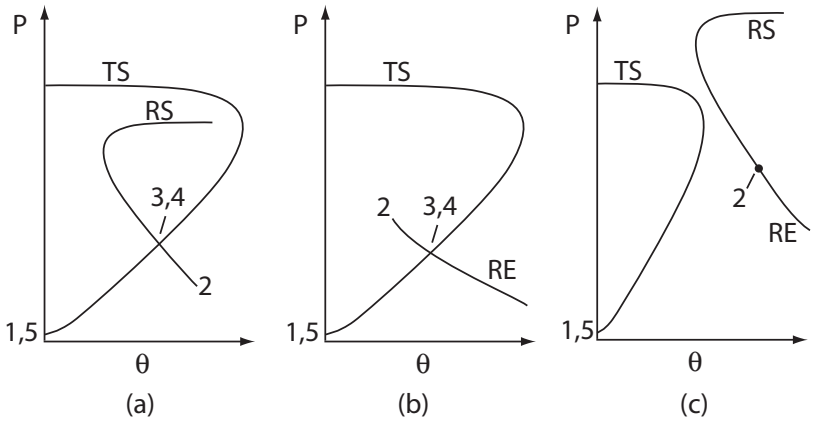

Figure 6.1: Pressure-deflection maps illustrating regular and irregular detonation refraction. Regular refraction case with a reflected shock (a), and reflected expansion (b). An irregular reflection (c) occurs when the transmitted shock curve TS does not intersect either the reflected shock RS or reflected expansion RE.

6.2 Characterization of equilibrium and frozen regions

The detonation refraction process can be divided into three regions (Fig. 6.2). These are the outer region, inner region, and transition region. The outer region occurs at a length scale Δ_{outer}, large enough for the flow to reach chemical and thermal equilibrium and for the complex three-dimensional structure influence of the detonation wave to be negligible. The inner region can be approximated as having a frozen composition, equal to that of the initial unreacted gas, at a distance, Δ_{inner}, close to the node. The transition region is the most difficult to analyze and essentially links the equilibrium and frozen solution.

The ZND model is used to quantify the length scales associated with the inner and outer solutions. Figure 6.3 shows the evolution of the temperature and density as a function of distance. The origin coincides with the location of the leading shock wave. The induction length Δ is defined as the distance from the Von Neumann point to 10% of the maximum thermicity indicated on the figure. The induction length is the critical length scale that separates the equilibrium and frozen regions. For this particular profile, corresponding to an ethylene-oxygen detonation at Φ=2.5 and 15

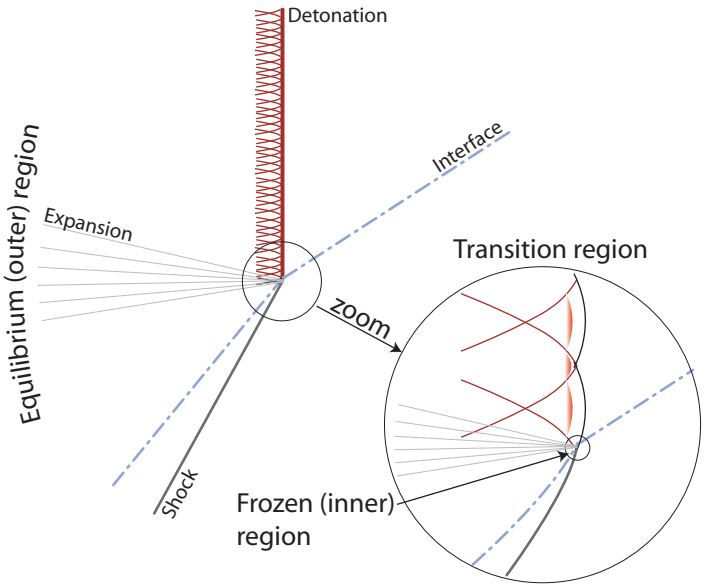

Figure 6.2: An illustration of a detonation propagating through a sharp interface. Both the equilibrium and frozen regions of the flow are shown along with the transition region.

kPa initial pressure, the induction length, Δ=0.06 mm, and the solution is close to equilibrium at Δ_{equil}=0.4 mm. By definition, the inner and outer region scales are related to the reaction zone and equilibrium lengths by

$$\Delta_{outer} \gg \Delta_{equil} > \Delta \gg \Delta_{inner}.$$

The sub-millimeter induction zone length indicates that we will not be able to observe the frozen region in these experiments. Detonations similar to that of Fig. 2.8b with a cell size comparable to the length scale of the experiment (15 cm) would be more appropriate to investigate the frozen solution.

6.2.1 Frozen solution

The frozen region can be treated as a non-reactive flow in which shock refraction theory (Sec. 6.1) describes the wave structure around the node. Since the frozen region is too small to observe in the present experiments and shock refraction is well

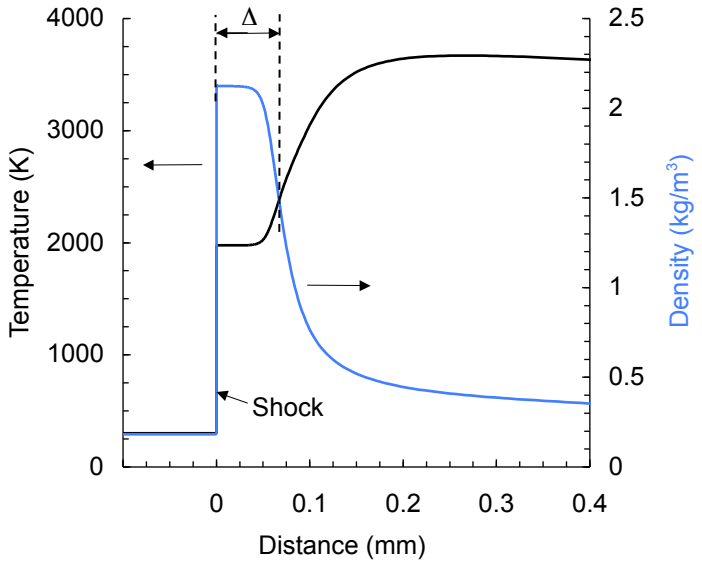

Figure 6.3: The ZND profile of an ethylene-oxygen detonation at Φ=2.5 and 15 kPa initial pressure. The temperature and density are plotted as a function of distance with the origin as the location of the leading shock wave.

studied, no further discussion is given here of this case.

6.3 Analytical description of equilibrium region

The following analysis considers a detonation wave, D, propagating through a contact surface CS_1 that is inclined at an angle α to the wave propagation direction (see Fig. 6.4a). The resulting transmitted wave T, reflected expansion RE, and contact surface CS_2 are illustrated for a typical interaction. The analysis, carried out in the reference frame of the node, has five uniform regions, labeled 1-5 in Fig. 6.4. Region 1 corresponds to the combustible driver gas and region 5 to the inert or oxidizing test gas. These regions contain unprocessed gas still in its initial state. Traversing the domain counterclockwise, regions 1 and 2 are separated by the detonation wave and region 2 contains equilibrium detonation products. The gas from region 2 then expands through the reflected wave, shown as an expansion, and reaches a new state in region 3. Region 4 contains gas from region 5 that has been processed by the transmitted shock. Particle paths P1 and P2 illustrate the trajectory of gas through

the system of waves with the angle η-α measuring the deflection of P1 across the detonation wave. The angles of the waves, labeled in Fig. 6.4b, are all referenced to the axis labeled x and measured in the counter-clockwise direction. The initial orientation of the contact surface or interface is α; the complement of α is the angle between the detonation and contact surface. The angles μ_1 and μ_2 denote the orientation of leading and trailing characteristics of the reflected expansion while δ and ϕ define the contact surface deflection and transmitted shock wave angles, respectively.

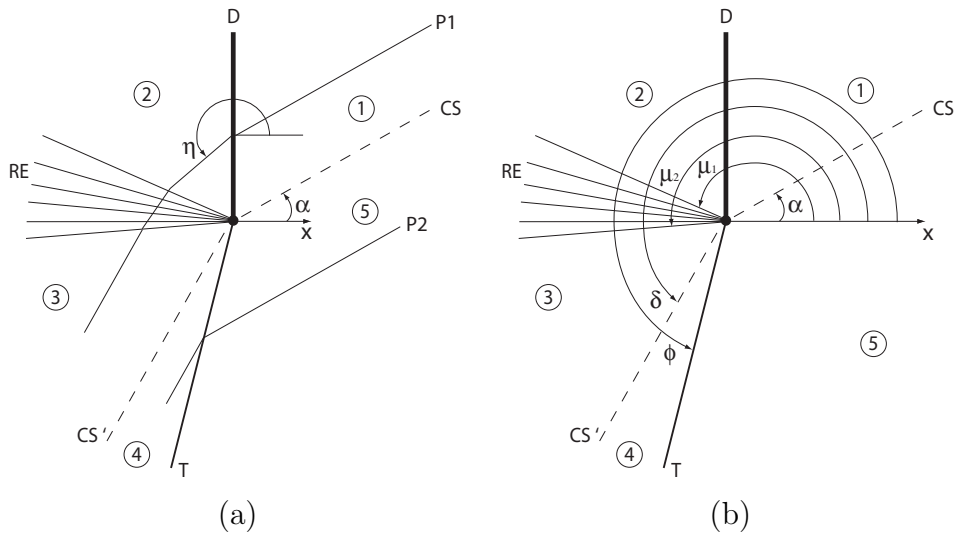

Figure 6.4: Detonation refraction configuration and labeling. (a) states and particle paths, (b) wave angles.

The analysis assumes that the detonation is a discontinuity with the state of the products determined by the Chapman-Jouguet (CJ) detonation theory. The shock waves are also considered as discontinuities. The thermodynamic state of a mixture passing from one state to another is determined by equilibrium chemistry computed by a program based on the Cantera chemical equilibrium software developed by Goodwin (2005). Diffusional and viscous effects as well as body forces are omitted from this study. The program first determines the specific angle where no reflected wave occurs, defined as the angle of intromission, α^*, and then imposes an expansion wave or shock wave as the reflected wave. The angles of intromission are determined by a separate analysis (see Sec. 6.3.4) and, for the mixtures in regions 1 and 5 of interest in this

study, occur at $\alpha = \alpha^* \approx 88°$. When $\alpha < 88°$, a reflected expansion results.

6.3.1 Geometrical relations

In the reference frame of the node, we consider that the unreacted mixture in region 1 and inert or oxidizer gas in region 5 are moving with velocities

$$\vec{w}_1 = -V_{CJ}\,\hat{i} - V_{CJ}\,\tan\alpha\hat{j} \tag{6.2}$$

$$\vec{w}_5 = \vec{w}_1 \tag{6.3}$$

where the detonation velocity is denoted by V_{CJ}. The directions of the velocities are tangent to the particle paths, P1 and P2, depicted in Fig. 6.4a. The velocity in region 2 is determined by the post-detonation conditions and is given as

$$\vec{w}_2 = -c_2\,\hat{i} - V_{CJ}\,\tan\alpha\,\hat{j} \tag{6.4}$$

$$\eta = \tan^{-1}\left(\frac{c_2\tan\alpha}{V_{CJ}}\right) + \pi \tag{6.5}$$

where $\vec{w}_2$ is the velocity of the detonation products moving at an angle η, and c_2 is the sound speed in region 2. The velocities $\vec{w}_3 = fn(\delta_3 - \eta, \alpha)$ and $\vec{w}_4 = fn(\phi, \alpha)$ are expressed as functions of the flow deflection angles δ_3 and δ_4, the transmitted shock angle, ϕ, contact surface angle, α, and the thermodynamic states of regions 2 and 5.

The velocity in region 4 is obtained using the geometrical relations

$$w_{5n} = |\vec{w}_5|\sin(\phi - \alpha - \pi) \tag{6.6}$$

$$w_{4v} = |\vec{w}_5|\cos(\phi - \alpha - \pi) \tag{6.7}$$

$$|\vec{w}_4| = \sqrt{w_{4n}^2 + w_{4v}^2} \tag{6.8}$$

$$\delta_4 = \phi + \tan^{-1}\left(\frac{w_{4v}}{w_{4n}}\right) - \pi/2. \tag{6.9}$$

The subscripts n and v denote the velocity component normal and perpendicular to the transmitted shock wave, respectively. The velocity component w_{4n} is determined by the shock jump conditions, and $\delta - \eta$ is calculated using the Prandtl-Myer expansion relation discussed in Sec. 6.3.2.

6.3.2 Governing equations and matching conditions

The geometric relations in Sec. 6.3.1 are used in conjunction with the conservation equations, equation of state, and matching conditions to uniquely determine the wave structure and thermodynamic states of the system. To treat oblique shock waves, the one-dimensional shock jump conditions

$$[\rho w_n] = 0 \tag{6.10}$$

$$\left[P + \rho w_n^2\right] = 0 \tag{6.11}$$

$$\left[h + \frac{w_n^2}{2}\right] = 0 \tag{6.12}$$

$$[w_v] = 0 \tag{6.13}$$

must be solved iteratively since the enthalpy h of an equilibrium ideal gas mixture is a nonlinear function of temperature and pressure. p, ρ, and w denote the local pressure, density, and velocity with $[f] = f_2 - f_1$ denoting the change in quantity f. The flow deflection angle, $\Delta\theta_E$, resulting from the reflected expansion fan is obtained by integrating

$$d\theta_E = \frac{\sqrt{M^2 - 1}}{1 + (\Gamma - 1)M^2}\frac{dM}{M} \tag{6.14}$$

where Γ is the fundamental gas derivative and M is the Mach number. Γ is defined as (see Thompson, 1988)

$$\Gamma \equiv \frac{c^4}{2v^3}\left(\frac{\partial^2 v}{\partial P^2}\right)_s = \frac{1}{c}\left(\frac{\partial(\rho c)}{\partial \rho}\right)_s \tag{6.15}$$

with subscript s denoting a path with constant entropy. To evaluate Eqn. 6.15 at a given state a script was written that calculated the finite difference approximation to the derivative by perturbing the initial density by 0.1% and then equilibrating with constant entropy and density to determine the new state. For a perfect gas the fundamental gas derivative reduces to $\Gamma = (\gamma + 1)/2$.

Pressure and flow deflection must match at the interface between regions 3 and 4, a requirement that closes the problem (see Thompson, 1988). This sets up a system of nonlinear algebraic equations

$$\delta_3(\Delta\theta_E, \alpha, S_1) = \delta_4(\phi, \alpha, S_5) \tag{6.16}$$

$$P_3(\Delta\theta_E, \alpha, S_1) = P_4(\phi, \alpha, S_5) \tag{6.17}$$

relating the transmitted shock angle and the flow deflection through the reflected expansion fan. The flow deflection angle between region 2 and region 3 is defined as $\Delta\theta_E \equiv \delta_3 - \eta$, and S_1 and S_5 refer to the thermodynamic states in these regions. Figure 6.5a is the shock polar graphical solution for a contact surface angle $\alpha = 20$ degrees. The mixture in region 1 is ethylene-oxygen with equivalence ratio of 2.5 and in region 5 is molecular oxygen. The initial temperature and pressure of regions 1 and 5 are 295 K and 15 kPa, respectively. The thermodynamic state of region 2 is determined by a unique point corresponding to the CJ detonation solution (see Sec. 1.4.2). If we considered the possibility of overdriven detonations there would exist a locus of end states for region 2 on the pressure flow deflection plane (see Austin, 2003); however, this is not shown in Fig. 6.5a. The corresponding wave structure is shown in Fig. 6.5b on a polar plot to highlight the wave angles. The expansion fan is bounded by the two Mach waves, μ_1 and μ_2 of regions 2 and 3, respectively. The deflected contact surface CS' separating regions 3 and 4 has a calculated flow deflection angle of 225 degrees.

For a given α there is a unique geometrical wave solution with a specified δ_i and P_i with subscript i denoting region 3 or 4. Figure 6.6 plots the pressure P_i normalized by the pressure in region 1 versus flow deflection angle δ_i for angles of $0 < \alpha < 90$.

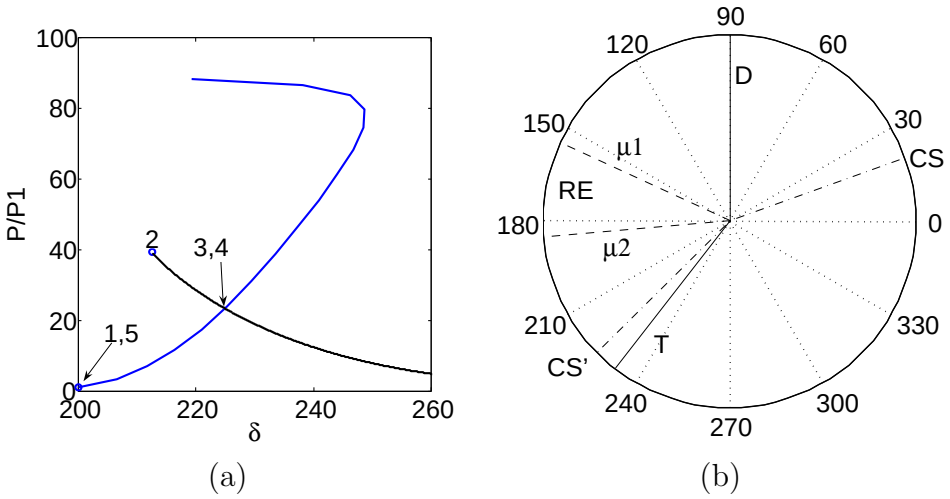

Figure 6.5: Graphical solution of an ethylene-oxygen detonation with equivalence ratio of 2.5 propagating into oxygen with contact surface $\alpha = 20$ and initial temperature and pressure of 295 K and 15 kPa, respectively. (a) pressure versus flow deflection, (b) polar plot indicating the wave structure.

The lines refer to solutions with ethylene-oxygen mixtures with equivalence ratios of 1, 2, 2.5, and 3. The initial temperature and pressure for regions 1 and 5 are 295 K and 15 kPa, respectively. Molecular oxygen is the gas that comprises region 5. The normalized pressure is maximized in the $\Phi = 2$ case.

For the limiting case when $\alpha = 0°$ (Fig. 6.7a), the solution is identical to the case studied by Dabora et al. (1965). The detonation products in the node fixed frame travel at the speed of sound of the burned products causing the angle of the expansion fan head to coincide with the detonation wave. Figure 6.7b is a polar plot indicating the geometrical structure when $\alpha = 0°$. Note that μ_1 coincides with the detonation D at an angle of 90 degrees, which is just a consequence of the CJ condition. This case is similar to the channel effect, investigated by Tanguay and Higgins (2004), in which a detonation in a thin layer of pentaerythritol tetranitrate (PETN) was used to compress a gaseous mixture layer in a rectangular channel. Note that region 1 and region 5 both lie on the 180° degree line of the pressure deflection polar in Fig. 6.7a. In the limit of $\alpha = 90°$ the interface becomes parallel to the detonation wave. Although this is a non-physical solution, the result indicates that the detonation wave never reaches the contact surface and continuously propagates in the combustible mixture.

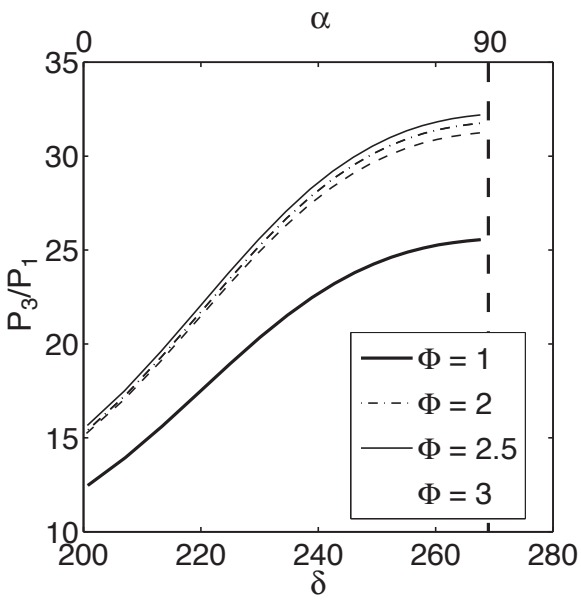

Figure 6.6: Normalized pressure vs. flow deflection plot showing the locus of solutions to regions 3 and 4 for $\alpha = [0, 90]$. Region 1: Ethylene-oxygen with Φ=1, 2, 2.5, 3. Region 2: Molecular oxygen. The initial pressure and temperature are 15 kPa and 295 K.

The deflection angle approaches 270° as the inflow velocity goes to infinity, which compacts the reflected and transmitted waves together.

6.3.3 Perfect gas approximation

If we make the additional approximations that the composition is frozen and the specific heats are independent of temperature across the reflected and transmitted waves, the relationships developed in sections 6.3.1 and 6.3.2 greatly simplify. The validity of these approximations is examined in Fig. 6.8, which illustrates the perfect gas solution versus equilibrium gas solution on a shock polar diagram. The two curves agree very well on the weak shock branch up to a pressure ratio of 75. In fact up to non-dimensional pressure ratios of about 65, the departure from the perfect gas is less than 6%. This means that the perfect gas approximation is useful for the cases of this study. With the specified conditions in regions 1 and 5, the reflected wave is always an expansion that acts to lower the temperature and pressure. In cases where a reflected shock is observed for a contact surface angle $\alpha > 89.5°$, the perfect gas

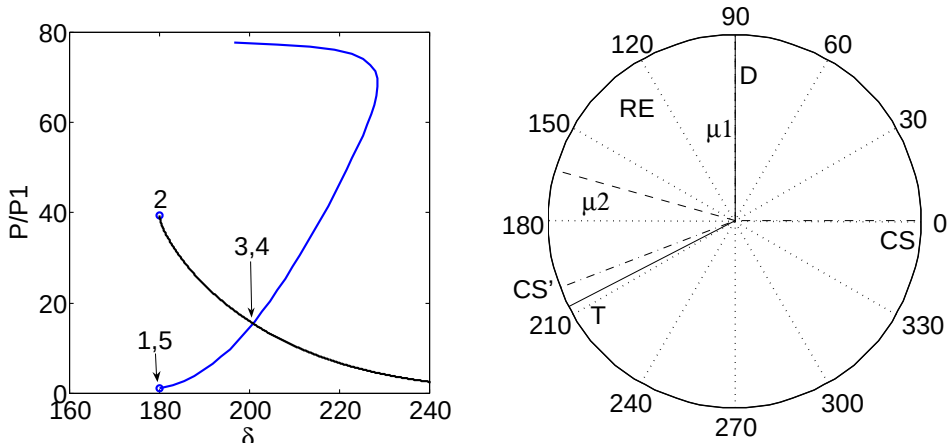

(a) (b)

Figure 6.7: Graphical solution of a ethylene-oxygen detonation with equivalence ratio of 2.5 propagating into oxygen with contact surface $\alpha = 0°$ and initial temperature and pressure of 295 K and 15 kPa, respectively. (a) Normalized pressure versus flow deflection, (b) Polar plot indicating the wave structure.

approximation increasingly becomes less valid.

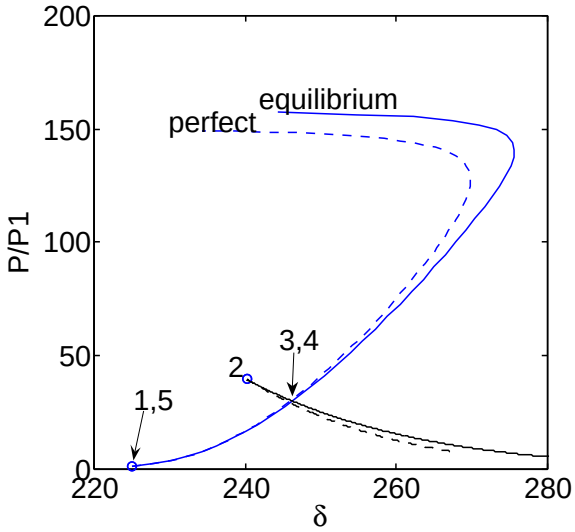

Figure 6.8: A pressure versus deflection plot comparing the perfect gas approximation with the equilibrium calculation. Region 1 is an ethylene-oxygen mixture with equivalence ratio of 2.5 propagating into oxygen in region 5 with contact surface $\alpha = 45$ and initial temperature and pressure of 295 K and 15 kPa, respectively.

6.3.3.1 Chapman-Jouguet detonation theory

Using the perfect gas approximation, the Chapman-Jouguet detonation theory simplifies dramatically. The simplified expressions for the detonation Mach number and pressure ratio are

$$M_{1n} = \sqrt{\mathcal{H} + \frac{(\gamma_1+\gamma_2)(\gamma_2-1)}{2\gamma_1(\gamma_1-1)}} + \sqrt{\mathcal{H} + \frac{(\gamma_1-\gamma_2)(\gamma_2+1)}{2\gamma_1(\gamma_1-1)}} \tag{6.18}$$

$$\mathcal{H} = \frac{(\gamma_2-1)(\gamma_2+1)\Delta h^\circ}{2\gamma_1 R_1 T_1} \tag{6.19}$$

$$\frac{P_2}{P_1} = \frac{\gamma_1 M_{1n}^2 + 1}{\gamma_2 + 1} \tag{6.20}$$

where Δh° is the enthalpy of reaction and subscripts 1 and 2 refer to the reactant and product states defined in Fig. 6.4. A full description of the theory can be found in Fickett and Davis (1979), and the two-γ-model results are given by Thompson (1988).

6.3.4 Angle of intromission

When the index of refraction n_R is unity, the interaction between the detonation and interface produces no reflected wave. This corresponds to a particular value of α, denoted as α^*, the angle of intromission that is the transition angle between a reflected shock and reflected expansion solution. In general, this condition is determined by matching the pressure and deflection angle at the interface of region 2 and region 4. When realistic thermo-chemistry is used, the solution must be found numerically. Figure 6.9a shows the angle of intromission versus the density of region 5. The data from stoichiometric hydrogen-oxygen, ethylene-oxygen, and propane-oxygen collapses onto a single curve, as shown in Fig. 6.9b, if the density of region 5 is normalized by the density of region 1.

If the perfect gas approximation is invoked, then an implicit expression for the angle of intromission α^* is obtained as a function of the thermodynamic properties in

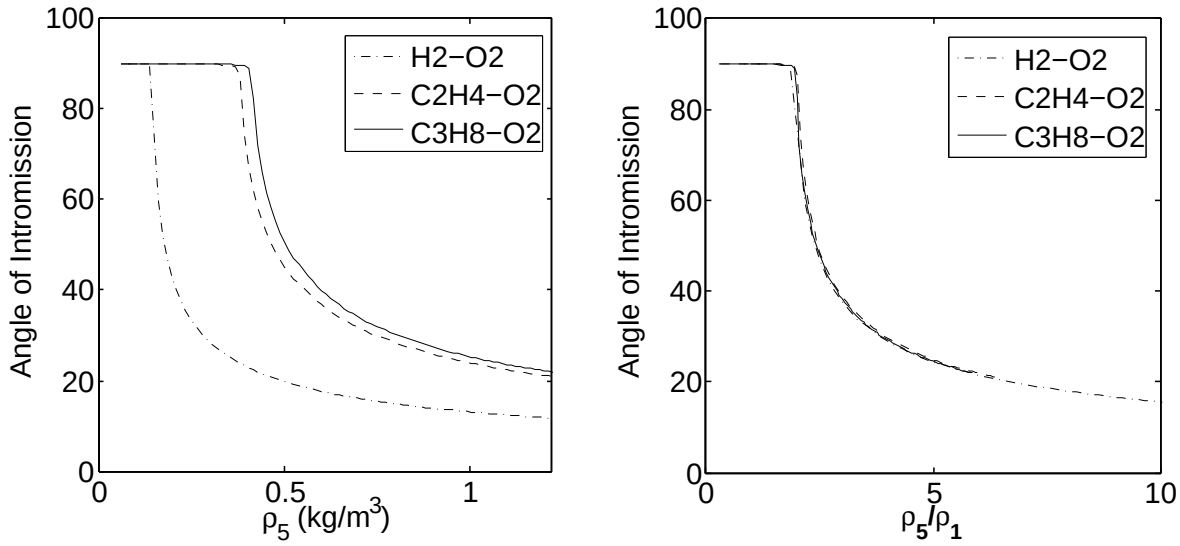

Figure 6.9: Angle of intromission vs. (a) density in region 5 and (b) the density of region 5 normalized by the density of region 1. Region 1 is composed of stoichiometric H_2-O_2, C_2H_4-O_2, and C_3H_8-O_2. The initial temperature and pressure are 295 K and 15 kPa, respectively.

regions 1 and 5. Using Eqns. 6.2-6.9, 6.18-6.20, and the oblique shock relations (see Thompson, 1988), we get the following implicit function

$$\tan\alpha^* \left(\frac{V_{CJ}}{c_2} - 1\right) = \left(1 + \frac{V_{CJ}\tan^2\alpha^*}{c_2}\right) \frac{2\cot\beta_{45}(M_5^2\sin^2\beta_{45} - 1)}{(\gamma_5+1)M_5^2 - 2(M_5^2\sin^2\beta_{45} - 1)} \tag{6.21}$$

where,

$$\beta_{45} = \sin^{-1}\left(\frac{1}{M_5}\sqrt{\left(\frac{P_2}{P_1} - 1\right)\frac{\gamma_5+1}{2\gamma_5} + 1}\right). \tag{6.22}$$

Here β_{45} is the angle of the oblique shock with respect to the vector $\vec{w}_5$. After some manipulation and the substitution $y = \tan\alpha$, Eqn. 6.21 can be rearranged and the constants grouped together to obtain

$$y(1 - \mathcal{C}_1) \quad = \quad \frac{\mathcal{C}_2(1 + \mathcal{C}_1 y^2)\sqrt{\mathcal{C}_3(1+y^2) - \mathcal{C}_3\mathcal{C}_4}}{\mathcal{C}_5 + \mathcal{C}_6(1+y^2)} \tag{6.23}$$

with the constants

$$\mathcal{C}_1 = \frac{V_{CJ}}{c_2} \tag{6.24}$$

$$\mathcal{C}_2 = c_5\sqrt{2}\left(\frac{P_2}{P_1}-1\right) \tag{6.25}$$

$$\mathcal{C}_3 = V_{CJ}^2 \tag{6.26}$$

$$\mathcal{C}_4 = \frac{c_5^2(\frac{P_2}{P_1}-1+\gamma_5(\frac{P_2}{P_1}+1))}{2\gamma_5 V_{CJ}^2} \tag{6.27}$$

$$\mathcal{C}_5 = c_5^2\left(1-\frac{P_2}{P_1}\right)\sqrt{\frac{P_2}{P_1}+1+\frac{\frac{P_2}{P_1}-1}{\gamma_5}} \tag{6.28}$$

$$\mathcal{C}_6 = \gamma_5 V_{CJ}^2\sqrt{\frac{P_2}{P_1}+1+\frac{\frac{P_2}{P_1}-1}{\gamma_5}}. \tag{6.29}$$

Through further manipulation of Eqn. 6.23 with constants defined by Eqns. 6.29, a sixth order polynomial is obtained as a function of the variable y. By making the substitution $y = x^2$, the polynomial reduces to a third order polynomial of the form

$$x^3 + Bx^2 + Cx + D = 0 \tag{6.30}$$

with constants

$$B = -\frac{\mathcal{C}_1\mathcal{C}_2^2\mathcal{C}_3(-2+\mathcal{C}_1(\mathcal{C}_4-1))+2(\mathcal{C}_1-1)^2\mathcal{C}_5\mathcal{C}_6+2(\mathcal{C}_1-1)^2\mathcal{C}_6^2}{\mathcal{C}_1^2\mathcal{C}_2^2\mathcal{C}_3-(\mathcal{C}_1-1)^2\mathcal{C}_6^2} \tag{6.31}$$

$$C = \frac{\mathcal{C}_2^2\mathcal{C}_3(1-2\mathcal{C}_1(\mathcal{C}_4-1))-(\mathcal{C}_1-1)^2(\mathcal{C}_5+\mathcal{C}_6)^2}{\mathcal{C}_1^2\mathcal{C}_2^2\mathcal{C}_3-(\mathcal{C}_1-1)^2\mathcal{C}_6^2} \tag{6.32}$$

$$D = \frac{\mathcal{C}_2^2\mathcal{C}_3(\mathcal{C}_4-1)}{\mathcal{C}_1^2\mathcal{C}_2^2\mathcal{C}_3-(\mathcal{C}_1-1)^2\mathcal{C}_6^2} \tag{6.33}$$

The cubic polynomial, solved by the transform $z = x+B/3$, as discussed in Zwillinger (1996), has three roots that in general are complex. The final solutions are

$$\alpha_i^* = \tan^{-1}\left(\sqrt{2\sqrt{-Q}\cos\left(\frac{\theta_c+n_i\pi}{3}\right)-\frac{B}{3}}\right) \tag{6.34}$$

with

$$Q = \frac{C}{3} - \frac{B^2}{9} \tag{6.35}$$

$$R = \frac{9BC - 27D - 2B^3}{54} \tag{6.36}$$

$$\theta_c = \cos^{-1}\left(\frac{R}{\sqrt{-Q^3}}\right). \tag{6.37}$$

The roots are real if the discriminant, $\mathcal{D} \equiv Q^3 + R^2$, is less than or equal to zero, which is true over the range of parameters that are of physical interest. The discriminant approaches zero as the angle of intromission approaches 90 degrees. The variable $n_i = 0, 2, 4$ for values of $i = 1, 2, 3$, respectively. Only one of the three solutions is relevant with respect to the physical process taking place. Analysis shows that Eqn. 6.34 is dependent on the ratio of molar masses of regions 1 and 5, justifying the collapse of the angle of intromission with density ratio shown in Fig. 6.9b.

6.4 Concluding remarks

The analysis in this chapter highlighted some of the key issues in detonation refraction through an interface. In general, for a given contact surface angle α, a transmitted and reflected system of waves exists to match the pressure and flow deflection angle δ_i in regions $i = 3, 4$. The reflected waves in this study were exclusively expansion fans.

It was shown that the frozen and equilibrium regions occur at length scales much smaller and larger than the induction zone length. The transition region linking the two regions must be studied either by numerical or experimental methods.

The detonation refraction analysis will be used in Chap. 7 to compare against the experimentally observed refraction angles. In addition, this analysis will serve as a starting point to examine the growth of the turbulent mixing zone at the deflected contact surface, CS'. Specifically, the thermodynamic states and velocities in regions 3 and 4 can be used to estimate shear layer growth (see Sec. 7.4).

Chapter 7

Results & Analysis: Detonation Interaction with a Sharp Interface

Experiments on detonation interaction with a sharp interface are described in this chapter. The basic idea, shown in Fig. 1.3, is a detonation in the test section that propagates through a sharp interface between the combustible gas and an inert or oxidizing test gas. The sharp interface is implemented using a nitro-cellulose membrane mounted on a thin wooden frame (see Sec. 2.0.2).

There has been limited experimental research carried out in this area. Gvozdeva (1961) did experiments using a methane-oxygen detonation that propagated through a nitro-cellulose interface at various angles to the oncoming flow. The test gas mixtures were less sensitive methane-oxygen mixtures or air. Dabora et al. (1991) and Tonello and Sichel (1993) have investigated detonation diffraction of combustible mixtures with varying sensitivity, separated in parallel channels. In their experiments, oblique detonation waves were observed to propagate in the less sensitive mixture.

In the following discussion the major gas dynamic features visible in the schlieren images will be identified and analyzed. The theory discussed in Chap. 6 is used to explain the wave structure, and additional analysis is presented to characterize the turbulent shear layer and Mach stem formation. The presence of combustion inside the turbulent mixing zone is also addressed.

7.1 Experimental setup

The general experimental setup is as discussed in Chap. 2. There are a few modifications for this set of experiments, namely the filling procedure and firing procedure, which are discussed here.

The difficulties in the filling procedure arise because of the use of a nitro-cellulose membrane. It is necessary to fill simultaneously on both sides of the membrane to avoid tearing it. These challenges have been explored by previous researchers (see Brouillette, 2002) interested in interface instabilities (such as the Richtmyer-Meshkov instability). In the current setup, the additional complexity is that the combustible mixture needs to be mixed once it is loaded into the GDT. The filling is accomplished by closing the sliding valve to separate the test section from the GDT. The GDT is then filled with the combustible mixture and mixed, and then the test section is filled with the test gas. At the end of this procedure the test gas is on both sides of the nitro-cellulose membrane situated at port 1. Removing the slug of test gas located between the nitro-cellulose membrane and sliding valve is done in the initial steps of the firing procedure.

Replacing the slug of test gas mixture with the combustible mixture in the GDT is accomplished by opening the sliding valve and allowing the gravity current to sweep out and mix with the test gas. The technique was based on observations made during the PLIF experiments in Sec. 3.3. The observations shown in Fig. 7.1 are that after 20 s the gravity current displaces the test gas from the test section. The sequence of images shows a bright region on the bottom representing the combustible mixture and a dark region on top representing the test gas. In the actual PLIF experiments, an acetone-helium surrogate was used instead of the combustible mixture (see Sec. 3.3).

The sliding valve is left open for two minutes, and then the fire button is pressed. The timing sequence is simplified since the sliding valve is manually opened at the beginning of the timing sequence and does not trigger the data acquisition system or capacitor discharge unit.

The technique of using a gravity current to displace and mix with the remaining

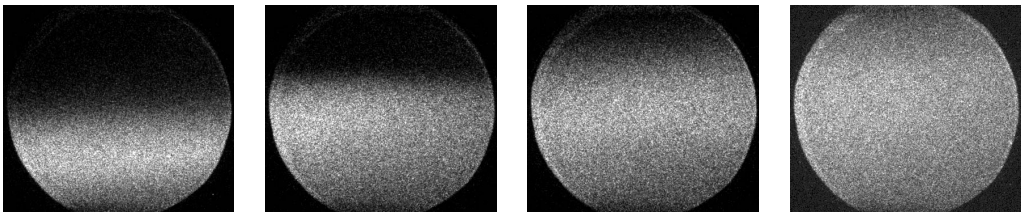

Figure 7.1: A sequence of PLIF images showing the gravity current filling in the test section. The images from left to right correspond to times of 5, 8, 10, 20 s measured from when the plate in the sliding valve assembly reaches the open position.

slug of test gas mixture was validated by propagating a detonation into the test section without an interface. A detonation observed from these tests is shown in Fig. 7.2. The detonation velocity is within 10% of the predicted CJ value and is observed to be slightly non-planar.

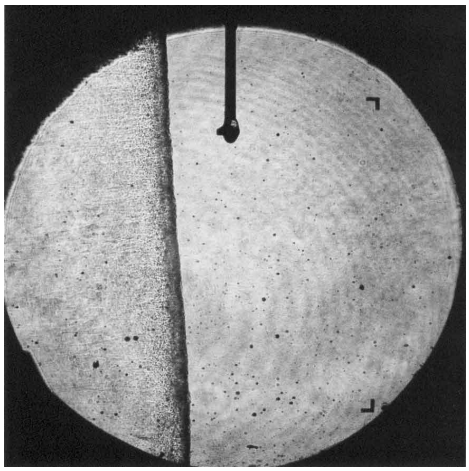

Figure 7.2: A schlieren image of a detonation propagating from left to right corresponding to Exp. #1903. The sting entering from the top is a remnant from a previous experiment.

7.1.1 Limitations of the current setup

There are some tradeoffs and associated uncertainties involved in the current setup; these are grouped into the general categories of filling procedure and interface type. Difficulties in the filling procedure as mentioned above were solved by using the sliding valve to isolate the diaphragm. The associated uncertainty lies in displacing

and mixing the 4.5 L of test gas between the sliding valve and the diaphragm with the gravity current.

One alternative is to simultaneously fill the combustible mixture (pre-made in a storage vessel) and the test gas. Although not practical in the current setup due to the large volume of the GDT, a smaller experiment would benefit from the reduction in mixture uncertainty. An automated filling system would lend itself well to this type of experiment.

The type of interface used is of fundamental importance to the experimental results. Nitro-cellulose is an ideal membrane because of its fracture properties and its one to ten micron thickness (see Kumar, 2002). In the present experiment the major source of error comes from inserting the membrane into the test section on a wooden frame. The abrupt change in cross-sectional area results in dramatic flow changes, namely, a reflected shock wave originating at the wood frame. The frame also blocks part of the detonation interaction with the interface.

The experimental setup could be modified to incorporate a square acrylic channel that slides into the test section. By having the channel extend upstream of the interface location it would allow the detonation to transfer from the test section into the channel, minimizing the effects of the area change at the interface. The acrylic channel would also not obstruct the field of view at the interface.

7.2 Detonation refraction experiments

The key features in the detonation refraction experiments are shown in Fig. 7.3. The schlieren image shows a detonation propagating from left to right in a Φ=2.5 ethylene-oxygen mixture through a nitro-cellulose membrane interface mounted on a wood frame into nitrogen. A transmitted shock wave and a turbulent mixing zone result from this interaction. There is also a reflected shock wave that originates from the wood frame. Detonation refraction theory predicts a weak reflected expansion for this interface-detonation configuration. One additional flow feature is a small Mach stem located along the top wall at the end of the transmitted wave. Small particles

are visible around the TMZ; these are remnants of the membrane.

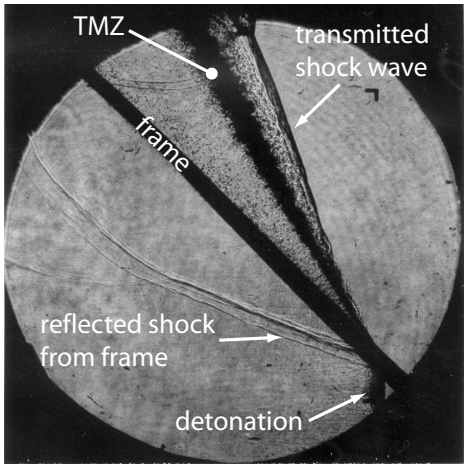

Figure 7.3: A schlieren image of a detonation propagating from left to right through an interface corresponding to Exp. #1922.

The experiment is sufficiently repeatable so that it is possible to construct a time sequence with the schlieren images. Figure 7.4 shows three images corresponding to experiments 1907, 1922, and 1906. These experiments use a Φ=2.5 ethylene-oxygen combustible mixture and nitrogen as the test gas. The varying image capture times are (a) 0 μs, (b) 8 μs, and (c) 27 μs with respect to image (a). It is observed that as the detonation moves from left to right the node, or point of origin of the transmitted shock, and TMZ moves progressively down the interface. The TMZ also increases in thickness at a given image height from image (a) to (c).

The angles of the various features are measured and compared with the detonation refraction theory developed in Chap. 6. The geometry of the interaction is the mirror image of the experiment reflected along the horizontal axis. Therefore the angles computed in Chap. 6 need to be subtracted by 180 degrees to compare with the experimental results. A typical example is shown in Fig. 7.5 for Exp. #1907. The interface angle is measured to be 42 degrees from the horizontal (see Fig. 7.5). The detonation wave is perpendicular to the horizontal axis and the transmitted shock wave is measured to be at an angle of 67$\pm$1 degrees. For this experiment, the detonation refraction theory predicts a transmitted wave angle of 70.4 degrees. The resulting

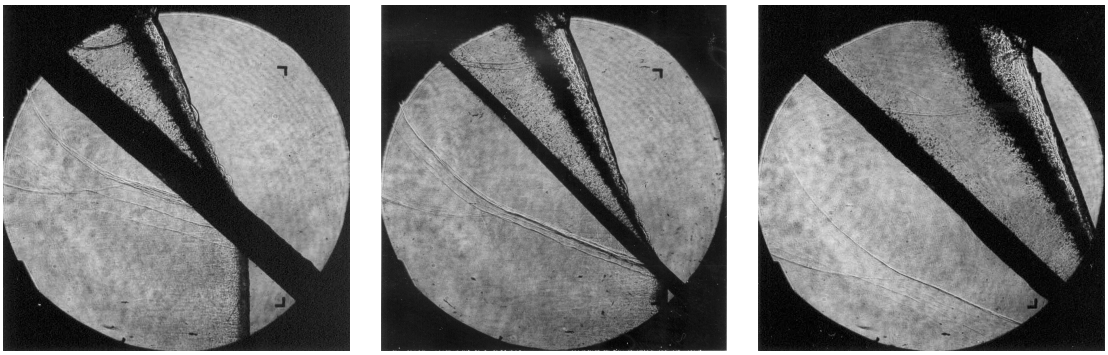

(a) (b) (c)

Figure 7.4: A sequence of schlieren images showing the interaction between a detonation and an interface. The interface is at 45 degrees with ethylene-oxygen (Φ=2.5) on the left side and nitrogen on the right side of the interface. The timing of the images with respect to P2 is (a) 0 μs, (b) 8 μs, and (c) 27 μs.

difference between experiment and theory is 6%. Theory predicts that the contact surface angle should be 66 degrees; however it does not factor in the growth of the mixing zone. In this experiment the TMZ is located between 60 and 64 degrees.

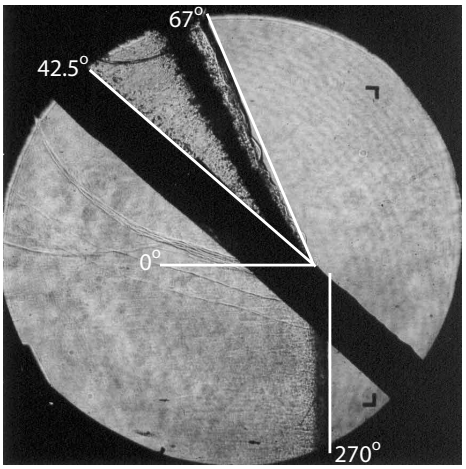

Figure 7.5: A schlieren image of a detonation propagating from left to right through an interface corresponding to Exp. #1907. The angles of the various waves and features are shown on the figure.

The measured transmitted shock angles reported in Table 7.2 are systematically lower than the predicted values by an average value of four degrees. A list of possible errors are shown in Table 7.1. The magnitudes of the uncertainties, measured in

degrees are reported if estimated. The largest source of error results from a non-planar detonation wave a product of the gas filling procedure used to sweep out the test gas (see Sec. 7.1.1). Other sources of error are from the warped wood frame and measuring the angles. The assumption that the deflected interface is treated as a contact surface and does not result in a shear layer also contributes to the error. The mixing-layers displacement thickness was shown to be a function of heat release (see Hermanson and Dimotakis, 1989) which modifies the matching conditions and thus the wave structure.

Source of error	Uncertainty
Non-planar detonation wave	$\pm 4^\circ$
Measurement error	$\pm 1^\circ$
Warped wood frame	$\pm 2^\circ$
Non-ideal contact surface	$\pm 2^\circ$
Schlieren light beam off axis	$< 0.1^\circ$
Schlieren stigmatism	negligible
Curved transmitted shock wave	
Membrane fragments	

Table 7.1: Possible sources of error addressing the discrepancy between the measured and predicted transmitted shock angle.

One important observation is that in the region close to the node where the transmitted shock and TMZ coalesce, the wave curves and tends to a smaller angle. This is observed in Fig. 7.5 where the detonation, TMZ, interface, and transmitted shock do not all meet at one point. Instead there is the intersection between the transmitted shock, TMZ, and frame and an intersection between the frame and detonation. The wave curvature responsible for this might in part be due to the diaphragm or complex detonation-interface interaction in the transient region.

7.2.1 Experimental parameters

In the sharp interface study, the ethylene-oxygen equivalence ratio and test gas mixture were varied. The results are quantified by measuring the angles of the transmitted shock wave, shear layer, and the gap between the two of them (see Fig. 7.6).

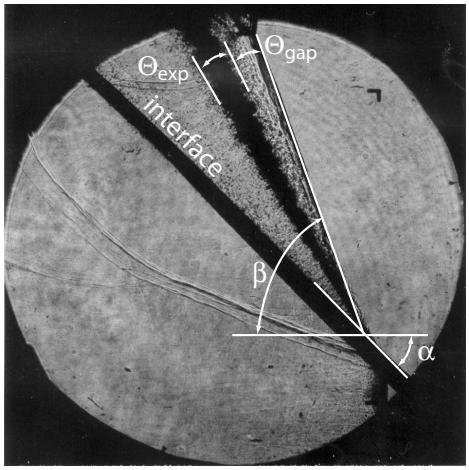

Figure 7.6: A schlieren image of a detonation propagating from left to right through an interface corresponding to Exp. #1922. The calculated growth rate angle Θ_{model} and angle Θ_{gap} between the transmitted shock and TMZ are defined.

The first stage of the analysis compares the observed transmitted shock wave angle to that predicted by the detonation refraction theory discussed in Chap. 6. Table 7.2 lists the detonation refraction experiments with their experimentally measured angles. The calculated transmitted shock angle is included for each case, with corresponding images located in Appendix D.

The growth of the turbulent mixing zone and the formation of the Mach stem are two features that are explored in Sec. 7.4 and Sec. 7.3, respectively. The shear layer is characterized by the growth rate, Θ_{model}, which is related to the shear layer thickness by

$$\Theta_{model} = \tan^{-1}\left(\frac{\delta_G}{x}\right).$$

The measured values Θ_{exp} are listed in Table 7.2 along with the gap angles, Θ_{gap}.

The Mach stem was observed to depend on the type of test gas. Figure 7.7 shows three Mach stems with (a) nitrogen, (b) oxygen, and (c) nitrous oxide. The overall size and thickness increases from image (a) to (c). The role of the test gas on Mach stem formation is investigated to determine the possibility that secondary combustion in the TMZ plays a role in determining Mach stem size.

Shot #	Φ	Test gas	α_{exp}	β	β_{exp}	Θ_{exp}	Θ_{gap}
1906	2.5	N_2	44	72.1	69	4.5	6
1907	2.5	N_2	41	70.4	67	6.5	3.5
1912	2.5	O_2	45	71.4	67	6	6
1914	2.5	O_2	43	70.2	63	6	3
1915	2.5	O_2	44	70.8	67	4	5
1916	2.5	N_2O	44	67.1	62	5	3
1917	2.5	N_2O	44	67.1	65	5	2
1919	1	N_2O	45	68.3	65	6.2	2
1920	1	N_2O	44	67.7	65	6	3
1921	1	N_2O	44	67.7	65	8.5	2
1922	2.5	N_2	45	72.7	70	7	7
1923	1	O_2	45	72.1	65	4.8	5
1925	1	O_2	44	71.6	67	4	5
1926	1	O_2	45	72.1		5.5	
1927	1	O_2	45	72.1	67	4.5	6

Table 7.2: Table of transmitted shock angle, β, angle, Θ_{exp}, and transmitted-shock-TMZ angle, Θ_{gap} with ethylene-oxygen mixtures, with equivalence ratio, Φ, and oxygen, nitrogen, or nitrous oxide as the test gas. Subscript *exp* denotes an experimental measurement.

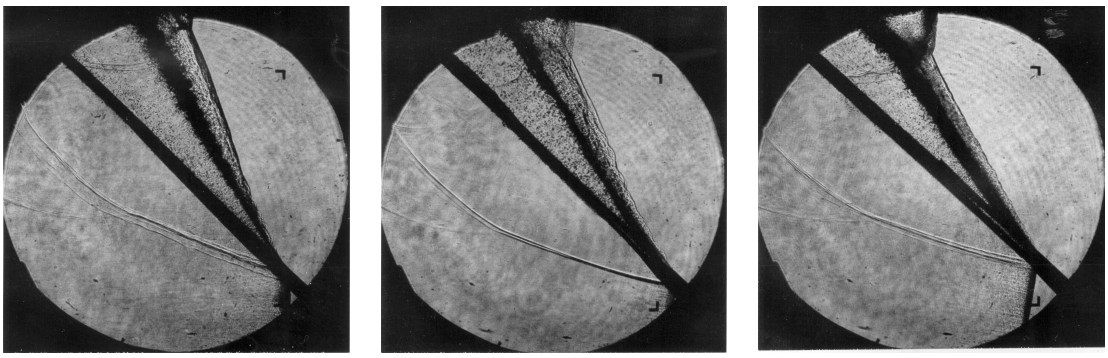

(a) (b) (c)

Figure 7.7: A set of schlieren images showing Mach stems for different test gases. The interface is at 45 degrees with ethylene-oxygen (Φ=2.5) on the left side and (a) nitrogen (shot #1922), (b) oxygen (shot #1915), and (c) nitrous oxide (shot #1916) on the right side of the interface. The specifics of these experiments are given in Appendix B.

7.3 Mach reflection

Mach reflection at the tip of the transmitted shock wave is clearly visible along the top wall of the test section (see Fig. 7.7). Normally, if a supersonic flow along a

solid boundary is deflected by an incident oblique shock wave, a regular reflection, as shown in Fig. 7.8, results in a reflected oblique shock wave to turn the flow so that it ends up parallel to the wall. If the fluid in state 2 cannot be turned back parallel to the rigid surface with a single reflected shock wave then Mach reflection occurs (see Liepmann and Roshko, 2001, Chap. 4), as illustrated in Fig. 7.8.

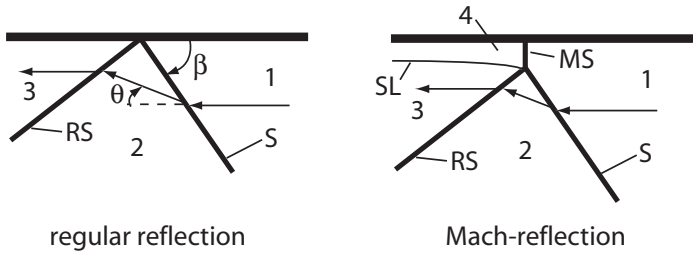

Figure 7.8: A sketch of regular and Mach reflection with states 1, 2, and 3 and the incident (S) and reflected shocks (RS) labeled. The flow behind the Mach stem (MS) is subsonic with a slip line (SL) separating states 3 and 4.

The condition for Mach reflection is shown graphically in Fig. 7.9 on a pressure versus flow deflection map. The incident shock polar shows the path from state 1 to state 2. For a regular reflection (Fig. 7.9a) to occur between state 2 and state 3, the reflected shock polar must cross or at least touch the pressure axis to satisfy the flow turning criteria. The limiting case in which a regular reflection can occur is shown in Fig. 7.9b where the maximum flow deflection of the reflected shock polar is tangent to the pressure axis. A Mach reflection occurs when the reflected shock polar does not intersect the pressure axis (Fig. 7.9c). In this case state 3 corresponds to the intersection of the reflected shock polar with the incident polar. The state behind the Mach stem is non uniform and subsonic. Hornung (1986) discusses the intricacies of Mach reflections under various flow conditions and describes the various types of regular and Mach reflections that can result depending on the flow conditions.

The condition for the onset of Mach reflection (Fig. 7.9b) is calculated for the gas moving from state 2 to state 3. It is necessary to carry out the analysis in a convective frame of reference coinciding with the point of intersection between the incident shock wave and the wall of the regular reflection (Fig. 7.8). The incident

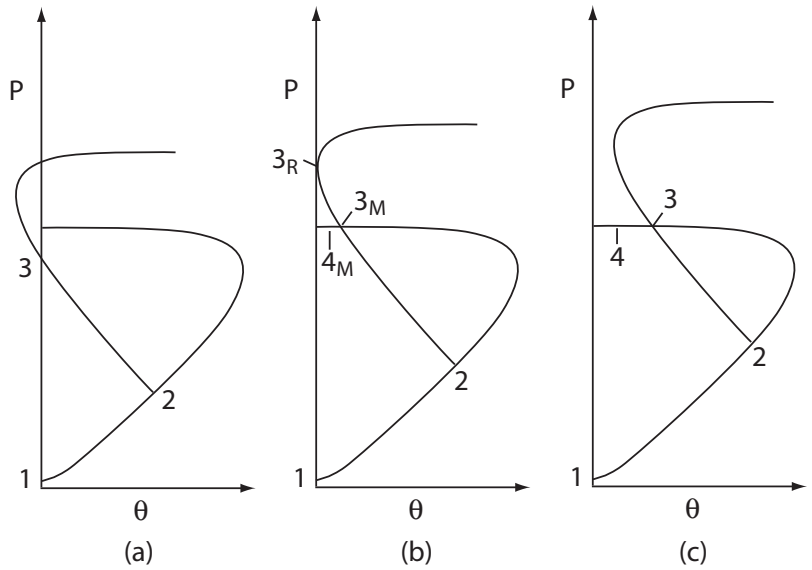

Figure 7.9: Pressure-deflection maps illustrating the regular (a) and Mach reflection (c) solutions shown in Fig. 7.8. The critical case (b) admits both regular and Mach reflection solutions denoted by subscripts R and M, respectively.

shock Mach number and angle β are specified from the experimental conditions and determine the fluid state 2 that is deflected toward the solid boundary. This analysis calculates the maximum angle the flow can turn from state 2 to state 3 with a reflected shock wave. If the angle is less than the incident deflection angle then Mach reflection results. In the case of a perfect gas the oblique shock equation

$$\tan\theta \;=\; 2\cot\beta\frac{M^2\sin^2\beta-1}{M^2(\gamma+\cos 2\beta)+2}, \tag{7.1}$$

which relates the flow turning angle, θ, to the incident Mach number, M, and the oblique shock angle, β, is maximized by imposing

$$\frac{d\theta}{d\beta} \;=\; 0. \tag{7.2}$$

Maximizing Eqn. 7.2 determines the critical value of β for a given Mach number that can then be plugged back in Eqn. 7.1 to determine Θ_{max}, which can be compared. Applying the condition Eqn. 7.2 to 7.1 while keeping the Mach number constant in

the differentiation yields

$$\gamma M^4 \cos 2\beta + (2 + M^2(1+\gamma)) \csc^2 \beta \;=\; M^2(1 - M^2). \tag{7.3}$$

The critical value of β is calculated for a given value M that is then substituted into Eqn. 7.1 to result in a maximum flow deflection angle, Θ_{max}. Table 7.3 lists the flow deflections after the incident oblique shock and the maximum turning angle possible using a reflected shock. In all cases the Mach number M_2 of the fluid after the incident shock is too small to generate the reflected shock needed to turn the parallel to the wall. Therefore, the regular solution is not possible. In some cases the post-incident-shock Mach number is less than one, which guarantees that a reflected shock cannot occur and therefore there is no value for Θ_{max}.

Test gas	Φ	α	θ	θ_{max}	β_{exp}	M_2
N_2O	2.5	45	49.3	7.45	65	1.30
N_2O	1	45	47.5	5.53	65	1.24
N_2	2.5	42	41.5	0.25	66	1.03
N_2	1	45	38.2		66	0.98
O_2	2.5	45	41.7	1.05	65	1.08
O_2	1	45	39.5	0.43	65	1.04

Table 7.3: Table of flow deflection angle from state 1 to state 2, θ, and maximum flow deflection angle from state 2 to state 3, θ_{max} resulting from a regular reflection. The results are shown for different test gases and ethylene-oxygen equivalence ratios using the experimentally measured shock angle, β_{exp}, and interface angle, α, and the calculated Mach number M_2 in state 2.

The convective velocity at the intersection of the incident shock and the top wall is determined using the geometrical construction shown in Fig. 7.10. The detonation-shock-interface structure is compared in two positions to determine the relationship between the detonation velocity and oblique shock velocity

$$U \;=\; V_{CJ}\left(1 - \frac{\tan\alpha}{\tan\beta}\right). \tag{7.4}$$

Using the detonation-refraction analysis developed in Chap. 6, Eqn. 7.4 is plotted in Fig. 7.11 as a function of the interface angle, α. The velocity, U, representing the

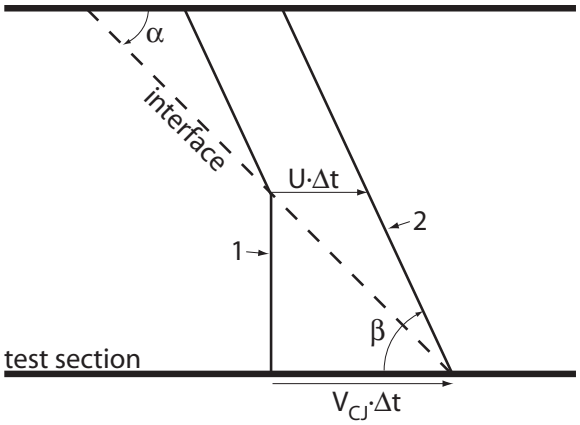

Figure 7.10: A schematic of the detonation-interface interaction at two instants in time. The detonation and transmitted shock (1), and the fully emerged transmitted shock (2) are used to determine the shock velocity U. The interface angle and shock angle are denoted by α and β, respectively.

horizontal displacement rate of the oblique shock is normalized by the detonation velocity. For $\alpha = 0$ the transmitted shock wave translates at the detonation velocity. As the interface angle increases the velocity ratio decreases from one and approaches a constant value for $\alpha > 70°$. Nitrous oxide, oxygen, and nitrogen are used as the test gas with ethylene-oxygen, $\Phi = 1$ (solid line), and $\Phi = 2.5$ (dashed line) as the combustible gas.

An oblique shock pressure-deflection graph is shown in Fig. 7.12a based on the regular reflection configuration (see Fig. 7.8). The incident flow velocity is fixed at $U = 1399$ m/s as determined by Eqn. 7.4 for the case of $\alpha = 45°$ and $\beta = 65°$ using nitrous oxide corresponding to the experimental conditions of shot #1916. The reflected shock (R) solution is also plotted. Graphically the reflected shock polar must cross the vertical axis for a regular reflection to occur. As this is not the case, a Mach stem forms to produce post-shock states over the range S_M occupying the region between the vertical axis and the intersection point between the reflected and incident shock polars (see Hornung, 1986).

It is also interesting to plot the non-standard shock polar obtained when the inflow velocity U is constrained by the angle β in Eqn. 7.4. In this configuration the locus of solutions for the incident pressure-deflection map is solely a function of α since

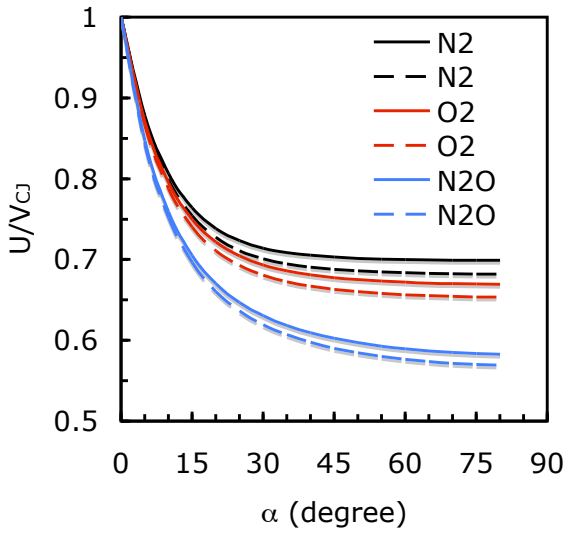

Figure 7.11: Normalized transmitted shock velocity, U, as a function of interface angle, α, using Eqn. 7.4. The combustible mixture used in the calculation was ethylene-oxygen with $\Phi = 1$ (solid line) and $\Phi = 2.5$ (dashed line).

detonation refraction theory (see Chap. 6) determines the value of β as a function of α. The shock polar shows the possible states of the experiment. The reflected shock polar is determined the same way as in Fig. 7.12a, by fixing the Mach number in state 2 and varying the shock angle β.

The Mach reflection discussion to this point has considered the composition to be frozen. Including the effect of dissociation and chemical reaction has been shown by Hornung et al. (1979) to either enhance or weaken the turning potential of the oblique shock. Generally, endothermic reactions result in larger flow deflection angles, while exothermic reactions result in smaller flow deflection angles. Of the test gases used in this study, oxygen and nitrogen are endothermic while nitrous oxide is exothermic (see Table 7.4).

For the shock Mach numbers dealt with in this study ($M < 9$) both oxygen and nitrogen are treated using frozen composition. Equilibrium analysis using STANJAN (see Reynolds, 1986) of the decomposition of nitrogen and oxygen behind shock waves indicated that for shock Mach numbers below nine, less than 5% of molecular oxygen or nitrogen dissociates. However, nitrous oxide decomposes exothermically under

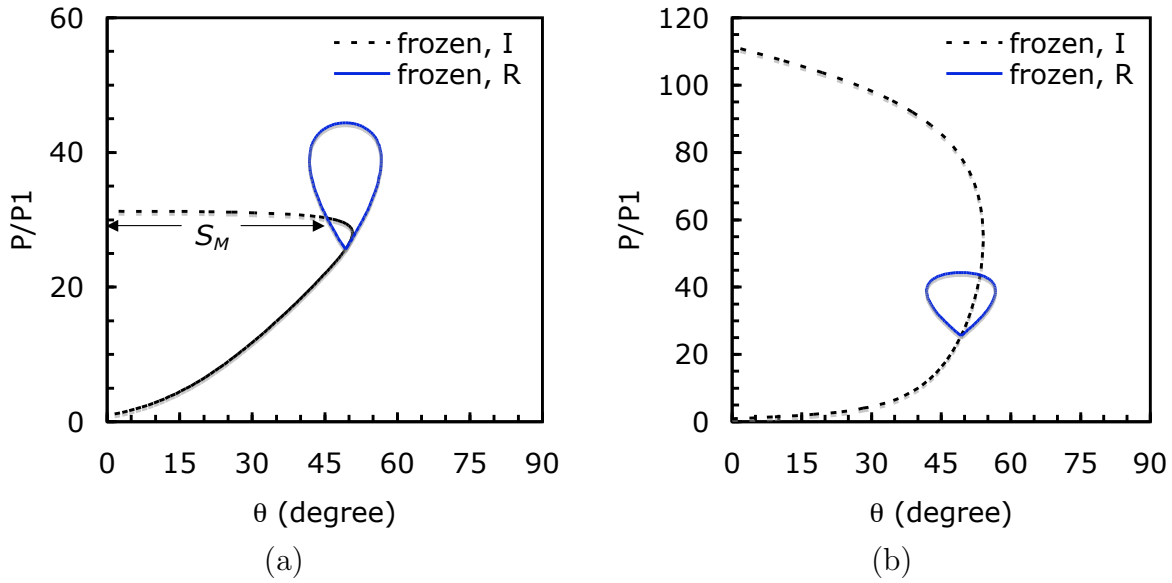

Figure 7.12: Oblique shock polar normalized pressure P/P_1 as a function of flow deflection angle θ for incident (I) and reflected (R) waves in nitrous oxide. (a) The inflow velocity $U = 1399$ m/s and (b) the inflow velocity U is determined by Eqn. 7.4 and is a function of α.

test gas	$\Delta_R h^\circ$ [kJ/mol]
O_2	249.2
N_2	472.7
N_2O	-81.6

Table 7.4: The standard heat of reaction $\Delta_R h^\circ$ for dissociation reactions of oxygen, nitrogen, and nitrous oxide.

these conditions.

Detailed chemical reaction calculations are carried out to resolve the decomposition of nitrous oxide behind the shock wave. The calculations were carried out using Cantera (Goodwin, 2005) solving the same equations used to determine the ZND solution (Sec. 1.4.2) with the difference that the incident shock velocity is imposed instead of the CJ condition. Equilibrium is reached as $t \to \infty$ when the flow conditions reach a steady value. The calculations used the GRI3.0 reaction mechanism (Smith et al., 2004) validated by Kaneshige et al. (1999) for use in nitrous oxide detonations. The distance (or time) behind the shock at which equilibrium is reached

decreases with increasing Mach number, a consequence of the Arrhenius dependent kinetics. To determine when equilibrium and frozen chemistry simplifications are valid it is important to compare the residence time of a convected fluid particle, τ_r, to the reaction time scale, defined as the time to attain 90% of the peak thermicity. The comparison is made in Fig. 7.13 where the reaction time is plotted as a function of Mach number for the exothermic decomposition of nitrous oxide. The fluid residence time scale was calculated to be $\tau_r \approx 62$ μs based on the detonation traveling 152.4 mm, the length of the wood frame. For the equilibrium regime it is necessary that the reaction time be much less than the convective time. In this study two orders of magnitude are imposed to separate the frozen from the equilibrium regions. These regions are shown as bounded by the lines τ_{fr} and τ_{eq} on Fig. 7.13. The Mach numbers corresponding to the frozen and equilibrium boundaries are $M = 6$ and $M = 8$, respectively. Between these two bounds, the transient behavior depends on the details of the chemical reaction process.

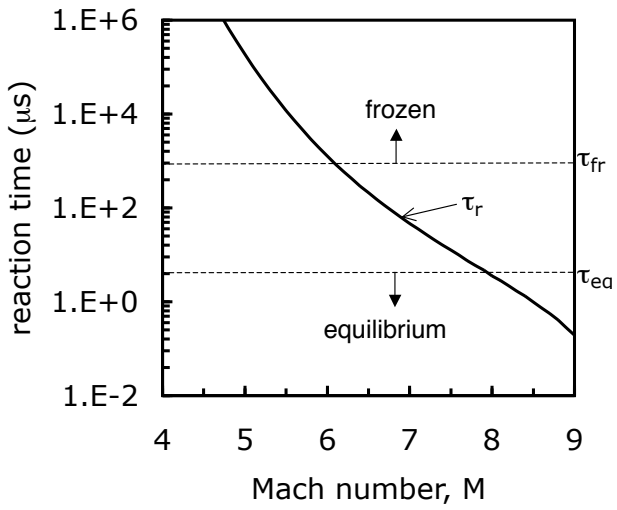

Figure 7.13: The chemical dissociation reaction time of nitrous oxide as a function of Mach number, M. The particle residence time, τ_r, equilibrium time threshold, τ_{eq}, and frozen threshold, τ_{fr}, are shown.

For Mach numbers greater than eight the decomposition of nitrous oxide occurs sufficiently fast compared to the motion of the fluid through the field of view such that the decomposition region can be considered thin compared to the other length scales

in the experiment. A time profile of the pressure and temperature in the reaction zone is shown in Fig. 7.14.

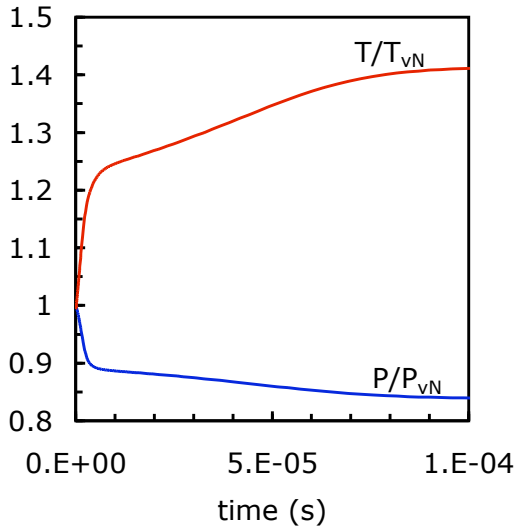

Figure 7.14: A normalized pressure and temperature versus time profile of the exothermic decomposition of nitrous oxide behind a $M = 8.5$ shock wave.

The equilibrium state is calculated as a function of Mach number and plotted in Fig. 7.15. The time limit on the calculation was set to 1000 s so that the equilibrium state at lower Mach numbers could be reached. Figure 7.15a compares the equilibrium and frozen pressure and density. All values are normalized with respect to the initial state. The frozen pressure and density are included for comparison; however, the frozen solution is not physical at these Mach numbers. The species profiles shown in Fig. 7.15b emphasize the equilibrium mole fractions of N_2, O_2, and NO above the CJ point ($M = 6.3$).

Ultimately, the point of the equilibrium calculations is to show what effect they have on the flow deflection. The goal is to resolve the observable differences in Mach stem size between the nitrous oxide and oxygen or nitrogen schlieren images from the sharp interface experiments (for example see Appendix D, shot #1917 versus shot #1922). Figure 7.16 are two pressure-deflection plots that compare frozen chemistry with equilibrium chemistry using nitrous oxide as the test gas. In Fig. 7.16a, the incident velocity is $U = 2622$ m/s, which corresponds to the detonation velocity of a

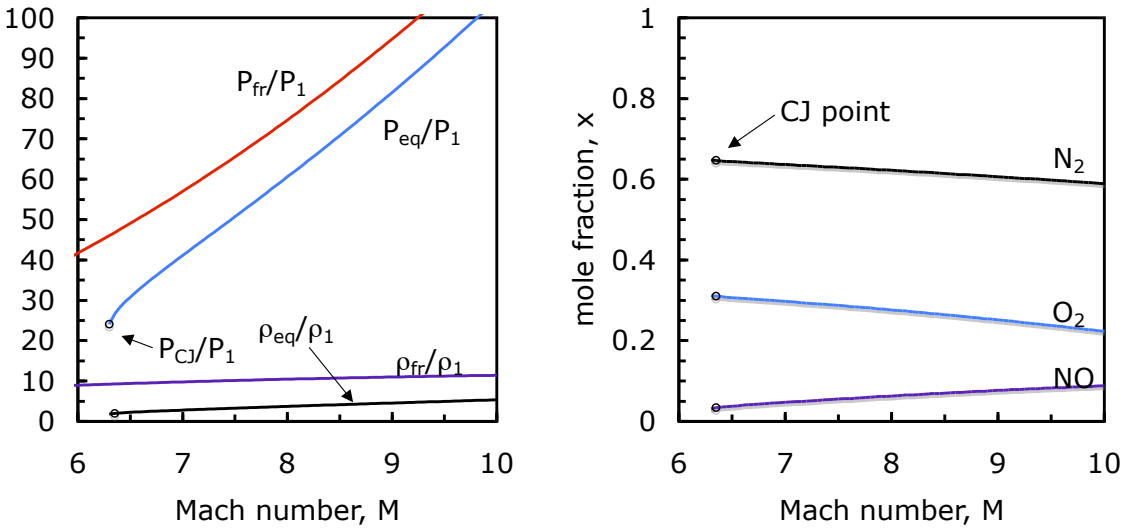

Figure 7.15: The equilibrium and frozen states of nitrous oxide behind a normal shock are plotted as a function of shock Mach number M. (a) The pressure and density normalized by the incident flow conditions are plotted for equilibrium (P_{eq}/P_1) and frozen (P_{fr}/P_1) states. (b) The equilibrium species mole fractions x.

$\Phi = 2.5$ ethylene-oxygen mixture. The shock angle is varied from $\beta = \sin^{-1}(c_1/U)$ to $\beta = 90°$. The equilibrium curve shows that at small shock angles, the reaction time is large, resulting in a frozen composition. As the angle β increases the nitrous oxide dissociates, denoted by the arrow from the frozen curve to the equilibrium curve. One important observation is that the equilibrium pressure-deflection curve lies inside the frozen curve. This is opposite to what occurs in endothermic dissociation with oxygen or nitrogen (see Sanderson et al., 2003). Figure 7.16b is a pressure deflection curve calculated by varying the interface angle, α, thus fixing the shock angle, β, and the incident inflow Mach number using the detonation-refraction analysis and Eqn. 7.4, respectively.

For $\alpha = 45°$ the post-shock solution is shown to lie on the frozen pressure deflection curve. This is consistent with the images obtained from shots #1916, 1917, and 1921 where immediately behind the dark line corresponding to the transmitted shock there is a light section that ends at the leading edge of the darkly shaded turbulent mixing zone. The transmitted shock ($M_n = 3.9$) has a decomposition reaction time larger

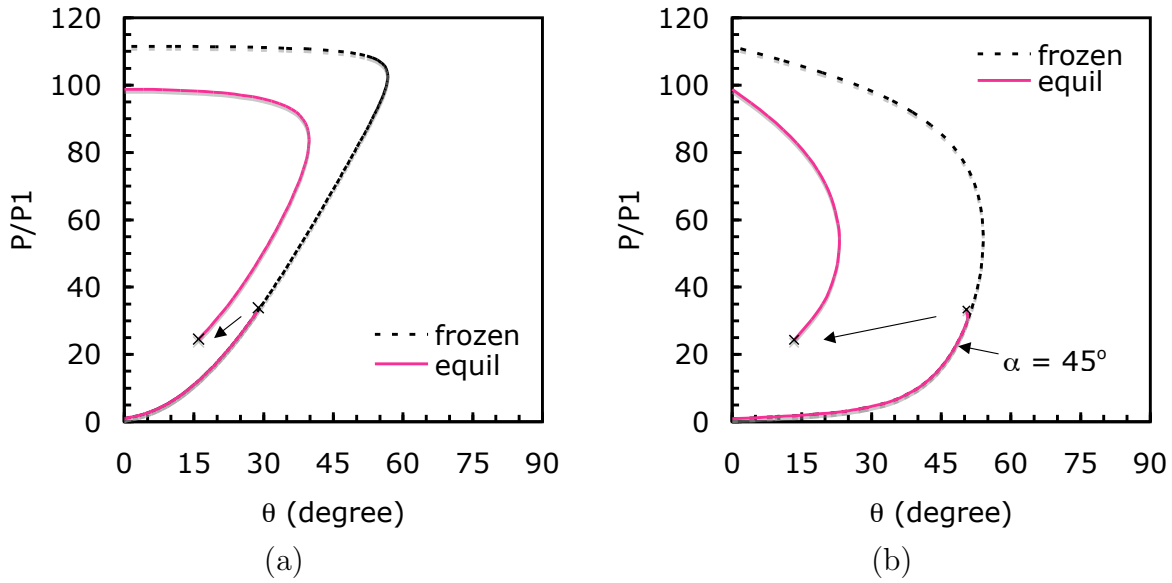

Figure 7.16: Oblique shock normalized pressure P/P_1 as a function of flow deflection angle θ is plotted for nitrous oxide with equilibrium and frozen composition. (a) Varying shock angle, β with $U = V_{CJ}$. (b) Varying shock angle, β, with U obtained by Eqn. 7.4.

than τ_{fr} and is therefore best treated using frozen chemistry. The Mach stem in these images is slightly curved and is measured to move at a mean velocity of $V_{CJ} = 2622$ m/s. At the CJ Mach number the post shock state is most accurately represented using equilibrium chemistry. Experimentally the Mach stems are thick dark lines, possibly indicating the decomposition of nitrous oxide. The exothermicity of the nitrous oxide enhances the Mach effect because it increases the normal component of the post-shock velocity and therefore reduces the maximum flow deflection angle shown in Fig. 7.16a. The CJ detonation velocity of a nitrous oxide decomposition is $V_{CJ} = 1691$ m/s. Thus the Mach stem velocity corresponds to a nitrous oxide detonation that is overdriven by a factor of 1.55.

7.4 Shear layer growth

The turbulent mixing zone visible in sharp interface experiments (for example Fig. 7.3) forms as a result of a mismatch in flow velocity at the post-detonation contact surface

CS'. Understanding the growth, entrainment of fluid, and subsequent mixing is essential in assessing the TMZ impact on the overall flow structure and the extent to which secondary combustion occurs.

A vast amount of research has been carried out in the field of turbulent shear layers as discussed in Sec. 1.4.4.2. In particular, the review articles by Dimotakis (1991) and Dimotakis (2005) are used to guide the following discussion.

The analysis in this section estimates the growth angle of the shear layer and the entrainment that results from both free streams. In order to make use of the existing theories and models it is essential to characterize the key parameters involved in shear layer formation. This is addressed in the following section.

7.4.1 Shear layer classification

Shear layer entrainment and growth is highly dependent on the free stream flow conditions and free stream thermodynamic states. The Reynolds number defined as

$$Re = \frac{\delta_G \Delta U}{\nu} \tag{7.5}$$

and Schmidt number

$$Sc \equiv \frac{\nu}{\mathcal{D}} \tag{7.6}$$

play important roles in classifying the type of mixing and growth that results. δ_G, ΔU, and ν represent the local shear layer thickness, the difference in velocity of the two streams, and the kinematic viscosity, respectively, with $\mathcal{D}$ being the species diffusivity. $Re \approx 10^4$ corresponds to the critical Reynolds number above which a transition to intense molecular mixing occurs in the shear layer (see Konrad, 1976, Koochesfahani and Dimotakis, 1986). The transition to a turbulent mixing layer results in visibly different shear layer behavior. The large fluid smooth vortical structures in low Re mixing layers give way to smaller scale structures (see Koochesfahani and Dimotakis, 1986). The value of Re for the current experimental data was calculated over the length of the shear layer and found to be equal to the transition Re for shear layer

thicknesses, $\delta_G \approx 1 - 2$ mm. Practically, this means that the shear layers are always turbulent and involve intense molecular mixing. Calculations of the Schmidt number yield $Sc \approx 1$ over the range of parameters in the sharp interface experiments. It is convenient to analyze the shear layer in a reference frame convecting with velocity U_c that is in the range

$$U_2 < U_c < U_1 \tag{7.7}$$

where U_1 and U_2 are the velocities of the fast and slow streams, respectively shown in Fig. 7.17. The value of U_c for incompressible flow is determined (Dimotakis, 1991) to be

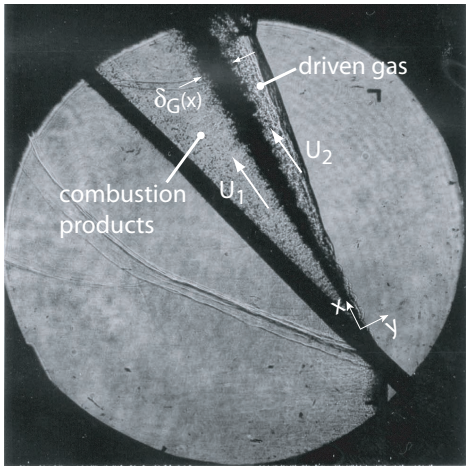

Figure 7.17: A schematic of a turbulent shear layer that forms when fluids with velocities U_1 and U_2 meet at the end of a splitter plate. The size of the shear layer at position x is denoted by the symbol, δ_G.

$$\frac{U_c}{U_1} \approx \frac{1 + r\sqrt{s}}{1 + \sqrt{s}} \tag{7.8}$$

using the continuity and momentum equation under the condition that the pressures on either side of the shear layer are equal. The parameters $r = U_2/U_1$ and $s = \rho_2/\rho_1$ relate the velocity and density of the top and bottom streams. In the current experiments the velocities U_1 and U_2 are obtained using the detonation refraction analysis in Chap. 6. U_1 corresponds to the velocity of the partially oxidized detonation products, and U_2 is the velocity of the shocked test gas. The velocities $\vec{w}_3$, $\vec{w}_4$, and

$\vec{w}_1$ and the contact surface deflection angle δ in the node-fixed reference frame are used to specify

$$U_1 = |\vec{w}_3| - |\vec{w}_1| \cos(\delta - \alpha - \pi), \tag{7.9}$$

$$U_2 = |\vec{w}_4| - |\vec{w}_1| \cos(\delta - \alpha - \pi). \tag{7.10}$$

Figures 7.18a,b show the velocity ratio r and the density ratio s as a function of the the interface angle, α, for the cases studied in the present work. The combustible mixture is ethylene-oxygen, $\Phi = 2.5$ at 15 kPa initial pressure, with results shown for oxygen, nitrogen, and nitrous oxide as the test gases. In both plots the values of r and s decrease with increasing α, eventually reaching a limiting value for $\alpha > 35°$. The values of r and s influence the growth of the shear layer and are discussed below.

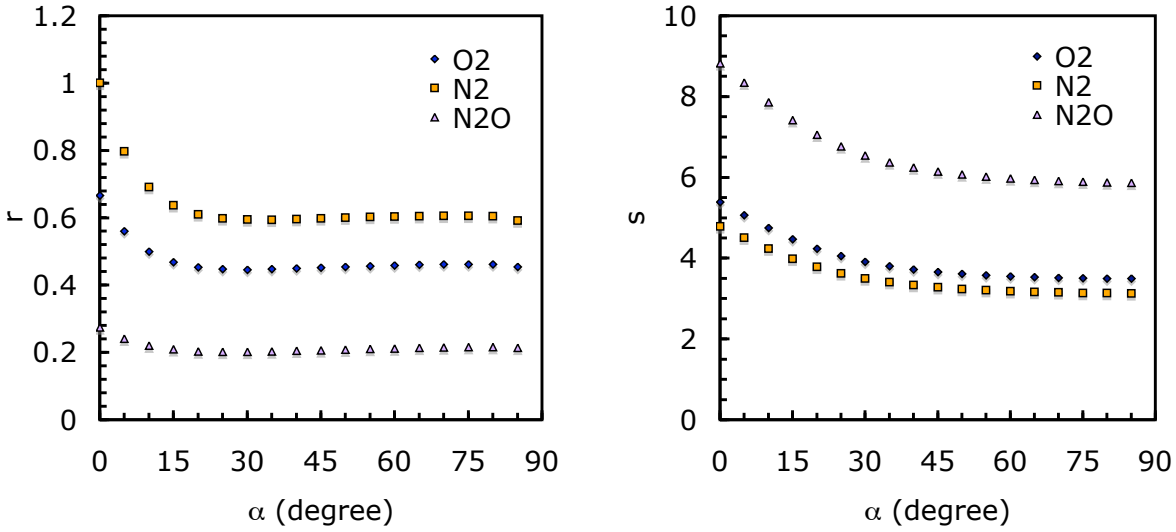

Figure 7.18: Density ratio s (a) and velocity ratio r (b) as a function of interface angle α with oxygen, nitrogen, and nitrous oxide as the test gas. The results are obtained using the detonation refraction analysis.

It is convenient to define convective Mach numbers,

$$M_{c1} = \frac{U_1 - U_c}{c_1},$$

$$M_{c2} = \frac{U_c - U_2}{c_2},$$

to gauge the compressibility of the two streams . Here M_{c1} and M_{c2} correspond to U_1 and U_2, respectively, and c_1 and c_2 are the local sound speeds of each stream. Brown and Roshko (1974) observed that the growth rate of a shear layer decreases with increasing free stream Mach number. The convective Mach numbers M_{c1} and M_{c2} are plotted as a function of interface angle α in Fig. 7.19. The combustible mixture is ethylene-oxygen, $\Phi = 2.5$ at 15 kPa initial pressure, with results shown for oxygen, nitrogen, and nitrous oxide as the test gas. The Mach number M_{c1} in Fig. 7.19a corresponds to the partially oxidized detonation products with the state determined using the detonation refraction analysis in Chap. 6 where oxygen, nitrogen, and nitrous oxide were the test gases. Peak values in the convective Mach number occur at $\alpha \approx 25°$ with values of 0.087, 0.053, and 0.18 for oxygen, nitrogen, and nitrous oxide, respectively. Convective Mach number M_{c2} corresponding to the state of the test gas is plotted as a function of α in Fig. 7.19b. Peak values occur at $\alpha \approx 25°$ of 0.084, 0.05, and 0.18 for oxygen, nitrogen, and nitrous oxide respectively. The influence of compressibility appears to be minimal with the largest convective Mach numbers found in the nitrous oxide mixtures. The convective flow is clearly subsonic in all cases.

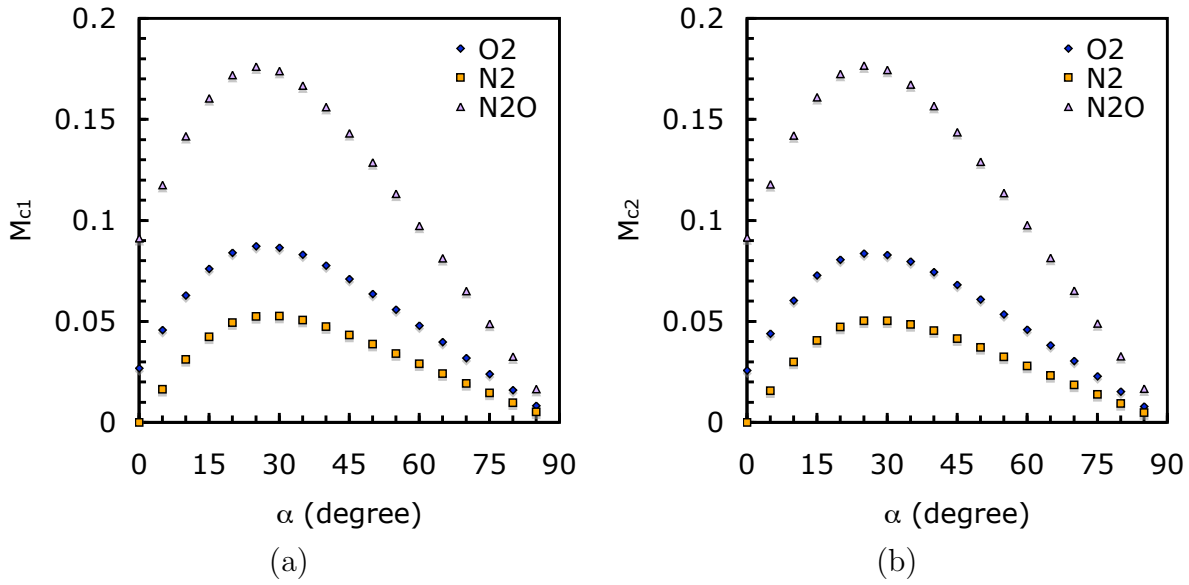

Figure 7.19: Convective Mach numbers (a) M_{c1} and (b) M_{c2} as a function of interface angle α with oxygen, nitrogen, and nitrous oxide as the test gas.

The shear layer thickness, δ_G, scales with the coordinate, x, defined as the downstream distance measured from the point of first contact of the two streams (see Fig. 1.7). The growth rate of the shear layer, δ_G/x, can be expressed (Dimotakis, 1991) as a function of the density ratio and velocity ratio to be

$$\frac{\delta_G}{x}(r,s) \approx C_\delta \frac{(1-r)(1+\sqrt{s})}{2(1+r\sqrt{s})}\left(1-\frac{(1-\sqrt{s})/(1+\sqrt{s})}{1+2.9(1+r)/(1-r)}\right), \tag{7.11}$$

for shear layers where the convective Mach number of both streams, $M_c \approx 0$. The constant C_δ was determined (see Brown and Roshko, 1974) to lie between the values

$$0.25 < C_\delta < 0.45. \tag{7.12}$$

According to Dimotakis (1991), the range in C_δ is attributed to the role that the initial flow conditions play on the shear layer growth. The growth rates computed from Eqn. 7.11 are shown as a function of α in Fig. 7.20a for various test gases. The initial conditions for this figure are the same as those of Figs. 7.18 and 7.19, with constant $C_\delta = 0.35$. The results are shown as an angle measured in degrees to characterize the growth. The angle is obtained by taking the inverse tangent of the growth rate δ_G/x. Except at small interface angles α the growth rate of the shear layer is quite insensitive to changes in interface angle. The growth rate is largest for nitrous oxide with a nominal angle of 19° followed by oxygen and then nitrogen with nominal angles of 9° and 5°, respectively.

The growth rates represented as angles in Fig. 7.20a are corrected for compressibility by the functional relationship

$$\frac{\left.\frac{\delta_G}{x}\right|_{M_{c1}}}{\left.\frac{\delta_G}{x}\right|_{M_{c1}\approx 0}} = (1-f_\infty)e^{-3M_{c1}^2} + f_\infty \tag{7.13}$$

developed by Papamoschou and Roshko (1988). Equation 7.13 relates the ratio of the compressible shear layer with convective Mach number M_{c1} to the growth rate of an equivalent system with $M_{c1} \approx 0$ as a function of M_{c1}. The asymptotic value of

the constant was determined to be $f_\infty = 0.2$. A more recent compressibility scaling parameter

$$\Pi_c = \max_j \left[\frac{\sqrt{\gamma_j - 1}}{a_j} \right] \Delta U \tag{7.14}$$

proposed by Slessor et al. (2000) accounts for kinematic to thermal energy conversion motivated by the conservation of energy equation for a perfect gas. The subsequent results are reported using Eqn. 7.13 with the corrected growth rates of Fig. 7.20a shown in Fig. 7.20b. The role of compressibility has the largest impact on the nitrous oxide system, especially for $\alpha < 50°$. This is to be expected since cases with nitrous oxide resulted in the highest convective Mach numbers over the range of parameters tested.

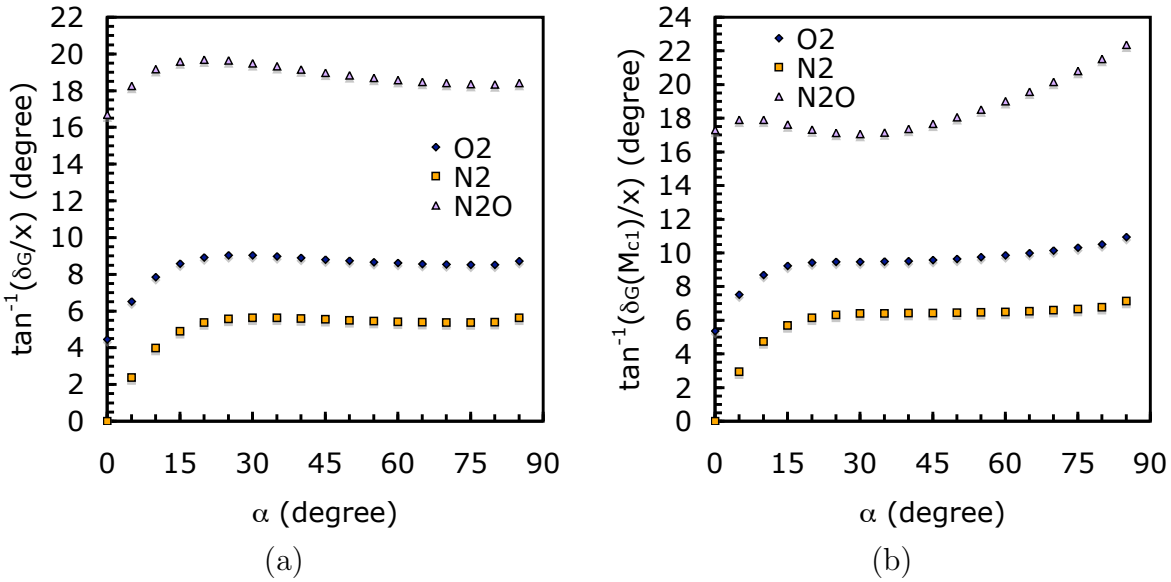

Figure 7.20: Shear layer growth angle (a) and compressibility-corrected growth angle (b) as a function of interface angle α with oxygen, nitrogen, and nitrous oxide as the test gas. The constant $C_\delta = 0.35$ was used for these calculations.

It is now a question of relating the computed values to those measured in the experiments. The difficulty lies in choosing the appropriate value of the coefficient C_δ. The shear layer growth angle, Θ_{exp}, is measured for each experiment and reported in Table 7.2. Each measurement has an uncertainty of one degree. The angle Θ_{gap} is

listed and defined as the angle between the transmitted shock and the leading edge of the TMZ (see Fig. 7.6).

Test gas	Φ	r	s	M_{c1}	M_{c2}	U_c (m/s)	Θ_{model}	Θ_{exp}	E_v	C_δ
O_2	2.5	0.45	3.67	0.13	0.04	183.3	6.6	5.3	2.3	0.28
N_2	2.5	0.60	3.28	0.08	0.02	178.9	4.7	6.0	2.1	0.45
N_2O	2.5	0.21	6.15	0.36	0.06	161.4	9.3	5.0	3.0	0.19
O_2	1.0	0.50	3.40	0.11	0.03	166.7	5.9	4.7	2.2	0.28
N_2	1.0	0.66	3.04	0.06	0.02	163.1	3.8		2.0	
N_2O	1.0	0.23	5.65	0.32	0.06	147.1	9.0	6.9	2.9	0.27

Table 7.5: Table comparing the calculated and experimentally averaged growth angles, Θ_{model} and Θ_{exp}, for ethylene-oxygen mixtures, with equivalence ratio, Φ, and oxygen, nitrogen, or nitrous oxide as the test gas. The convective Mach numbers, velocity ratio, density ratio, and entrainment ratio, E_v, are listed.

The experimentally measured growth angle Θ_{exp} is plotted as a function of density ratio s in Fig. 7.21 with data corresponding to the experiments listed in Table 7.2. For comparison the predicted growth rate angle is shown by the solid line with $C_\delta = 0.35$. Upper and lower bounds of the calculation are included in the figure to illustrate the range of values possible by varying C_δ from 0.25 (lower curve) to 0.45 (upper curve). The experiment and theory are consistent for low density ratios where either nitrogen or oxygen was used as the test gas. The experimental results for large density ratio are lower than the predicted growth angle.

The dependence of C_δ on initial conditions adds complexity when trying to estimate the growth rate. Slessor et al. (2000, Appendix) developed a methodology to calculate C_δ using the ratio of the experimental growth rate to the compressibility-corrected growth rate normalized by the unknown coefficient C_δ with results shown in Table 7.5. As shown, C_δ ranges over the previously observed values $0.25 < C_\delta < 0.45$ depending on the initial conditions.

The volumetric entrainment ratio E_v relates the entrainment of high-speed fluid to the low-speed fluid. Konrad (1976) observed that the two streams do not contribute equally to the shear layer, and a model was proposed by Dimotakis (1986) for the entrainment ratio,

$$E_v = \frac{U_1 - U_c}{U_c - U_2}\left(1 + C_l \frac{1-r}{1+r}\right). \tag{7.15}$$

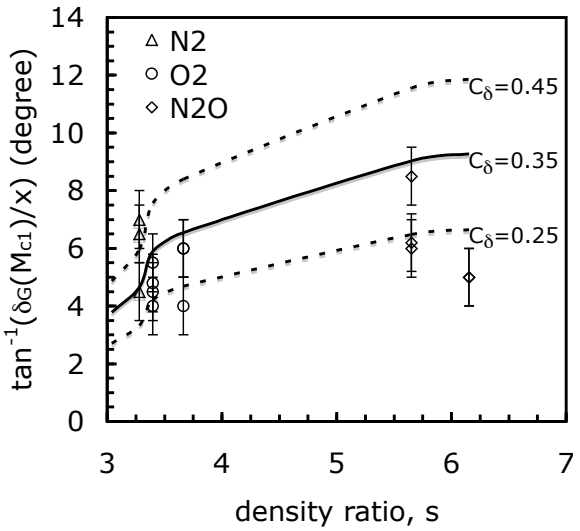

Figure 7.21: The experimental and calculated (Eqn. 7.11) growth angle plotted as a function of density ratio.

The value of coefficient C_l is approximately equal to 0.68. Table 7.5 gives the entrainment ratio values computed using Eqn. 7.15 and corrected for compressibility (see Hall and Dimotakis, 1987) over the range of initial conditions that are important when considering combustion and subsequent energy release in the shear layer. The entrainment ratio of the partially oxidized detonation products and test gas in the shear layer is around 2-2.5.

The Damköhler number

$$Da \equiv \frac{\tau_m}{\tau_i} \tag{7.16}$$

is the ratio of the mixing time scale τ_m to the chemical time scale τ_i. The chemical reaction time scale, calculated using the homogeneous mixing ignition time (see Sec. 5.3.2), is on the order of 1 μs for partially oxidized combustion products mixed with oxygen or nitrous oxide. The calculations are carried out with $\alpha = 45°$, which is consistent with the experiments. τ_m is estimated using the ratio of the downstream distance x, and the convective entrainment velocity $U_c - U_2$. The mixing time is on the order of 1 ms using the half height of the GDT as a value for x which results in $Da \approx 1000$. The high Damköhler number for the conditions in the experiments indicates that the chemical reaction rate is much faster than the mixing rate meaning

that the "fast" chemistry limit is relevant in all cases. This means that as soon as fluid from the two streams are molecularly mixed, the chemical reactions proceed to form products determined by the local equivalence ratio. The limit of fast chemistry results in $\delta_p < \delta_m$, where δ_p is the thickness of the region where chemical reactions have reached completion. Since δ_p depends on the local equivalence ratio, a function of position in the shear layer, the total region where chemical reactions have reached completion will always be less than δ_m. For gas phase flows (see Dimotakis, 1991) with $Re > 10^4$, results in the ratio

$$\frac{\delta_m}{\delta_G} = 0.49. \tag{7.17}$$

The ramification of Eqn. 7.17 is that only half of the visible turbulent shear layer is mixed on a molecular level which can then react to form products based on the local mixture composition.

7.5 Summary

Detonation refraction experiments were carried out that used a nitro-cellulose membrane to separate an ethylene-oxygen mixture from either oxygen, nitrogen, or nitrous oxide. The experimentally measured wave angles were found to agree with the detonation refraction analysis (Chap. 6) predictions. The choice of combustible mixture allowed for secondary combustion to occur in the TMZ. Mixture equivalence ratios of 1 and 2.5 were tested and determined to have minimal impact on the wave features observed.

A Mach stem formed in all experiments because the transmitted oblique shocked fluid could not be deflected back tangent to the wall with a reflected shock wave. The enhanced Mach stem when nitrous oxide was used as the test gas is attributed to the exothermic decomposition that occurs behind the normal shock that is visible in the experimental images as a thick dark Mach stem compared to cases with oxygen and nitrogen. Both oxygen and nitrogen are endothermic, and within the time scales of

this analysis the composition of the test gas remains frozen.

Analysis of the shear layer growth, mixing, and ignition process revealed that the combustion rate is limited by the rate of molecular mixing. In addition, the thickness of the mixing region is estimated to be only half the visible thickness of the turbulent shear layer. The effect of chemical reactions inside the shear layer has been shown by Hermanson and Dimotakis (1989) to decrease the growth rate and consequently, the volumetric entrainment, linearly as a function of the heat release. This is because the expansion due to the heat release reduces the entrainment requirements of the shear layer. Experiments with different equivalence ratios (see Table 7.2) were carried out, and it was found that the shear layer growth angle decreases when nitrous oxide is used as the test gas while the growth angle does not change for oxygen as the test gas. Hermanson and Dimotakis has also shown that exothermic reactions result in a change in the sign of displacement thickness of the shear layer from negative (non-reactive) to positive (reactive). It is the change in sign of displacement thickness that could possibly result in the small increase in impulse determined experimentally in Sec. 5.3.

Chapter 8

Conclusion

8.1 Summary

The experiments carried out in this study addressed detonation propagation through sharp and diffuse interfaces. In addition, the fuel-rich ethylene-oxygen combustible mixture and oxidizing test gas enabled combustion inside the turbulent mixing zone to be observed and quantified.

The experiments are the first to visualize a detonation with velocity normal to the diffuse composition gradient vector, with secondary combustion occurring in the TMZ. Diffuse interfaces were composed of an equivalence ratio composition gradient or inert diluent composition gradient and resulted in curved detonation waves (see Fig. 8.1a). The top portion of the curved detonation in Fig. 8.1a corresponds to the local mixture composition with the maximum CJ detonation velocity. For most hydrocarbon mixtures the maximum detonation velocity occurs between equivalence ratios of 2 and 3.

The main implication of the mixture composition gradient was to cause the detonation wave to curve: eventually the reaction zone decouples from the leading shock wave for a sufficiently oblique wave. The wave curvature is attributed to the decrease in lead shock velocity resulting in lower post-shock temperatures. The reaction zone decoupling results when the post-shock induction time becomes too large. Experiments show that the decoupling of the detonation wave results in a gap forming between the transmitted shock and the turbulent mixing zone. The mixture compo-

sition along the height of the test section was modeled with an error function with parameters determined from the gravity current experiments in Chap. 3.

The diffuse interface was made with a gravity current. The formation and propagation of the gravity current was examined in the test section using acetone PLIF and in a half scale water channel to understand the early time development of the GC. The thickness of the diffuse interface was estimated from the thickness of the region of vorticity from the water channel data and then rescaled for the gas phase experiments.

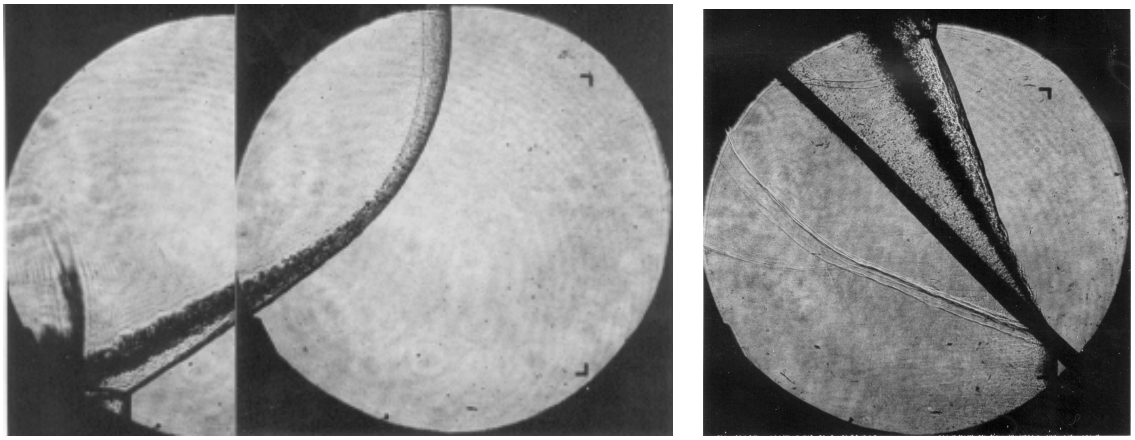

(a) (b)

Figure 8.1: Detonation propagation through a diffuse interface (a) and a sharp interface (b) corresponding to Exp. #1878-79 and 1922, respectively.

Sharp interfaces were made using a nitro-cellulose membrane to separate the combustible mixture from the test gas. The membrane was mounted on a wood frame and inserted at a 45 degree angle with respect to the detonation velocity vector.

Schlieren images of the detonation-refraction process (see Fig. 8.1b) were obtained. The detonation-refraction process indicated that the detonation decoupling was abrupt at the node. A transmitted shock wave and shear layer formed with wave angles in agreement with the detonation refraction theory presented in Chap. 6. Although previous experiments have been carried out with combustible-combustible interfaces, these are the first experiments to examine combustible-oxidizer interfaces and the possibility of reaction in the TMZ.

A Mach stem is formed when the transmitted shock wave reflects on the top wall and is a result of the inability of a single reflected shock wave to deflect the flow back parallel to the solid boundary. All the experimental configurations studied were predicted and observed (see Tab. B.3) to form Mach stems. When nitrous oxide was used as the test gas, exothermic decomposition was observed as a dark region on the schlieren image behind the Mach stem. When oxygen or nitrogen were used as the test gas, significant dissociation was not observed in agreement with estimates based on both the chemical equilibrium and detailed reaction kinetics.

The growth and entrainment of the turbulent shear layer was measured and compared with theory. Although the axial flow in the experiment is highly supersonic ($M \approx 5-6$), the convective Mach numbers in the reference frame of the shear layer were less than or equal to 0.18. Under those conditions the shear layer has been previously shown to be molecularly mixed in a region the size of half the visible thickness ($\delta_m/\delta_G = 0.49$).

Secondary combustion in the turbulent shear layer was investigated in both the diffuse and sharp interface studies. The measured impulse over a fixed time interval was used as a figure of merit to quantify the degree to which chemical reactions took place. Comparison was made between otherwise identical experiments with the sole difference being the choice of test gas. The impulse difference was between 2 and 6%, which provided new evidence that quantified the amount of secondary combustion in the TMZ.

A model was developed that estimated the volume expansion of a fluid element in the TMZ and the increase in impulse that resulted as a consequence. The impulse was then computed and compared to the impulse behind a shock wave with no energy addition. This estimate was based on the growth in thickness of the molecularly mixed shear layer and was found to be in reasonable agreement with the observed variation in impulse.

8.2 Future work

There are a wide range of experiments that can be carried out to further understand the detonation refraction phenomena. Experimental setup modifications (see Sec. 7.1.1) for sharp interfaces could remove the wood frame reducing flow obstructions and allowing a full view of the interface. It is also of interest to look at mixture ignition in the shear layer by replacing the oxidizing test gas by an insensitive combustible mixture.

Much work was done to understand the development of the gravity current. Future work capable of precisely measuring the mixture composition across the gravity current interface would allow more quantitative comparison of the detonation wave curvature and reaction zone decoupling from the shock wave.

Bibliography

R. Akbar. *Mach Reflection of Gaseous Detonations*. PhD thesis, California Institute of Technology, Pasadena, California, August 1997. 16, 23

T.D. Aslam and J.B. Bdzil. Numerical and theoretical investigations on detonation-inert confinement interactions. In *12th International symposium on detonation*, San Diego, CA, 2002. Office of Naval Research. 8

Joanna Austin. *The Role of Instability in Gaseous Detonation*. PhD thesis, California Institute of Technology, Pasadena, California, June 2003. 16, 22, 23, 24, 94

T.B. Benjamin. Gravity currents and related phenomena. *J. Fluid Mech.*, 31:209–248, 1968. 28, 30

D. Bjerketvedt, O.K. Sonju, and I.O. Moen. *The influence of experimental condition on the re-initiation of detonation across an inert region*, volume 106 of *In: Dynamics of explosions*. AIAA Inc., New York, NY, 1986. 7, 42

R.E. Britter and J.E. Simpson. Experiments on the dynamics of a gravity current head. *J. Fluid. Mech*, 88:223–240, 1978. 4, 33

M. Brouillette. The richtmyer-meshkov instability. *Annu. Rev. Fluid Mech.*, 34:445–468, 2002. 4, 5, 11, 103

G.L. Brown and A. Roshko. On density effects and large structure in turbulent mixing layers. *J. Fluid Mech.*, 64(4):775–816, 1974. 124, 125

S. Browne. Personal communication, 2005. 9

W.H. Calhoon and N. Sinha. Detonation wave propagation in concentration gradients. In *43rd AIAA Aerospace Sciences Meeting and Exhibit*, 2005. 8, 42, 43

D.L. Chapman. On the rate of explosions in gases. *Phil. Mag. 47*, 5th series, No. 284: 90–104, 1899. 9

H.F. Coward and G.W. Jones. Limits of flammability of gases and vapors. Technical report, Bulletin 503, Bureau of Mines, 1952. 43

E.K. Dabora, D. Desbores, C. Guerraud, and H.G. Wagner. Oblique detonations at hypersonic velocities. *Progg. Aero. Astro.*, 133:187–204, 1991. 8, 102

E.K. Dabora, J.A. Nicholls, and R.B. Morrison. The influence of a compressible boundary on the propagation of gaseous detonations. *Tenth Symposium on Combustion*, pages 817–830, 1965. 8, 87, 95

Yu.N. Denisov and Ya.K. Troshin. Pulsating and spinning detonation of gaseous mixtures in tubes. *Dokl. Akad. Nauk.*, 125:110–113, 1959. 10

P.E. Dimotakis. Two-dimensional shear-layer entrainment. *AIAA Journal*, 24(11): 1791–1796, 1986. 127

P.E. Dimotakis. *Turbulent Free Shear Layer Mixing and Combustion*, chapter 5, pages 265–340. American Institute of Aeronautics and Astronautics, Inc., 1991. v, 5, 12, 13, 84, 121, 122, 125, 129

P.E. Dimotakis. Turbulent mixing. *Annu. Rev. Fluid Mech.*, 37:329–356, 2005. 12, 13, 121

W. Döring. über den detonationsvorgang in gasen. *Analen der Physik*, Band 43: 421–436, 1943. 9

W. Fickett and W.C. Davis. *Detonation*. University of California Press, 1979. 9, 98

D. Goodwin. Cantera object-oriented software for reacting flows. Technical report, California Institute of Technology, 2005. URL `www.cantera.org`. 9, 56, 79, 91, 116

L.G. Gvozdeva. Refraction of detonation waves incident on boundary between 2 gas mixtures. *Soviet Physics-Technical Physics*, 6(6):527–533, 1961. 8, 102

J.L. Hall and P.E. Dimotakis. A simple model for finite chemical kinetics analysis of supersonic turbulent shear layer combustion. In *AIAA/SAE/ASME/ASEE 23rd Joint Propulsion Meeting*, 1987. 128

C. Hartel, F. Carlsson, and M. Thunblom. Analysis and direct numerical simulation of the flow at a gravity-current head. part 2. the lobe-and-cleft instability. *Journal of Fluid Mechanics*, 418:213–229, 2000. 29

L.F. Henderson. On the refraction of shock waves. *J. Fluid. Mech.*, 198:365–386, 1989. v, 5, 8, 86, 87

J.C. Hermanson and P.E. Dimotakis. Effects of heat release in a turbulent, reacting shear layer. *J. Fluid Mech.*, 199:333–375, 1989. 108, 130

H.G. Hornung. Regular and mach reflection of shock waves. *Ann. Rev. Fluid Mech.*, 18:33–58, 1986. 111, 114

H.G. Hornung, H. Oertel, and R.J. Sandeman. Transition to mach reflexion of shock waves in steady and pseudosteady flow with and without relaxation. *J. Fluid Mech.*, 90(3):541–560, 1979. 115

H. Huang, D. Dabiri, and M. Gharib. On errors of digital particle image velocimetry. *Meas. Sci. Technol.*, 8:1427–1440, 1997. 32

Patrick Hung. *Algorithms for Reaction Mechanism Reduction and Numerical Simulation of Detonations Initiated by Projectiles*. PhD thesis, California Institute of Technology, Pasadena, California, 2003. 51

K. Ishii and M. Kojima. Propagation of detonations in mixtures with concentration gradients. In G. Roy, S. Frolov, and J. Shepherd, editors, *Application of detonation to propulsion*, 2004. 8, 42

E. Jouguet. Sur la propagation des reactions chimiques dans les gaz. *J. Mathematique*, page 347, 1905. 9

M. Kaneshige, E. Schultz, U.J. Pfahl, J.E. Shepherd, and R. Akbar. Detonations in mixtures containing nitrous oxide. In *22 nd (Int.) Symposium on Shock Waves*, 1999. URL www.galcit.caltech.edu/~EDL/publications.html. 116

M.J. Kaneshige. *Gaseous detonation initiation and stabilization by hypervelocity projectiles*. PhD thesis, California Institute of Technology, Pasadena, California, January 1999. 51, 52

G.H. Keulegan. An experimental study of the motion of saline water locks into fresh water channels. Technical Report Rep. 5168, US Nat'l Bur. Stand., 1957. 39

J.H. Konrad. *An experimental investigation of mixing in two-dimensional turbulent shear flows with applications to diffusion-limited chemical reactions*. PhD thesis, California Institute of Technology, 1976. 121, 127

M.M. Koochesfahani and P.E. Dimotakis. Mixing and chemical reactions in a turbulent liquid mixing layer. *J. Fluid Mech.*, 170:83–112, 1986. 121

Sanjay Kumar. *An experimental investigation of Richtmyer-Meshkov instability*. PhD thesis, California Institute of Technology, 2002. 19, 105

K.K. Kuo. *Principles of Combustion*. Wiley & Sons, New York, 1986. 9

M.S. Kuznetsov, S.B. Dorofeev, A.A Efimenko, V.I. Alekseev, and W. Breitung. Experimental and numerical studies on transmission of gaseous detonation to a less sensitive mixture. *Shock Waves*, 7:297–304, 1997. 7, 42, 49

J.H.S. Lee. Dynamic parameters of gaseous detonations. *Annual Review of Fluid Mechanics*, 16:311–336, 1984. 10

H. Liepmann and A. Roshko. *Elements of Gasdynamics*. Dover, 2001. 5, 82, 111

B.J. McBride, S. Gordon, and M.A. Reno. Thermodynamic data for fifty reference elements. Technical paper 3287, NASA, 1993. 79

D. Papamoschou and A. Roshko. The compressible turbulent shear layer: an experimental study. *J. Fluid Mech*, 197:453–477, 1988. 125

F. Pintgen and J.E. Shepherd. Secondary pressure waves from rich fireballs. In *20th International Colloquium on the Dynamics of Explosions and Reactive Systems*, Montreal, Canada, 2005. ICDERS. 2, 5

P.B. Puranik, J.G. Oakley, M.H. Anderson, and R. Bonazza. Experimental study of the richtmyer-meshkov instability induced by a mach 3 shock wave. *Shock Waves*, 13:413–429, 2004. 4

M.I. Radulescu and J.H.S. Lee. The failure mechanism of gaseous detonations: Experiments in porous wall tubes. *Combustion and Flame*, 131(1-2):29–46, 2002. 43

W.C. Reynolds. The element potential method for chemical equilibrium analysis: Implementation in the interactive program STANJAN, version 3. Technical report, Dept. of Mechanical Engineering, Stanford, CA, 1986. 6, 115

R. Samtaney and D.I. Pullin. Self-similar hypervelocity shock interactions with oblique contact discontinuities. *Shock Waves*, 8:299–310, 1998. 8, 87

S.R. Sanderson, H.G. Hornung, and B. Sturtevant. Aspects of planar, oblique and interacting shock waves in an ideal dissociating gas. *Physics of Fluids*, 15(6):1638–1649, 2003. 8, 87, 119

K.I. Shchelkin and Y.K. Troshin. *Gasdynamics of Detonations*. Mono Book Corp., Baltimore, 1965. 10

J.E. Simpson. *Gravity currents: in the environment and the laboratory*. John Wiley and sons Inc, 1987. 28, 33

M.D. Slessor, M. Zhuang, and P.E. Dimotakis. Turbulent shear-layer mixing: growth-rate compressibility scaling. *J. Fluid. Mech*, 414:35–45, 2000. 126, 127

G.P. Smith, D.M. Golden, M. Frenklach, N.W. Moriarty, B. Eiteneer, M. Goldenberg, C.T. Bowman, R.K. Hanson, S. Song, W.C. Gardiner, V.V. Lissianski, and Z. Qin. GRI-Mech 3.0. http://www.me.berkeley.edu/gri_mech, 2004. 79, 116

V. Tanguay and A.J. Higgins. The channel effect: Coupling of the detonation and the precursor shock wave by precompression of the explosive. *Journal of Applied Physics*, 96(9):4894–4902, 2004. 95

G. Taylor. The instability of liquid surfaces when accelerated in a direction perpendicular to their planes. In *Proc. of the Royal Society of London, A201*, pages 192–197, 1949. 11

G.O. Thomas, P. Sutton, and D.H. Edwards. The behaviour of detonation-waves at concentration gradients. *Combustion and Flame*, 84(3-4):312–322, 1991. 7, 42

P.A. Thompson. *Compressible-Fluid Dynamics*. Advanced engineering series, 1988. 5, 56, 93, 94, 98, 99

Mark C. Thurber. *Acetone laser-induced fluorescence for temperature and multiparameter imaging in gaseous flows*. PhD thesis, Department of Mechanical Engineering, Stanford University, 1999. 37

M.C. Thurber and R.K. Hanson. Pressure and composition dependences of acetone laser-induced fluorescence with excitation at 248, 266, and 308 nm. *Appl. Phys. B*, 69:229–240, 1999. 37

N. A. Tonello and M. Sichel. Mechanisms of detonation transmission in layered h_2-o_2 mixtures. In *Proc. of the 14th Int. Coll. on the Dynamics of Explosions and Reactive Systems (ICDERS)*, Coimbra, Portugal, August 1993. 8, 102

A. Veser, W. Breitung, and S.B. Dorofeev. Run-up distances to supersonic flames in obstacle laden tubes. *Journal de Physique, IV France, Proceedings*, 12(7):333–340, 2002. 16

M. Vetter and B. Sturtevant. Experiments on the richtmyer-meshkov instability of an air/sf6 interface. *Shock Waves*, 4(5):247–252, 1995. 84

J. von Neumann. Progress report on theory of detonation waves. Technical report, Office of Scientific Research and Development, OSDR Rep. No. 549, Proj. Rep. No. 238, 1942. 9

D.R. White. Turbulent structure of gaseous detonations. *The Physics of Fluids*, 4/4: 465–480, 1961. 10

C.E. Willert and M. Gharib. Digital particle image velocimetry. *Experiments in Fluids*, 10(4):181–193, 1991. 32

M. Wolf, D.H. Lieberman, and J.E. Shepherd. Characterization of gravity currents in a water channel for use in detonation refraction experiments. Fm2005-006, Graduate Aeronautical Laboratories, California Institute of Technology, 2005. 29

Y.B. Zel'dovich. On the theory of the propagation of detonation in gaseous systems. NACA TM, No. 1261, ursprgl. JETP10 (1940), 1950. 9

D. Zwillinger, editor. *Standard Mathematical Tables and Formulae*. CRC-Press, 1996. 100

Appendix A

Position Versus Time Plots

Position versus time plots comparing the transmitted shock wave time of arrival with the one-dimensional idealized theory. See section 5.1.

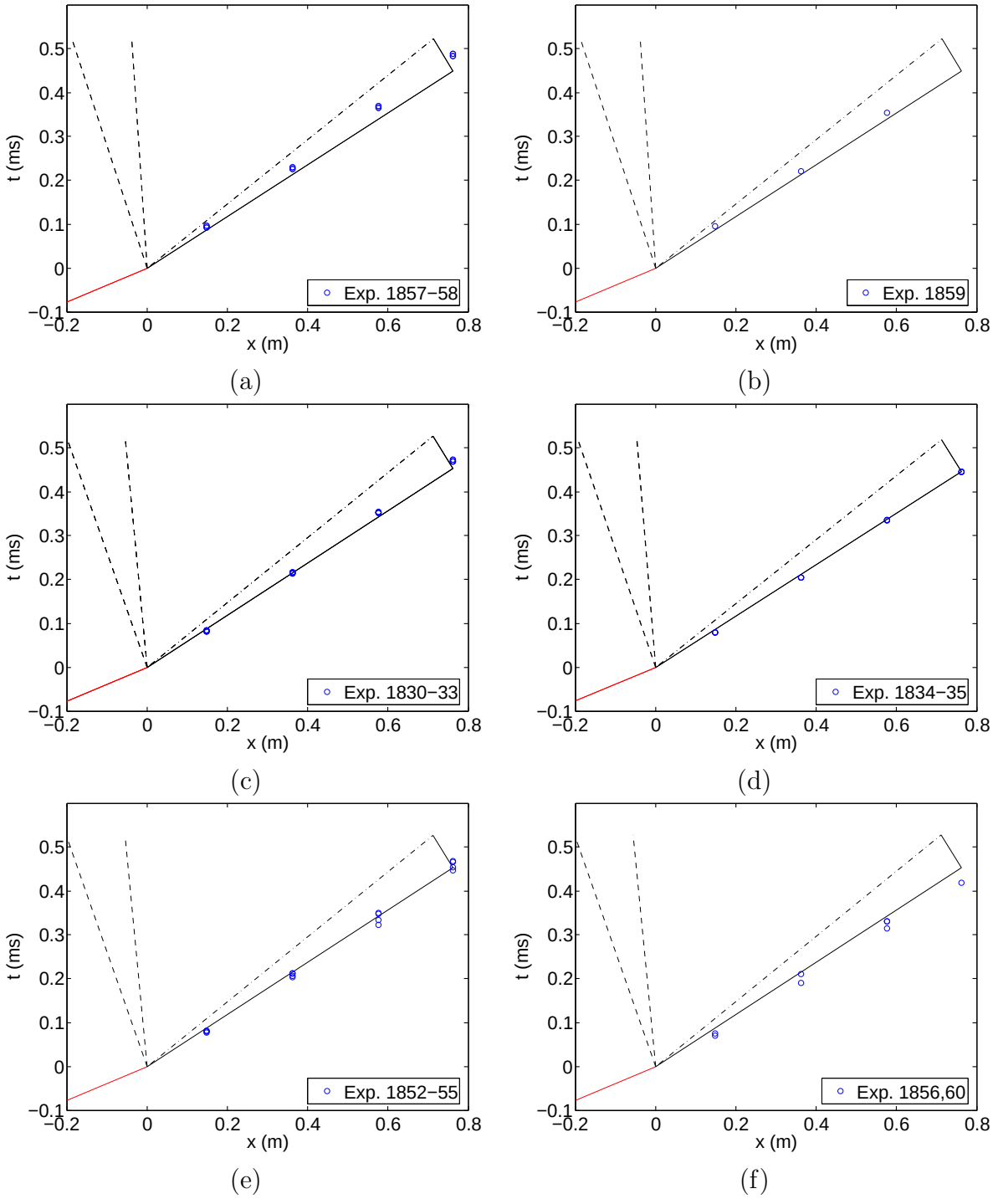

Figure A.1: A time vs. position plot comparing the experimental data with one dimensional shock transmission theory. The valve gate delay is zero. (a) $2C_2H_4$+$3O_2$, O_2 test gas, (b) $2C_2H_4$+$3O_2$, N_2 test gas, (c) $2.5C_2H_4$+$3O_2$, O_2 test gas, (d) $2.5C_2H_4$+$3O_2$, N_2 test gas, (e) $3C_2H_4$+$3O_2$, O_2 test gas, (f) $3C_2H_4$+$3O_2$, N_2 test gas.

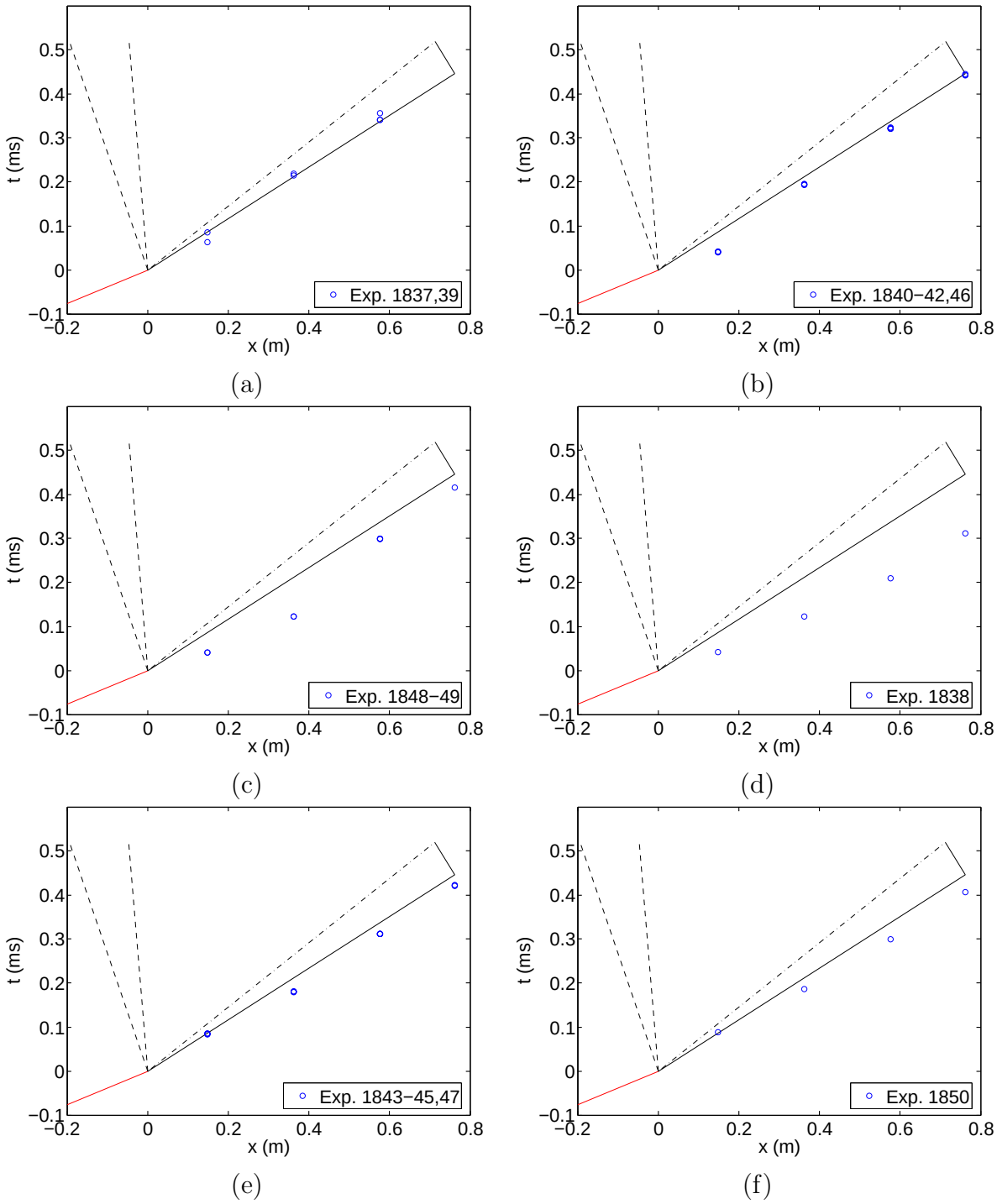

Figure A.2: A time vs. position plot comparing the experimental data with one dimensional shock transmission theory. The mixture in the GDT is $2.5C_2H_4+3O_2$ and in the test section (a) O_2 test gas, 1 s gate delay, (b) O_2 test gas, 3 s gate delay, (c) O_2 test gas, 5 s gate delay, (d) O_2 test gas, 10 s gate delay, (e) N_2 test gas, 3 s gate delay, (f) N_2 test gas, 5 s gate delay.

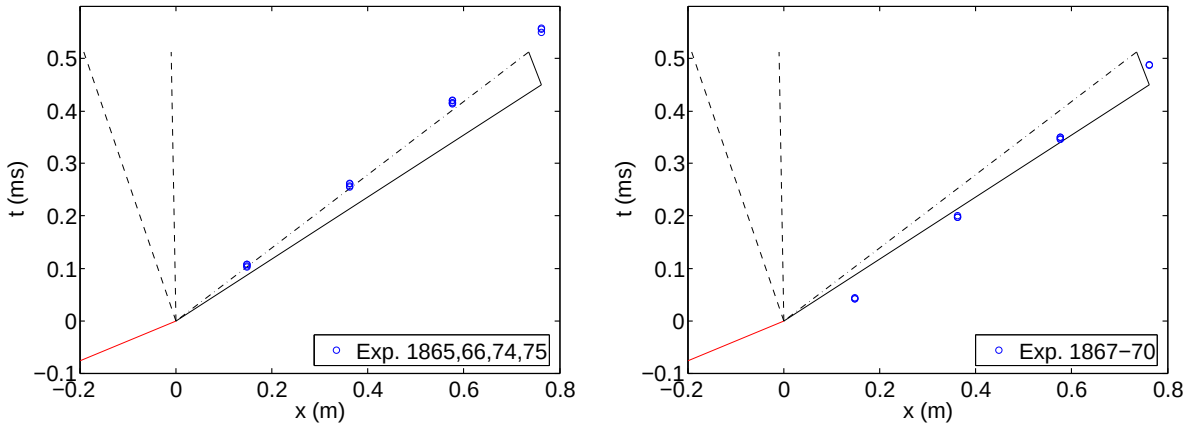

(a) (b)

Figure A.3: A time vs. position plot comparing the experimental data with one dimensional shock transmission theory. The mixture in the GDT is $2.5C_2H_4+3O_2$ and in the test section (a) N_2O test gas, 0 s gate delay, (b) N_2O test gas, 1 s gate delay.

Appendix B

Experiment Shot List

Table B.1: A list of the soot foil experiments used to characterize the cell size of the combustible mixture.

Table B.1:

Shot #	**P (kPa)**	**Mixture**	Φ
1770	5	H_2-O_2	1
1771	10	H_2-O_2	1
1772	10	H_2-O_2	2
1773	10	H_2-O_2	3
1774	10	C_2H_2-O_2	1
1775	10	C_2H_2-O_2	2
1776	10	C_2H_2-O_2	3
1777	10	C_2H_2-O_2	2.5
1778	15	C_2H_2-O_2	2.5
1779	15	C_2H_2-O_2	3
1780	15	C_2H_2-O_2	3
1781	15	C_2H_2-O_2	3.5
1782	15	C_2H_2-O_2	3.5
1783	15	C_2H_2-O_2	4

Table B.2: A list of the mylar diaphragm and deflagration to detonation transition (DDT) experiments. Ethylene-oxygen mixtures at equivalence ratio Φ were used as the combustible mixture. All visualizations from shot #1784 to 1797 have the window in the port 2 configuration with Δt_{img} being zero at pressure transducer P6. The DDT tested the initiation of the ethylene-oxygen mixtures using a set of obstacles. The initial pressure for all experiments is 15 kPa.

Table B.2:

Shot #	Φ	**Test gas**	Δt_{img} (μs)	**Series**
1784	2.5		0	detonation
1785	2.5		0	detonation
1786	2.5	O2	8	mylar
1787	2.5	O2	8	mylar
1788	2.5	O2	8	mylar
1789	2.5	O2	8	mylar
1790	2.5	O2	18	mylar
1791	2.5	O2	28	mylar
1792	2.5	O2	38	mylar
1793	2.5	O2	48	mylar
1794	2.5	O2	58	mylar
1795	2.5	O2	58	mylar
1796	2.5	O2	68	mylar
1797	2.5	O2	300	mylar
1798	2.5			DDT
1799	2.5			DDT
1800	3			DDT
1801	3			DDT
1802	3			DDT
1803	3			DDT

Continued on next page

Table B.2 – continued from previous page

Shot #	Φ	**Test gas**	Δt_{img} (μs)	**Series**
1804	3			DDT
1805	3.5			DDT
1806	3.25			DDT
1807	3			DDT

Table B.3: A list of the sliding valve experiments in the galcit detonation tube (GDT). Ethylene-oxygen mixtures at equivalence ratio Φ were used as the combustible mixture. All visualizations from shot #1788 to 1875 have the window in the port 2 configuration with Δt_{img} being zero at pressure transducer P6. All visualizations from shot #1876 onward have the window in the port 1 configuration with Δt_{img} being zero at pressure transducer P4. The initial pressure for all experiments is 15 kPa.

Table B.3:

Shot #	Φ	**Test gas**	**Delay (s)**	Δt_{img} (μs)	**Series**	**Notes**
1815	2.5	O_2	0	18	diffuse	
1823	2.5	O_2	0	0	diffuse	
1824	2.5	O_2	0		diffuse	no img
1825	2.5	O_2	0	10	diffuse	
1826	2.5	O_2	0	10	diffuse	
1827	2.5	O_2	0	9	diffuse	
1828	2.5	O_2	0	58	diffuse	
1829	2.5	O_2	0	56	diffuse	
1830	2.5	O_2	0	55	diffuse	
1831	2.5	O_2	0		diffuse	no img
1832	2.5	O_2	0	272	diffuse	
1833	2.5	O_2	0	57	diffuse	
1834	2.5	N_2	0	79	diffuse	
1835	2.5	N_2	0	58	diffuse	
1836	2.5	O_2	0	58	diffuse	see shotlist
1837	2.5	O_2	1		diffuse	no img
1838	2.5	O_2	10	203	diffuse	
1839	2.5	O_2	1	73	diffuse	
1840	2.5	O_2	3		diffuse	no img

Continued on next page

Table B.3 – continued from previous page

Shot #	Φ	Test gas	Delay (s)	Δt_{img} (μs)	Series	Notes
1841	2.5	O_2	3		diffuse	no img
1842	2.5	O_2	3	59	diffuse	
1843	2.5	N_2	3		diffuse	no img
1844	2.5	N_2	3		diffuse	no img
1845	2.5	N_2	3		diffuse	no img
1846	2.5	O_2	3	49	diffuse	
1847	2.5	N_2	3	57	diffuse	
1848	2.5	O_2	5		diffuse	no img
1849	2.5	O_2	5	48	diffuse	slow valve
1850	2.5	N_2	5	32	diffuse	slow valve
1851	3	O_2	3		diffuse	no img
1852	3	O_2	0	12	diffuse	
1853	3	O_2	0		diffuse	no img
1854	3	O_2	0	56	diffuse	
1855	3	O_2	0	74	diffuse	
1856	3	N_2	0	94	diffuse	
1857	2	O_2	0	24	diffuse	
1858	2	O_2	0	39	diffuse	
1859	2	N_2	0	52	diffuse	
1860	3	N_2	0	70	diffuse	
1861	3	O_2	3	37	diffuse	
1862	3	N_2	3	33	diffuse	
1863	2	O_2	3	17	diffuse	
1864	2	N_2	3	28	diffuse	
1865	2.5	N_2O	0	-2	diffuse	
1866	2.5	N_2O	0	47	diffuse	

Continued on next page

Table B.3 – continued from previous page

Shot #	Φ	Test gas	Delay (s)	Δt_{img} (μs)	Series	Notes
1867	2.5	N_2O	1	114	diffuse	dark img
1868	2.5	N_2O	1	49	diffuse	dark img
1869	2.5	N_2O	1		diffuse	no img
1870	2.5	N_2O	1	48	diffuse	
1871	2.5	N_2O	1	26	diffuse	
1872	2.5	N_2O	1	5	diffuse	
1873	2.5	N_2O	1	-16	diffuse	
1874	2.5	N_2O	0	61	diffuse	
1875	2.5	N_2O	0	20	diffuse	
1876	2.5	O_2	0	-25	diffuse	
1877	2.5	O_2	0	34	diffuse	
1878	2.5	O_2	3	-3	diffuse	
1879	2.5	O_2	3	28	diffuse	
1880	2.5	O_2	8	-1	diffuse	no img
1881	2.5	O_2	6	-1	diffuse	no img
1882	2.5	O_2	8	-3	diffuse	
1883	2.5	N_2	3	-1	diffuse	
1884	2.5	N_2	3	-34	diffuse	
1885	2.5	O_2	3	18	diffuse	
1886	2.5	N_2	3	17	diffuse	
1887	2.5	O_2	1	-6	diffuse	
1888	2.5	O_2	1	-9	diffuse	
1889	2.5	O_2	2	6	diffuse	
1890	2.5	O_2	2	-10	diffuse	
1891	2.5	N_2	0	2	diffuse	
1892	2.5	N_2	0	31	diffuse	

Continued on next page

Table B.3 – continued from previous page

Shot #	Φ	Test gas	Delay (s)	Δt_{img} (μs)	Series	Notes
1893	2.5	N_2	1	5	diffuse	
1894	2.5	N_2	1	-21	diffuse	
1895	2.5	N_2	2	-2	diffuse	
1896	2.5	N_2	2	-29	diffuse	
1897	2.5			-38		taped
1898	2.5				bubble	
1899	2.5			7	bubble	
1900	2.5			9	bubble	
1901	2.5			8	bubble	
1902	2.5			-21	sharp	validation
1903	2.5			-3	sharp	validation
1904						no experiment
1905	2.5	N_2		22	sharp	mylar on wood
1906	2.5	N_2		29	sharp	nitro-cellulose
1907	2.5	N_2		2	sharp	nitro-cellulose
1908	2.5	N_2		-21	sharp	tissue paper
1909	2.5	N_2		-22	sharp	tissue paper
1910	2.5	N_2		-11	sharp	tissue paper
1911	2.5	O_2		16	sharp	tissue paper
1912	2.5	O_2		11	sharp	nitro-cellulose
1913	2.5	O_2			sharp	nitro-cellulose
1914	2.5	O_2		-3	sharp	nitro-cellulose
1915	2.5	O_2		10	sharp	nitro-cellulose
1916	2.5	N_2O		6	sharp	nitro-cellulose
1917	2.5	N_2O		21	sharp	nitro-cellulose
1918	1	N_2O		21	sharp	nitro-cellulose

Continued on next page

Table B.3 – continued from previous page

Shot #	Φ	**Test gas**	**Delay (s)**	Δt_{img} (μs)	**Series**	**Notes**
1919	1	N_2O		-1	sharp	nitro-cellulose
1920	1	N_2O		-23	sharp	nitro-cellulose
1921	1	N_2O		16	sharp	nitro-cellulose
1922	2.5	N_2		10	sharp	nitro-cellulose
1923	1	O_2		-16	sharp	nitro-cellulose
1924	1	O_2		-18	sharp	nitro-cellulose
1925	1	O_2		-2	sharp	nitro-cellulose
1926	1	O_2		56	sharp	nitro-cellulose
1927	1	O_2		30	sharp	nitro-cellulose

Appendix C

GDT Gravity Current Shot List

Shot	Mixture (GDT)	Mixture (test section)	Details
gc1	C_3H_6O + He	N_2	
gc2	C_3H_6O + He	N_2	
gc3	C_3H_6O + He	N_2	
gc4	C_3H_6O + He	O_2	Fill error
gc5	0.452 C_3H_6O + 0.547 He	O_2	
gc6	C_3H_6O + He	O_2	
gc7	C_3H_6O + He	N_2	
gc8	N_2	C_3H_6O + He	aperture, f5.6
gc9	N_2	C_3H_6O + He	
gc10	N_2	0.78 C_3H_6O + 0.34 He	ICCD image error
gc11	N_2	0.78 C_3H_6O + 0.34 He	

Table C.1: A shot list for the gravity current PLIF experiments. The initial pressure and temperature for all experiments was 112.5 kPa and 297 K, respectively. The ICCD camera settings used an MCP voltage of 800 and a 5 picture per second frame rate with an exposure time of 50 μs. The lens aperture was set to 8 unless otherwise specified.

Appendix D

Schlieren Images

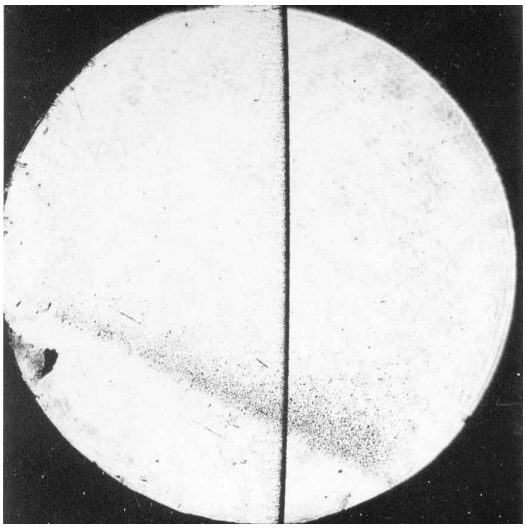

Shot 1784.

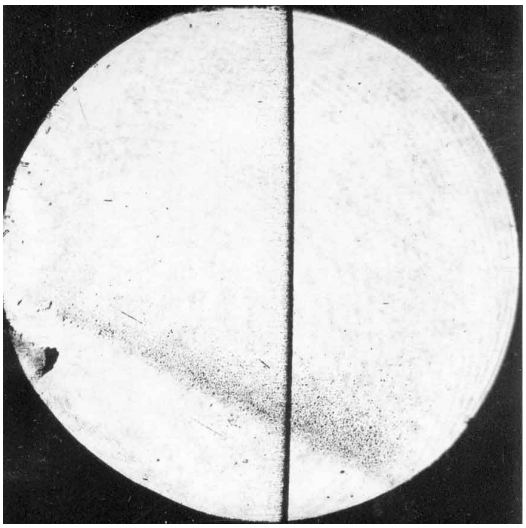

Shot 1785.

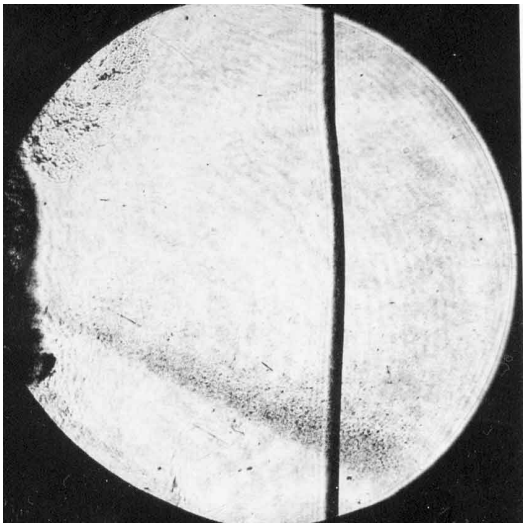

Shot 1787.

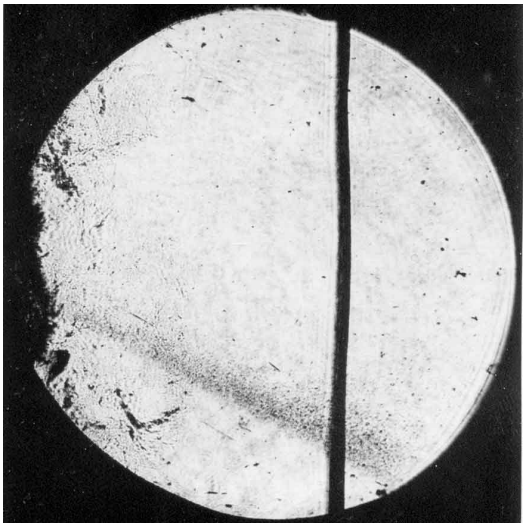

Shot 1789.

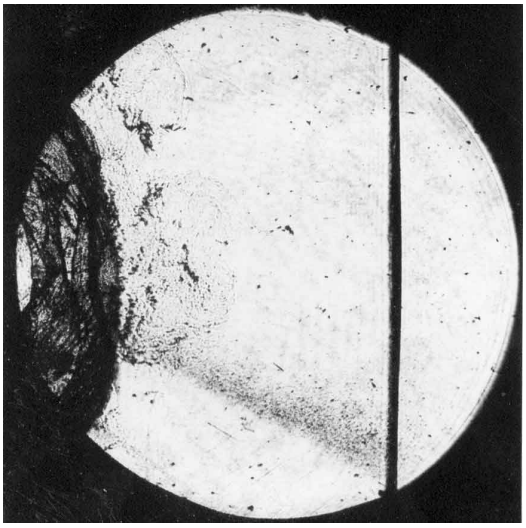

Shot 1790.

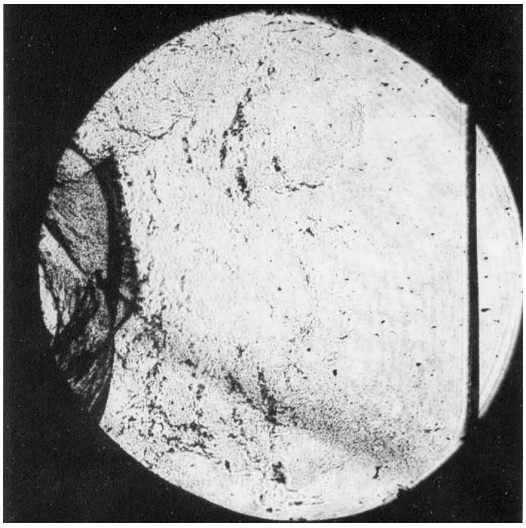

Shot 1791.

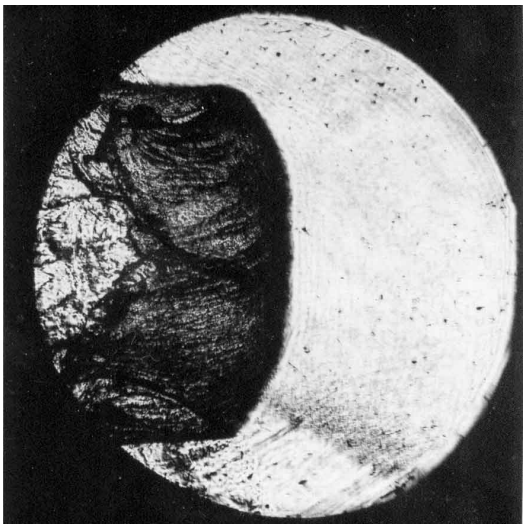

Shot 1792.

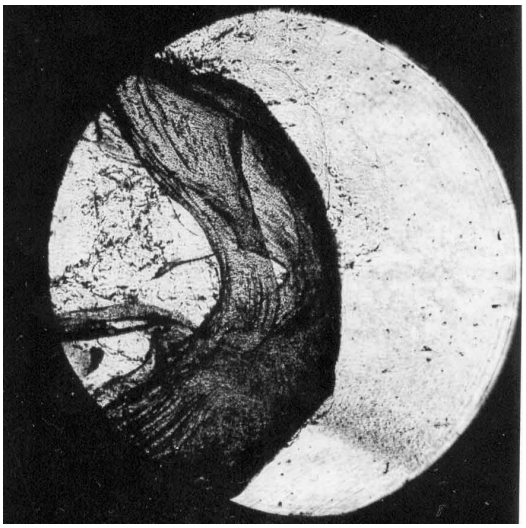

Shot 1793.

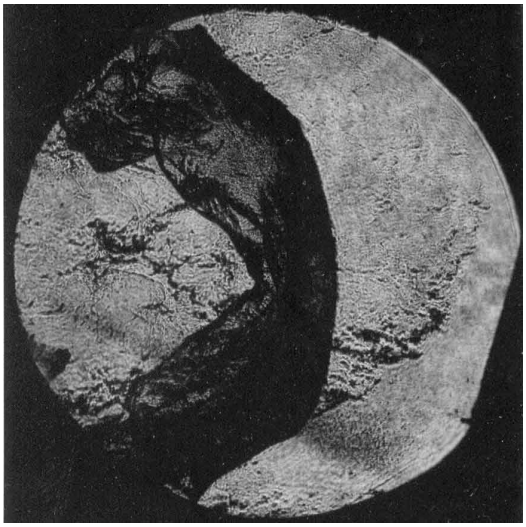

Shot 1795.

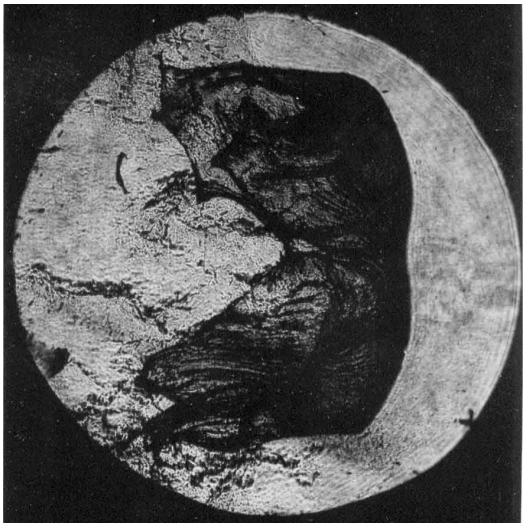

Shot 1796.

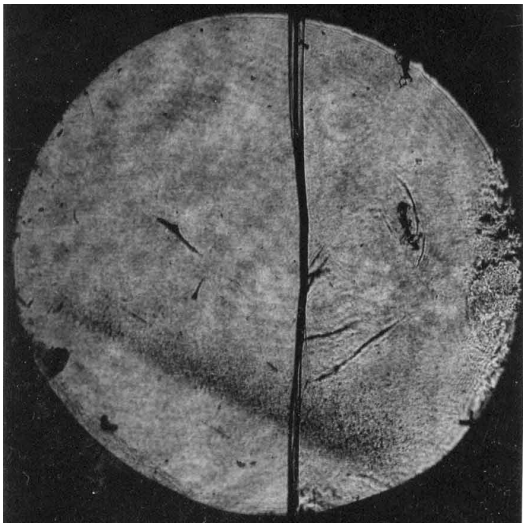

Shot 1797.

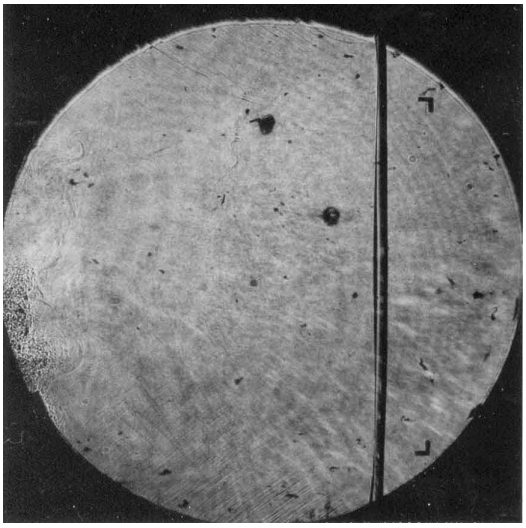

Shot 1815.

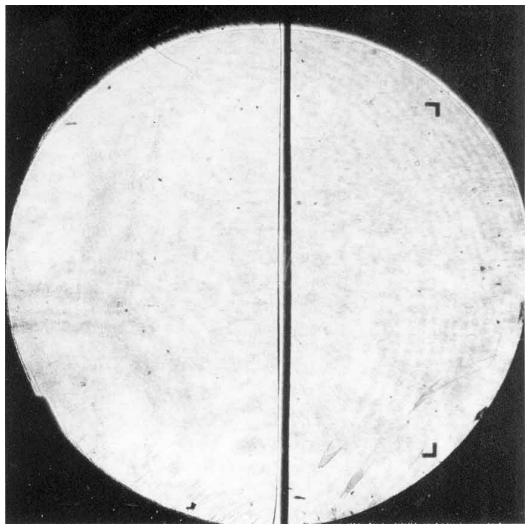

Shot 1820.

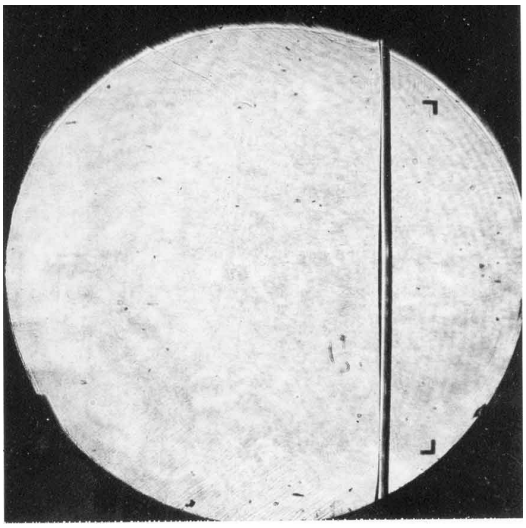

Shot 1821.

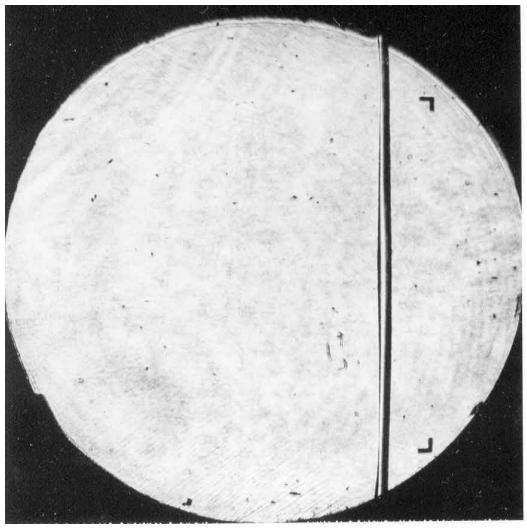

Shot 1823.

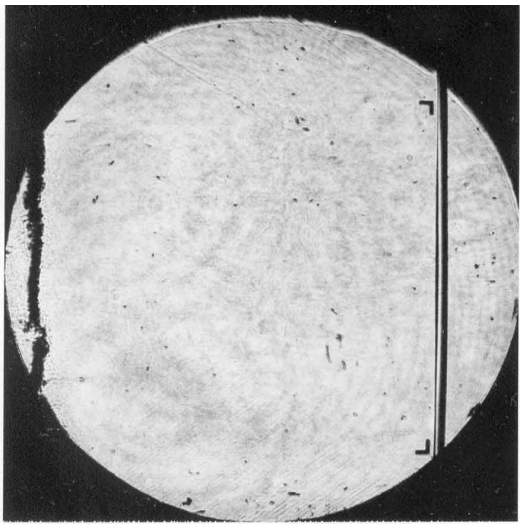

Shot 1825.

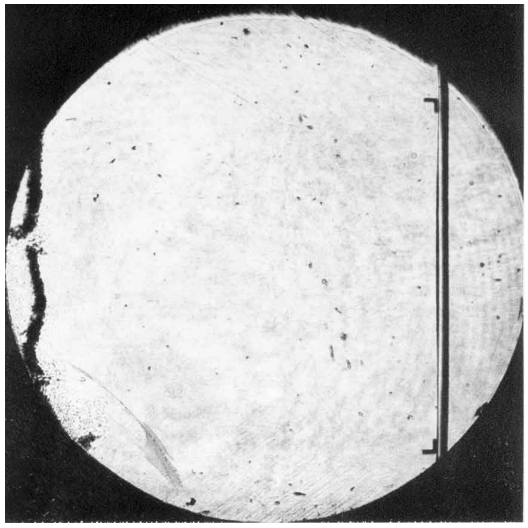

Shot 1826.

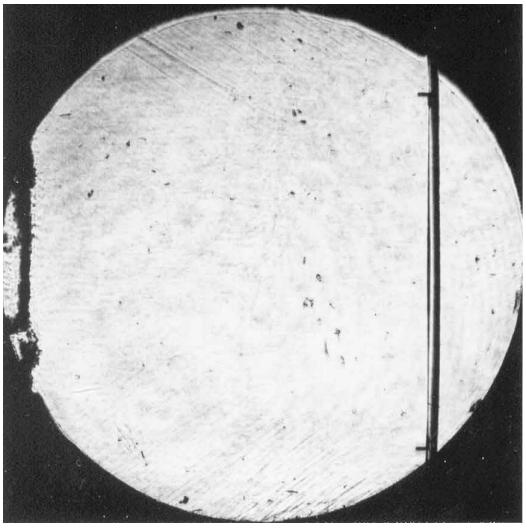

Shot 1827.

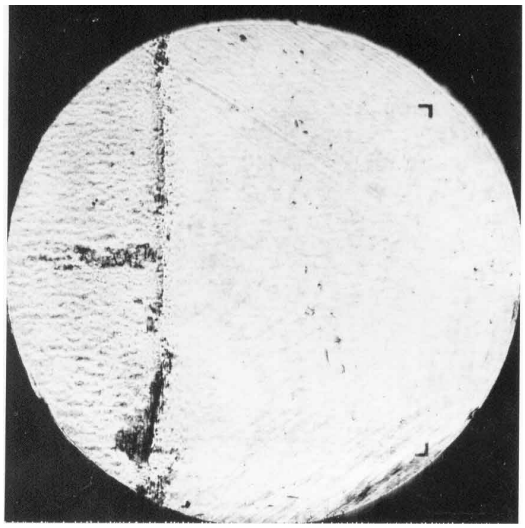

Shot 1828.

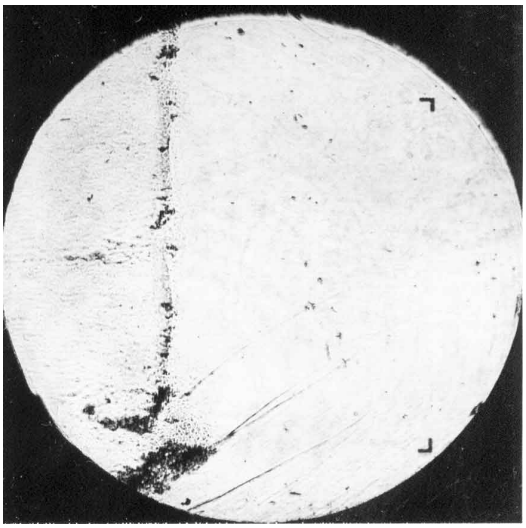

Shot 1829.

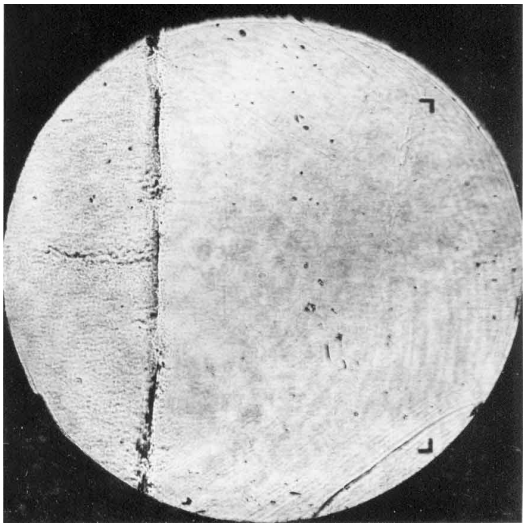

Shot 1830.

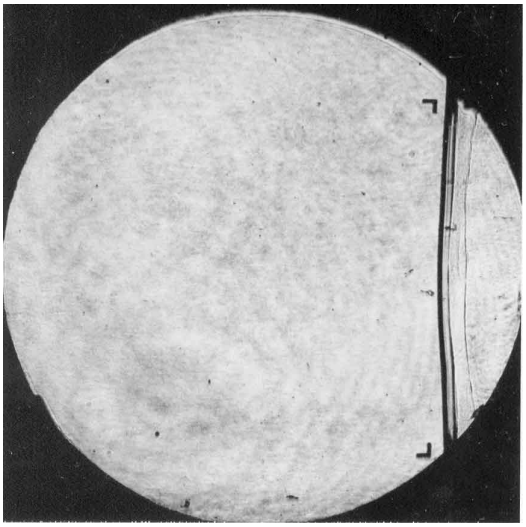

Shot 1832.

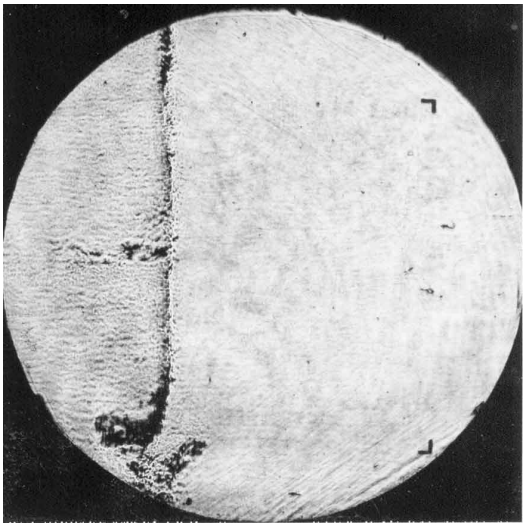

Shot 1833.

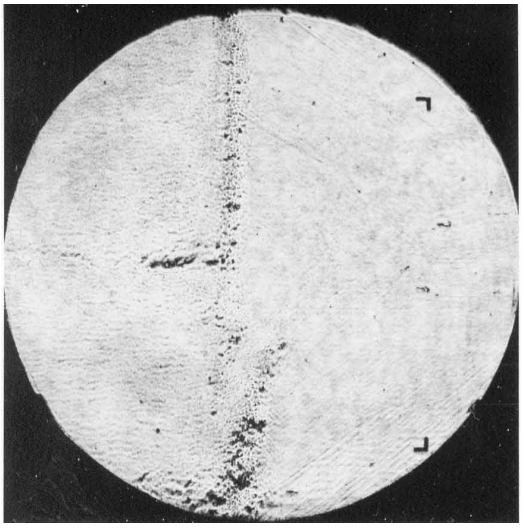

Shot 1834.

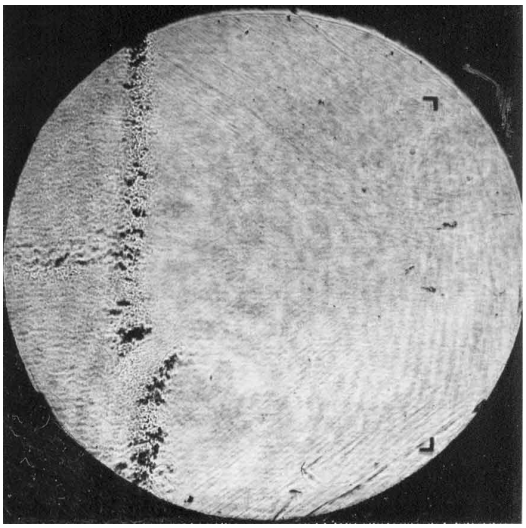

Shot 1835.

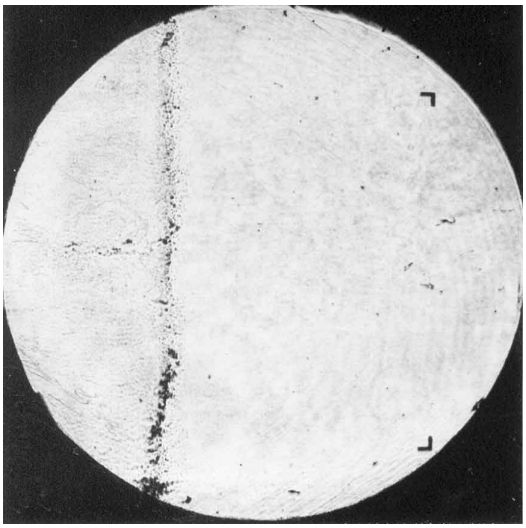

Shot 1836.

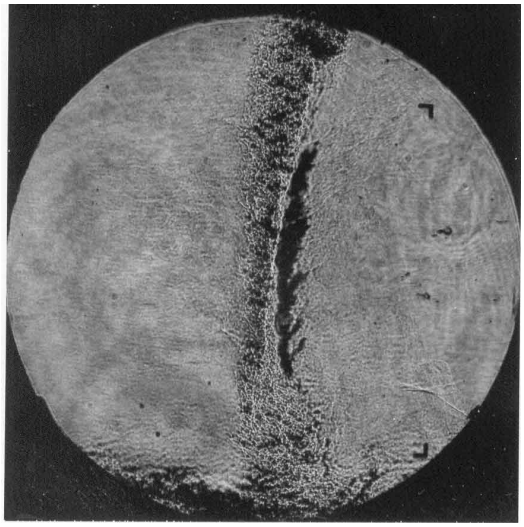

Shot 1839.

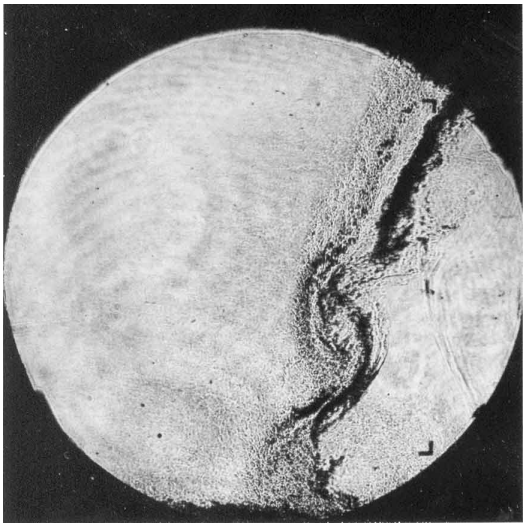

Shot 1842.

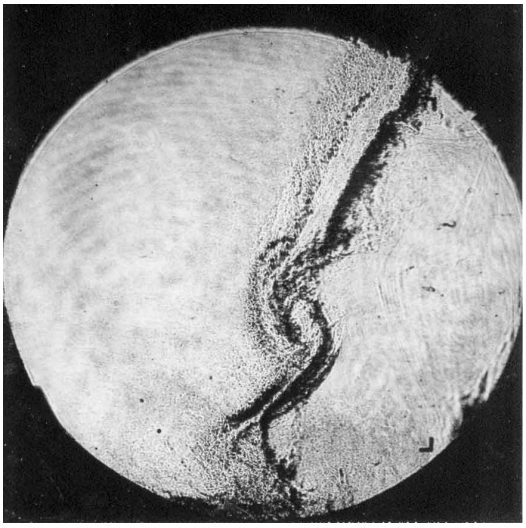

Shot 1846.

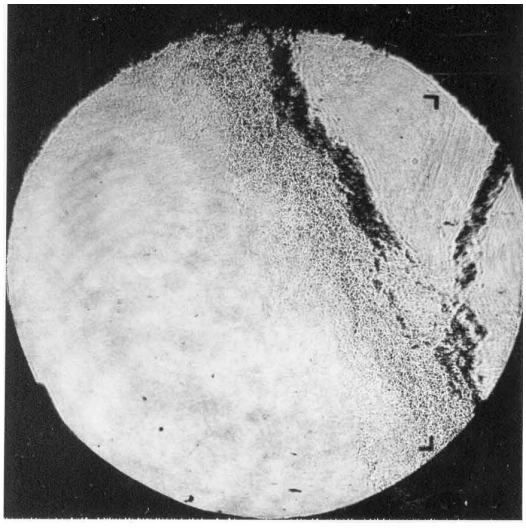

Shot 1847.

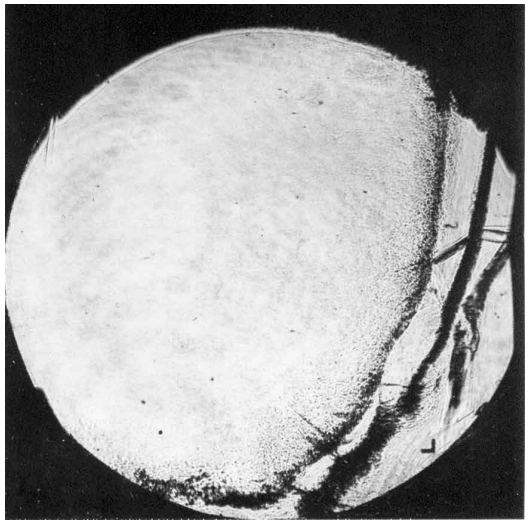

Shot 1849.

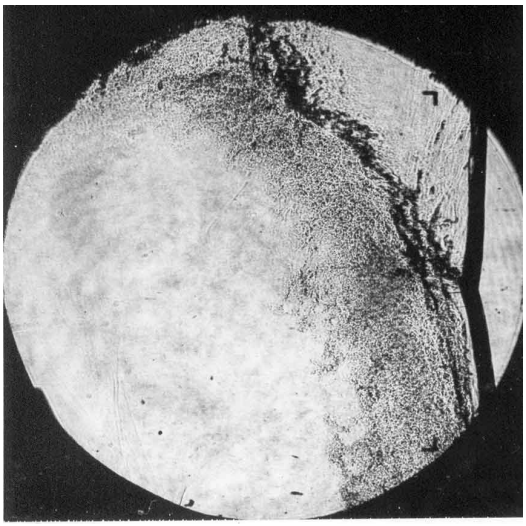

Shot 1850.

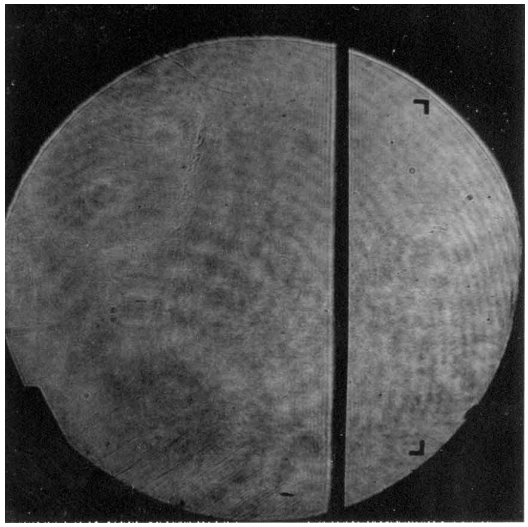

Shot 1852.

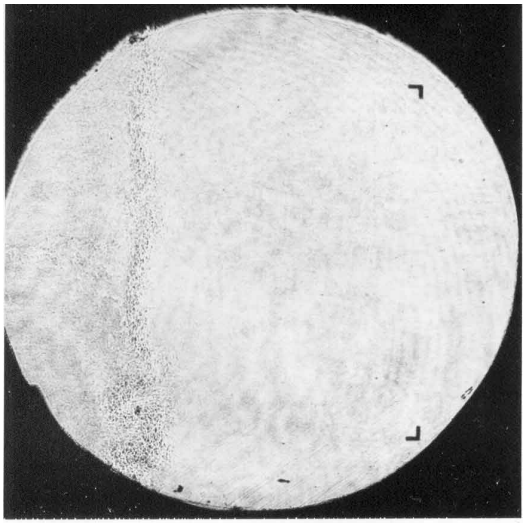

Shot 1854.

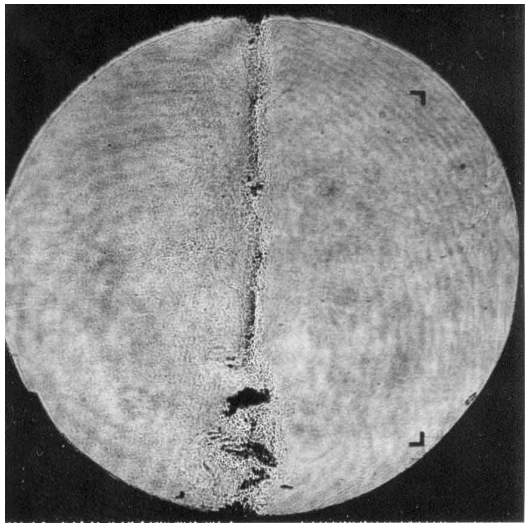

Shot 1855.

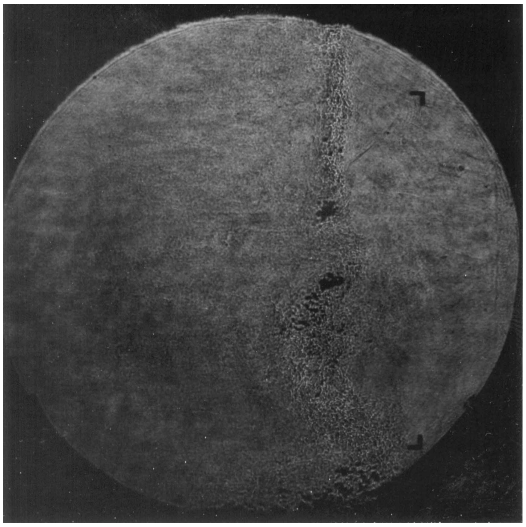

Shot 1856.

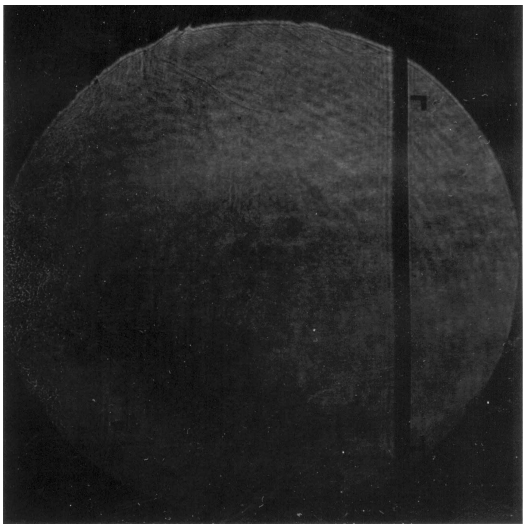

Shot 1857.

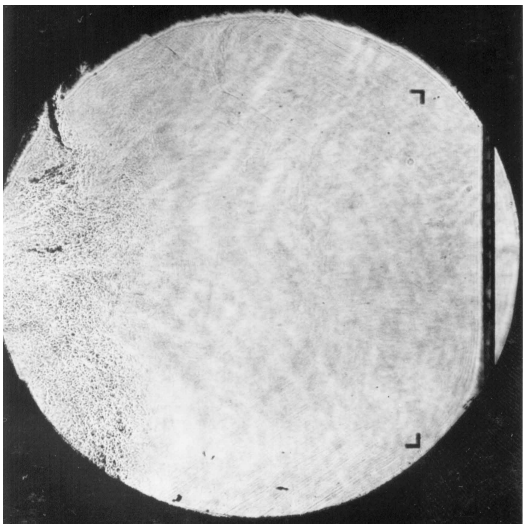

Shot 1858.

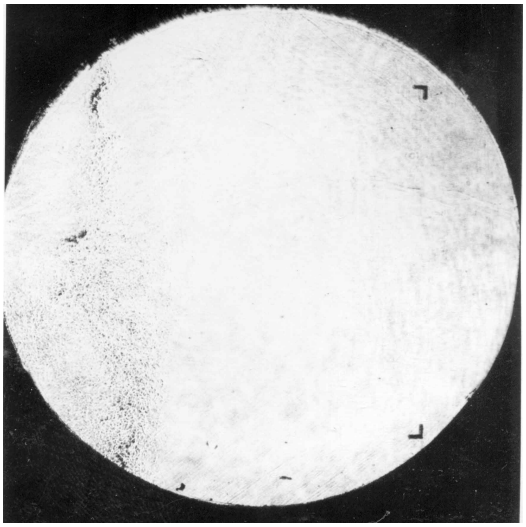

Shot 1859.

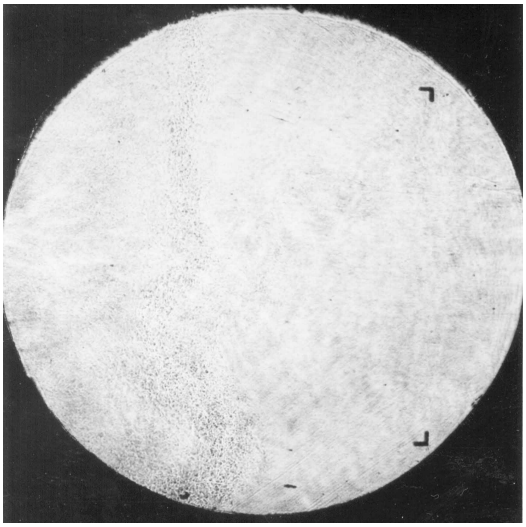

Shot 1860.

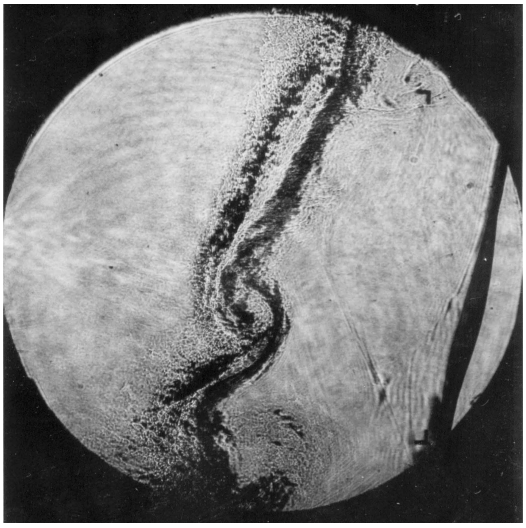

Shot 1861.

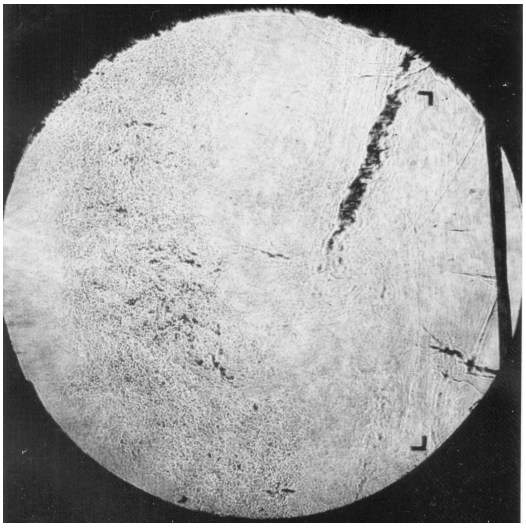

Shot 1862.

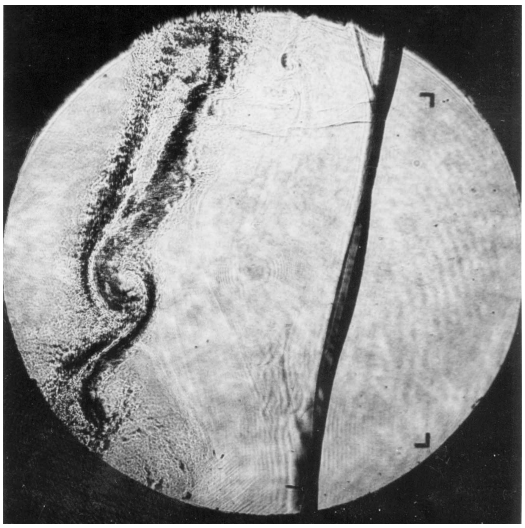

Shot 1863.

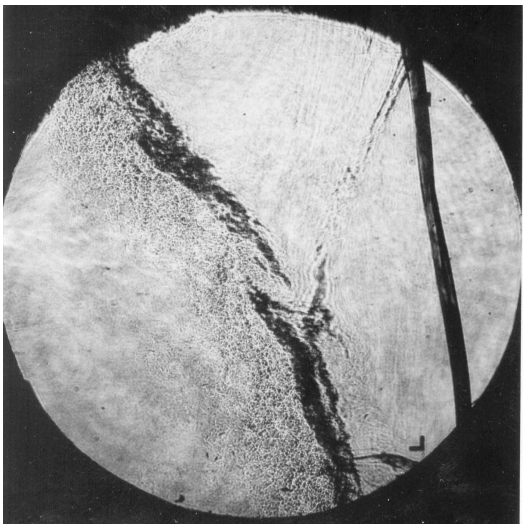

Shot 1864.

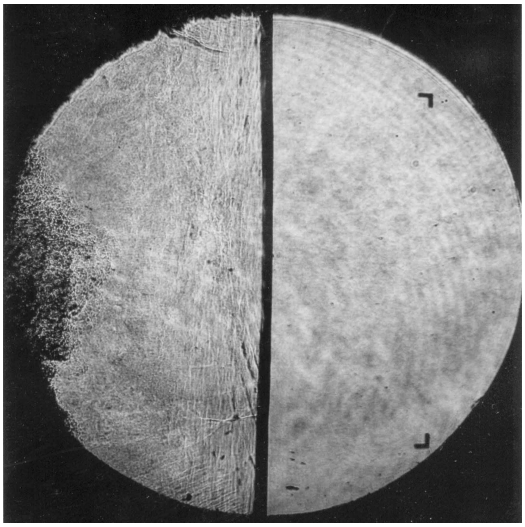

Shot 1865.

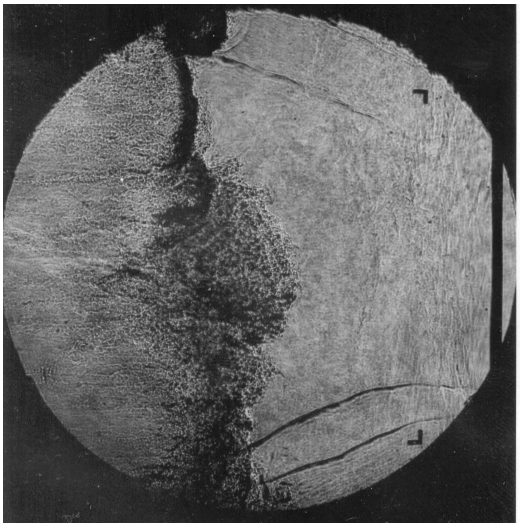

Shot 1866.

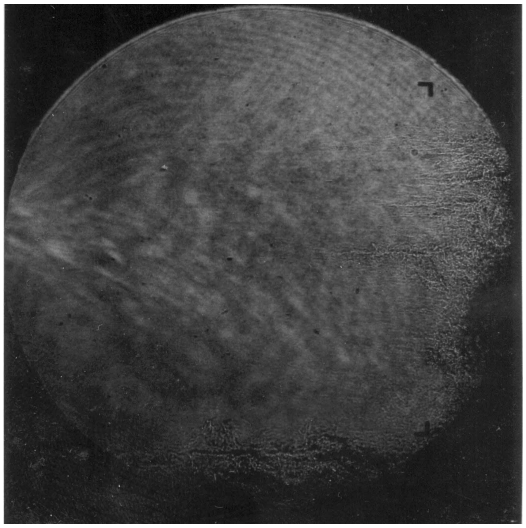

Shot 1867.

Shot 1868.

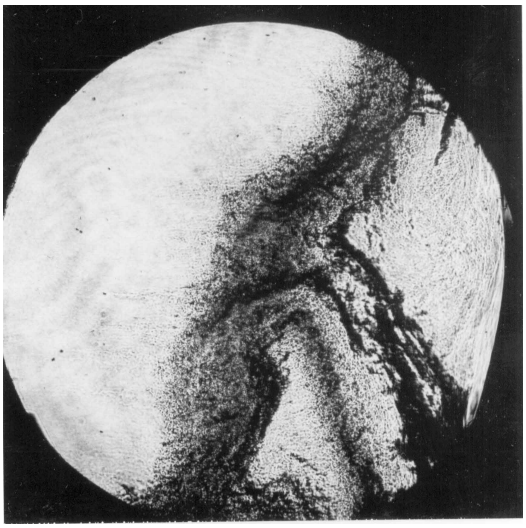

Shot 1870.

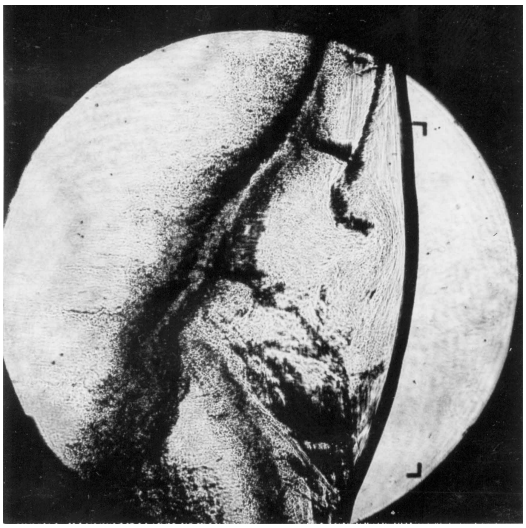

Shot 1871.

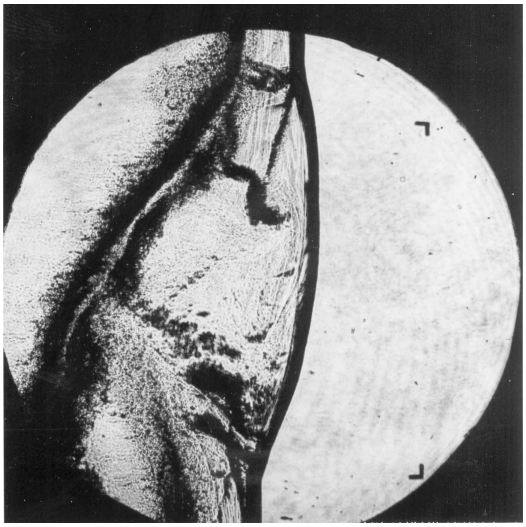

Shot 1872.

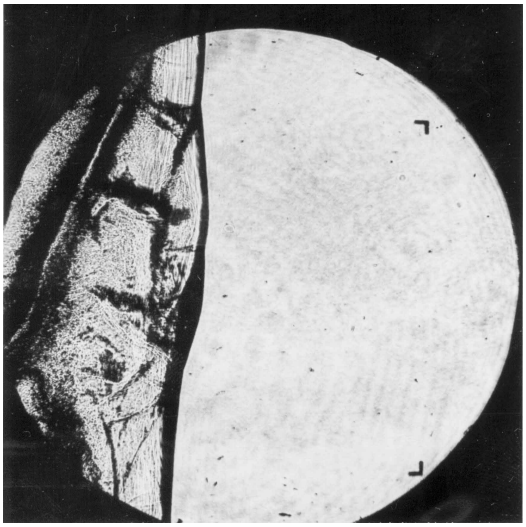

Shot 1873.

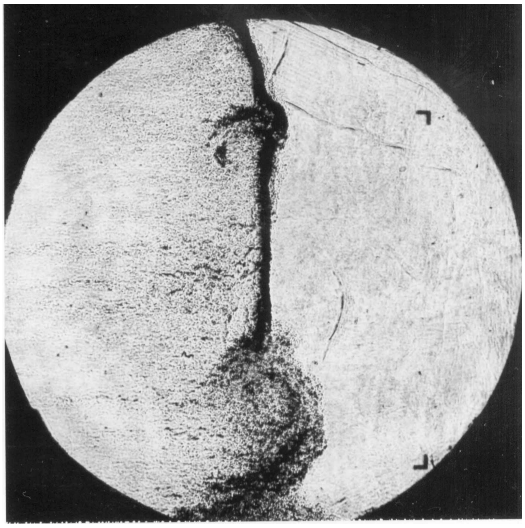

Shot 1874.

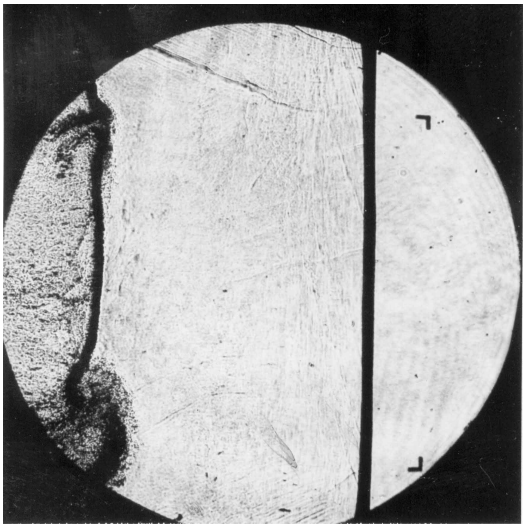

Shot 1875.

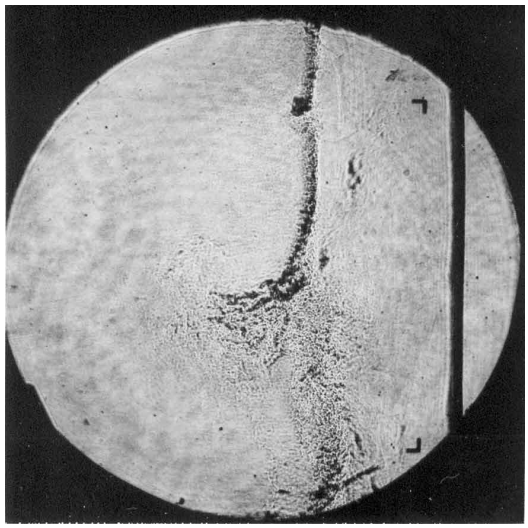

Shot 1876.

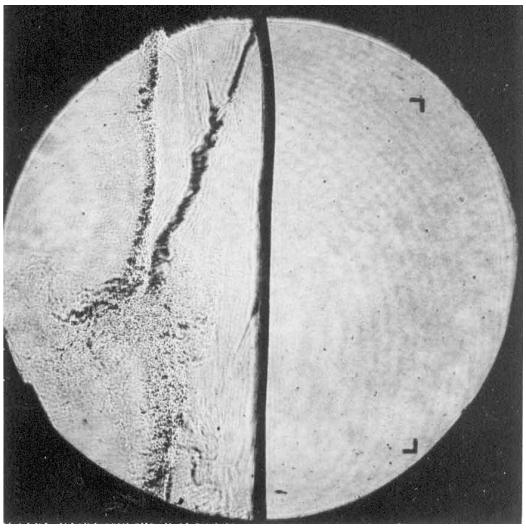

Shot 1877.

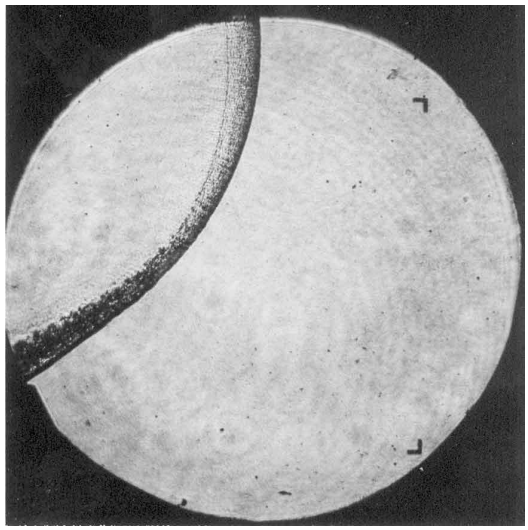

Shot 1878.

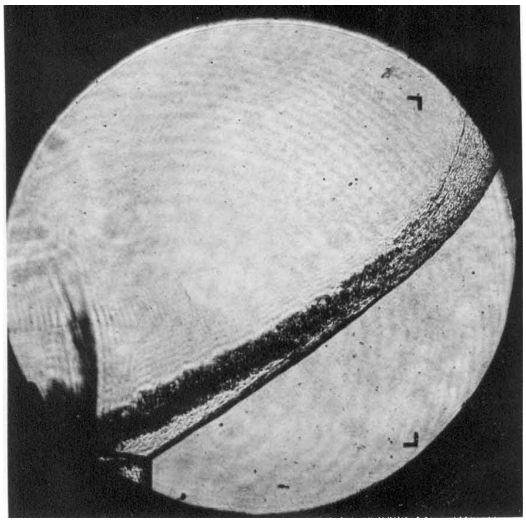

Shot 1879.

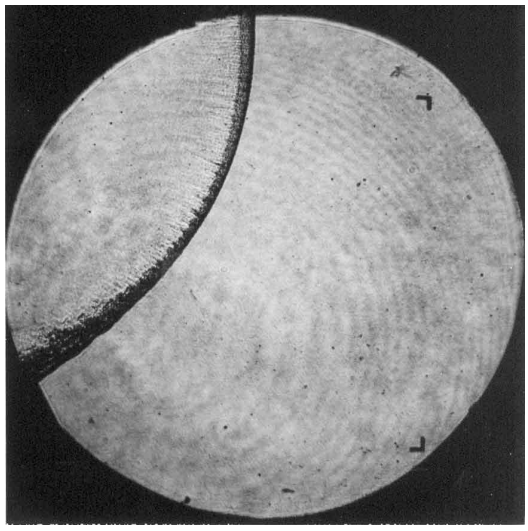

Shot 1882.

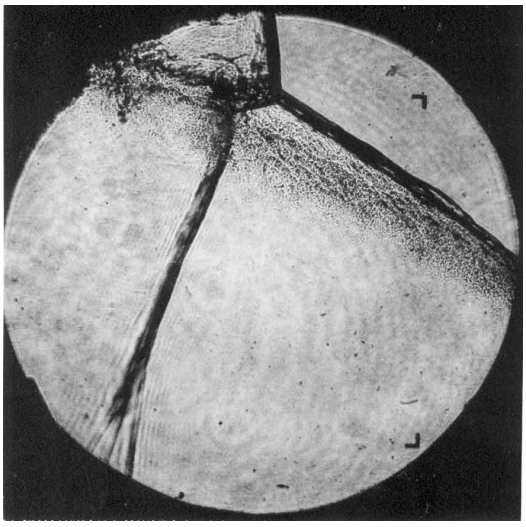

Shot 1883.

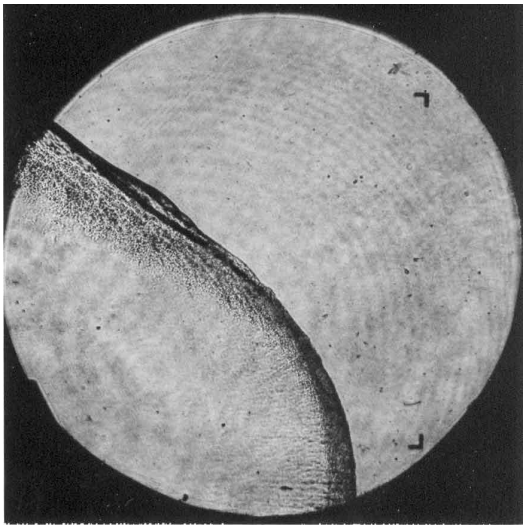

Shot 1884.

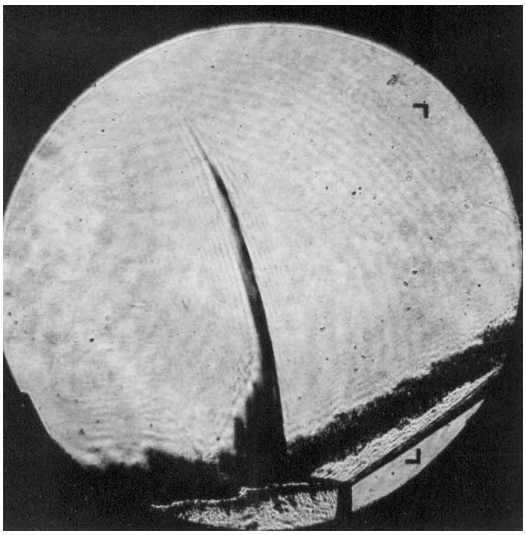

Shot 1885.

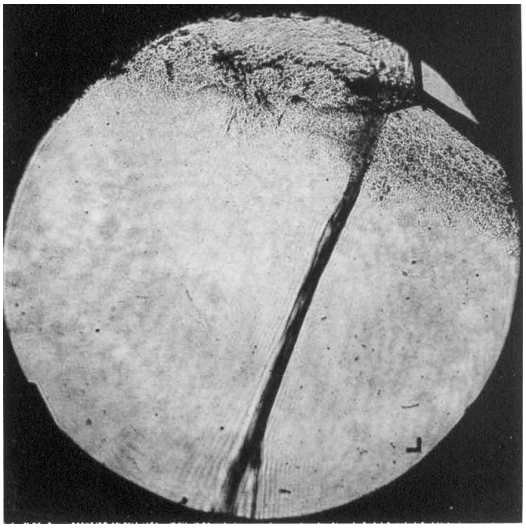

Shot 1886.

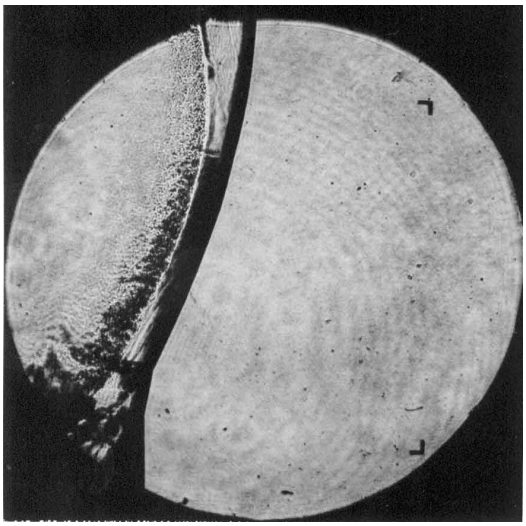

Shot 1887.

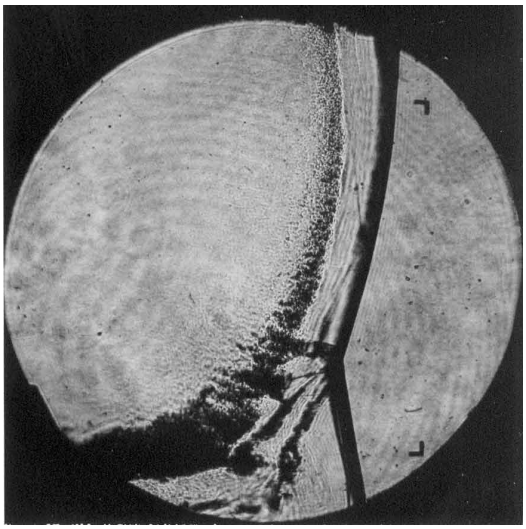

Shot 1888.

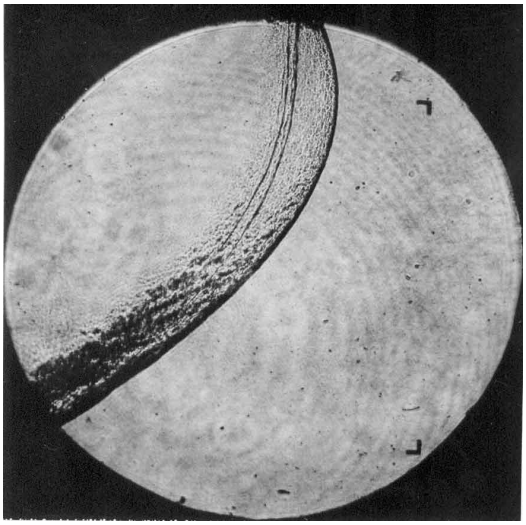

Shot 1889.

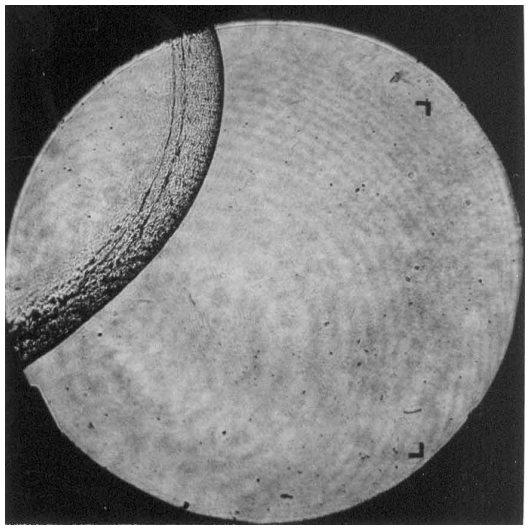

Shot 1890.

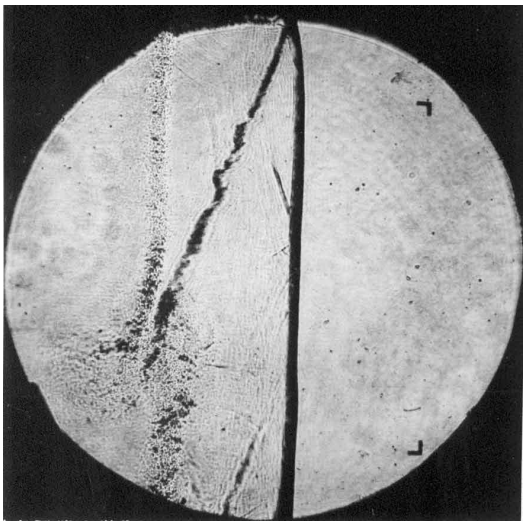

Shot 1891.

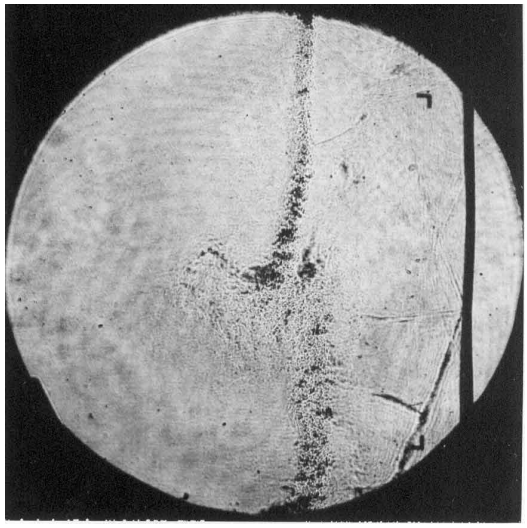

Shot 1892.

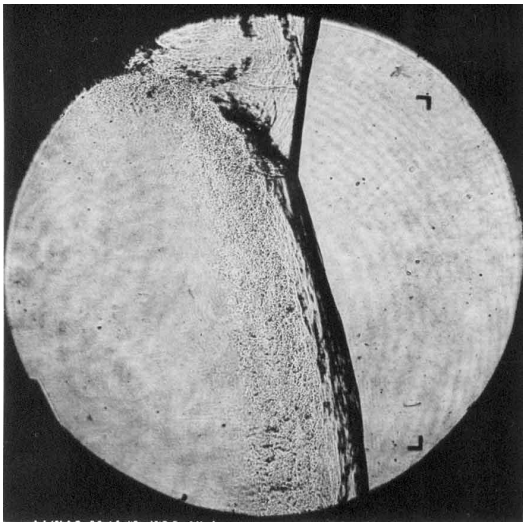

Shot 1893.

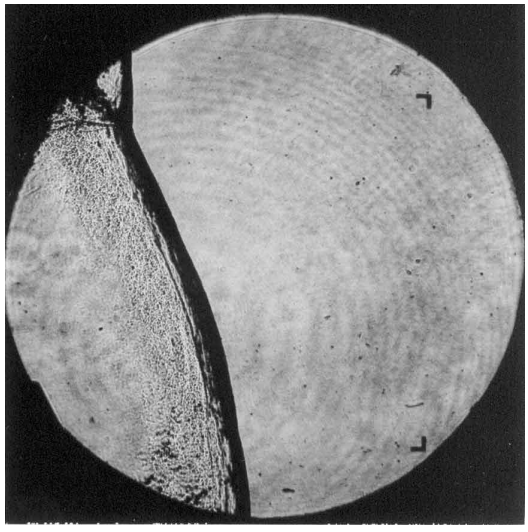

Shot 1894.

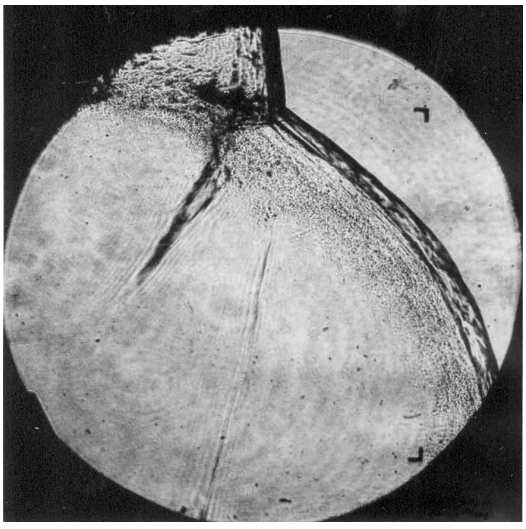

Shot 1895.

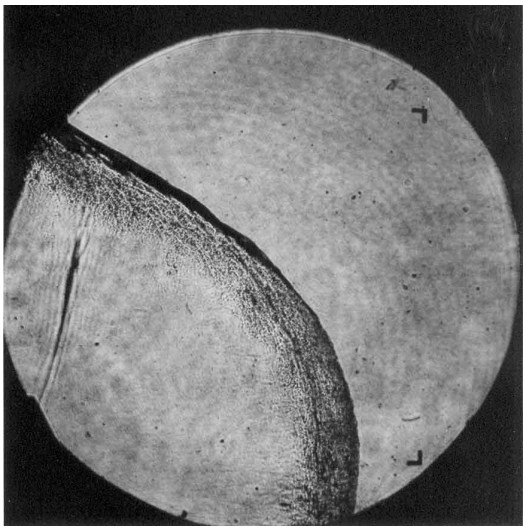

Shot 1896.

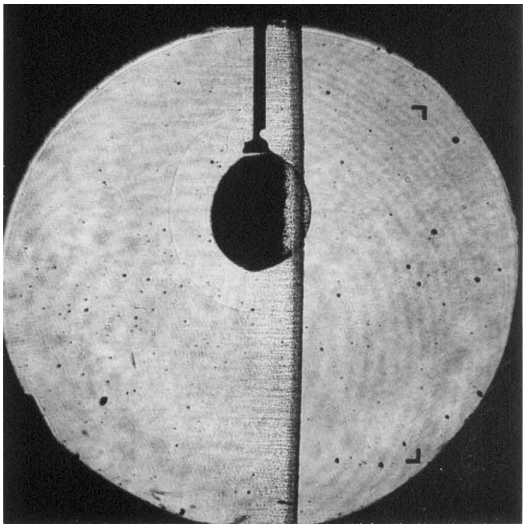

Shot 1898.

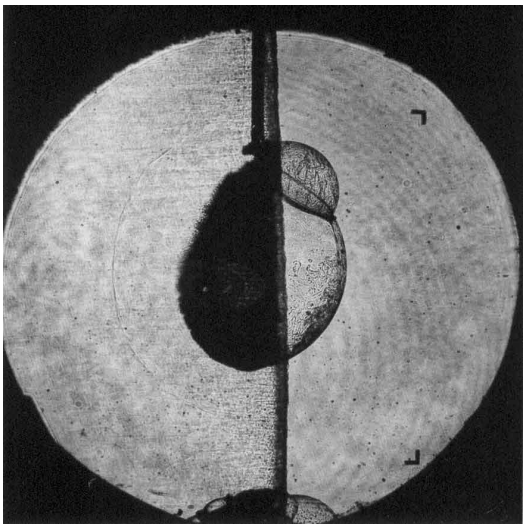

Shot 1899.

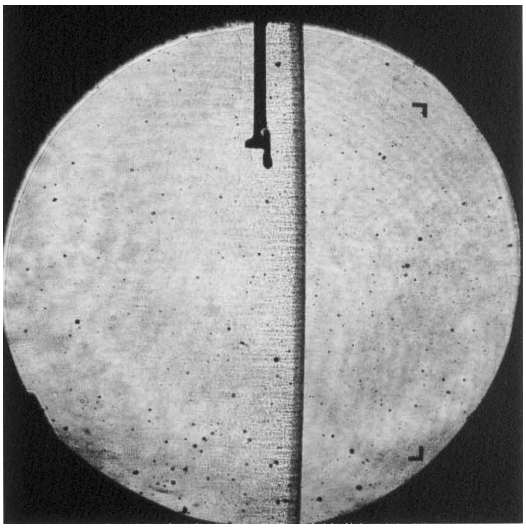

Shot 1900.

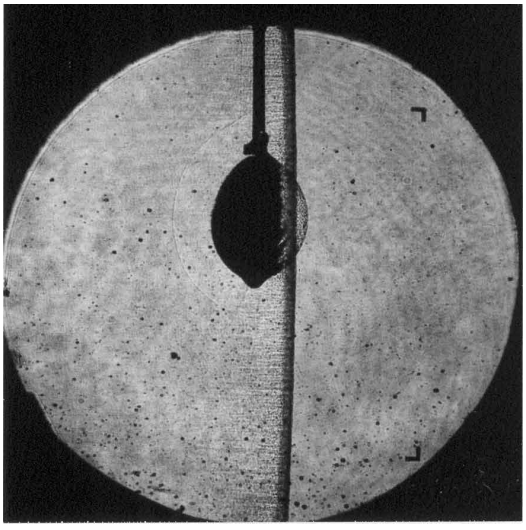

Shot 1901.

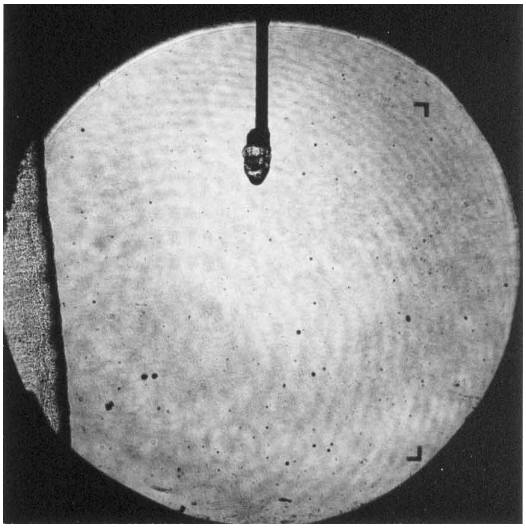

Shot 1902.

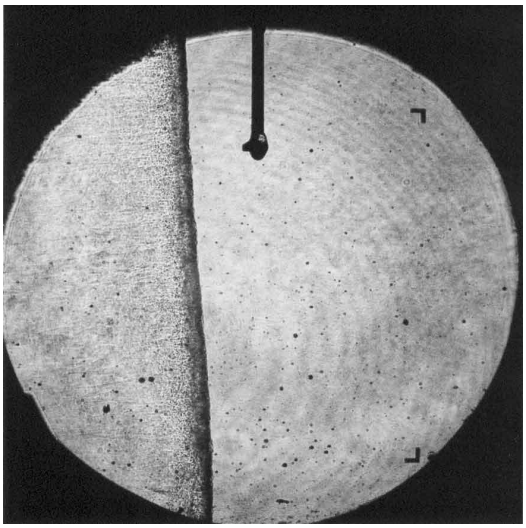

Shot 1903.

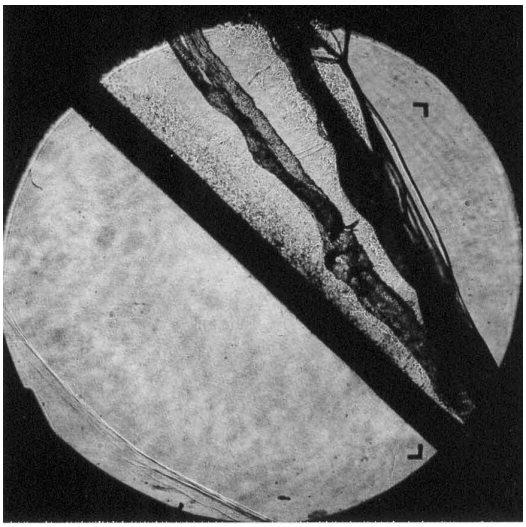

Shot 1905.

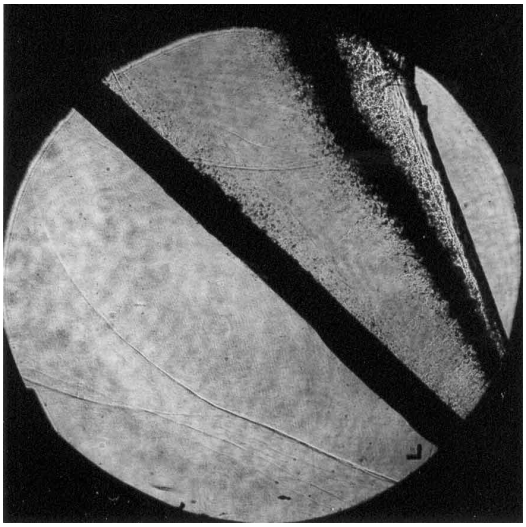

Shot 1906.

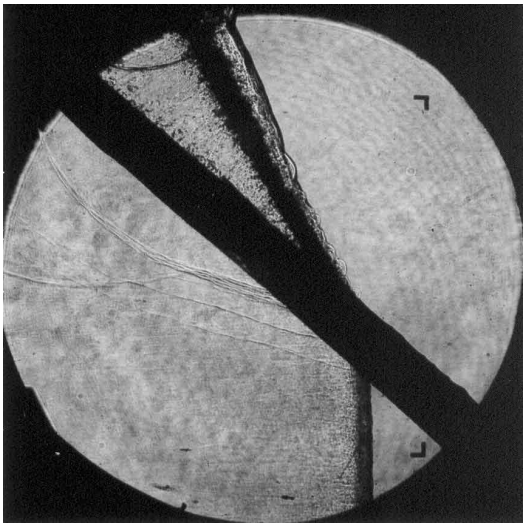

Shot 1907.

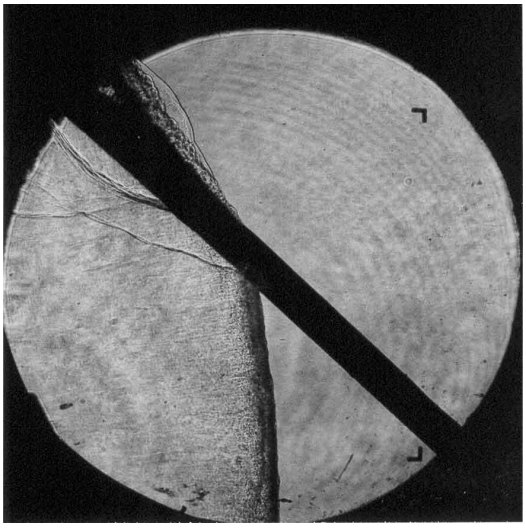

Shot 1909.

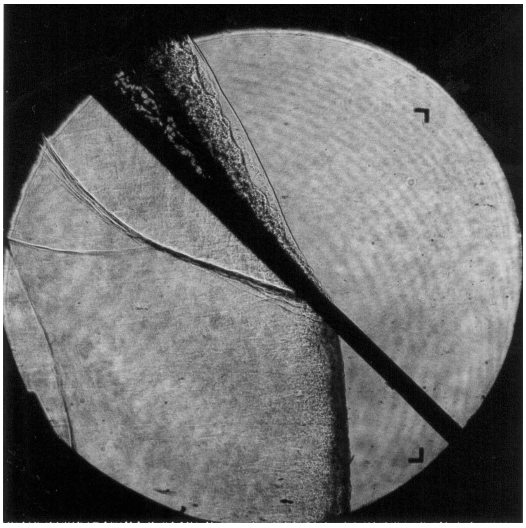

Shot 1910.

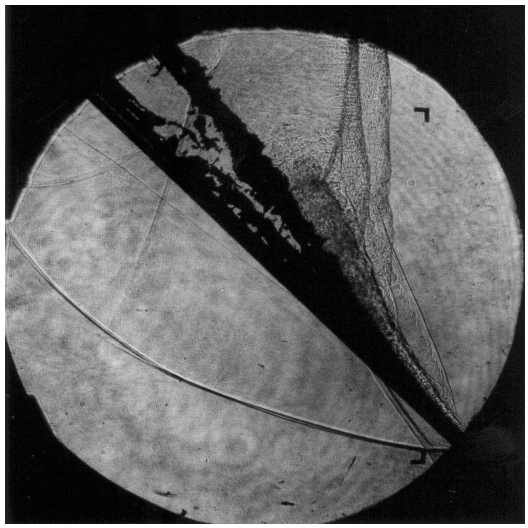

Shot 1911.

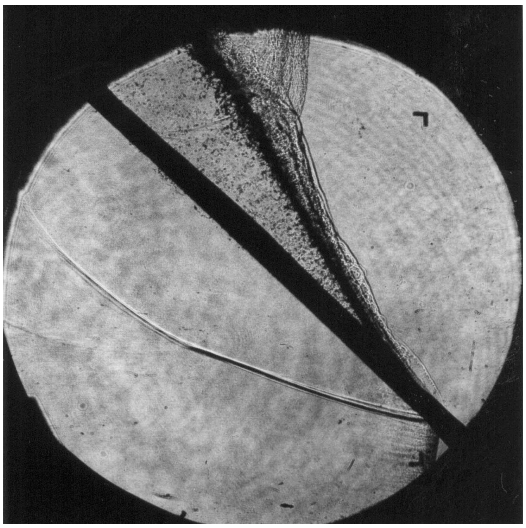

Shot 1912.

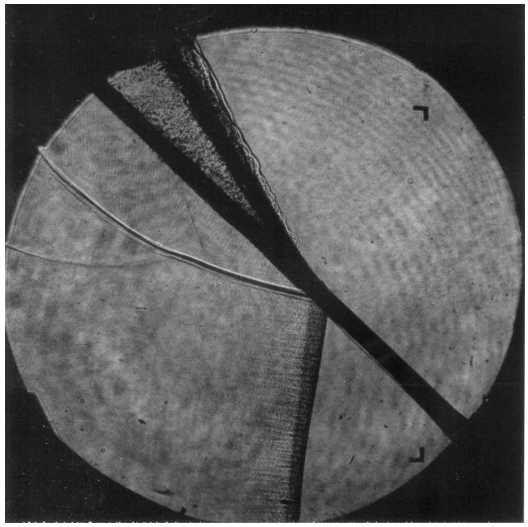

Shot 1914.

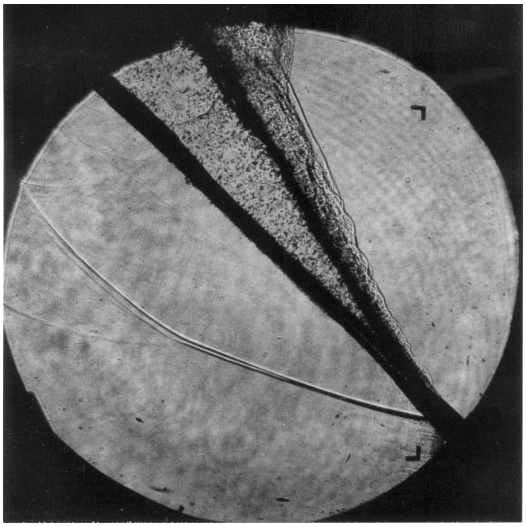

Shot 1915.

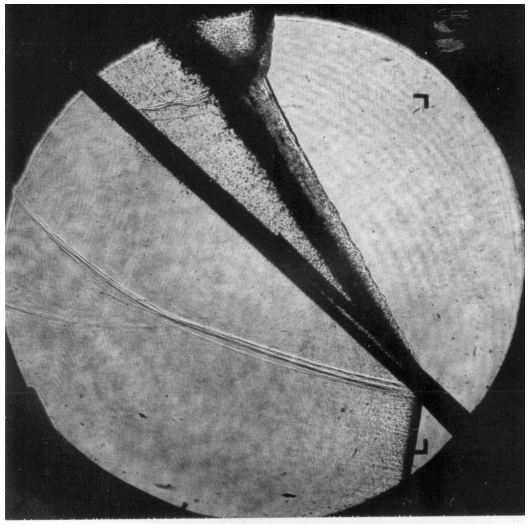

Shot 1916.

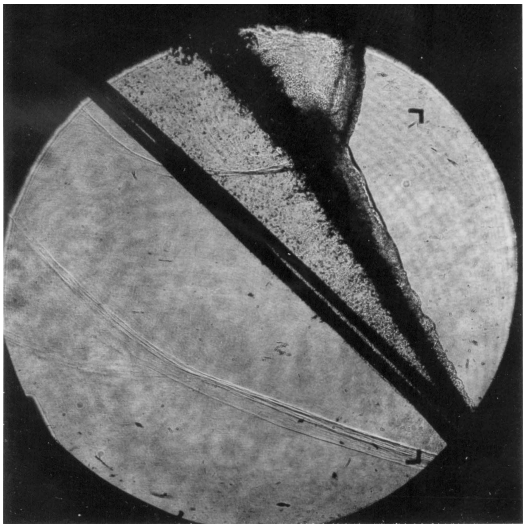

Shot 1917.

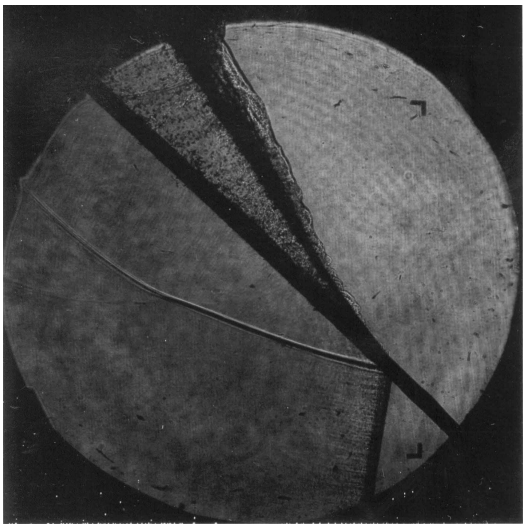

Shot 1919.

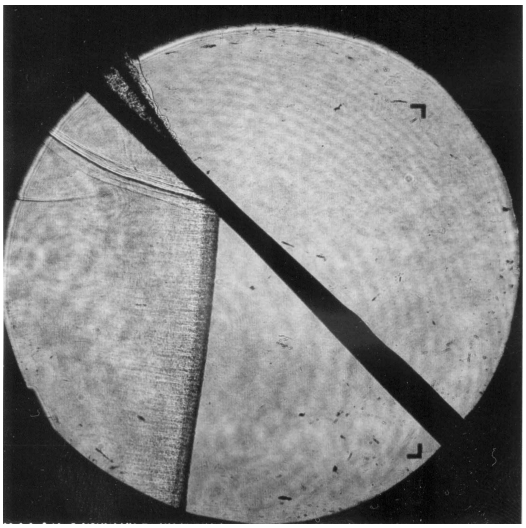

Shot 1920.

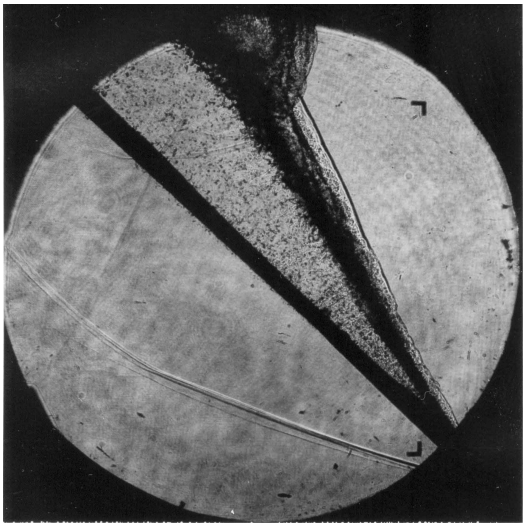

Shot 1921.

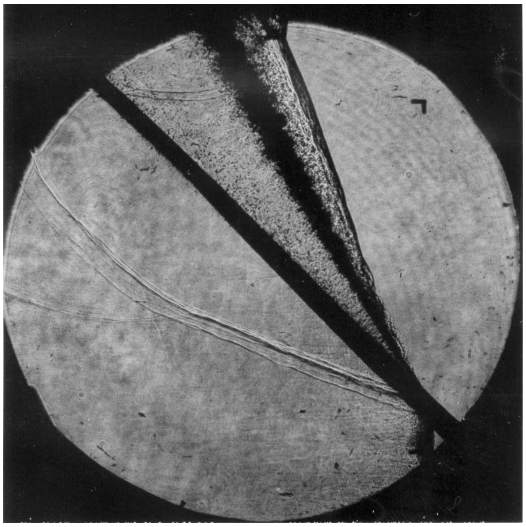

Shot 1922.

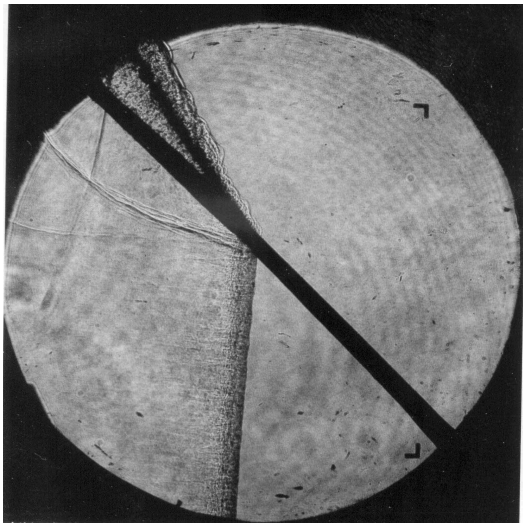

Shot 1923.

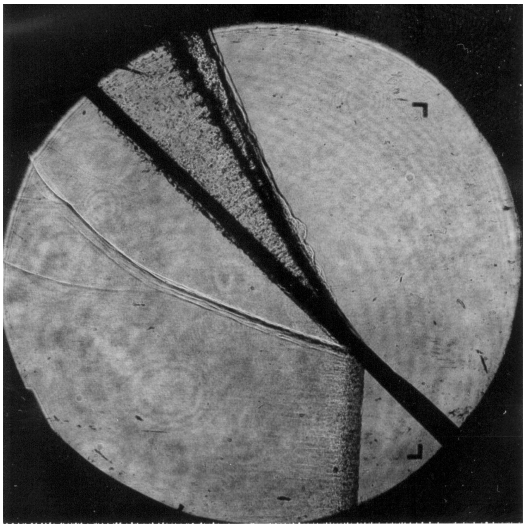

Shot 1925.

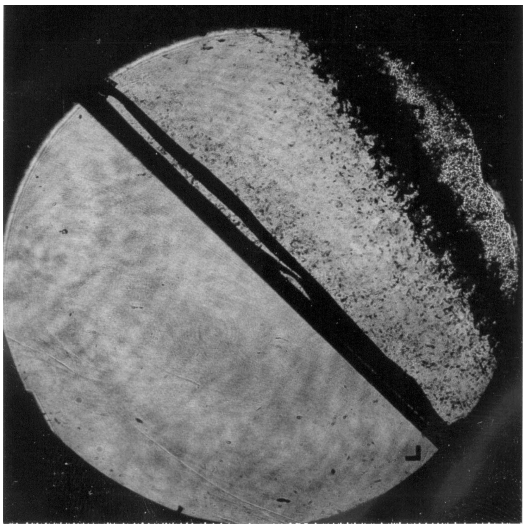

Shot 1926.

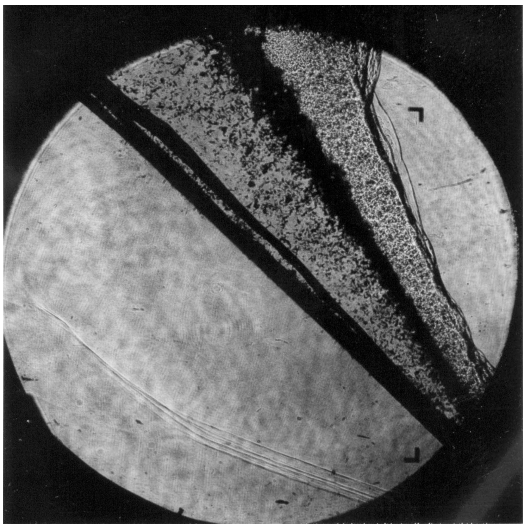

Shot 1927.

Appendix E

PLIF Images of Gravity Currents in the GDT

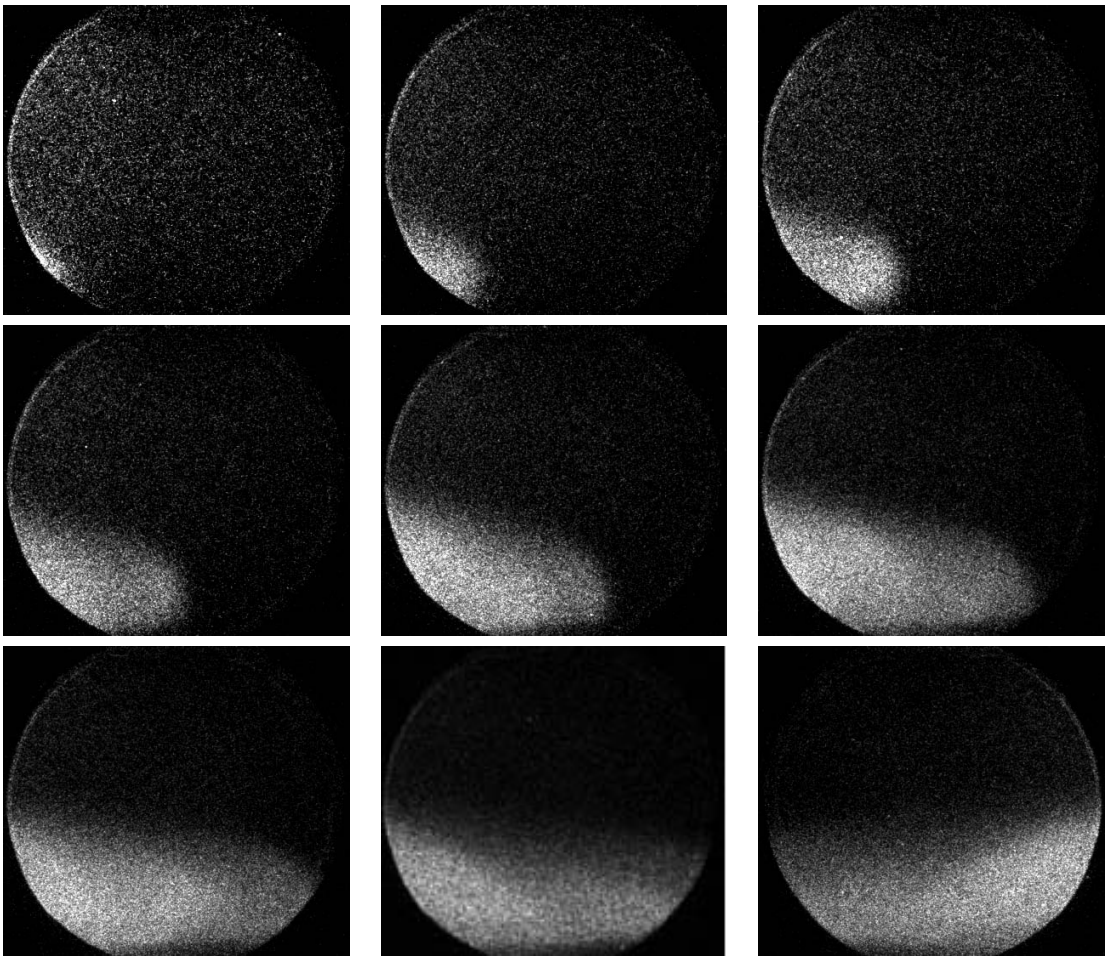

Figure E.1: A sequence of planar laser-induced fluorescence images showing the gravity current propagation (Exp.#gc2). The first image corresponds to a time of 0.6 s measured from when the plate in the sliding valve assembly moves to the open position. Each image is taken at a 0.2 ms time increment.

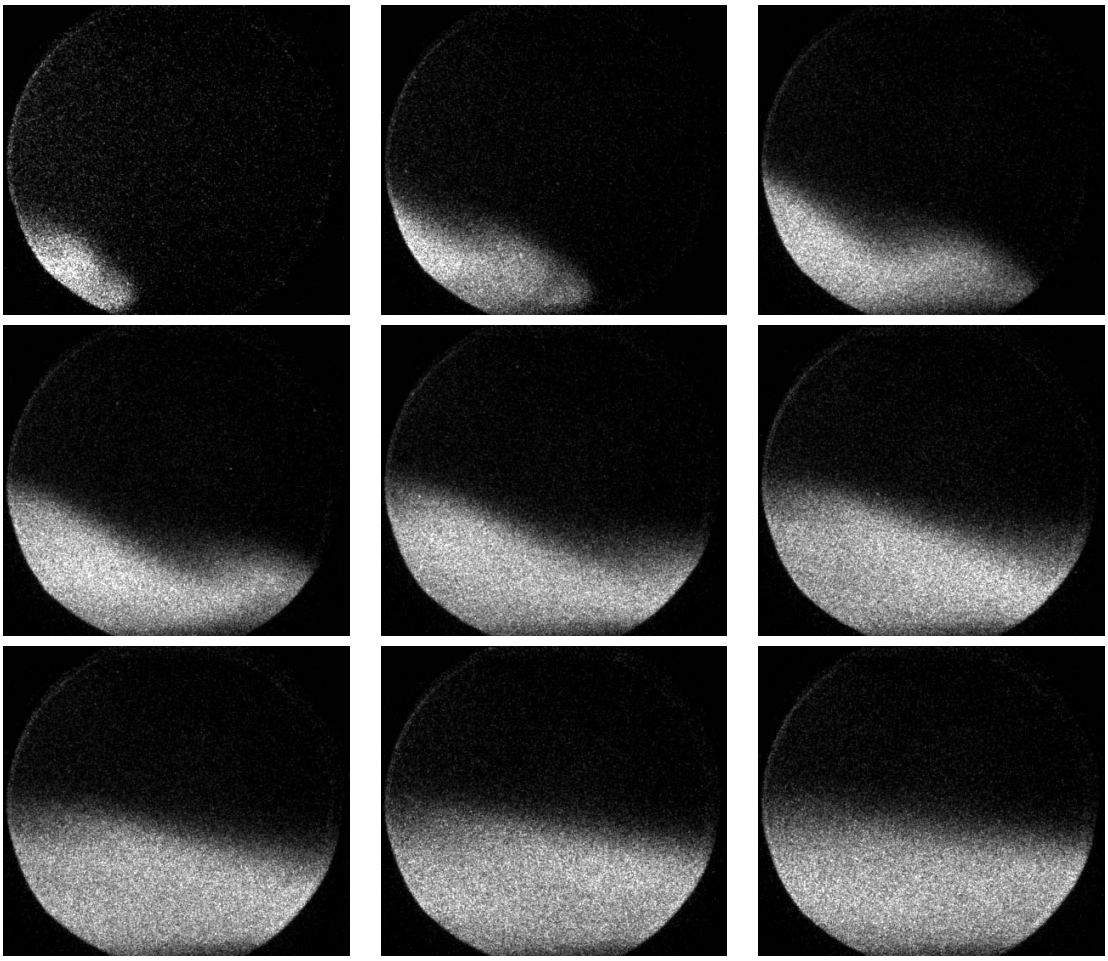

Figure E.2: A sequence of planar laser-induced fluorescence images showing the gravity current propagation (Exp.#gc3). The first image corresponds to a time of 0.6 s measured from when the plate in the sliding valve assembly moves to the open position. Each image is taken at a 0.2 ms time increment.

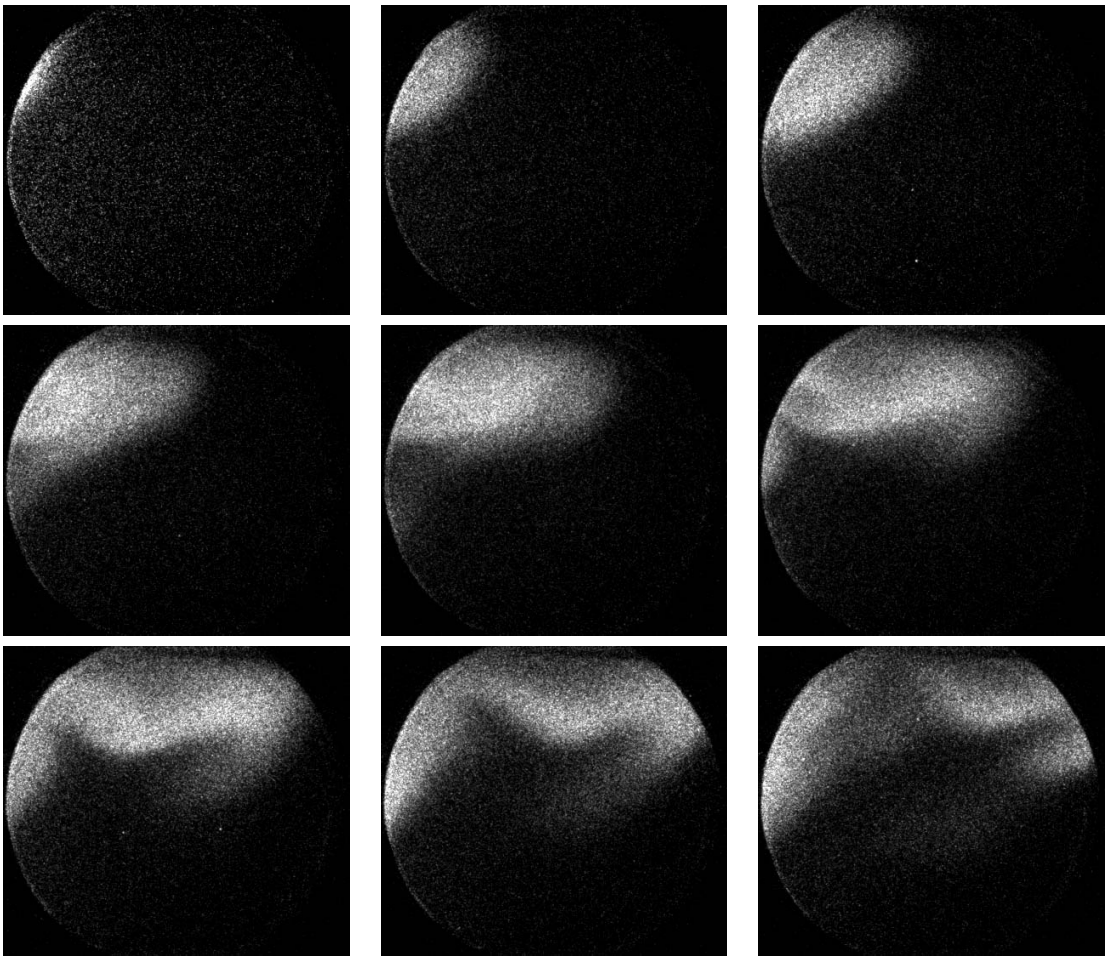

Figure E.3: A sequence of planar laser-induced fluorescence images showing the gravity current propagation (Exp.#gc5). The first image corresponds to a time of 1 s measured from when the plate in the sliding valve assembly moves to the open position. Each image is taken at a 0.2 ms time increment.

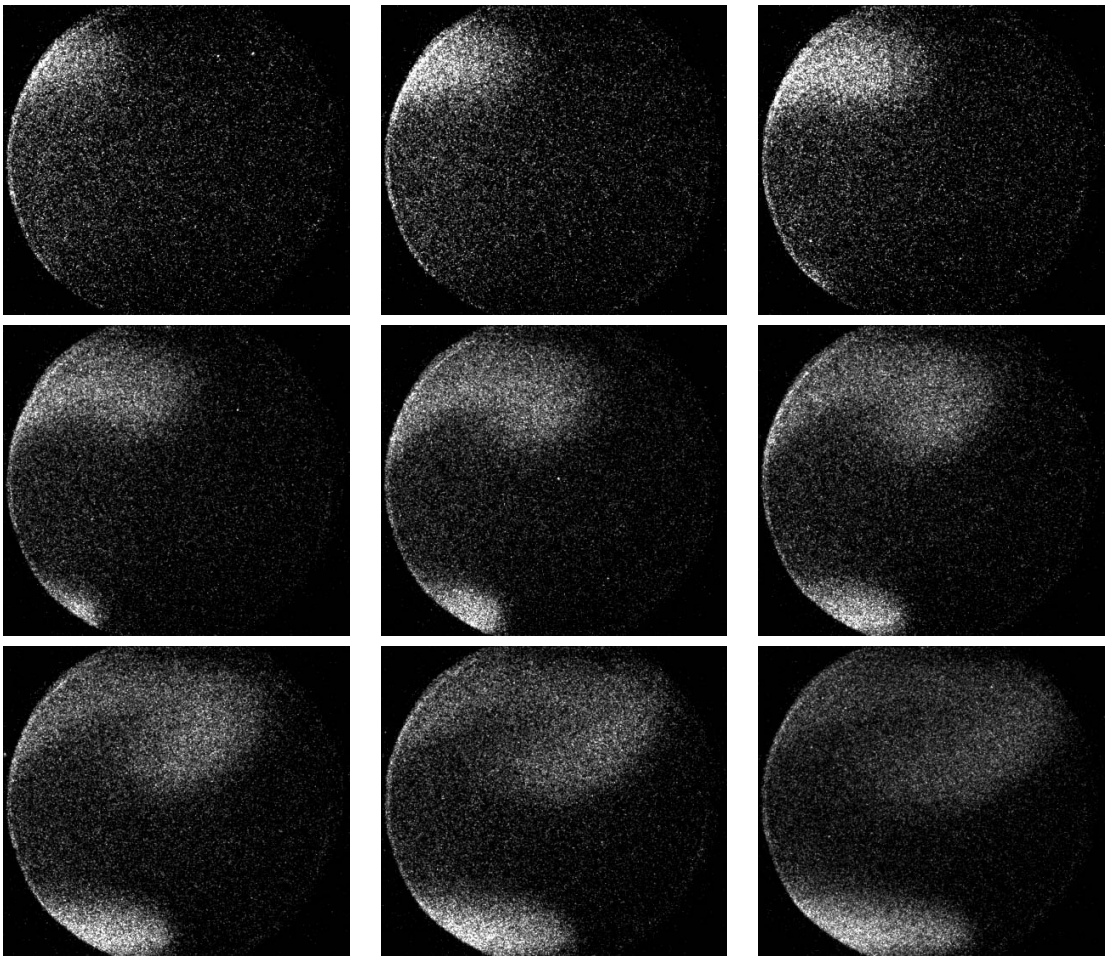

Figure E.4: A sequence of planar laser-induced fluorescence images showing the gravity current propagation (Exp.#gc6). The first image corresponds to a time of 1.8 s measured from when the plate in the sliding valve assembly moves to the open position. Each image is taken at a 0.2 ms time increment.

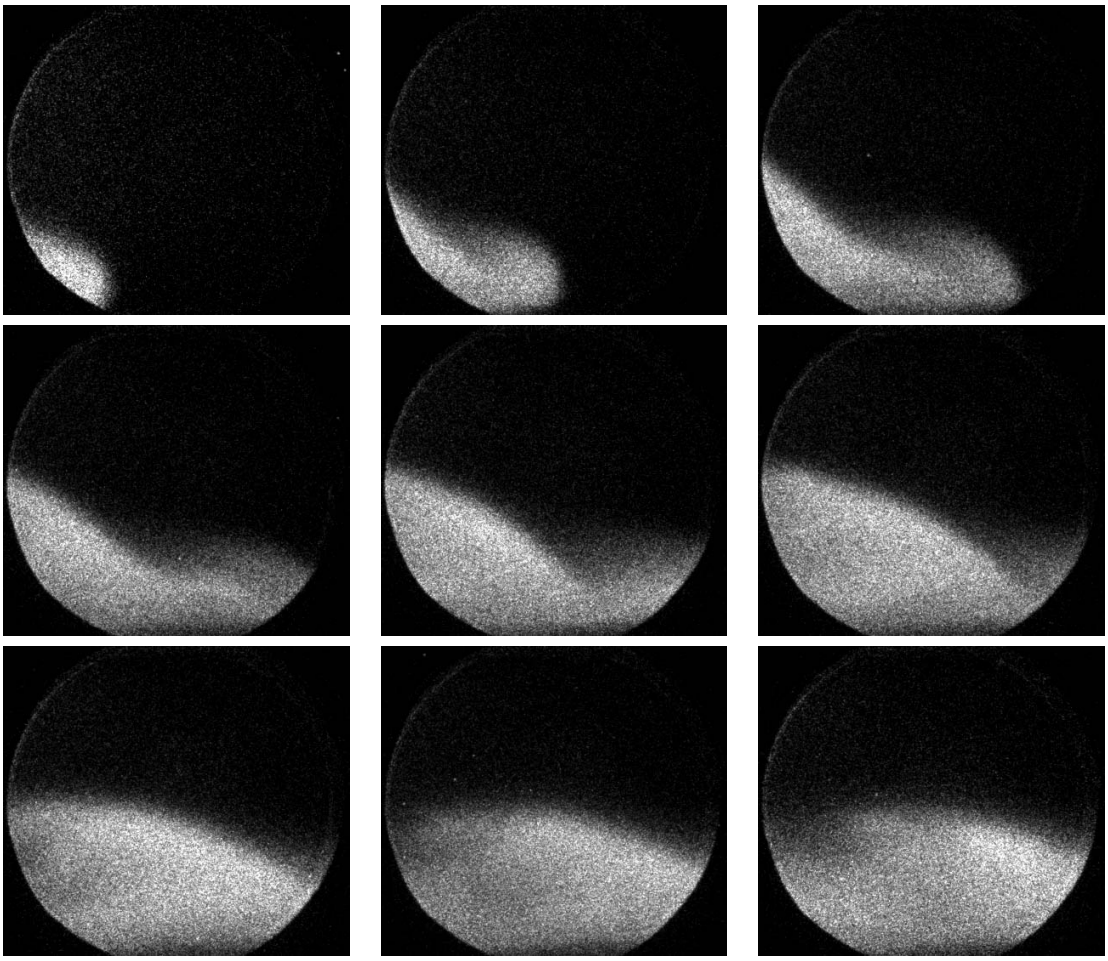

Figure E.5: A sequence of planar laser-induced fluorescence images showing the gravity current propagation (Exp.#gc7). The first image corresponds to a time of 0.8 s measured from when the plate in the sliding valve assembly moves to the open position. Each image is taken at a 0.2 ms time increment.

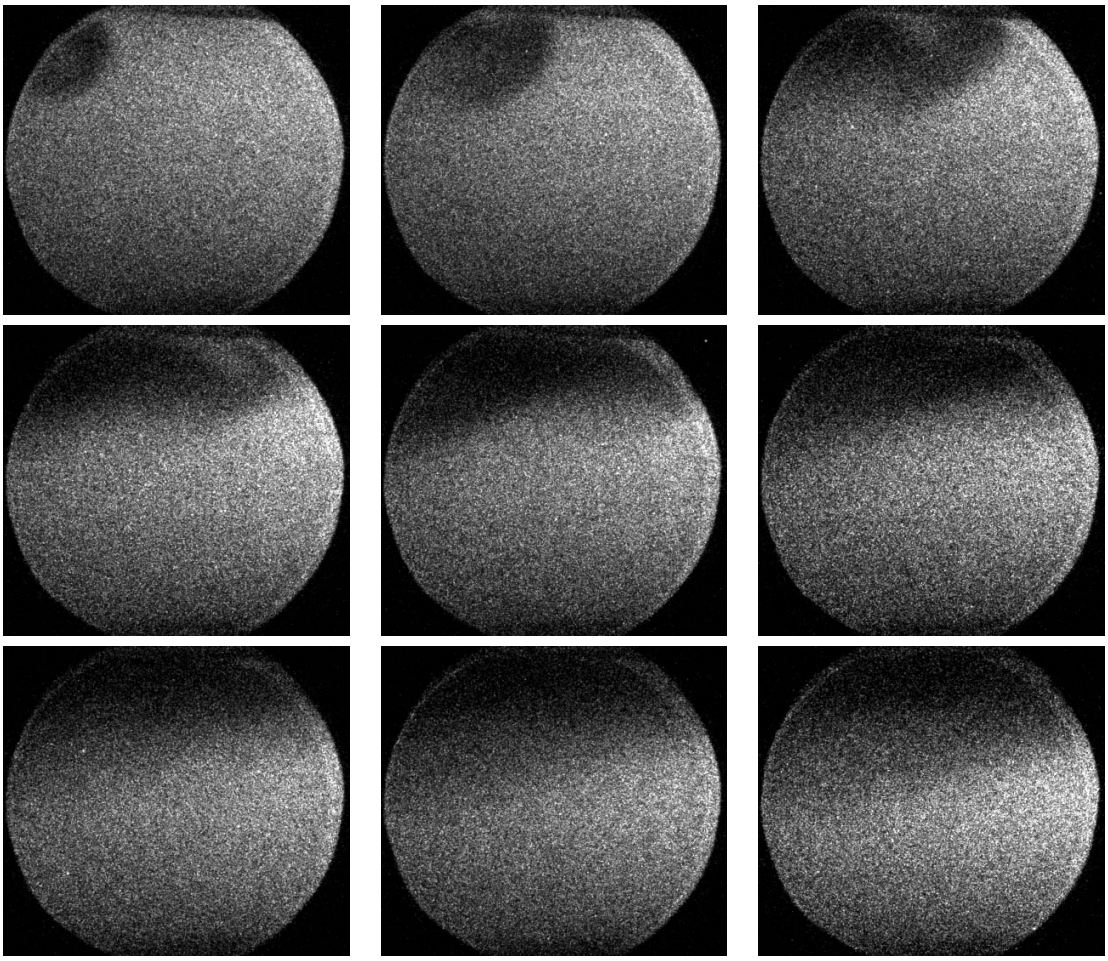

Figure E.6: A sequence of planar laser-induced fluorescence images showing the gravity current propagation (Exp.#gc8). The first image corresponds to a time of 0.8 s measured from when the plate in the sliding valve assembly moves to the open position. Each image is taken at a 0.2 ms time increment.

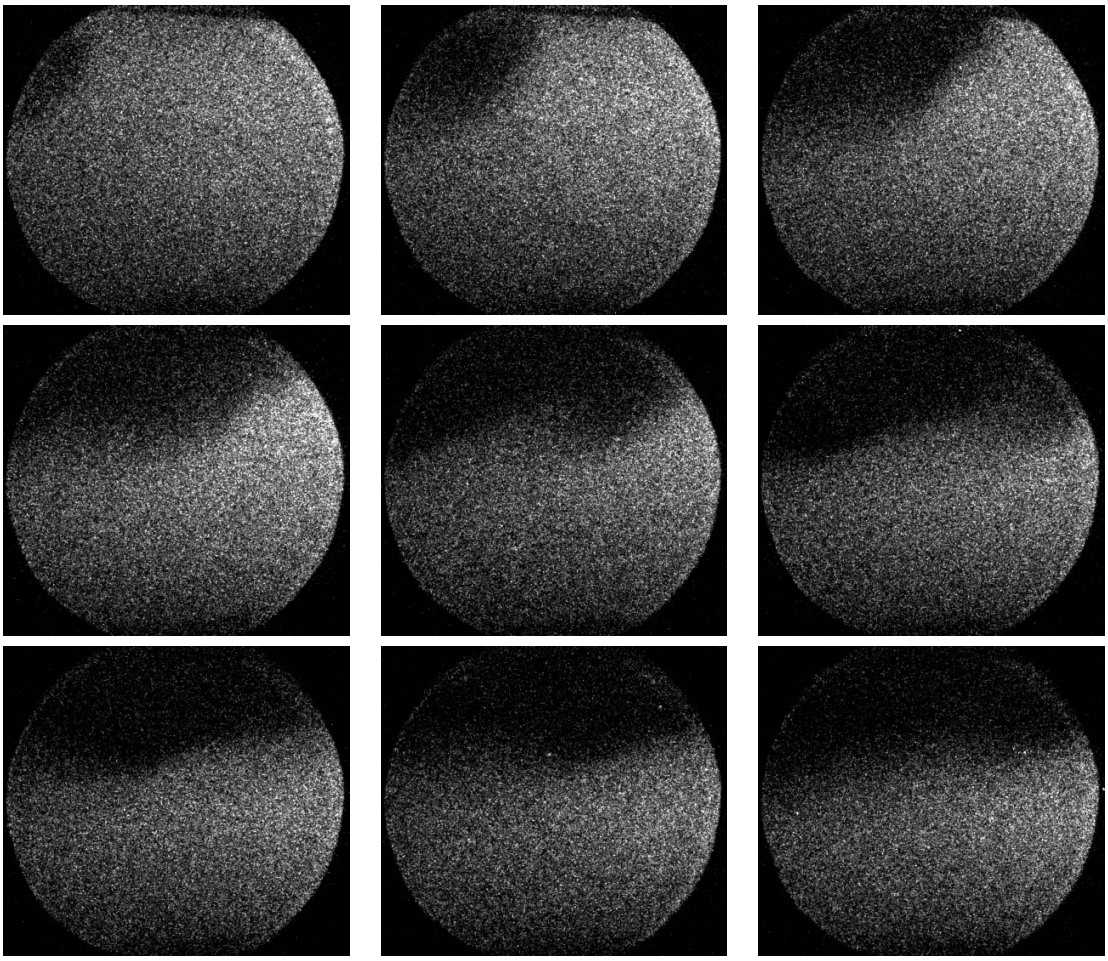

Figure E.7: A sequence of planar laser-induced fluorescence images showing the gravity current propagation (Exp.#gc9). The first image corresponds to a time of 1 s measured from when the plate in the sliding valve assembly moves to the open position. Each image is taken at a 0.2 ms time increment.